Cardiff University

School of Engineering

Condition Monitoring and Fault Diagnosis of Tidal Stream Turbines Subjected to Rotor Imbalance Faults.

A thesis submitted to Cardiff University, for the Degree of Doctor of Philosophy

By

Matthew Allmark

1240237

Abstract

The main focus of the work presented within this thesis was the testing and development of condition monitoring procedures for detection and diagnosis of HATT rotor imbalance faults. The condition monitoring processes were developed via Matlab with the goal of exploiting generator measurements for rotor fault monitoring. Suitable methods of turbine simulation and testing were developed in order to test the proposed CM processes. The algorithms were applied to both simulation based and experimental data sets which related to both steady-state and non-steady-state turbine operation.

The work showed that development of condition monitoring practices based on analysis of data sets generated via CFD modelling was feasible. This could serve as a useful process for turbine developers. The work specifically showed that consideration of the torsional spectra observed in CFD datasets was useful in developing a, 'rotor imbalance criteria' which was sensitive to rotor imbalance conditions. Furthermore, based on the CFD datasets acquired it was possible to develop a parametric rotor model which was used to develop rotor torque time series under more general flow conditions.

To further test condition monitoring processes and to develop the parametric rotor model developed based on CFD data a scale model turbine was developed. All aspects of data capture and test rig control was developed by the researcher. The test rig utilised data capture within the turbine nose cone which was synchronised with the global data capture clock source. Within the nose cone thrust and moment about one of the turbine blades was measured as well as acceleration at the turbine nose cone. The results of the flume testing showed that rotor imbalance criteria was suitable for rotor imbalance faults as applied to

generator quadrature axis current measurements as an analogue for drive train torque measurements. It was further found that feature fusion of the rotor imbalance criterion calculated with power coefficient monitoring was successful for imbalance fault diagnosis.

The final part of the work presented was to develop drive train simulation processes which could be calculated in real-time and could be utilised to generate representative datasets under non-steady-state conditions. The parametric rotor model was developed, based on the data captured during flume testing, to allow for non-steady state operation. A number of simulations were then undertaken with various rotor faults simulated. The condition monitoring processes were then applied to the data sets generated. Condition monitoring based on operational surfaces was successful and normalised calculation of the surfaces was outlined. The rotor imbalance criterion was found to be less sensitive to the fault cases under non-steady state condition but could well be suitable for imbalance fault detection rather than diagnosis.

Acknowledgements

Bosch Rexroth and National Instruments were industrial partners on this research project, accordingly I would like to thank them for their support – particularly, Peter Harlow, Liam Adams and Ian Bell. The project was funded through the SUPERGEN UKCMER Grand Challenges, in particular, 'The Effects of Realistic Tidal Flows on the Performance and Structural Integrity of Tidal Stream Turbines', as such I would like to thank SUPERGEN UKCMER and EPSRC that provide the funding. I also want to thank the wider group of members and young researchers that work or worked on the SUPERGEN and other similar projects – during my time researching on this project an engaging and talented community of researchers helped to drive curiosity and quality in my research, thank you.

I would like to thank all the members past and present of the Cardiff Marine Energy Research Group and particularly the Principle Investigator on the project Prof. Tim O'Doherty. I would also like to acknowledge the huge contribution made by Dr Carl Byrne in producing the $1/20^{th}$ scale turbine – his patience and skill throughout the course of the project were incredible. I would also like to thank Dr Rob Poole and Tiago Jesus-Henriques at the University of Liverpool that helped with the flume testing. A special acknowledgement is required for my supervisors Paul Prickett and Dr Roger Grosvenor. Throughout my time researching they have been a continued source of inspiration, guidance and knowledge. I would also like to recognise all the staff in the Research Office at Cardiff University for their help and guidance.

Thank you to my mum and sister, Kim and Emelye Allmark for their support throughout my time researching. Likewise I owe a debt of gratitude to Malcolm Probert for his support and hospitality over the last 3 years. Lastly, I would like to thank my partner, Angharad Probert, her kindness, patience and loving nature really meant that I was able to work to the

best of my ability. Thank you for putting up with all the stress and for taking my mind of things when I needed a break – you're the best!

I dedicate this work to my father, David Allmark. I'm certain this would have brought him great pride.

Contents

List of Figures

List of Tables

Nomenclature

λ	Tip Speed Ratio
θ	Rotor displacement, ^{o}
ρ	Fluid Density, Kgm^{-3}
τ	Torque, Nm
φ	Magnetic Flux, Wb
ω	Rotational Velocity, $Rads^{-1}$
A	Rotor Area, m^2
a_i	Harmonic Amplitude
C	Rotor Imbalance Measure
C_l	Logarithmic Rotor Imbalance Measure
C_p	Power Coefficient
C_T	Thrust Coefficient
C_θ	Torque Coefficient
f_s	Sampling Frequency, Hz
i_d, i_q	Generator Current Quadrature and Direct Axis, Amps
J	Moment of Inertia, Kgm^2
j	Imaginary Number
L_d, L_q	Inductance, H
P	No. Poles
P_i	Harmonic Phase Angle
$1P$	Rotational Speed of Turbine in Hz

Acronyms

BEMT	Blade Element Momentum Theory
CFD	Computational Fluid Dynamics
CM	Condition Monitoring
EMD	Empirical Mode Decomposition
FFT	Fast Fourier Transform
FMEA	Failure Mode Effects Analysis
HATT	Horizontal Axis Tidal Turbine

HHT	Hilbert-Huang Transform
IGBT	Insular Gate Bipolar Transistor
NBC	Naïve Bayes Classifier
NI	National Instruments
PLC	Programmable Logic Controller
PMSM/PMSG	Permanent Magnet Synchronous Machine / Permanent Magnet Synchronous Generator
PSD	Power Spectral Density
PWM	Pulse Width Modulation
PXI	Rugged PC and Real-Time based platform for measurement and automation systems.
RPM	Revolutions per Minute
RPN	Risk Priority Number
SOSE	Sum of Surface Error
STFT	Short Time Fourier Transform
TCP/IP	Modbus TCP/IP Communications Protocol
TMS	Transient Monitoring Surface
TSA	Time-Synchronous Averaging
TSR	Tip Speed Ratio
TST	Tidal Stream Turbine
VATT	Vertical Axis Tidal Turbine
VOC	Vector Oriented Control

1 Introduction

1.1 Tidal Energy

Energy extraction from the ocean's tides has gained widespread acceptance as a potential contributor to the UK energy mix (DECC, 2013). The driving factor behind the uptake in tidal energy extraction has, in part, been driven by the realisation of finite global resources and environmental impacts of burning fossil fuels (Zhang and Zeng, 2013). The EU Renewable Energy Directive outlines ambitions of the EU community to fulfil 20% of its energy needs via renewable sources by 2020 – it is foreseen that tidal energy extraction could go some way to helping achieve this target (European Union Committee, 2008).

Tidal energy falls into two categories tidal range and tidal stream (Morris, 2014), the focus of this research is on the latter. Tidal stream energy generation directly extracts energy from tidal current, details of the resource in the UK and the technologies currently envisioned are given in Sections 1.2 and 1.3, respectively. A number of tidal stream energy devices have now passed the prototyping phase with companies recently gaining permission to install MW arrays of marine current turbines (Renewable Energy World, 2013). Tidal stream turbines of the horizontal axis arrangement are likely to become the industry standard, although competing design arrangements are still being considered (Chen et al, 2012). At this stage of development tidal energy technology has yet to be proven with regard to long term operational availability and reliability. It is accepted that the harsh marine environments and problems with accessibility for maintenance may exasperate availability and reliability problems. Minimising uncertainty surrounding the operation and maintenance of such devices will thus be crucial in improving investor confidence and achieving economically viable power extraction (Bahaj, 2011).

1.2 UK Tidal Resource

It has been reported that 10 – 15 % of the world's tidal stream resource and 50% of the European tidal stream resource is available in the national waters of the UK (Black and Veatch, 2005). Initially Black and Veatch reported that 58% of the resource of the UK was situated of the coast of Scotland. However, a more recent study by Black and Veatch report a more equal distribution of tidal stream resources of the cost of England, Scotland and Wales (Black and Veatch, 2011). Figure 1.1 shows the distribution of the tidal stream resource throughout the UK (Crown Estate, 2011).

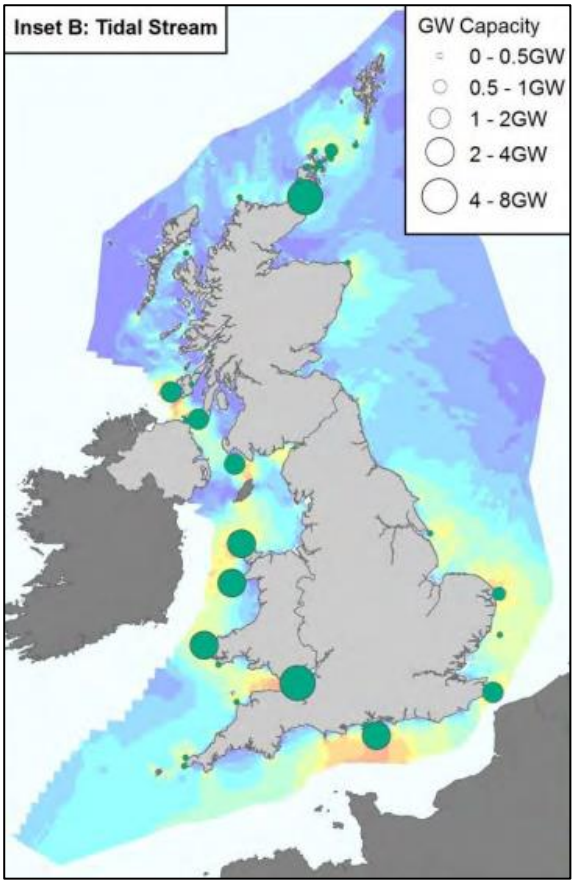

Figure 1.1: Tidal stream resource around the UK (Crown Estate, 2011)

1.3 Tidal Stream Device Types

There are a variety of energy extraction technologies that have been proposed of tidal stream energy extraction. The majority of these devices are tidal stream turbines

characterised by the rotational motion and categories by the axis of rotation as vertical axis tidal stream turbines (VATT) or horizontal axis tidal stream turbines (HATT).

1.3.1 Vertical Axis Tidal Stream Turbines

Vertical axis tidal turbines are characterised by having the axis of rotation perpendicular to the flow direction (Renewable UK, 2011). Whilst the VATT setup hasn't been as widely adopted as the HATT counterpart, VATTs have one distinct advantage in that the can operate regardless of the flow direction without major impacts on operational efficiencies (Eriksson et al, 2008). Operating efficiencies for VATTs of 37% to 40% have been reported (Han et al, 2013; Eriksson et al, 2008) although it has been argued that these lower efficiencies could be due to less research into the operating principle during wind turbine development (Eriksson et al, 2008). The ability to utilise straight turbine blades with little or no twist has also been sighted as an advantage of the VATT setup, leading to a reduction manufacturing cost for VATTs in comparison to the more complex blade designs required for HATT devices (Khan et al, 2009). Figure 1.2 shows two examples of the VATT namely the Kobold turbine and Gorlov turbine.

Figure 1.2: Examples of vertical axis tidal stream turbines (Morris, 2014)

1.3.2 Horizontal Axis Tidal Stream Turbines

Horizontal Axis Tidal Turbines (HATT) are characterised by the rotational axis of the turbine being parallel to the fluid flow (EMEC, 2012). The majority of tidal stream devices currently under development or full-scale deployment are of this type (Chen el al, 2012). HATTs required more hydro-dynamically complex blade designs incorporating complex blade profile, tapers and twists (Khan et al, 2009). However HATTs generally have higher efficiencies than VATTs; reported peak efficiencies range from 39% to 48% of the energy in the fluid flow over the swept area of the turbine (Mason-Jones, 2010; Jo et al, 2013; Faudot et al, 2013; Walker et al, 2013). In order for HATTs to operate in both flood and ebb tides HATTs must incorporate a global yawing system, blade pitch or bi-directional blades which can add to the manufacturing cost and reliability burden of such devices (Liu and Veitch, 2012; Nicholls-Lee, 2011). HATTs exhibit faster rotational velocities than VATT counterparts which to some degree alleviates the problem of generator matching (Khan et al, 2009). Figure 1.3 shows a number of HATTs currently under commercial or prototype deployment.

MCT Seagen S (Marine Current Turbines, 2013)

b) Alstom DeepGen (Alstom, 2013)

c) TEL Delta Stream (Tidal Energy Ltd, 2014)

d) SME Plat-O incorporating Schottel Instream Turbines (SIT) (Sustainable Marine Energy Ltd, 2016)

e) OpenHydro Open Centre Turbine (Brooks-Roper, 2012)

f) Atlantis AS 140 (Atlantis Resources, 2008)

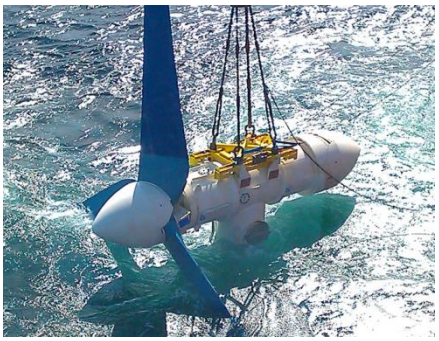

g) Altantis AR1000 (Atlantis Resources, 2012)

Figure 1.3: Examples of HATT under development, prototyping and deployment.

1.4 HATT Operating Principle

The theoretical power available for extraction by HATTs is equal to the energy flux through the swept turbine area normal to the predominant fluid flow direction. This is given by the well-known equation:

$$P = 0.5\,\rho\,A\,U^3 \tag{1.1}$$

Where ρ is the density of the sea water, A is the swept area of the turbine given by $\pi\,R^2$ and U is the free stream velocity of the water. This is the power in the fluid stream hitting a turbine of swept area A. However, full extraction of this power is physically unachievable.

Application of the conservation of momentum and Bernoulli's equation to an actuator disk can be used to calculate the maximum extractable power within a tidal stream of a given swept area. This work was originally undertaken by Albert Betz in 1920 (Betz, 1920) and Manwell et al (2009) present a thorough outline of this process. Figure 1.4 shows an actuator disk within a tidal stream control volume.

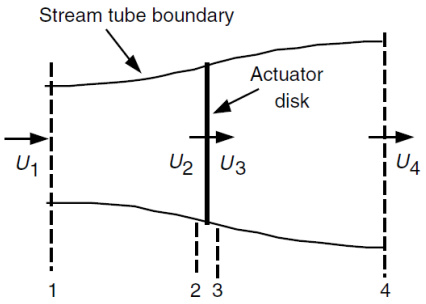

Figure 1.4: Schematic of a tidal stream tube and actuator disc (Manwell et al, 2009).

The setup is subject to the following assumptions:

1. The fluid is incompressible, homogenous and the flow is steady-state ($u_2 = u_3$).
2. No friction drag;
3. Infinite number of turbine blades;
4. Non-rotating wake;

5. Static pressure far upstream and downstream of the turbine is equal to the undisturbed ambient pressure ($p_1 = p_4$).

The thrust on the turbine can then be calculated via conservation of momentum, where the force on the control volume is equal and opposite to that of the thrust. The thrust is then given by:

$$T = \dot{m}\,(U_1 - U_4) \tag{1.2}$$

where $\dot{m}$ is the mass flow rate. The thrust on the actuator disc is positive meaning that U_4 is lower than U_1.The thrust on the disk can also be expressed in terms of the net forces on the disc, in this way the thrust is given by:

$$T = A_2(p_2 - p_3) \tag{1.3}$$

As no work is done between points 1 to 2 and between points 3 to 4, Bernoulli's relation can be used to express p_2 in terms of U_1 and p_3 in terms of U_4, equation 1.3 can then be written as follows:

$$T = 0.5\rho A_2(U_1^2 - U_4^2) \tag{1.4}$$

Equating equations 1.2 and 1.4, given that $\dot{m}$ can be set equal to $\rho A_2 U_2$ results in the following expression for the velocity at the turbine rotor in terms of the inlet and outlet velocities:

$$U_2 = \frac{U_1 + U_4}{2} \tag{1.5}$$

one can define an axial induction factor a that considers the drop in velocity between the free stream and the turbine rotor as a fraction of the free stream velocity:

$$a = \frac{U_1 - U_2}{U_1} \tag{1.6}$$

The axial induction factor a is a measure of the reduction in flow speed downstream of the turbine rotor. When a = 0.5 the fluid velocity downstream of the turbine rotor becomes zero. The power generated by the turbine can then be written as the product of the thrust on the actuator diskand the fluid velocity at the actuator disk:

$$P = 0.5\rho A_2(U_1 - U_4)U_2 \quad (1.7)$$

here, A_2 refers to the area of the actuator disk. Writing U_2 and U_4 in terms of the free stream velocity and the axial induction factor, then completing the square in the resulting equation the power extracted from the fluid by the rotor can be written as:

$$P = 0.5\rho AU^3 4a(1-a)^2 \quad (1.8)$$

One can then define the power extracted by the turbine rotor as:

$$P = 0.5C_p\rho AU^3 \quad (1.9)$$

Where Cp is the power coefficient for the rotor:

$$C_p = \frac{P}{0.5\rho AU^3} \quad (1.10)$$

Using $Cp = 4a(1-a)^2$, by equations 1.8 and 1.9, one can find the theoretical maximum efficiency of a given rotor, which is known as the Betz limit and is equal to 0.5926. Similar treatments lead to coefficients for the thrust, C_t and the torque C_θ developed at the turbine rotor.

$$C_t = \frac{T}{0.5\rho AU^2} \quad (1.11)$$

$$C_\theta = \frac{T}{0.5\rho ArU^2} \quad (1.12)$$

Equations 1.10 to 1.12 are three equations characterising the performance of a given rotor in extracting power, developing thrust and torque from the on-coming fluid velocity, in terms of the free stream velocity approaching the turbine rotor. The non-dimensional quantities are often used for comparison between differing turbine designs and can be utilised to model the expected power output, thrust loading and torque developed for a given rotor and upstream fluid velocity.

Lastly, the tip speed ratio (λ) is the ratio of the tangential velocity of the blade tip to the velocity of the fluid flow perpendicular to the turbine rotor plane. The tip speed ratio or λ is given by:

$$\lambda = \frac{\omega \cdot r}{U} \quad (1.13)$$

Often the non-dimensional parameters outlined in equations 1.10 to 1.12 are plotted against λ allowing comparisons of turbines of differing scales and dimensions.

1.5 Research Objectives

The aims of this work were to consider the condition monitoring of tidal stream turbine rotors. Specifically the work considered the approach of utilising generator measurements to detect rotor damage under non-steady state turbine operation. This aim was met by the following objectives:

- Investigate the suitability of utilising transient CFD model data for generation of condition monitoring approaches.
- Development of a variety of condition monitoring approaches for testing and development in both steady-state and non-steady state turbine operating conditions based on easily acquired generator signals.
- Development of scale model turbine for testing of condition monitoring processes under flume testing conditions.
- Utilise flume results taken at a variety of operating condition to develop a parametric rotor model for real-time turbine simulations.
- Development of drive train simulation apparatus and model to replicate non-steady state turbine operation for testing of CM processes on the data sets acquired from non-steady state turbine operation.

1.6 Thesis Structure

The thesis has been organised to provide the reader with clarity regarding the sequential contributions to the above research objectives achieved during each phase of simulation and testing. As such the thesis has been arranged, henceforth, into the three chapters addressing

differing stages of development; both of the condition monitoring approaches and testing/simulation methods. The three chapters proceed as follows:

Chapter 2 - Literature Review:

The literature review presents a selection of findings from literature relating to turbine reliability, condition monitoring of HATTs. The review also draws experience from rotor monitoring of WTs and the development of scale model TST by researchers.

Chapter 3 - Methodology:

The methodology presents an outline of a condition monitoring architecture and associated development process. The development process is then applied to monitoring of turbine rotor imbalance faults. Lastly the specifics of the monitoring approaches in terms of physical considerations and processing methods are outlined.

Chapter 4 - Initial Steady State Simulatio**:**

The chapter outlines a parametric approach to transient TST rotor simulations based on CFD data which is then developed further in Chapter 6. The structure and details of the condition monitoring algorithms utilised throughout. The chapter provides initial confirmation of the effectiveness of the condition monitoring algorithms applied in the steady state – constant omega.

2 Literature Review

2.1 Introduction

This chapter provides a survey of relevant literature relating to the research activities covered within this thesis. This review was conducted to give scope and guide research activities throughout the period of study. The aim of the presentation of literature is to construct a basis upon which a clear methodology for condition monitoring research could be built. Furthermore the literature review allows for the identification of required and novel areas of condition monitoring research related to the tidal stream turbine (TST) application. The chapter is starts by giving an initial overview of reliability issues facing the TST energy sector, in Section 2.2. The goal of this section is to identify key TST sub-assemblies which can be successfully aided via the adoption of condition monitoring (CM). This notion is developed further in Section 2.3 where the failure modes and reliability of TST rotors is considered. Condition monitoring research specifically related to TSTs is considered in Section 2.4 with the goal of identifying candidate condition monitoring processes for testing and development. Identification of successful monitoring approaches is then presented in Section 2.5 with the goal of gaining insight from the similar application of CM practices. Lastly literature related to scaled TST testing and development is outlined in Section 2.7. The goal of this section is to produce a set of possible testing and simulation procedures which could be adopted for realistic testing and development of the previously proposed condition monitoring processes.

2.2 Tidal Stream Turbine Reliability

The improvement and assurance of the reliability of tidal stream turbines and their sub-assemblies must be considered to be a major factor in the realisation of a well-functioning

tidal stream energy industry. Tidal stream turbines are to face operation in the harsh marine environment and are to be exposed to cyclic and extreme loading. Cyclic loading is enforced on the tidal stream device both the presence of turbulence in the fluid field and due to semi-diurnal tidal cycles which dominate the UK tidal resource. Mixed tidal cycles are found in many other areas where tidal stream energy extraction is feasible. It has been argued that in order to achieve a localised cost of energy (LCOE) that is competitive within the market place, component and turbine availability should be above 75% (Maganda et al, 2014). In moving toward a higher technology readiness level (TRL) and to underpin the significant levels of investment required it has also been stated that the reliability of TSTs and their components must be demonstrated (Wolfram, 2006; Weller et al, 2015).

In order to better understand the reliability challenges facing TSTs, research into their reliability has begun to proliferate. The research presented includes work by the author's research group (Prickett et al, 2011). The limited level of actual TST device installation and implementation means that much of this current work considers TST reliability under minimal operational feedback. Scenarios are applied assuming simplified mechanisms such as the stochastic and cyclic loading of TST assemblies (Wolfram, 2006; Delrom et al, 2011; Delrom, 2014). For this reason one key aspect of the research published over the last ten years is the issue of the effective sharing and organisation of TST operational data. The need for such information to support the industry's understanding of TST reliability issues and challenges has been identified (Wolfram, 2006; Weller, 2015). As an alternative a number of the works published consider the use of surrogate failure data which is modified and then related to the operation of TST components. This enables scenarios to be explored within differing applications to help develop reliability estimates relating to the use of such components in the TST application. In this regard the experience drawn from the wind turbine (WT) industry has been shown to be helpful in generating understanding of TST reliability issues (Wolfram, 2006; Val, 2009).

To date research conducted specifically to address the reliability of TSTs, whilst essential to the sector, hasn't produced a definitive reliability study. The lack such a study, which would fully characterise the reliability issues facing differing TST sub-assemblies, means the CM research could end up being somewhat misguided (Allmark et al 2013). In order to remedy this, the author considered the results of a collection of reliability studies undertaken considering the failure data acquired during wind turbine deployment.

The approach of utilising failure data from related industries to guide TST development has been considered to be suitable by a variety of researchers. The approach of using WT to consider reliability issues within the TST industry has been tested (Val 2009) and it was argued that TSTs will be required to be more robust than WTs. A methodology for conducting an Failure Modes Effects Analysis (FMEA) based on estimations regarding the severity, likelihood of occurrence and the likelihood of detection of faults using analogous wind turbine behaviour has been reported (Prickett et al, 2011). The process was informed by applicable data from relevant industries and the insight of experienced engineers. A similar approach used failure data from WTs of a similar power rating to the counterpart TSTs, as well as other marine industries, to populate a number of TST reliability models (Delorm et al 2011). The reliability models were populated with failure data related to surrogate industries and were then utilised to generate understanding of the reliability issues faced by differing TST setups.

A novel approach to conducting FMEA studies whereby the indicators traditionally used to calculate Risk Priority Numbers (RPNs) were replaced by measures relating to the cost of failure has been presented (Xie 2013). The approach incorporated historical WT data into the reliability analysis presented illustrating this was done to allow for more clarity when comparing the RPNs developed under differing reliability studies.

To consider the overall reliability and the impacts of failures of differing sub-assemblies for tidal stream turbines WT reliability data has been presented and considered (Tavner,

2010). The selection of a sub-assembly to which CM research could be usefully applied was therefore based on this work. Figure 2.1 shows the observed number of failures per annum and the downtime, in days, associated with sub-assembly failure for WTs. The data shows a number of critical sub-assemblies which either have a high likelihood of occurrence or which have long down times associated with the failure of the given sub-assembly. It was considered that failure of the rotor sub-assembly would result in prohibitively long downtimes and had a reasonably high likelihood of occurrence. As such the author chose to direct the CM research activities undertaken within this doctoral project towards detection and diagnosis of TST rotor fault conditions.

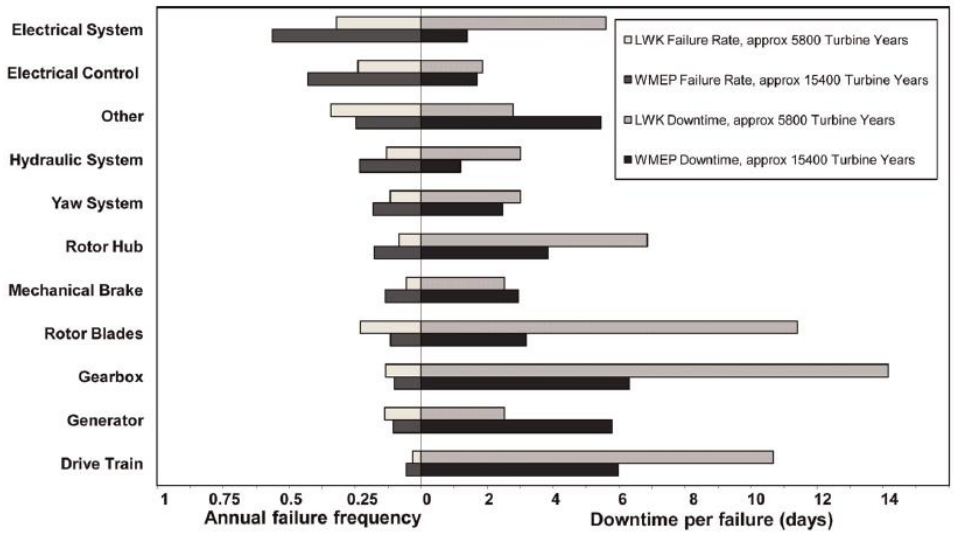

Figure 2.1: Failure rates and downtimes for differing turbine sub-assemblies (Tavner et al, 2010).

2.3 TST Rotor Reliability and Failure Modes

A number of research papers have been published considering the reliability of TST rotor blades. Most recently Kumar and Sarkar (2016) provided a review of hydrokinetic turbine reliability as part of a broader review of the industry. The review considers that torque fluctuations have a major impact on turbine reliability due to fatigue loading and vibration. This view is supported by the consideration of the work conducted by Hu et al (2012) which explores both time dependent and instantaneous probability of turbine rotor failure. The

work reported that the time dependent probability of failure has a greater impact on turbine reliability than the instantaneous probability of rotor failure.

Chen et al 2014 also provides a brief review of many of the works published and outlined many of the contributing factors impacting on TST rotor blade reliability. Chen points out that extreme loading, cyclic loading, the saline environment and biofouling will have an impact on TST blade reliability. Byrne et al (2011) investigate the likelihood and conditions required for cavitation to occur during the operation of TSTs. In considering the effects of cavitation Byrne et al note that the cavitation can cause or exacerbate blade pitting which can result in reduced power output, water ingress and rotor imbalance.

Sloan et al (Sloan et al, 2009) conducted a reliability assessment of tidal stream turbines or ocean turbines and address in detail the effects of biofouling on tidal stream turbine operation. Initially the study highlights biofouling, impact of marine life, fluid salinity, underwater turbulence and difficulties in accessing machinery as key factors effecting tidal stream turbine operation. The authors, as well as highlighting the effect of biofouling on the ability of TSTs to efficiently generate electrical energy, also point out the effect of biofouling on rotor condition monitoring systems. The authors acknowledge that biofouling will reduce the ability of sensors to measure key rotor condition indicators and could well lead to sensor data masking rotor fault conditions. The study goes on to consider methods for reducing the extent to which biofouling will occur by considering the micro-geometry of turbine blade coatings.

Val et al (2014) considered the reliability of TST rotor blades when subjected to extreme loading due to turbulent velocity fluctuations impacting a TST subjected blade pitch control. Specifically the work generates a probabilistic model of the likelihood of bending failure considering the stochastic nature of the fluid velocity, the resistance of turbine blades and the pitch response cut-off frequency. The paper generates results relating to design safety factors in terms of load factors and resistance factors.

Li et al (2014) present a hydrokinetic turbine blade reliability study considering the effect of cyclic loading on composite blade fatigue life. Three differing blade structures were compared within the study, namely a hollow blade, a blade filled with a reinforcement foam core and a blade with a shear web. The study used Hashin damage theory (Hashin, 1980) to identify key failure modes and critical design points for each of the blade structures. A coupled BEM-FEM method was then utilised to calculate the stress response of each of the blade designs to hydrodynamic loading. The hydrodynamic input to the model was developed utilising the Expansion Optimal Linear Estimation (EOLE) method and the Hashin damage initiation criteria was applied to the stress response results to identify critical design points and failure modes for each of the blade designs.

This section has considered elements of the current body of research relating to TST rotor reliability. This has shown that attention has been paid to methods of estimation of TST rotor reliability. In the cases used the failure modes considered are likely to result in rotor weight imbalance (water ingress) or hydrodynamic performance imbalance (biofouling, blade pitting, pitching mechanism failure, composite delamination). Less clear consideration has been given to the physical mechanisms of TST rotor failure and the symptoms of such failures. In the author's view the body of research currently available gave little guidance on how to simulate rotor fault conditions. Such simulations are required to underpin research aimed at producing reliable TST rotor CM methods.

2.4 Condition Monitoring of Tidal Stream Turbines

Experience within the wind energy sector has suggested that online CM and fault detection could minimise maintenance costs and improve availability of the energy extraction technology (Hameed et al, 2010; Yang et al, 2010; Tian and Jin, 2011). The definition of effective CM practices at this stage in the device technological development will also offer the added benefit of informing the design process. Not least of the considerations that can be made relate to the embedding of monitoring functions into the

device; the use of sensors that are already included in the design of the device can reduce cost and increase effectiveness. In particular it is envisaged that operating conditions leading to failure can be examined in detail as a consequence of the development and testing of monitoring functions, providing invaluable insight into robust turbine design. Whilst the design enhancements enabled by CM will give rise to such benefits, at this stage of technological development the largely undefined and novel nature of the energy extraction technology poses significant difficulties in producing robust well suited monitoring approaches. This notion of the novel application area was reflected in the state of the research conducted into CM of TST rotors.

In order to identify research aimed specifically at CM approaches for TSTs a comprehensive search of publications in the topic was made. The search was conducted using 5 prominent publication databases, namely ACM, Compendex, Google Scholar, IEEE explore and Scopus. The search was conducted using the following terms for TST devices, “Tidal Stream Turbines”, “Marine Current Turbines”, “Ocean Turbines” and “Hydrokinetic Turbines”. The device terms were coupled with the following process terms “Condition Monitoring”, “Fault Diagnosis” and “Fault Detection”. The searches were set to return results containing both one of the device terms and the process terms in either the publication title or body of text. This resulted in 12 search queries over 5 research databases. The search results are presented in Table 2.1, where it can be seen that 173 papers were returned via the search.

Table 2.1: Results of the literature survey into condition monitoring research aimed specifically at tidal stream turbines.

Database	No. of Results Returned via Search Term.	No. of RELEVANT Results Returned via Search Term.
ACM	0	-
Compendex	4	0
Google Scholar	95	10
IEEE Explore	50	13
Scopus	24	14

Of the 173 publications returned during the search, 37 publications were considered to specific relevance to the application of condition monitoring techniques to tidal stream turbines. Due to results repeated in multiple databases the final figure of unique publications deemed to have relevance specifically to the condition monitoring of tidal stream turbines was found to be 30. Lastly it was noted that 5 of the 30 unique results were publications upon which the researchers was a lead or named author.

Caselitz and Giebhardt (2005) presented one of the earliest papers aimed specifically at the condition monitoring of TSTs. The paper aimed to apply and adapt knowledge acquired in the condition monitoring of both on-shore and off-shore WTs to the task of CM of TSTs. Figure 2.2 shows an example of the possible structure and hardware of a condition monitoring system of TSTs. The system contains many of the elements included in a WT monitoring systems, including accelerometers for gearbox and baring vibration monitoring and fibre bragg gratings for blade and structural load monitoring. The system is supported by environmental measurements, specifically by measurements of the fluid velocity upstream of the turbine rotor. This work goes on to outline the generalities of some condition monitoring algorithms to be applied to TSTs based on the hardware setup outlined. The algorithms presented include overall performance monitoring to observe deviation of power

output for a given fluid velocity from the characteristic output for the turbine. Other algorithms mentioned within the publication involve vibration measurement of structural components with subsequent observation of Eigen frequencies with the deviation of Eigen frequencies from expected values highlighting changes in structural properties of the component being monitored. The paper lastly considers internet based communications and database management systems.

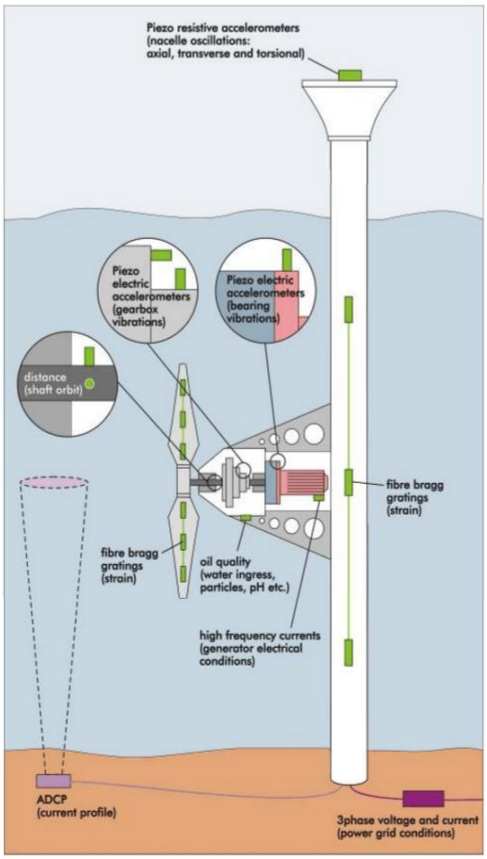

Figure 2.2: Figure showing the possible structure of a condition monitoring system for use in TST deployments (Caselitz and Giebhardt, 2005).

Beaujeany et al (2009) presented considerations of many of the reliability issues faced by TSTs and the associated monitoring hardware. Mjit et al (2010) conducted work considering order analysis of vibrational data as a means of fault detection, the work was first conducted on a commercial fan and later extended to monitoring of a small boat propeller. The work also discussed elements of the data storage and capture processes. The order analysis

methods applied were successful in identification of imbalance and misalignment. The research undertaken and presented by Mjit et al was extended in 2011 (Mjit et al, 2011a) to incorporate a more fully developed Smart Vibration Monitoring System (SVMS) which handled much of the data capture storage and processing autonomously. The system included many of the techniques performed off-line by vibration monitoring specialists including advanced signal processing of vibration data. Specifically the software processed raw vibrational data via Power Spectral Density, Fractional Octave, Cepstrum, Hilbert Envelope, Wavelet Transform and overall vibrational statistical characteristics. The process was developed using LabVIEW and tested using a drive train test rig setup to harbour fault conditions by attaching weights to the drive train. Changes to the performance metrics calculated via the advanced signal processing operations listed above were successfully tracked for three differing levels of fault severity and for two rotational velocities.

Further works were published by (Mjit et al, 2011b), the publication presented an overview of many of the condition monitoring processes as applied by the researchers to the TST drive train simulation apparatus previously developed (Mjit et al, 2011a). The work presents details of power spectrum analysis, Cepstrum Analysis, kurtosis measurements, STFT and Hilbert transform processes as applied to vibrational data captured using the outline test rig, Figure 2.3Figure 2.2 shows a schematic of the test rig used.

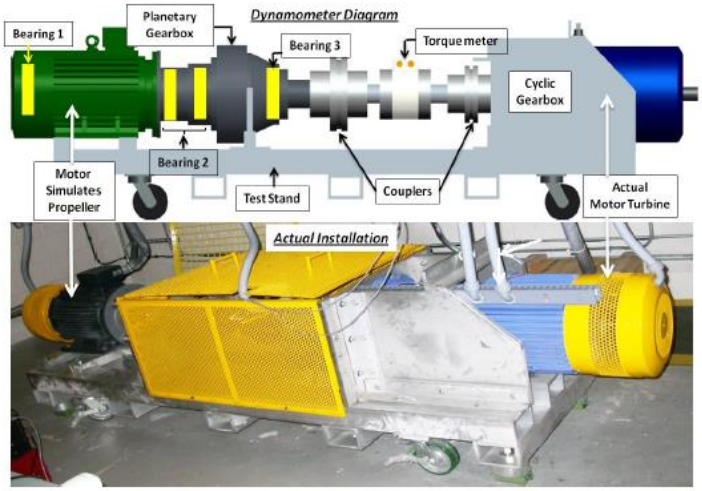

Figure 2.3: Schematic and photograph of a dynamometer test rig for undertaking TST simulations for CM process development (Mjit et al, 2011a).

Research based upon a dynamometer setup similar to that shown in figure 2.3 was reported by Duhaney et al (2011a). One important aspect of this research considered the fusion of data from numerous accelerometers, both low and high frequency, mounted throughout the dynamometer. Specifically low frequency accelerometers were mounted on components between the high speed shaft of the generator and the motor used to simulate turbine rotor inputs to the system. The components between the generator and motor included two planetary gearboxes. Faults in the system were then simulated by applying periodic impacts to the gearbox connected to the turbine simulating motor. The impacts were applied at two differing intensities. The researches acquired data from the six accelerometers for baseline or normal turbine operation, low fault severity and high fault severity. The data sets were pre-processed to extract time-frequency information via the Haar Wavelet transform, resulting in 18 files of 10,000 readings. Seven machine learning processes (decision tree, Naive Bayes, 5-NN, Logistic Regression, MLP, SVM and random forest) were then applied to the data sets in order to test the ability of the machine learning procedures to make successful fault or no-fault classification. Mixed results were found for the differing machine learning algorithms with the random forest and decision tree classifiers having 100% correct classifications and Naïve Bayes, 5-Nearest Neighbour and logistic regression having the highest misclassification rates.

In related research (Dehaney et al, 2011b) consideration of feature fusion processes were also considered. This involved a similar application of the vibration monitoring and machine learning processes to a commercial fan, which was subjected to 'tilting' faults and a fault case achieved by slowing the fan rotor via a foreign object. The study showed that feature fusion resulted in more effective classification of the fault vs no-fault state of the fan rotor. A third publication by Dehaney et al (2011c) builds directly upon the study previously presented. The work considers the same test rig setup along with the same fault simulation procedures but develops the work by further fusion of the information extracted via the Haar

wavelet transform. As well as further fusion of each of the accelerometer channels, differing feature selection processes were applied to reduce the dimensionality of the fused application before applying machine learning algorithms. The study was also extended to include five-fold cross validation in the training and application of the machine learning and feature selection processing. A varying number of the features ranked by the feature selection algorithms were chosen and used to train the fault detection machine learning algorithms. The results show that fault detection can be improved via feature fusion and can perform well under the use of a reduced number of features as highlighted by the feature selection processes.

Dehaney et al (2012a) also extended the application of machine learning processes in TST fault detection. The goal of this extended study was to consider the effects of class imbalance (having more data related to one state than the other) on the successful implementation of machine learning method for TST fault characterisation. The study found that the performance applied machine learning algorithms suffered significantly when large class imbalances were simulated. The same researchers also published further research based on the experimental setup previously outlined in (Dehany et al, 2011a). The methods applied were concerned with the application of Wavelet transforms as a feature extraction technique and the subsequent comparison of feature fusion and non-feature fusion applications of machine learning algorithms (Dehaney et al, 2012 b-e). The research was further extended in 2013 to the classification of turbine state rather than fault detection. The work showed that the five nearest neighbour algorithm gave 100% correct classifications (Dehaney and Khoshgoftaar, 2013).

Two publications by Waters et al in (2012 and 2013) presented research considering the detection, localisation and identification of bearing faults in TST applications. The two papers presented similar studies within which models for bearing loading under bearing race cracking were developed. The models were then used to guide the development signal

processing methods which were then applied to vibration signals acquired from two accelerometers mounted on dynamometer test beds. In order to detect bearing damage the power spectral density of the measured accelerometer signals was utilised as well as the coherency between them. A fault condition was said to exist if the power observed at frequencies of interest (found via impact test) exceeded a given threshold. The fault was then localised to a given bearing by comparison of the power spectral density measurements at the frequencies of interest from the two accelerometer measurements. Envelope tracking was then used to identify the fault type (inner vs outer race fracture) by considering the timing of the observed impacts yielding the observed increases in spectral power at the frequencies identified.

The need, requirement and impact of the adoption of CM systems within the TST industry was considered by Elasha et al (2013). The publication lists a number of observed failures during the limited number of TST deployments. These are:

1. The failure of turbine blades mounted on the open hydro device in 2009 due to fatigue in the Bay of Fundy.
2. A single blade failure of the two-bladed Atlantis AK100 in Orkney during 2010 due to a manufacturing fault.
3. Removal of the Race Rock turbine from Middle Island in 2011 due to large reductions in power output caused by a build-up of micro algae, Figure 2.4.

Figure 2.4: Condition of the Race Rock turbine after deployment (Elasha et al, 2013).

The researchers also present a comparison of the load cases of a wind turbine and TST of similar power ratings, the comparison is presented in table 2.2. The authors then develop CM approaches to gearbox monitoring, gearbox monitoring was considered due to the high torque loads expected in TST drive trains and the long down times observed in the WT industry for such failures. They then outlined the structure of a horizontal axis turbine with a hydraulic yaw system and use the MADe software to model reliability of the system. The model considered a number of operating parameters for each of the components of the turbine including the functionality of each assembly, the associated failure modes and symptoms and lastly the criticality of each component. The model was then used to generate RPNs for each of the components.

Table 2.2: Comparison of the operating parameters of a TST and WT of similar power ratings (Elasha et al, 2013).

Wind Turbine Parameters	**Tidal Turbine Parameters**
Density = 1.22 kgm^{-3}	Density = 1000 kgm^{-3}
Rotor Diameter = 27.1 m	Rotor Diameters = 9.31 m
Velocity = 12 ms^{-1}	Velocity = 2.6 ms^{-1}
Thrust Load = 146 kN	Thrust Load = 675 kN
Torque = 564 kNm	Torque = 837 kNm

The impact of CM on system reliability was then studied using the developed model. Specific attention was given to the reliability analysis of the gearbox sub-assembly under vibration, oil debris and torque monitoring regimes. The work showed that the adoption of CM strategies must be developed with consideration of the failure modes and symptoms of related to the given failure mode. The paper also noted the highest improvement in sub-assembly reliability after adopting a CM regime was observed for the turbine blades, gearbox, yaw system and generator sub-assemblies.

Work undertaken within the author's research group considering the use of TST stanchion thrust measurements for CM of TST blades has been published (Grosvenor et al, 2014). This utilised a combination of CFD modelling exercises with flume testing experiments to develop and test a CM approach based on frequency analysis of both computed and measured turbine thrust signals. The work showed that increasing presence of the turbine rotational frequency observed in thrust spectra was a useful indicator of turbine rotor imbalance. The work utilised a combination of CFD modelling and flume testing results to study the applicability of thrust monitoring – this process of utilising both CFD modelling and testing to develop and test monitoring hypothesis will be utilised within this research.

Whilst the number of research publications in the specific area of TST condition monitoring was found to be limited, research in this area has been highlighted as an important aspect of TST development. To support this notion a research project known as TidalSense was setup and funded under a European Commission in 2009, (CORDIS, 2009). The project was then extended to become TidalSense Demo in 2011 (CORDIS, 2012). The work undertaken by the research project utilised a number of industrial partners and research institutions with the goal developing and demonstrating approaches to the CM of TST. The work focused on the use of Long Range Ultrasonic Technology (LRUT) to inspect cabling and turbine blades (CORDIS, 2012). The process of using guided Ultrasonic waves imparted

by an actuator with the blade response to the waves recorded by sensors was developed and illustrated over the course of the two projects (Makaya et al, 2011; TidalSense, 2011). The work developed throughout the overall TidalSense project allowed for the imbedding of ultrasonic sensors during composite turbine blade manufacture creating a robust solution.

2.5 Experience in Failure and Monitoring of Wind Turbine Rotors and Blades

Wind turbine blades can account for between 15% and 20 % of the capital cost of a given wind turbine (Liu et al, 2015). The large portion of the cost attributed can to some degree be attributed to the growth in the diameter of wind turbine rotor in recent years. By necessity TST rotor diameters are set to be significantly smaller than those of wind turbines of a similar rating. However, due to the higher loading on a TST, it is likely the blade cost will still account for a significant portion of the whole capital cost.

Within the literature a variety of WT blade and hub failure modes have been considered including rotor imbalance and asymmetries, blade and hub corrosion, blade cracking and deformation, fatigue damage, reduced blade stiffness and increased surface roughness (Liu et al, 2015, Qiao and Lu, 2015a and Qiao and Lu, 2015b). Rotor imbalance failures have been noted to arise from two main sources aerodynamic imbalance and blade mass imbalance, furthermore it has been reported that 20% of wind turbines operated with either mass or aerodynamic imbalance (Losi and Becker, 2009). Aerodynamic imbalance occurs when the aerodynamic properties of the blades are not balanced leading to differing levels of thrust and tangential force developed by each blade. Aerodynamic imbalance can also occur due to pitch control actuator failure (Zeng et al, 2013), asymmetric icing, accumulation of dirt or blade damage due to impact or fatigue loading (Kusnick et al, 2015; Gardels et al, 2010; Gong and Qiao, 2012).

Blade mass imbalance occurs when the distribution of mass about the rotor is not balanced correctly. This can occur due to manufacturing error, errors during construction

and varying degrees of shift and wear of blades over the operating life of the turbine (Kusnick et al, 2015; Gardels et al, 2010; Gong and Qiao, 2012). Blade mass imbalance can also occur due to water ingress and distortion of the blade (Hyers and McGowan, 2006; Giebhardt, 2007). It must also be noted that the associated rotor imbalance leads to increased stress on the turbine system via the introduction of speed and torsional fluctuations. This can reduce the operational of many turbine sub-assemblies, including the rotor assembly, drive train and gearbox assemblies (Hyers and McGowan, 2006; Hameed et al, 2009).

Failure of rotor blades due to fatigue damage occurs due to the cyclic loading of the blades over the operational life of the turbine. It has been stated that fatigue damage of WT blades can lead to delamination of composite blade materials as well as cracking of turbine blades (Qiao and Lu, 2015a). The nature of cyclic loading in the marine environment may be considered to be greater than that of the operational environment of wind turbines; as such fatigue damage to TST rotor assemblies is set to be a major cause for concern for TST developers.

Increases in blade roughness and decrease in blade surface conditions occur in WTs due to icing and the build-up of debris. In the context of TSTs this problem is thought to be exacerbated due the saline environment of the ocean and the biofouling that is likely to occur as a result of operation in the ocean environment.

2.6 Applicable Condition Monitoring techniques

Due to the large number of failure modes and the associated expense of such failures wind turbine rotor assemblies are the subject of a range of research projects. A number of these have been conducted to consider effective ways to monitor wind turbine rotor condition. This section outlines the main research trends in four classes of monitoring methods and processes, namely: acoustic emission monitoring, vibration monitoring, electrical signal monitoring and strain monitoring. The selected methods were identified from within more comprehensive reviews of CM research applied to WTs (Qiao and Lu,

2015a and 2015b, Liu et al, 2015 and Antoniadou et al, 2015). An example of this is given in Table 2.3 which shows details of the CM processes applied to WTs (Qiao and Lu, 2015a).

Table 2.3: Outline of the use of differing monitoring approaches (Qiao et al, 2015a).

Signal	Monitored components	Intrusive	Complexity		Capability					SNR/ Sampling frequency	Cost	Std	Used in Com CMS
			Install	Signal process	Online/ Offline	Incipient fault detection	Fault detection	Fault location	Fault identify				
Vibration	Bearing, blade, gearbox, generator, shaft, tower	Yes	High	Medium	Online	Yes	Yes	Yes	Yes	High/ Medium	High	Yes	Yes
AE	Bearing, blade, gearbox	Yes	High	High	Online	Yes	Yes	Yes	Yes	High/High	High	Yes	Yes
Strain	Blade	Yes	High	Medium	Online	Yes	Yes	Yes	Yes	High/low	High	No	Yes
Torque	Blade, gearbox, generator, shaft	Yes	High	Medium	Online	Yes	Yes	Yes	Yes	High/ Medium	High	No	No
Temp	Gearbox, generator, bearing, power converter	Yes	Medium	Low	Online	Possible	Yes	Possible	No	High/Low	Medium	Yes	Yes
Oil parameters	Bearing, gearbox, generator	Yes	Medium	Low	Both	Possible	Yes	Possible	Possible	High/Low	Medium or high	No	Yes
Electrical signals	Bearing, blade, gearbox, generator, motor, power converter, sensor, shaft, tower	No	Low	High/ medium	Online	Possible	Yes	Yes	Yes	Low/ Medium	Low	No	Yes
SCADA signals	Blade pitch, control system, generator, hydraulic system, power converter, sensor, overall system	No	–	Medium	Online	Possible	Yes	Possible	Possible	Low/Low	Low	No	No
NDTs	Blade	Yes	Low	Low	Both	Possible	Yes	Yes	Yes	High/–	High	No	No

2.6.1 Acoustic Emissions Monitoring

Acoustic emissions are resultant from the release of energy in the form of elastic waves within a material subject to dynamic deformation (Balageas et al, 2006). Turbine blades which are subjected to stresses and strains may emit sound waves referred to as acoustic emissions (Bouno et al, 2005). Typical sources of AE include such events as, crack initiation and propagation, breaking of fibres, matrix cracking, fretting between surfaces at de-bonds and de-laminations (Schubel et al, 2013). The potential causes of AE can be linked to the failure mechanism expected in wind turbine blades, suggesting that AE can be utilised for WT blade monitoring purposes. AE are generally measured via piezoelectric sensors mounted directly on the turbine blade and AE detected by the sensors which are deemed to be outside normal operating conditions are referred to as ‘hits’ that are characterised by amplitude, energy counts, rise time and average signal level, as well as other characteristics (Schubel et al, 2013). Many properties of the ‘hits’ encountered by the sensor equipment are

used to determine if, what and where damage has occurred in the turbine blade. The application of AE to tidal stream turbine monitoring could well be useful and more research in this area is required. It considered the harsh marine environment may cause reliability issues for the imbedded sensors required for such a monitoring approach.

2.6.2 Vibration Monitoring

Vibration monitoring has been used consistently in commercially deployed WTs for CM. It has been used for fault detection in sub-assemblies and has to some degree been standardised by the introduction of the ISO 10816 standard (2014). The goal of vibration monitoring of turbine blades is to view changes in the vibrational response of turbine blades under differing blade fault conditions. Often to enable the vibration monitoring of turbine blade condition the sensor (which may be an accelerometer, velocity sensor or displacement sensor) is mounted directly on the turbine blade (Qiao and Lu, 2015b and Kusnick et al, 2015). Generally two types of feature extraction process are used in the analysis of vibration data, namely; statistical and time-frequency methods. Typical examples include the use of vibration monitoring to identify WT rotor asymmetry by changes in the observed 1P frequency (Caselitz and Giebhardt, 2005). In other work researchers applied Empirical Mode Decomposition (EMD) to vibration data and used the extracted Intrinsic Mode Functions (IMFs) as an indicator of blade cracking (Abdelnasser and Alhussien, 2012). In another case accelerometers were applied to blade tips and changes in the RMS and mean values of the vibration data used to observe the effect of rotor pitch imbalance; the method was able to identify which blade was misaligned (Kusnick et al, 2015). Whilst vibration monitoring could well be suitable for application to TST rotor monitoring further research in this area is required. As with AE monitoring it is considered that there may be reliability issues relating to the vibration sensors due to the harsh marine environment.

2.6.3 Electrical Signal Monitoring

Measuring changes to the current and voltage at the generator terminals has been utilised to undertake monitoring of a number of turbine assemblies. Academic researchers and commercial WT operators have deployed this technique to monitor WT rotor imbalance (Qiao and Lu, 2015b). The use of such monitoring practices has gained significant attention in research due to the ease of implementation and the negation of need for additional sensors suits (Qiao et al, 2015). Generally monitoring of generator stator currents in the frequency domain is used to observe frequencies relating to rotor fault behaviours, predominantly an increase in the 1P frequency which has been reported to be a good indicator of rotor imbalance (Caselitz and Giebhardt, 2005; Kusnick et al, 2015; Qiao et al, 2015). This approach is considered to be suitable to the TST application, whilst early detection may be infeasible utilising such methods, it was considered that this approach has the advantage of not requiring additional sensors which may have reliability issues. The research presented within seeks to develop understanding in the application of such processes to TST rotor monitoring.

2.6.4 Strain Monitoring

Strain monitoring of turbine blades requires embedded sensors in the turbine blade and has been used for blade monitoring in a variety of ways (Qiao and Lu, 2015b). It has been reported that strain measurements can be utilised for detection of structural defects, blade icing, mass imbalance and lightning strikes (Crabtree et al, 2014). Strain measurement sensors are available in two main categories electrical sensors, for example traditional resistance strain gauges, and fibre optic sensors such as, Fibre Bragg Gratings (Schubel, 2013). Generally Fibre Bragg Gratings are preferred to the traditional electrical resistance based methods for WT blade monitoring (Hyers et al, 2006). Fatigue damage monitoring via FBGs has undertaken by monitoring load cycles and creating RUL estimates based on S-N

curves for a given blade material (Hyers et al, 2006). Strain measurements have been used for crack initiation detection citing uniform strain, compressive strain and non-uniform strain as potential crack initiation indicators (Pereira et al, 2015). Recently strain monitoring has been utilised for potential blade-tower impact monitoring via estimation of blade deflection fromm strain measurements. The process used linear correlation between measured strain and blade deflections to generate alarms if possible blade-tower impacts could occur (Lee et al, 2016).

2.7 TST Scale Model Development and Testing

The CMERG has previously developed two working 0.5m meter diameter flume based turbines. These have been used to conduct turbine design studies using CFD. Both of the turbines were developed using the horizontal axis tidal turbine (HATT) form. Details of the first turbine setup can be found in (Mason-Jones, 2010). This turbine consisted of a rotor submerged in a re-circulating flume tank. The rotor could be coupled via either a flexible or rigid drive shaft to a 1.28 KW Baldor brushless AC servomotor, which was situated above the flume. The Baldor motor was used to supply a braking torque to the rotor to provide control over the turbine's rotational velocity for a given flow rate. The regeneration energy produced was dumped into a 1 KΩ resistor and dissipated as heat. Testing with the first generation turbine was successful in validating and informing CFD models developed within the research group. The turbine did, however, have shortcomings in the form of limited operational data produced. This consisted of only torque (via motor current) and angular velocity (via motor encoder) measurements. There were also problems in use arising due to the long drive train coupling between the turbine rotor and the braking motor.

During this early work on turbine characterisation and model validation a BEMT model was used to test the given blade design for optimum pitch angle of the blade tip measured relative to the rotational plane of the turbine (Mason-Jones, 2010). The optimum pitch angle for the blade profile used was found to be 6^{o}. . The previously proven blade design was used

in the 2nd generation turbine model. This allowed the same blade sets to be used on each turbine, minimising the relatively high cost of blade manufacture; each of the 21 blades manufactured cost approximately £1 000. Furthermore this allowed further testing to confirm the observed power coefficient of 0.4 in the original set of flume tests which were subject to high levels of uncertainty. The high levels of uncertainty observed in these test was considered to be an artefact of using the non-direct drive coupling.

The details of second-generation turbine are outlined in (Mason-Jones et al, 2012) (Morris, 2014). It was developed by mounting the braking motor directly behind the turbine rotor. The turbine rotor and braking motor were directly coupled via a short drive shaft. This required that the motor was mounted inside the turbine housing, i.e. in the manner that is similar to many commercial turbine setups with the motor taking the position of a permanent magnet synchronous generator (typically used for direct drive applications). The turbine was made waterproof via the use of O-rings and threaded end plates. The thrust on the turbine structure, including the stanchion, was measured via a 50 Kg force block mounted at the connection between the turbine stanchion and the crossbeam holding the stanchion in the centre of the flume working section. This turbine was used extensively in studying the power converted and wake recovery associated with the rotor under plug flows, profiled flows, and under wave current interaction scenarios (Tedds et al, 2011) (Mason-Jones et al, 2012) (de Jesus Henrique, 2013).

Limitations of this turbine setup arose due to the motor used to oppose hydrodynamic torque. It was found that the setup was unable to provide enough power to operate the turbine over the full range of operating conditions required. Specifically, testing was only able to proceed between the freewheeling and peak power portion of the associated turbine power curve. Furthermore the data capture from the motor drives was at a sample rate of 1.75 Hz and the sample rate for thrust measurements was 47.6 Hz leading to problems when performing frequency analysis on the acquired datasets. An identified shortcoming of the

second and first generation turbines was the lack of synchronisation or global timestamping of data captured from differing sources. This limited the study of turbine rotational displacement against points of interest in the acquired datasets. It should, however, be noted that the test rig setups were suitable when designed. The initial goal of the testing was to validate steady-state CFD models and as such the data was predominately averaged over time to generate non-dimensional power curves – accordingly, high sample rates were not required.

The third generation turbine, detailed throughout the remainder of the chapter, was considered as an evolution of the previous turbine setups created within CMERG. It was therefore convenient to maintain the HATT form and also to design the new turbine to be capable of using the same blade geometry. This was done so that the blade sets already manufactured could be re-used to allow for direct comparisons of research findings, as well as producing cost savings. At this stage consideration was given to lab-scale turbines developed outside of the research group to inform the turbine specification process and help in developing best practices for the new turbine setup.

In Bahaj et al (2007) outline the design and testing of a similar lab scale turbine for both cavitation tunnel and tow tank testing. The turbine was 800mm in diameter and was instrumented with an inline strain gauge dynamometer, located immediately behind the rotor, for torque and thrust measurement. The dynamometer was wired into a full bridge circuit with two gauges on each bridge arm with the output of the bridge wired through slip rings to conditioning circuitry. The measurement range of the instrumentation allowed for accuracies of 71.3% for power and 71.1% for thrust at the expected loading magnitudes. The bridge voltages and signal conditioning was achieved via a Flyde box the output of which was acquired via an A/D card connected to a laptop. The drive shaft was connected via a pulley and timing belt through the vertical support to a further system of pulleys and finally to a DC generator mounted on a platform above the water surface. The DC generator was

connected to three rheostats which, for each flow velocity, were altered to control the speed of the turbine rotor.

Various tests were performed in a cavitation tunnel using five pitch angles ranging from 15^o to 30^o with tunnel speed of up to 2.0 ms^{-1}. For each test the turbine RPM was increased or decreased until cavitation occurred. As well as cavitation testing, tow testing was also conducted for two tip immersion depths of 150mm (0.19D) and 440m (0.55D) at speeds between 0.8 and 1.5 ms^{-1}. Yaw angles of 0^o to 30^o were investigated along with the operation of the turbine with the addition of a second dummy rotor. The testing regime shows that the rig design was versatile and gave consistent results which were validated against established BEMT theory. From this work the importance of well-considered signal conditioning and turbine control was evident; as such the turbine designed was specified in order to adhere to these good practices.

Clarke et al (2007) designed a turbine for tank testing to study the positive effects of utilising a contra rotating turbine design to minimise reaction torque on the turbine support structure and swirl in the turbine wake. The diameter of each rotor was 820 mm and the spacing between each rotor was adjustable from 45mm to 100mm. Opposing torques were achieved by the mechanical action of applying a hydraulically actuated disk brake. In order to maintain zero net torque on the drive shaft the braking load was applied to both rotors. Consequently a differential gearbox was designed in order to allow the blades to rotate at different speeds. The turbine was instrumented with optical encoders placed on each of the drive shafts above the water level. Strain gauges were used to measure the thrust on the support, the braking force and therefore the frictional torque as well as the in-plane and normal bending moment on a single blade on each rotor. LabView was used for data sampling and processing with the final solution implementing multiplexing between the various strain gauges on a single LabView input channel. Data was sampled at 1.3 KHz equating to a rotor angular resolution of less than 1^o. The design of the turbine highlighted

the need for measurement synchronisation or global timestamping and required sample rates in excess of 1 KHz. This was required to study in detail the transient relationships of blade loading over a single turbine rotation. Also of merit was the use of strain gauges to measure blade loading. The paper mentions difficulties in synchronising data when initially recording at hub level, later recorded via LabVIEW. It was noted that this problem must be considered and mechanism for synchronising hub measurements for hub level logging within the new hub had to be devised.

Walker et al (Walker et al, 2014) produced a model turbine to study the effects of blade roughness and bio-fouling on the TST energy extraction process. The turbine used was a two-bladed 0.8 m diameter model, based on the NREL turbine design. The blade profile adopted was the NACA 63-618. The test was conducted in a towing tank with the velocity of the tow carriage set to 1.68 ms^{-1}. The dimensions of the tank were 116 m in length, 7.9 m in width and 4.9 m in depth. The turbine was connected directly to a dynamometer and then through a 90^{o} gearbox to a differential electromagnetic brake system for turbine speed control. The dynamometer was used to measure the thrust and torque generated by the turbine rotor. The rotational velocity and displacement of the turbine was measured via an encoder. The sample rate for the data acquisition was set at 700 Hz from each of the various sources. The measurement uncertainty was estimated via Taylor series techniques and a confidence figure of 95% was given. Also a process of removing offset bias was built into the system whereby measurements from each of the sources are taken prior to a testing period, then averaged and the DC bias is removed.

For experimental investigations into turbine mean wake characteristics in shallow turbulent flows Stallard et al (2014) produced a 0.27 m diameter model turbine. The testing was undertaken in a channel of 5 m width and 0.45 m depth. A 3 bladed rotor was used to drive a 90^{o} bevel gearbox which was coupled, via a 4 mm diameter drive shaft, to a motor, mounted above the water level, used to control the turbine velocity. The blade profile used

was the Göttingen 804. Thrust on the turbine was measured via strain gauges connected in a full bridge configuration mounted on the rotor support shaft.

The effect of turbulence intensity on TST performance was studied by Mycek et al via a three bladed HATT of 0.7 m diameter (Mycek et al, 2013; Mycek et al, 2014a and Mycek et al, 2014b). The rotor was connected to a speed control motor through a gearbox and used NACA 63418 profile blades. A six component load cell was used to measure the thrust and moment on the turbine, the instrumentation was rated for 1500 N and 1500 Nm and was sampled at 100 Hz. A torque sensor was mounted behind the motor and was sampled at 100 Hz. Flow measurements were made with a laser Doppler velocimeter (LDV).

The work outlined in the papers presented above gave a suitable overview of the current research trends regarding the deployment of scale TST for flume and tow-tank testing. Of particular interest is the focus on load measurements which have been carried out in all cases to some degree of success. The turbine developed and outlined herein was expected to achieve high quality load measurements, both on a turbine wide and single blade scales. Currently the experimental trend within research is to use experimental data to study mean effects at differing operating conditions, with the exception of, whereby higher sample rates were attend to afford transient analysis of the turbine performance datasets. The developed turbine was conceived to make progress into the capture and analysis of transient datasets relating to turbine performance and as such high sample rates were sort after.

3 Methodology

3.1 Introduction

This chapter outlines the approach to HATT rotor imbalance monitoring utilised throughout the research presented. To supplement the outlining of the condition monitoring and fault detection procedures the process of using a combination of CFD modelling, parametric rotor modelling and flume testing to test the applicability of the monitoring approaches is also outlined.

3.2 Overall Testing and Simulation Methodology

The following section outlines the approach adopted to effectively develop and confirm the successful application of the monitoring approaches as applied to rotor fault detection. As outlined below there are three interacting methods of verification, the relationship between them is outlined in this section. An overview of the testing and simulation methodology is presented in Figure 3.1. The three methods of testing are namely, CFD based simulations, $1/20^{th}$ turbine flume testing and lastly, drivetrain simulation and testing. The combinations of the three methods have been used to study the condition monitoring algorithms under various operating conditions and turbine scales. Figure 3.1 shows the relationship between each of the three processes. Utilising the three approaches has been advantageous in that the simulations have been developed in stages. At each stage complexity has been added and the monitoring processes applied, tested and developed. In this way the strengths and weakness of the monitoring approaches have been appraised and developed in a logical manner allowing for the creation of implementation recommendations for turbine manufacturers. Whilst advantageous the various scales and operating conditions inherent to each of the three approaches has required care, both in comparison and in data interpretation at each stage.

The CFD based methods represent near full-scale (5m radius turbine) simulations in the steady-state and are related to a narrow operating range of the turbine, at roughly peak power. The CFD simulations are used two-fold; firstly CFD data is used to develop initial rotor condition monitoring approaches based on the structure of drive shaft torque time-series under fault conditions. Secondly, the CFD data is used to parameterise a turbine rotor torque model which is then utilised to conduct quasi-steady-state simulations based on a fixed turbine rotational velocity and fluctuating fluid velocity. This initial simulation is outlined in Chapter 4.

The $1/20^{th}$ scale turbine testing was conducted for a wider range of operating conditions and the data acquired from this experimentation were inherently more stochastic due to the inclusion of measurement error and small scale turbulence. The data produced during the $1/20^{th}$ scale testing is clearly related to a much smaller scale turbine. However, this data will also be used to appraise monitoring techniques and parameterise a more complex rotor torque model over a greater range of turbine operating conditions (i.e at a wider range of λ values (TSRs)). This more complex model will be utilised in the drivetrain simulations and testing. The development of the $1/20^{th}$ scale turbine is presented in Chapter 5, with results presented in Chapter 6.

The drivetrain simulations and testing utilised coupled deterministic and stochastic modelling techniques along with more realistic turbine control processes and fluid velocity simulations to provide non-steady-state verification and development of the monitoring approaches. In-terms of turbine scale, the physical testing conducted on the drive train test bed will be conducted at the $1/20^{th}$ scale.

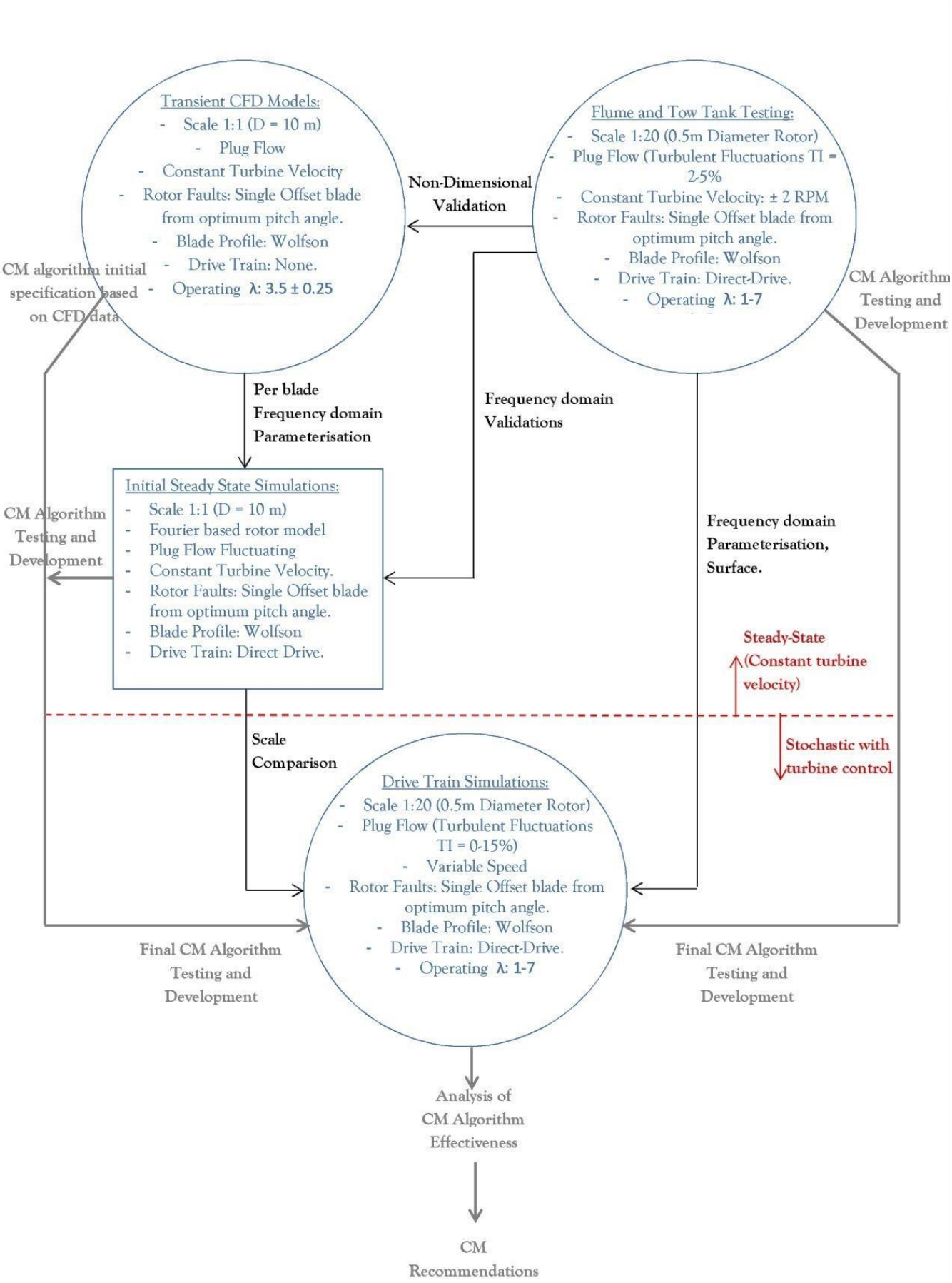

Figure 3.1: Overview of the testing and simulation methodology followed throughout the research.

3.3 Blade fault and rotor imbalance simulation

It was proposed that off-setting the pitch angle of turbine blades in varying combinations and to varying degrees offered a convenient method of simulating turbine rotor imbalance faults. This convenience was afforded across each of the three simulation and testing phases outlined above. As such, blade-offsetting functioned in this research as a convenient and economical method for generating simulations and test scenarios relating to HATT operation under rotor imbalance. As noted in Chapter 2, Section 2.3 imbalanced rotor conditions can arise from a number of turbine rotor fault conditions and can be significant in reducing the useful life of the turbine and its sub-assemblies. Furthermore, offset blade faults can occur in turbines adopting blade pitching control strategies. Although offsetting a single turbine blade was considered to be a convenient method of simulating rotor imbalance faults it is noted here that this method has short-comings. Specifically it was noted that this process creates a non-dynamic rotor imbalance fault due to the fixed change in hydrodynamic characteristics resultant from the blade offset. A number of other approaches to rotor imbalance fault simulation were considered, such as attaching masses to differing blades or changing areas of the surface finish of certain blades. Although this notion was explored it was considered that many of these fault simulation approaches were impractical for CFD and flume simulations as such the blade offset approach was adopted.

3.4 Application of Generator Signal Monitoring to Rotor Fault Detection

As discussed in Section 2.6.3 the main focus of the research presented is the use of generator signals to monitor turbine rotor condition. The use of such processes were researched as it was believed such processes could be useful in the HATT context and help alleviate reliability issues faced by other monitoring approaches such as strain and vibration monitoring.

3.4.1 Tidal Stream Turbine Topology

The drive train setup and generator type used within a given TST topology impacts on the processes used for rotor imbalance monitoring based on generator signals. In order to consider the process of generator parameter monitoring for rotor fault detection a TST topology studied was first defined. The topology to be considered is that of the direct-drive permanent magnet synchronous generator type, connected to the grid via back-to-back power converters. A schematic of the setup can be seen in Figure 3.2: Schematic of the TST topology represented throughout out the work presented. The figure shows a grid connected direct drive turbine with a Permanent Magnet Synchronous Generator (PMSG). A full-rated convert setup is also shown with the grid side VSC utilised for turbine control and the grid-side VSC utilised for control of power flow to the grid (Anaya-Lara et al, 2009).as adapted from (Anaya-Lara et al, 2009).

The impact of having a direct drive setup is twofold and both impact on the generator sizing. Firstly as the power balance through the gearbox, neglecting losses, is unity; an increase in rotational velocity by a factor equal to the gear ratio will result in a reduction in the torsion on the high speed shaft connected to the generator rotor. Heuristically, it is considered that generator sizing has a near directly proportional relationship to the torque magnitude applied to the generator rotor. Therefore the higher torque values related to the tidal stream turbine application will result in the requirement of a larger generator to allow for the higher expected torque. A larger size generator is required for higher torque applications as higher currents will be developed in the generator windings leading to the requirement of larger generator winding sections and the implementation of generator cooling. Furthermore due to the larger loads associated with the higher torque application a larger structure will also be required. In such applications a gearbox is often used to negate the need for a high torque generator, however the addition of a gearbox can lead to reliability problems.

Secondly, in order to maintain power quality in the system a full rated convert is often required adding to the electrical conditioning requirements of the application.

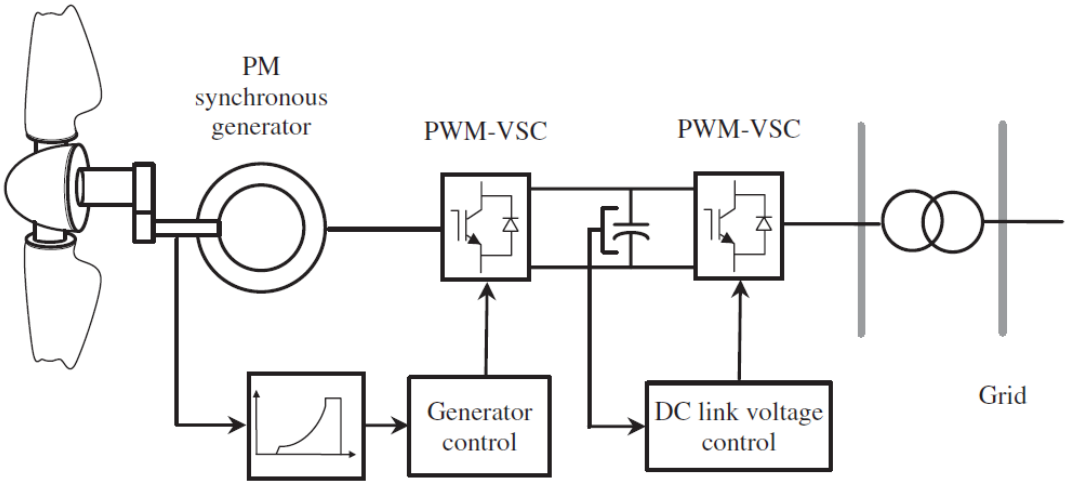

Figure 3.2: Schematic of the TST topology represented throughout out the work presented. The figure shows a grid connected direct drive turbine with a Permanent Magnet Synchronous Generator (PMSG). A full-rated convert setup is also shown with the grid side VSC utilised for turbine control and the grid-side VSC utilised for control of power flow to the grid (Anaya-Lara et al, 2009).

The topology shown in Figure 3.2 (Anaya-Lara et al, 2009), highlights a direct drive TST coupled to the grid through two Voltage Source Control (VSC) power converters. In this case a 6 – level Insulated-Gate Bipolar Transistor (IGBT) converter is utilised to allow for the control of the generator shaft, and hence turbine rotational velocity, via the generator side converter. The generator side converter controls the field current flowing into the DC bus effectively controlling the load on the turbine generator. Power flow to the grid is then controlled via the grid side converter, with the requirement of a DC bus with a high capacitance between the two converters. It is further noted that the use of IGBTs for turbine control as outlined above will require the inclusion of a filter bank over each of the three phases to filter out harmonics introduced by the high speed switching of the IGBTs. The research was not focused on the development of turbine control strategies and topologies so full details of the setup have been omitted here and are covered more fully in Chapter 7, Section 7.5. At this stage it noted that the proposed turbine setup allows for variable speed turbine control schemes, such as optimal lambda control, which is achieved by controlling

the generator feedback torque. Furthermore, the turbine drive shaft will be directly coupled to the turbine rotor on one side and the generator rotor at the other.

3.4.2 Steady–state operation of PMSG direct drive TST

Central to the process of utilising readily available generator signals for rotor monitoring is the impact of the rotor condition on the characteristics of the torque delivered to the turbine drive shaft by the rotor. Both the mean and transient characteristics of the tidal turbine rotor induced drive shaft torque can in theory be interrogated to provide information on the condition of the turbine rotor. This notion follows directly from the ability of the turbine blades, based on their condition, to develop lift and drag forces as a result of the fluid flow over them. Furthermore, cyclic changes in the torque magnitude over a single or multiple rotations of the turbine can be exploited to further inform rotor fault detection and diagnosis.

The process of exploiting generator parameters was proposed by Yang et al (Yang et al, 2008; Yang, 2014). In the development of this notion the dynamic equations for the turbine were exploited, the dynamic equations governing the turbine behaviour, neglecting losses, can be expressed as:

$$J\frac{d\omega}{dt} = \tau_{Rotor} - \tau_{pm} \tag{3.1}$$

by simply considering steady-state operation of the turbine (ω = constant) it is clear that the following holds:

$$J\frac{d\omega}{dt} \approx 0 \tag{3.2}$$

therefore:

$$\tau_{pm} \approx \tau_{Rotor} \tag{3.3}$$

This consideration leads to notion that generator feedback torque can be utilised to measure the rotor input torque and hence provide information on the condition of the turbine rotor. Further consideration is now required to show that measuring the generator feedback torque is possible and less costly than installation of a torque transducer on the turbine drive shaft. Transducers or sensors of this type may be expensive and prone to reliability issues. The consideration follows the standard formulation of the equations governing the behaviour of a synchronous generator in the direct and quadrature (dq) reference frame. In the dq reference frame the generator torque developed is given by the cross-product of the stator flux and the stator current, as derived from the Lorentz force equation (Heaviside, 1889; Anaya-Lara et al, 2009; Pyrhönen et al, 2008):

$$\tau_{SG} = \varphi_{ds} \cdot i_{qs} - \varphi_{qs} \cdot i_{ds} \tag{3.4}$$

The stator flux in the d-q reference frame can be calculated by approximating the generator as a set of three inductance coils organised on the d-q axis. The stator coils have induced voltages v_{qs} and v_{ds}, which results from the rotating magnetic field developed in the rotor by the application of the rotor voltage v_f and the resulting current i_f. The voltages induced in the stator coils if connected to a load will result in currents to flow, i_{ds} and i_{qs}. The currents generate a sinusoidal magnetic flux in the generator air gap as a result of current flowing through inductances L_d and L_q. The magnetic flux magnitude in the air gap is then given by the following equations (Anaya-Lara et al, 2009):

$$\varphi_{ds} = -L_{ls} \cdot i_{ds} + L_d(-i_{ds} + i_f) \tag{3.5}$$

$$\varphi_{qs} = -L_{ls} \cdot i_{qs} + L_q(-i_{qs}) \tag{3.6}$$

Where the L_{ls} are self-inductance terms and lead to losses in the system. Substituting the (3.5) and (3.6) into (3.4) and simplifying gives the following expression for the torque developed via the generator:

$$T_{SG} = ((L_q - L_d)i_{ds} + L_d i_f)i_q \quad (3.7)$$

For a permanent magnetic synchronous generator the term $L_d\ i_f$ is replaced by the magnetic flux of the permanent magnets. This is proportional to product of the poles in the motor and the magnetic flux associated with each pole pair, denoted here as φ_{pm}:

$$T_{PM} = ((L_q - L_d)i_{ds} + \varphi_{PM})i_q \quad (3.8)$$

The optimal torque to current ratio for a PMSG generator is achieved when the rotor flux vector and the stator flux vector are at 90^o to each other. This can be achieved by setting the direct axis current to zero, $i_d = 0$. As such if the generator is operating at its greatest efficiency then the feedback torque of the PMSG can be given by:

$$T_{PM} = \varphi_{PM} \cdot i_q \quad (3.9)$$

From the above considerations it can then be concluded that under the steady-state assumption presented in (3.3) that the rotor torque can then be approximated by:

$$T_{rotor} \approx T_{PM} = \varphi_{PM} \cdot i_q \quad (3.10)$$

The above considerations are utilised in the development of the vector oriented control (VOC) scheme for a PMSG (Anaya-Lara et al, 2009; Liang and Whitby, 2011; Whitby and Ugalde-loo, 2014) and if such a control scheme is adopted measurements of the i_d and i_q currents developed within the generator can be calculated from measured three phase currents flowing to the generator side converter. This is in fact required for the execution of VOC, therefore the signals proposed for rotor condition monitoring can be taken directly from the turbine control scheme and so will require no additional instrumentation. Thus savings on instrumentation cost can be achieve by utilising the proportionality of i_q to the generator feedback torque and under steady state operation to the rotor torque developed.

3.5 Outline signal processing techniques utilised

3.5.1 Time Synchronous Averaging

Time Synchronous Average has been utilised extensively in the application of vibration monitoring to rotating machines (Vachtsevanos et al, 2006; Tavner et al, 2008; Ha et al, 2015) and has a natural application in this area. The algorithms utilised are often simple and seek to characterise the underlying transient artefacts in a signal taken from rotational machinery. The general process of TSA can be considered to consist of three phrases:

1. Data Capture in the time-domain,
2. Re-sampling to fixed locations in the displacement domain, and
3. Averaging over multiple machinery rotations at each (re)sample location.

The effect of averaging at specific sample points for multiple rotations has the effect of reducing noise in the signal and highlights any underlying characteristic fluctuations over a single turbine rotation.

Although TSA is a promising technique there are shortcomings and caveats to be noted. The re-sampling exercise and the true representation of the signal being measured at the defined displacement indexes are highly dependent on the interpolation scheme utilised and

the rotation velocity of the machine. The rotational velocity has an impact on the required time-domain sampling rate which must be,

$$f_s = 2 \cdot X \cdot \omega_{max} \tag{3.11}$$

Where *X* is the number of displacement points over which the interpolation is conducted. The effectiveness of the interpolation scheme is highly dependent on the statistical nature of the signal being measured and the method assumes that the data related to each interpolation displacement point is normally distributed.

In this work encoder measurements were available for the experimental data and the position of the turbine at each calculation time step was used in the case of the simulations. In this case the process of conducting TSA is simplified. Figure 3.3 shows the overall process undertaken, and was adapted from the work of Ha et al (2015). The algorithm for conducting TSA is illustrated via the following pseudo code.

1. Use encoder data to identify zero crossing sample number.
2. Split the measured data at the zero crossing samples, right inclusion (Each zero sample belongs to the proceeding rotation.
3. Resample, M, measured data points with time index to, N, data points with fixed displacement index using cubic spline interpolation.
4. Calculate ensemble average.

The effectiveness of the TSA process is highly dependent on the number of rotations used to create the ensemble average. The noise reduction given by applying the TSA process has been quoted as having been effectively modelled by (Ha et al, 2015), *1/sqrt(number of rotations).* As the specific noise reduction requirements will vary depending on the specific application, averaging over various numbers of rotations will be conducted to find the most appropriate noise reduction factor whilst minimising the number of rotations averaged.

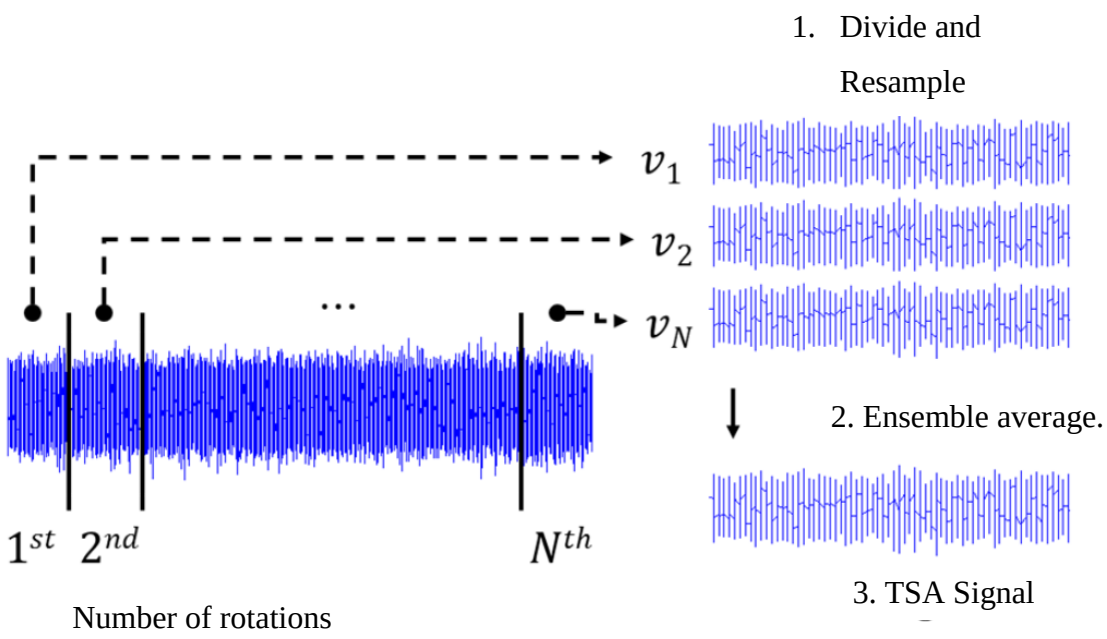

Figure 3.3: Schematic of the TSA process (Ha et al, 2015).

3.5.2 Discrete Time Fourier Transform

Feature extraction for rotating machines has for many years been conducted utilising frequency domain representations of time-domain signals (Vachtsevanos et al, 2006; Tavner et al, 2008). The frequency characteristic extraction processes adopted for such feature extractions are thus numerous and are related to the characteristics of the signal being considered. The most basic method is the Fourier transform. This has formed the foundations of many transformations of time series data into the frequency domain. As the data utilised throughout this thesis has been sampled or synthesised through discrete modelling processes the discrete counter-part of the Fourier transform, namely the Discrete Fourier transform (DFT) is deployed here. Both the discrete and continuous Fourier transforms are taken by considering the projection of a time domain signal onto the orthogonal basis of sinusoidal functions (Osgood, 2007). This process is represented mathematically by the following discrete case formula (Smith, 1997):

$$X(f) = \sum_{n=-\infty}^{\infty} x(nT)e^{-2\pi jfTn} \tag{3.12}$$

The DFT is calculated throughout this research utilising the Matlab implementation of the FFT (Mathwork, 2016). The implementation is based on the open source FFTW library and allows the calculation of 3.12 with *n log n* calculations rather than the required n^2 if calculating the transform directly via 3.12 (Frigo and Johnson, 2005).

3.5.3 Short-Time-Fourier-Transform and the Spectrogram

Spectrograms are produced by windowing time-series (or indeed displacement series data) into segments and taking the Fourier transform of each segment. This gives an estimation of the change in frequency content of a given signal over time. The Fourier transform can be, in simple terms, considered as a projection of a data set onto a basis of sine and cosine (complex exponential) terms at increasing frequencies highlighting the frequency content of a given dataset. The resolution of the Fourier transform is given as the reciprocal of the data set length or indeed -the window length when producing a spectrogram. The maximum observable frequency is then given by the half the reciprocal of the sample period. The windowing process is given mathematically by multiplying the signal x(t) by a window function w(τ-t) and observing the Fourier transform. The windowing function is then progressed through the dataset with a given overlap between transforms. This is known as the Short Time Fourier Transform (STFT) (Feng et al, 2013) and is given by:

$$STFT_x(t,f) = \int_{-\infty}^{\infty} x(\tau)w(\tau - t)\,\mathrm{EXP}(-j2\pi f\tau)\,d\tau \qquad (3.13)$$

Within the process of conducting the STFT it is assumed the signal is stationary at the scale of the window length used to segment the dataset. This along with the fixed nature of the time frequency resolution for a given window length and the unresolvable issues associated with the Heisenberg uncertainty principle means that the transform is best suited

for analysing quasi-static (stationary at the scale of the windowing function) signals (Feng et al, 2013).

The application of the STFT results in a Spectrogram as the output. Throughout the course of the research Spectrograms were utilised to inspect the results of applying the STFT signal processing to time series of interest. As such the author has included a brief guide to the format and interpretation of the spectrogram figures presented throughout the thesis. To present the correct interpretation of a spectrogram and indeed, to show that the process of calculating the spectrograms throughout the thesis was correct a spectrogram of a known signal was created. The following signal was generated using Matlab:

$$x(t) = 5 \cdot \sin(200 \cdot 2 \cdot \pi \cdot t) + 1 \cdot \sin(0.25 \cdot 2 \cdot \pi \cdot t^3) \qquad (3.14)$$

The signal was created to harbour content of both fixed and varying frequencies. One can note in equation (3.14) that the signal is made up of two sinusoids the first with an amplitude of 5 and a fixed frequency of 200 Hz; the second sinusoid has an amplitude of 1 and has a frequency that increases as a function of time. Figure 3.4 shows the spectrogram of the above signal generated via the STFT in Equation (3.13). The interpretation of the spectrogram can be readily understood by noting that the x-axis refers to time, the y-axis frequency and lastly the colour of spectrogram to amplitude. It can be seen that the fixed frequency sinusoid appears as a straight line through the spectrogram and the time-varying frequency can be observed as polynomial varying with time. Furthermore is can be noted that the fixed frequency content sinusoid has the lightest colour as it has the highest amplitude of 5 and the time varying sinusoid has a slight darker colour corresponding to an amplitude of 1. Throughout the thesis the spectrograms calculated, via both the STFT and the Hilbert-Huang Transform, are presented to give the reader a qualitative view of the observed changes in spectrums for differing turbine rotor imbalance settings. The amplitudes of interest are extracted as time-series, as outlined in Sections 3.6.4 to 3.6.6, and then used to train and test

a naïve Bayesian classifier, as presented in Section 3.6.7 – this given a quantitative indicator of the performance of each monitoring approach.

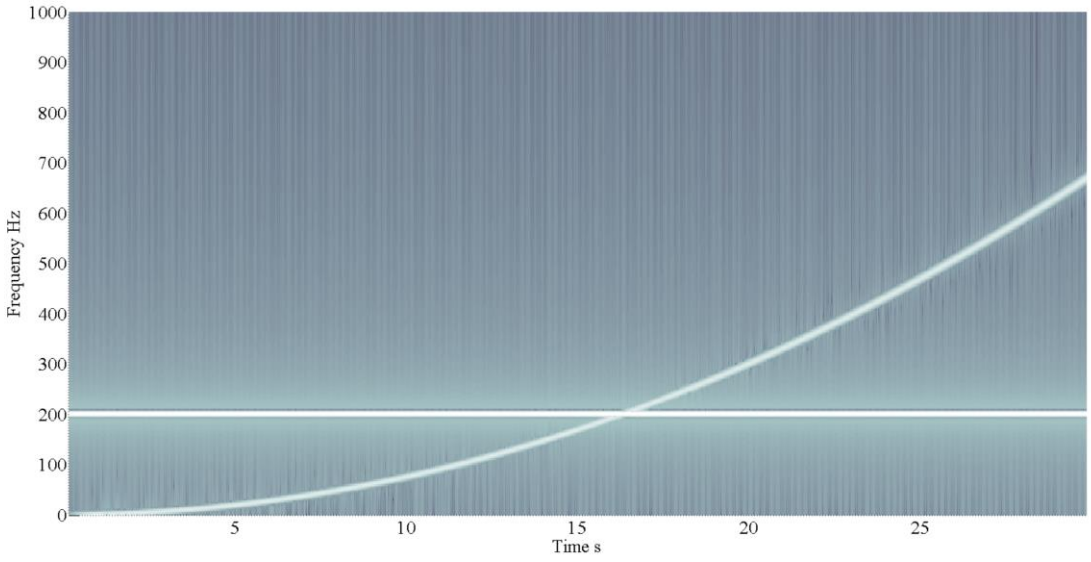

Figure 3.4: Spectrogram of the test signal defined by Equation (3.14).

3.5.4 Empirical Mode Decomposition

This section considers the use of Empirical Mode Decomposition (EMD) for fault feature extraction. EMD is considered as a strong candidate for feature extraction as the selection of a prior basis on which to decompose the given signal is not required. The process generates a basis empirically adapting to the specific data set at hand. EMD was developed originally as the initial step required during the Hilbert-Huang transformation and generates a series of monotonic signal components to which the Hilbert transform can be applied in order to accurately estimate instantaneous frequency of the monotonic components, although just the EMD process is studied here.

EMD utilises the intuition of local high frequency artefacts in a signal. These can be estimated by considering, for example, two subsequent extrema. Utilising this intuition and considering the overall ‘trend’ or structure of the time series local high frequency artefacts can be extracted from the overall time series in an iterative manner (Rilling et al, 2003). EMD is utilised to represent the signal as a sum of Intrinsic Mode Functions (IMFs) which adhere to the mono-component requirement needed for suitable estimate of the

instantaneous frequency for a given signal. An IMF function must satisfy two stipulations (Yang et al, 2008b):

1. The number of extrema and zero crossings in the IMF must be equal of vary at most by 1.
2. The mean at any point in the signal of the maxima envelope and the minima envelope must be zero.

The EMD process involves IMF sifting, an iterative process for extracting IMFs by cubic spline interpolation of local minima and maxima for envelope estimation, a detailed algorithm can be found in (Huang et al, 1998). Essentially the output from the EMD process is the signal as a summation of IMFs with an associated residue which gives the underlying slow moving changes in the signal. This is written as:

$$x(t) = \sum_{i=1}^{n} c_i(t) + r_n(t) \tag{3.5}$$

where $c_i(t)$ is the ith IMF and $r_n(t)$ is the process residual.

3.5.5 Hilbert Huang-Transform.

The extension of the EMD process outlined in the section above to the full Hilbert Huang transform involves taking the Hilbert transform of each of the developed IMFs acquired from application of the EMD procedure developed in the previous section. The instantaneous frequency of the IMF can then be estimated by calculating the derivative of the phase information resultant from the application of the Hilbert transform with respect to time. The summation in equation can then be expressed as a generalised Fourier decomposition of the IMFs as such:

$$x(t) = \sum_{i=1}^{n} a_i(t) exp\,(j \int 2\pi f_n(t) dt) \tag{3.6}$$

this information can then be plotted as a time-frequency amplitude surface or contour plot. This method creates a generalised time-frequency representation of a given signal without requiring stationarity of the signal being analysed (Huang et al, 1998). Throughout the thesis the Hilbert Spectrograms created will be plotted to be consistent with the STFT spectrograms, as such the interpretation presented in Section 3.5.3 will apply equally.

3.6 Formulation of feature extraction techniques

3.6.1 The initial CFD dataset

Cardiff marine energy research group (CMERG) has expertise in producing and validating CFD models (Mason-Jason 2010; Mason-Jones et al, 2012; Morris, 2013; Frost et al, 2014). In order to conduct an initial study into TST rotor monitoring this knowledge base was utilised. Research group members with CFD experience were asked to provide CFD model results for differing rotor conditions. The rotor utilised has generally been consistent throughout the CFD modelling work conducted within the research group. This provides a high level of confidence that the data sets produced are closely representative of the expected turbine characteristics for the given rotor type as indicated by the various validation campaigns undertaken (Mason-Jones, 2010; Mason-Jones et al, 2012).

Within the CFD models a 5m radius rotor equipped with three adapted Wortman FX-63 -137 blades was utilised. Figure 3.5 shows the previously derived and validated non-dimensional performance curves for the rotor (Mason-Jones et al, 2012). The models were setup with constant fluid velocity at the model inlet, both in time and spatially (plug-flow). Through previous research it was found that the optimum blade pitch angle, balancing power extraction and thrust loading, was at 6^{o} to the rotor plane (Mason-Jones, 2010). To conveniently model rotor fault conditions of varying levels of severity a single-blade (blade 1) was offset from the optimum pitch angle by varying degrees. Table 3.1 shows the fault cases modelled.

The fluid domain for the model was 150 m by 50 m by 50 m and utilised a moving reference frame at the turbine rotor. The mesh had approximately 6 million elements and the model utilised a shear stress transport viscous model. The inlet fluid velocity was set to 3.09 ms^{-1}. The turbine rotational velocity was set to 2.23 $rads^{-1}$ resulting in a λ value of 3.61 for each of the simulations which correspond to operation at peak power coefficient for the rotor used.

Table 3.1: Blade fault scenarios modelled via CFD.

Fault Class	Blade 1 Offset
Optimum	No offset blades
Sensitivity Case	Blade 1 Offset by +0.5^o
Minor Fault	Blade 1 Offset by + 3 ^{o}
Major Fault	Blade 1 Offset by +6 ^{o}

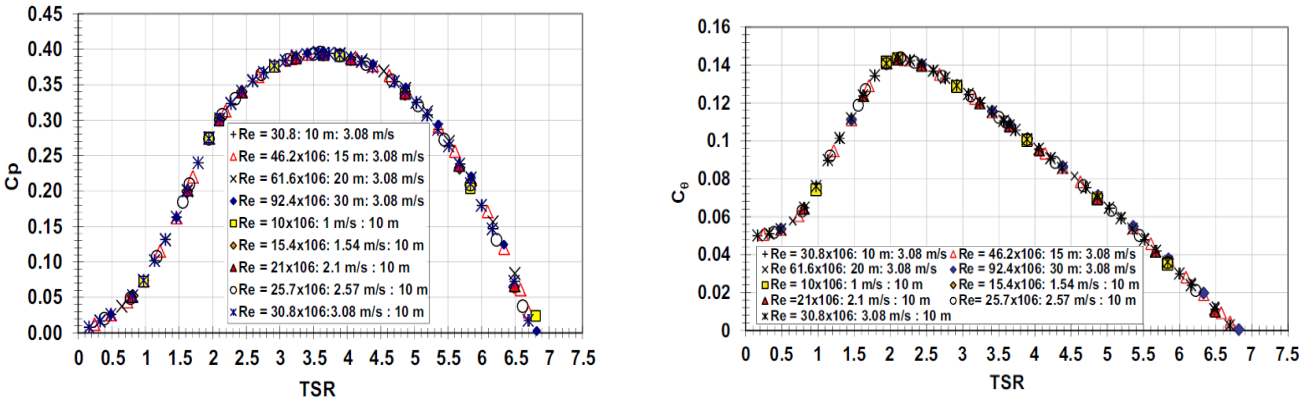

Figure 3.5: Performance curves developed for the adapted Wortmann FX 63 - 137 bladed rotor utilised throughout this research [Mason Jones et al, 2012].

Figure 3.6 shows the data output from the CFD models for the optimum rotor setting case. The figure highlights both the cyclic nature of the drive shaft torque imposed by the rotor and the form of the results output from the CFD modelling exercise. Conveniently the data is output in the form of the overall torque imposed on the turbine drive shaft and the

contribution by each blade to the turbine drive shaft torque. This was exploited in the initial steady state simulations where the overall rotor torque contribution was considered for condition monitoring process development, as this will be the quantity measured in reality, and the blade contribution datasets where utilised to construct a parametric rotor torque model (Section 4.2.4).

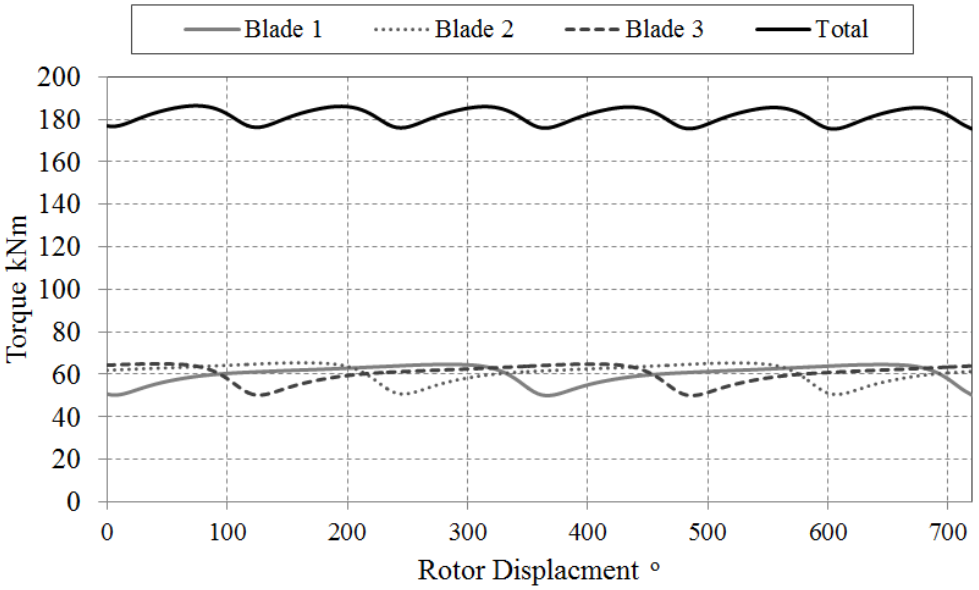

Figure 3.6: Example of the CFD data output for plug flow steady state simulations with optimum rotor conditions.

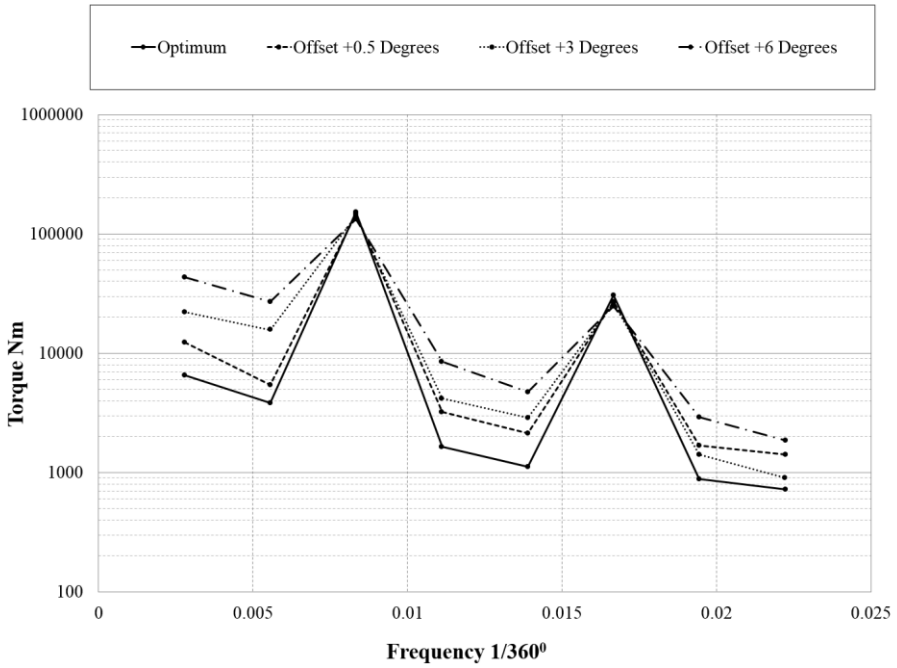

Figure 3.7: Drive shaft torque spectrum for optimum, offset +0.5°, offset +3° and offset +6° conditions.

3.6.2 Power Monitoring

As the power output of a TST is likely to a readily available measurement of the turbine performance it makes a suitable measurement for rotor fault detection and diagnosis. A simplistic method, assuming adequate measurements of the on-coming fluid velocity, was used as an illustrative example within this research. The process consists of using fluid velocity and rotational velocity measurements to lookup the expected power coefficient for the given turbine conditions. The measurement of the on-coming fluid velocity and the power output from the turbine are then used to calculate that actual power coefficient. This process is applied in Section 6.4.1.

3.6.3 Rotor imbalance criterion

CFD data was utilised to study the frequency content of the resultant turbine drive shaft torque under various rotor conditions in order to develop rotor fault indication metrics. Figure 3.7 shows the drive shaft torque spectrum in the turbine displacement domain. The peak amplitude in the drive shaft torque spectrum is shown as being three times per turbine rotation (0.00833 Hz); this can be attributed to the blade passing or 'shadowing effect'. More interestingly it was noted that the amplitude of the rotational frequency of the turbine (0.00278 Hz) is increased with increasing levels of rotor imbalance or damage. This again was conveniently simulated via varying the pitch angle of a single blade for the CFD simulations. Furthermore, it was observed that the shadowing frequency is reduced, albeit to a lesser degree, with increased rotor imbalance. This affect allowed the author to develop two condition monitoring criteria based on the outlined amplitude shifts for differing levels of rotor damage. Specifically the monitoring metrics developed were given by:

$$C = \frac{A_{1\omega}}{A_{3\omega}} \tag{3.7}$$

$$C_l = 20\log\frac{A_{1\omega}}{A_{3\omega}} \tag{3.8}$$

where $A_{1\omega}$ and $A_{3\omega}$ are the amplitudes of the rotational frequency of the turbine and the blade passing frequency of the turbine, respectively.

Here the amplitude refers to the amplitude extracted via the signal processing method used. The sections below discuss two methods used to calculate $A_{1\omega}$ and $A_{3\omega}$ as they vary over time. The monitoring criteria C and C_l in this case can be considered as a measure of the rotor imbalance which could be a valuable fault indicator in an overall monitoring system. The two metrics were developed in the above forms to provide a neutral estimate of the rotor imbalance state and an exaggerated estimate of the rotor imbalance state, given by equations (4.1) and (4.2) respectively.

3.6.4 Extracting the imbalance measures using the STFT

In order to estimate the rotor imbalance criteria C and C_l the frequency content of the drive shaft torque had to be extracted. This section describes a general algorithm used for the estimation of the rotor imbalance criteria C and C_l based on the STFT. The mathematical formulation of the transform was outlined in Section 3.5.3. To apply the rotor imbalance criterion the following algorithm was developed, assuming the batch processing of data. The implementation can be summarised as follows:

Procedure 1: Procedure utilised to calculate the imbalance criteria C and Cl via STFT amplitude extraction.

1. Apply the STFT to the torque or generator q-axis current data to produce a spectrogram:
   A. Generate STFT settings. Typically these are:
      Window Length = 5 Rotations,
      Overlap = 4 Rotations,
      Window Type = ‘Hanning’ (Default) and
      Sample Rate = 100 Hz.
   B. Calculate the STFT via ‘[…] = spectrogram(STFT Settings…)’
   C. Store the results.
2. Calculate condition monitoring criteria ‘*C’* and ‘C_l’:

A. Calculate rotational velocity of turbine in Hz (ω) and 3 times the rotational velocity in hertz (3ω). Note: these are fixed for current simulations.
B. Extract time varying amplitude at $\omega \pm 0.05Hz$ and $3\omega \pm 0.05Hz$ done via comparison and logical indexing of the frequency axis output of the spectrogram.
C. Calculate 'C' and 'C_l' via (3.16) and (3.17), respectively.

3. End.

3.6.5 Extracting the imbalance measure using EMD

In a similar manner to that of the STFT based algorithm an alternative algorithm for extracting the required frequency content based on the process of empirical mode decomposition was also developed and tested. This utilises the EMD process outlined in Section 3.5.4 is based on the EMD algorithm produced by (Tan, 2008). The Matlab script implementing the calculations of criteria *'C'* and *'C_l'* can be summarised as follows:

Procedure 2: Procedure utilised to calculate the imbalance criteria C and Cl via EMD amplitude extraction.

1. Capture X samples of the drive shaft torque or generator q-axis current signal and rotational velocity. Where X is any convenient number of samples to take.
2. Apply the EMD algorithm to the drive shaft torque data.
3. For each intrinsic mode function calculate its FFT and store the amplitude spectrum.
4. Store the IMFs with the greatest amplitude at ω and 3*ω.
5. Use the Hilbert transform to estimate the amplitude of the two IMFs identified.
6. Calculate imbalance criterion *'C'* and *'C_l'* where the amplitude of the IMF relating to the 1st harmonic is substituted into (3.16) and (3.17) as A_1 and the amplitude of the IMF relating to the 3rd harmonic of the rotational frequency as A_3.
7. End.

3.6.6 Extracting the imbalance measure using the HHT

The process of calculating the imbalance measures using the HHT follows the same process as described in Procedure 1 from step 2. The HHT is calculated as described in Section 3.5.5 to give a spectrum of the data – step 2 from Procedure one is then applied to the outputted spectrum.

3.6.7 Testing the effectiveness of the imbalance measure

In order to test the effectiveness of the imbalance measures generated, using the processes described above, the imbalance measures calculated for the various simulation and testing phases were input into a naïve Bayes classifier. Naïve Bayes classification is termed as such because it involves the, so called, Naïve application of Bayes rule to classification. The application is Naïve in the sense that it assumes differing measures used in making a classification are conditionally independent – i.e. one measure used in making a classification has no impact on another. As the classification processes within the research generally used a single indicator this assumption has minimal impact on the results given. Stated simply a naïve Bayes classifier makes classifications based on the arguments using Bayes rule:

$$argmax[P(state|data)] = argmax\left[\frac{P(data|state) \cdot P(state)}{P(data)}\right] \qquad (3.19)$$

The equation gives that the classification of the turbine state is attributed to that which maximises the probability of the state given the data, P(state|data). This can be calculated via the marginal probability distributions on the right hand side of the equality. The calculation requires two steps, initially training and secondly classification.

In order to conduct the training and classification stages using the imbalance criteria data calculated the data is split into two parts. The first segment is used to train the classifier which requires choosing and fitting a PDF to the data for each state – this in effect gives the term P(data|state) on the left hand side of the equality in Equation 3.18. For the research presented Kernal PDFs were used for fault detection classifications and normal or Gaussian PDFs were used for fault diagnosis or fault type classification. The PDFs were fitted using the common maximum likelihood approach (Bishop, 2006)(Matlab, 2015).

The second segment of data can then be used to calculate the right hand term in the equality by appraising the fitted distributions at each data point in the second data segment. The term P(state) is a discrete PMF and was set to an equal value for each of the states thus making the assumption that all fault cases are equally likely. The term P(data) is the sum of the probability for the data value input appraised at each of the fitted PDFs for each P(data|state). The classification is given to the output of the highest probability. This process was undertaken using the built in Matlab Naïve Bayes classifier tool. The results of each classification procedure are presented in Appendix A and the classification discussed within the appropriate results section.

3.6.8 Monitoring surface generation

The notation of defining a surface of observed harmonic amplitudes over a range of operational λ was initially considered within this research as a modelling device, see Chapter 7. These surfaces were then utilised to develop the drive train simulations. It is shown in Section 7.4.5 that the amplitude at harmonics of the rotational velocity, when normalised by the mean torque value, were in close proximity for various fluid velocities for specific λ values. This notion led to the development of so called, Transient Monitoring Surfaces (TMS), which are developed and tested as a condition monitoring tool.

To utilise the TMS as a monitoring tool a trending or characterisation process is first required to initially generate the TMS relating to normal turbine operation. Then future operational characteristics in the form of observed relative amplitudes at various harmonics and at differing λ values can be compared with the trained. The comparison process can be utilised to generate alarm conditions or diagnostic reasoning and to further characterise the normal turbine operation TMS.

This section accordingly outlines the general process for developing the aforementioned TMS. More detailed procedures for creating TMSs under differing turbine control strategies and under non-steady state conditions is presented in Chapter 8 – this was done as the

specific process can be more clearly described after consideration of the simulation method presented in Chapter 7. The process for generating a TMS is similar to that outlined in Chapter 7, however the surfaces generated for condition monitoring relate to the quadrature axis current observed in the generator. The general algorithm utilised for the TMS generation was:

1. Normalise data.
2. Time Synchronous Average data.
3. Take the FFT of the TSA data.
4. Add spectrum to surface indexed by harmonics and TSR

The general algorithm was dependent on correct normalisation and indexing during TMS creation. It was found during the construction of TMS that the normalising and indexing for surface creation became less well defined with increasingly transient turbine operation, for example under high turbulence loading combined with variable speed control. To this end, sections 8.4.3 and 8.4.4 present a more detailed approach to monitoring surface generation under turbulence intensity of 10% for both optimal TSR control and fixed rotational velocity turbine control, respectively.

To use TMS as monitoring tool a training and comparison approach was utilised. The approach in this research was to generate surfaces under normal turbine operating conditions as the baseline TMS. TMS generated under differing conditions were then compared with the baseline TMS generated utilising data form normal turbine operation. The difference between the TMSs were then capture by the so-called sum of surface error (SOSE). To calculate the SOSE the magnitude of the discrepancies between the baseline TMS and current operational TMS are summed over each of the data points generated.

4 Initial Steady State Simulation

4.1 Introduction

This chapter presents an initial approach to testing the effectiveness of the rotor imbalance criteria which were developed by the author based on CFD simulation results presented in Section 3.6.1. The imbalance criterion were developed based on the prior use of two differing signal processing approaches and associated feature extraction methods. Each of the processing approaches and their application to the calculation of the rotor imbalance criteria were presented in Section 3.5 and Section 3.6, respectively.

To test the effectiveness of the outlined approach to rotor imbalance detection a parametric rotor model was developed based on the frequency content of the CFD data presented in Section 3.6.1. The model was developed to harbour the frequency characteristics observed in the CFD data but was structured to allow for the generation torsional time series under varying levels of turbulence. The model structure is presented in Section 4.2. The use of the model to develop TST drive shaft torque time series under various conditions is presented in Section 4.3. The results of the simulations and the application of the rotor imbalance criteria are presented in Sections 4.4 and 4.5. Lastly the impact of the results on the development of rotor imbalance criteria calculation methods is discussed in Section 4.6.

4.2 TST Drive Shaft Torque Simulations

4.2.1 Turbine Rotor Torque Simulation Overview

A simulation process was constructed to test the applicability of the rotor imbalance measure as a condition monitoring metric. Specifically the simulations were created to test the application of the proposed algorithms under near steady state conditions. In this context near steady state conditions are defined as having a fixed turbine rotational velocity with varying fluid conditions characterised by turbulence of intensities ranging from 0.5% to 2.0%.

In order to construct a parametric rotor model the effects of rotor transients, as seen in the transient CFD data, were combined with the expected mean rotor torque for a given operating condition. The specifics of the parametric model are outlined in the following sections. A flow chart of the process is shown Figure 4.1 as decomposed of steady state and transient torque components. In Figure 4.1 the terms in equation 4.6 are highlighted to further indicate the structure of the parametric turbine rotor model. It was considered that for a given time step, the current fluid velocity (from simulated data, Section 4.2.2) as well as the turbine position are measured. These measurements along with the fixed rotational velocity of the turbine, the characteristic curves for the given rotor and the model parameters derived from the CFD results are then used to calculate the expected torque developed by the turbine rotor for the given flow speed and condition. This process is shown in Figure 4.1 with the mathematical formulations outlined in the following sections. In section 4.2.5 the software implementation of both the model parameterisation process and the simulation process are both outlined.

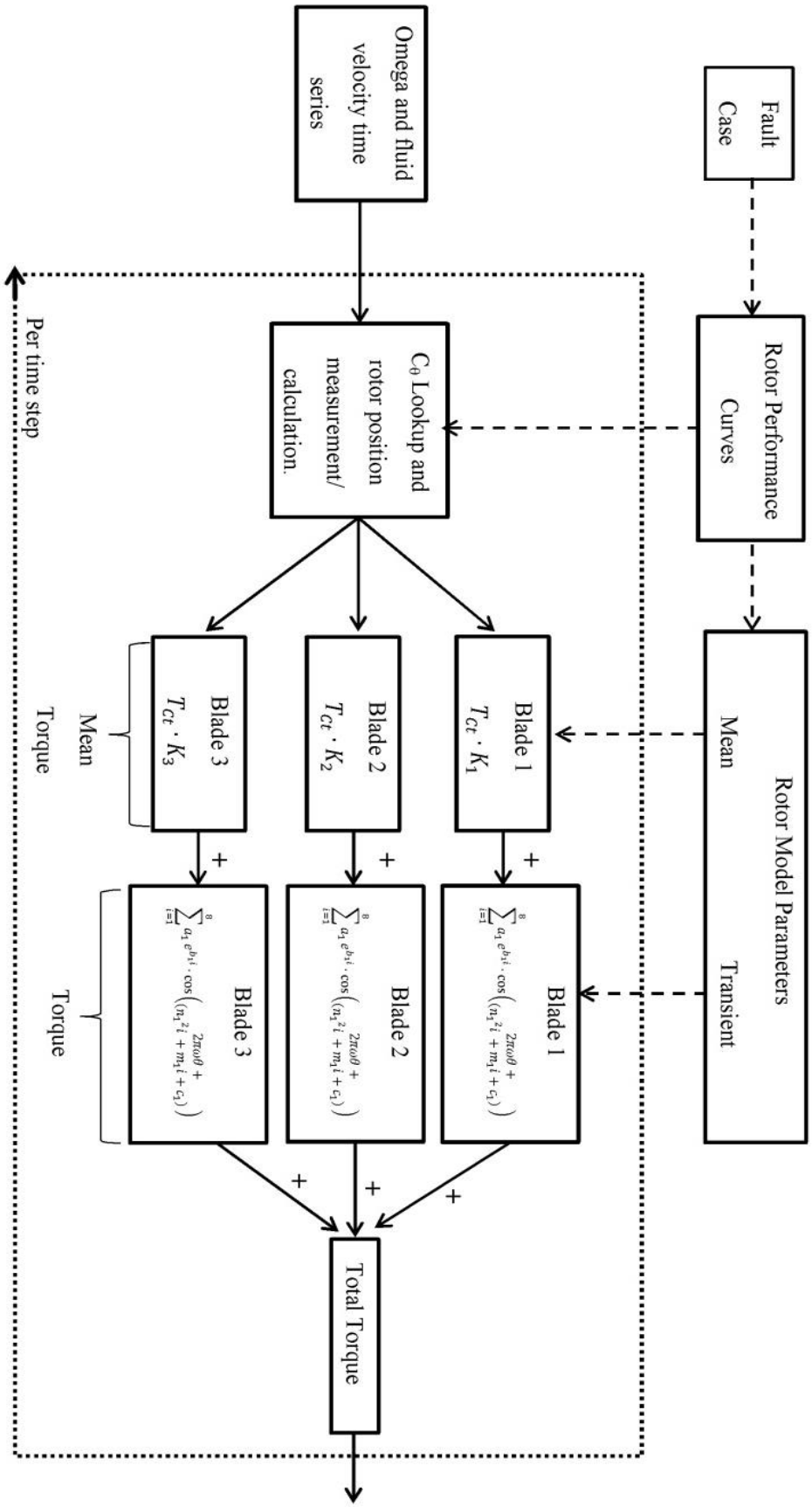

Figure 4.1: Overview of the parametric rotor simulation process.

4.2.2 Fluid Velocity Model

The current study presented utilises a simple approach to fluid velocity simulation. A simple resource simulation method was sought in order to test the validity of drive shaft torque monitoring coupled with the proposed signal processing methods. The model utilised is of the following form:

$$U_x(t) = \overline{U_x} + u'_x(t) \tag{4.1}$$

where $U_x(t)$ is the fluid velocity at time t decomposed into a stationary mean fluid velocity $\overline{U_x}$ and a fluctuating component, $u'_x(t)$ which is time varying with the x direction perpendicular to the turbine rotor plane. The fluctuating component for this study was simulated via a normally distributed random variable with zero average and standard deviation equal to the standard deviation required for the specific turbulence intensity. Turbulence intensity here is defined as:

$$TI = \frac{\sigma_u}{\overline{U}} \tag{4.2}$$

Where, σ_u is the standard deviation of the fluctuation fluid velocity component, $u'_x(t)$.

4.2.3 Turbine Performance Curves

Figure 3.5 shows the power curve and the torque curve for the turbine. The data producing curves were input as lookup tables in the simulation and cubic spline interpolation was used to calculate the torque coefficient between sample points. The magnitude of the drive shaft torque is then calculated by:

$$\tau_{ct} = \frac{1}{2} \cdot C_\theta \cdot \rho \cdot A \cdot r \cdot U^2 \tag{4.3}$$

where τ_{ct} is the magnitude of the rotor torque, C_θ is the torque coefficient found via a lookup table, ρ is the density of the fluid, A is the swept area of the turbine, U is the fluid velocity and r is the turbine radius.

4.2.4 Parametric Model

The CFD simulations outlined were used by the author to determine the parametric model form and parameter set. This was convenient as the output of CFD models enable the evaluation of single blade fault conditions and blade by blade transient torque contributions. The characteristics and in particular the periodic nature of the drive shaft torque fluctuations under various rotor conditions have accordingly been captured via a parametric model of the form of three eight-term Fourier series, one for each blade. The output of the model is a simulated rotor torque time series.

The frequency content of the drive shaft torque calculated via CFD modelling was decomposed into the torque contribution by each turbine blade. Figure 3.6 shows two revolutions of transient simulation results for each blade contribution and the overall drive shaft torque. The setup for the case shown is optimal.

Figure 4.2 shows the amplitude spectrums for each blade and rotor condition the frequency index for the spectrums, the form in Equation 4.4 is shown above the figure with the harmonic indexes highlighted. This was scaled relative to turbine position as the data related to constant rotational velocity operation. It can be observed that blade offsetting distorts the harmonic content of the frequency domain representation from the optimum case. Each spectrum also exhibits an exponentially decaying tendency with differing peak

values and decay rates, this was utilised in the parametric model as can be seen in Equation 4.4. The drive shaft torque parametric model utilised a Fourier series of the form:

$$\tau_{rotor}(\theta) = \tau_{Ct} \cdot \left(k_1 + \sum_{i=1}^{8} a_1 e^{b_1 i} \cdot \cos\left(2\pi\omega\theta + \left({n_1}^2 i + m_1 i + c_1\right)\right)\right) + \tau_{Ct} \cdot \left(k_2 + \sum_{i=1}^{8} a_2 e^{b_2 i} \cdot \cos\left(2\pi\omega\theta + \left({n_2}^2 i + m_2 i + c_2\right)\right)\right) + \tau_{Ct} \cdot \left(k_3 + \sum_{i=1}^{8} a_3 e^{b_3 i} \cdot \cos\left(2\pi\omega\theta + \left({n_3}^2 i + m_3 i + c_3\right)\right)\right) \quad (4.4)$$

where θ is the turbine position and ω the turbine rotational velocity. The remaining parameters are discussed below.

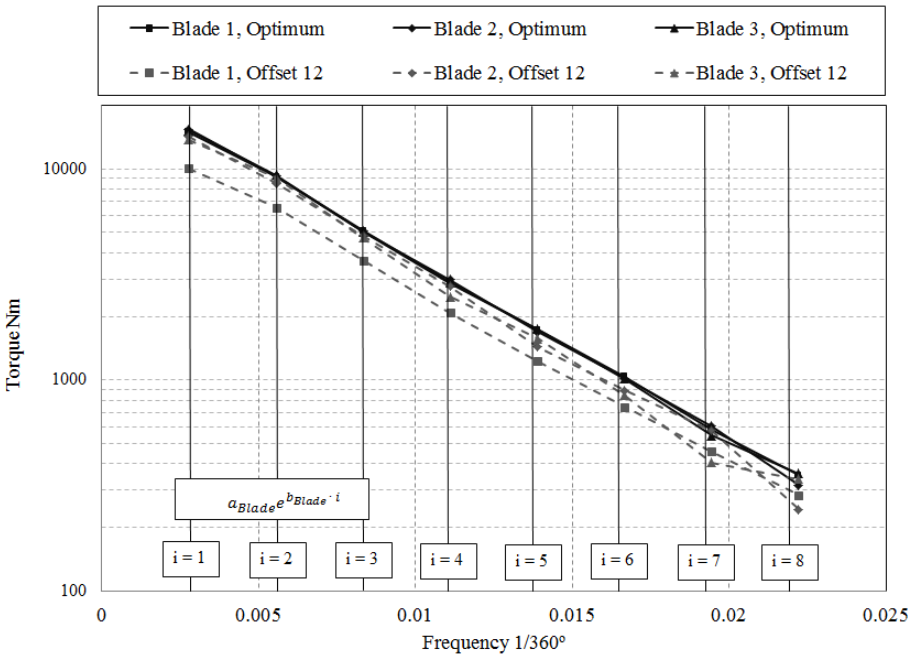

Figure 4.2: Spectrum of drive shaft torque for each blade contribution under differing rotor conditions, the observable exponential decay over multiple harmonics of the turbine rotation were exploited for the parametric model.

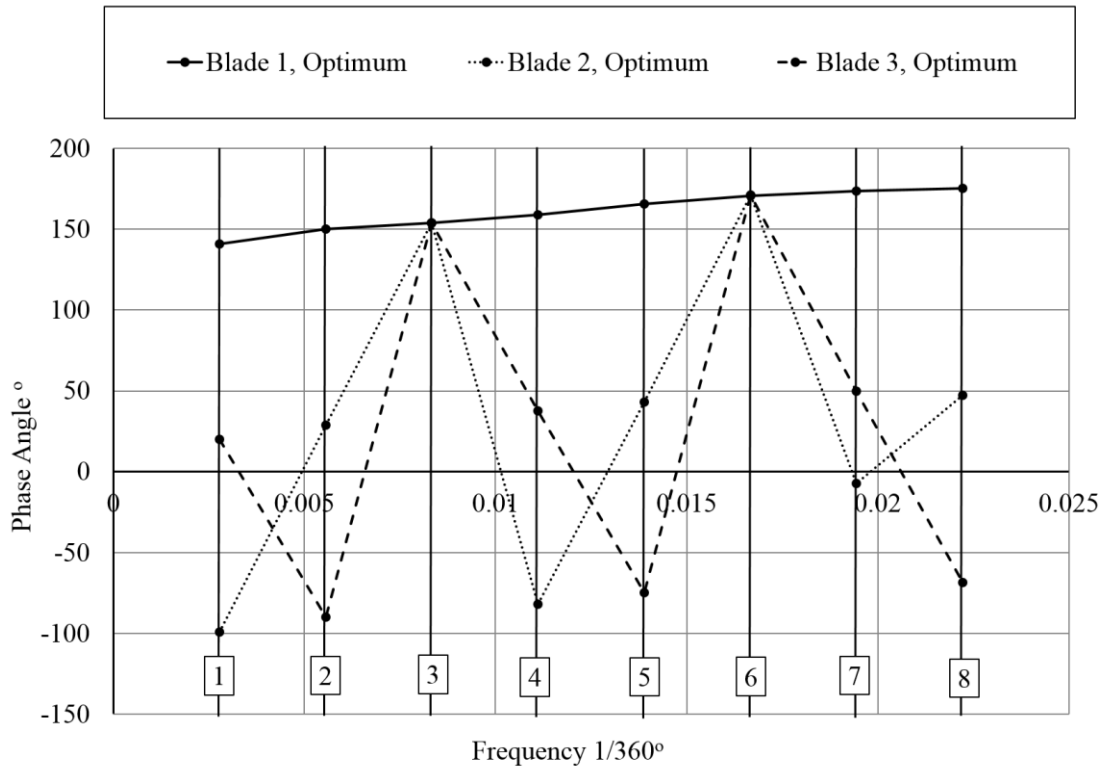

Figure 4.3: Phase spectrum observed for each blade contribution to the turbine rotor torque calculated via CFD data, with phase angles in degrees.

$$n_{Blade}{}^2 i + m_{Blade} i + c_{Blade}$$

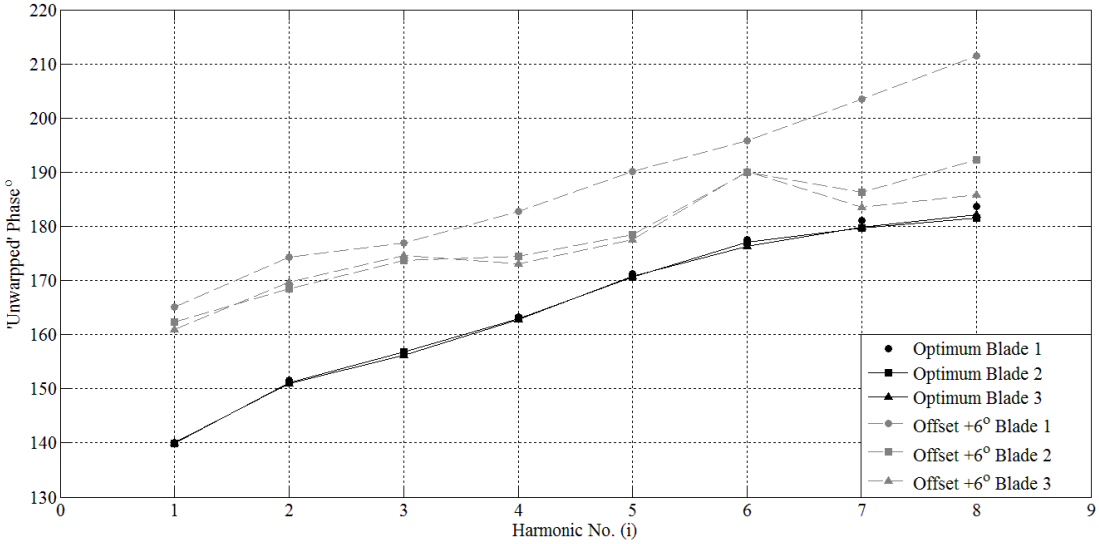

Figure 4.4: Unwrapped phase spectrum for each blade for the optimum and +6° offset cases, showing the appropriate choice of 2nd order polynomial form utilised within the parametric model.

It can be seen in equation (4.4) that the relationship between the observed phase angles at each harmonic for differing rotor conditions was captured via the parameterisation of the quadratic equation with a set of three parameters *'m', 'n'* and *'c'* for each rotor condition. Figure 4.3 shows the phase spectrum observed for the optimum rotor condition with the phase angle in degrees with the rotational frequency harmonic numbers shown. The figure shows the phase spectrum with no processing to, 'unwrap' phase angles. It can be seen that the phase spectrum shown exhibits linear trends with phase separation between blades. This was not easily characterised by the quadratic form mentioned. Specifically, blade 1 shows an almost linear phase spectrum for the optimum case but this was not found for blades 2 and 3. It was noted that the phase angles for harmonics 3 and 6 were of a similar value for all three blades. Further investigation highlighted that a specific pattern of phase shifting could be observed for blades 2 and 3 relative to blade 1 for the harmonics where inconsistent phase angles were observed.

To further interrogate the structure of the observed inconsistences it was considered that the phase shifts observed maybe related to the blade locations, i.e. related to 120 ^{o} displacement between blades. It was found that this reasoning was correct and a sequence of phase angle shifts could be applied at each harmonic to create consistency between the phase spectrums observed for blades 1, 2 and 3. The specific phase angle shifting required to create such consistence is presented in Table 4.1: Phase relationship observed over 8 harmonics of rotation and for each blade. It is noted here that the reasoning behind the observed phase angle relationship was not fully considered and the above process was applied to afford convenience in parametric model form and parameterisation. The phase shifting process was then applied to the phase spectrums observed for each rotor case. Furthermore the phases were unwrapped to fall between the range $0^{o} \leq ß \leq 360^{o}$. The results of the phase shifting process are shown in Figure 4.4, along with the parametric form utilised

to model the phase angels observed for each harmonic number for differing blades and rotor conditions.

Table 4.1: Phase relationship observed over 8 harmonics of rotation and for each blade.

Harmonic No.	Phase Shift Blade 1	Phase Shift Blade 2	Phase Shift Blade 3
1	0 º	+240 º	+120 º
2	0 º	+120 º	+240 º
3	0 º	0 º	0 º
4	0 º	+240 º	+120 º
5	0 º	+120 º	+240 º
6	0 º	0 º	0 º
7	0 º	+240 º	+120 º
8	0 º	+120 º	+240 º

The focus of this investigation was, by necessity, on TST operation at close to peak power conditions, rather than across the entire power curve. Accordingly, parameters where determined for a tip speed ratio of 3.6. Although it was likely that, as a result of the fluid velocity fluctuations, a wider TSR range would be observed the constant parameter assumption was deemed acceptable for the current baseline study. Developments to the model have been included in further simulations utilising results of a flume testing campaign (see Chapter 7 and Chapter 8). These additions to the research created later in the research activities show that the parameter values of such a model vary minimally across $3.45<\lambda<3.75$. This assumption allowed the parameters in the model to be held constant relative to the TSR and parameterisation to be undertaken utilising data from a single operating condition (as was the format of the CFD data). Then referring to equation 4.4 the parameter set was as follows:

k – Blade torque contribution for a given TSR

a – Depth of shadowing effect

b – Harmonic decay of the shadowing effect

n – Phase non-linearity

m – Phase gradient

c – Phase offset.

The parameter k gives the relative contribution of each blade to the total drive shaft torque; this in effect sets the DC value of the torque for a given TSR. The parameters a and b give the depth of the shadowing effect and the rate of decay of the eight harmonics for each blade; this in effect defines the magnitude of torque fluctuations due to the aforementioned shadowing effect. Lastly, parameters m, n and c define the phase relationships over the eight harmonics for each blade.

As stated previously, parameter sets were obtained for an optimum case (all blade pitch angles set to the 6^{o}) and the three single-blade offset cases. A visual comparison of the parametric model and CFD simulations is provided in Figure 4.5.

4.2.5 Software implementation of parameterisation and simulations.

The software implementation of the model parameterisation was again undertaken using Matlab. The process of rotor model parameterisation was undertaken via the following process:

Procedure 3: Procedure used for model parameterisation using the prior CFD dataset.

8. Gather CFD data and organise into a convenient data structure (‘*Steady_State_Parameters’* in this case.)
9. Resample the data to include torque data for two turbine revolutions indexed at each degree.
10. Generate frequency data for curve fitting to find parameters ‘*a’, ‘b’, ‘c’, ‘m’*, and *‘n’*. This was done using the ‘Ftrans’ which implements the built in ‘FFT’ function and outputs discretised amplitude and phase spectrums. The amplitude spectrums have been scaled by half the number of points used for the FFT to preserve the units of Nm for the amplitudes observed.
11. Parameterise *‘k’, ‘a’* and *‘b’* for blade 1 utilising the current dataset:

A. Create required variables for indexing.
B. 'k' is parameterised by equating with the ratio of the mean torque for blade 1 to the mean torque developed by the rotor (as calculated utilising the rotor characteristics curves).
C. Scale the amplitude spectrum by the mean drive shaft torque developed by the rotor (as calculated utilising the rotor characteristics curves).
D. Curve fit a decaying exponential to the scaled amplitudes as indexed by harmonics 1 to 8 where x = *harmonic no.* and y = *scaled amplitude*. "eb1 = fit(HarmonicIndex,RelativeAmp,'exp1');"
E. Set parameter *'a'* to the exponential scaling parameter and set parameter *'b'* to the exponential decay rate.

12. Repeat sub-steps 4 for blades 2 and 3.
13. Parameterise *'m', 'n'* and *'c'* utilising the current dataset, for blade 1:
    A. Unwrap phase spectrum and convert to degrees, range (0 º to 360 º).
    B. Fit 2nd order polynomial to phase angles for each harmonic 1 to 8, where x = *harmonic no.* and y = *phase angle*. [pb1 = fit(HarmonicIndex,phase,'poly2');]
    C. Equate parameters '*m', 'n'* and *'c'* with the x^2, x^1 and x^0 coefficients.
14. Parameterise 'm', 'n' and 'c' utilising the current dataset, for blades 1 and 2:
    A. Unwrap phase spectrum and convert to degrees, range (0 º to 360 º).
    B. Correct phase relationships as per section 4.4.4.
    C. Fit 2nd order polynomial to phase angles for each harmonic 1 to 8, where x = *harmonic no.* and y = *phase angle*. pb1 = fit(HarmonicIndex,phase,'poly2');
    D. Equate parameters *'m', 'n'* and *'c'* with the x^2, x^1 and x^0 coefficients.
15. Repeat for each rotor condition and output parameters to data structure – '*Steady_State_Parameters'*.

The software implementation of the simulations based on the above parameterisation process was also engineered utilising Matlab. The process of the undertaking the simulation was implemented as a Matlab function using the following algorithm:

Procedure 4: The procedure followed to create the parametric simulations of the rotor torque given the model parameters and simulated fluid time series.

1. Import required simulation details: Rotor Radius, Turbine Rotational Velocity, Mean Fluid Velocity, Turbulence Intensity, Fault setting and *Steady_State_Parameters'*.
2. Create position, time indexes and harmonic frequency index (scaled by postion).

3. Get model parameters from '*Steady_State_Parameters'* and make pre-allocation of output variables.
4. Create fluid velocity time series via random sampling from normal distribution as in: Output.Vel=(randn(1,20001)'*(Vmean*(TI/100)));
5. For each time step:
    a. Get current fluid velocity (index the fluid time series vector created in step 4) and turbine rotational velocity (fixed).
    b. Calculate current tip-speed ratio and use to lookup current C_θ value, done via linear interpolation of the rotor torque performance curve.
    c. Calculate mean torque using (4.6).
    d. Calculate harmonic amplitudes for blades 1, 2 and 3 using parameters *'a'* and *'b'* and the exponential form in (4.7) and scale by mean torque.
    e. Calculate phase angles at harmonic intervals for blades 1,2 and 3, using parameters 'm', 'n' and 'c' and the quadratic form in (4.7).
    f. For blades 2 and 3 undo phase wrapping required for linear fit.
    g. Calculate the transient torque component using the Fourier series in (4.7) with amplitude and phase angles calculated in
    h. Calculate the mean torque contribution for blades 1, 2 and 3 using parameters 'k' and the overall mean torque.
    i. For each blade sum the mean and fluctuating torque components and output.
    j. Sum each blade contribution.
6. Repeat for each time step.
7. End.

4.3 Condition Monitoring Study

4.3.1 TST Rotor Fault Simulations

In order to appraise the effectiveness of rotor the imbalance criteria C and C_l, extracted via the signal processing methods outlined, a set of TST drive train torque time series simulations were developed. The simulations were generated for the 10 m fixed pitched diameter turbine outlined with a 3.086 ms^{-1} free-stream flow velocity. The optimum pitch angle for the rotor design (adapted Wortman FX 63-137 profile) was 6^o, for the study three blade 1 offset cases of $+0.5^o$, $+3^o$ and $+6^o$ from the optimum pitch angle were considered as dictated by the CFD data utilised. For each rotor condition 50 simulations were constructed.

Each of these was 200 seconds in length. The time step for the simulations was 0.01 equating to 20,000 samples. The simulations were conducted for various levels of turbulence intensity to further interrogate the ability of signal processing algorithms to extract fault features under stochastic conditions. Specifically the datasets were produced with turbulence intensities of 0 %, 0.5 %, 1 % and 2 %. Although it was noted that TI values of between 10 % and 15 % are to be expected for fluid velocities of greater than 2 ms^{-1}, the levels of turbulence intensity were selected to adhere to the fixed parameter assumption made during the development of the parametric rotor model. The signal processing methods and subsequent extraction of the rotor imbalance criteria C and C_l were applied to 5 of the 50 simulation outputs for each of the turbulence intensity values considered; the 5 cases were chosen at random. For each of the cases to which the signal processing methods were applied the effect of turbulence on the extraction of the required amplitudes, A_1 and A_2, was considered. Finally the 5 cases for each turbulence intensity setting were used as training data for a naïve Bayes classifier, as described in Chapter 3, Section 3.6.7. The output of the training of the naïve Bayes classifier was studied via consideration of the likelihood function (that is, the probability of the data given the fault setting) found for each of the fault cases and turbulence intensities. This was done to objectively appraise the use of the monitoring criteria for fault detection and diagnosis via a simplistic classification method.

4.4 Simulation Results

Figure 4.5 shows the parametric model output for the drive shaft torque contribution by each blade for each of the blade cases with TI = 0%. Also displayed are the CFD results used to parameterise the model. An average RMSE of approximately 0.0551 Nm was obtained. Figure 4.6 shows an example of the simulation results. The figure shows model output for the optimum rotor case with increasing levels of turbulence. The first case has no turbulent loading and the time series patterns correspond to the reported frequency content

for the torque models. The three other cases have increasing turbulences, set at 0.5 %, 1.0 % and 2.0% of the mean flow velocity respectively.

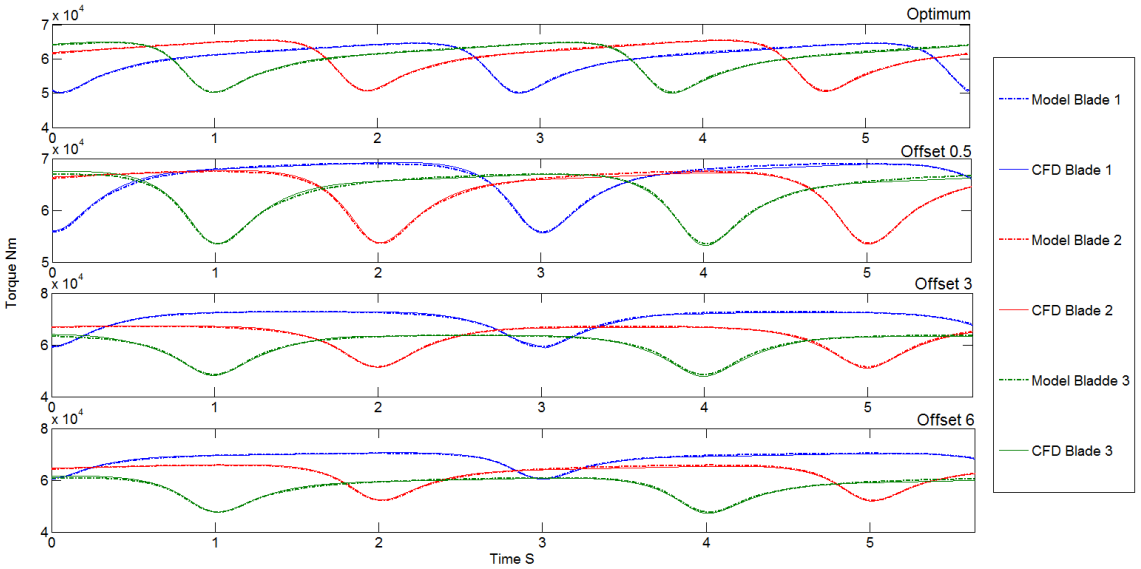

Figure 4.5: Comparison of the parametric model output with the CFD data used to parameterise the model.

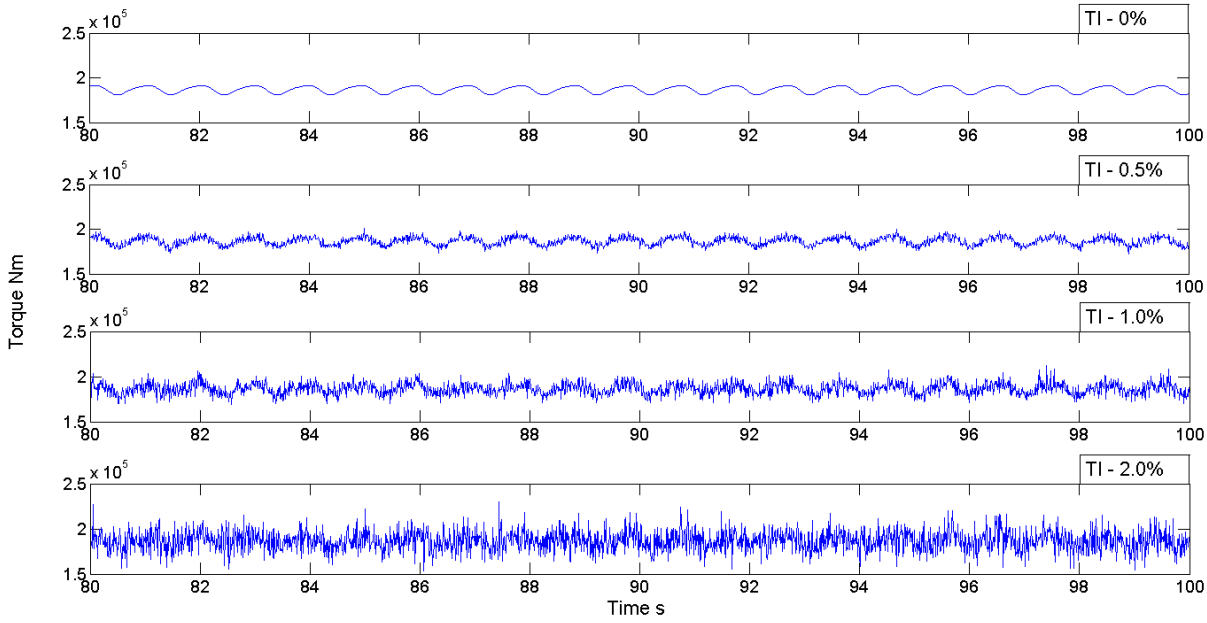

Figure 4.6: Torque time series output from the simulation process for optimum conditions and varying levels of turbulence intensity.

4.5 Monitoring Criteria Performance

4.5.1 STFT Amplitude Extraction

Figure 4.7 shows an instance of the application of the STFT amplitude extraction process defined in Section 3.6.4. The example shown presents the spectrograms and extracted A_1 and A_3 amplitudes for the offset $+6^o$ case with increasing levels of turbulence.

It can be seen from Figure 4.7 that the STFT algorithm worked well in extracting the frequencies of interest for each of the turbulence intensity levels considered. However, it can also be seen that the presence of the amplitudes at the harmonics of interest relative to the spectrum noise floor is decreased with increasing turbulence intensity. It was considered that this observed trend would become problematic during turbine operation in higher turbulence levels as expected during full-scale deployment. Furthermore, it was also noted that extracted amplitudes became increasingly spread with turbulence intensity, i.e. a higher standard deviations were be observed.

It was also noted that the time-frequency resolution was poor. In the steady-state case presented in this chapter the poor time-frequency resolution did not impact on the result. However, it was considered that under more transient turbine operation the time-frequency resolution could become prohibitive. Lastly, to note, the application of the STFT feature extraction process was relatively convenient with low computational times and data burdens.

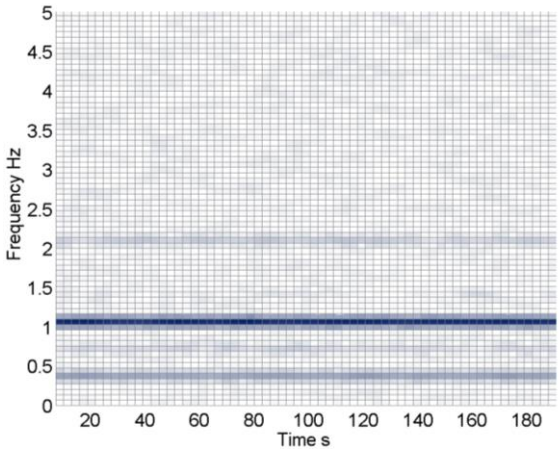

a1) Spectrogram Offset +6º TI = 0.5%

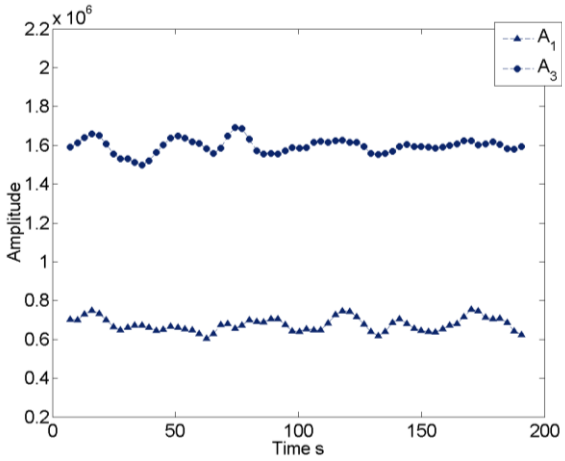

b1) Extracted Amplitudes Offset +6º TI = 0.5%

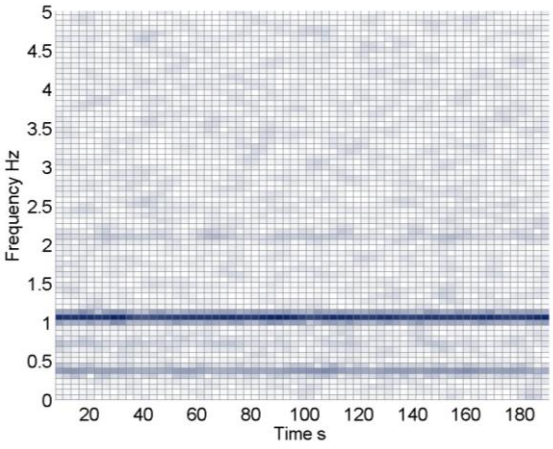

a2) Spectrogram Offset +6º TI = 1.0%

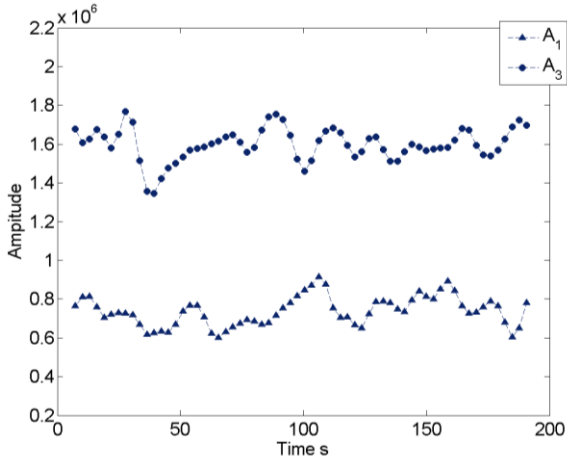

b2) Extracted Amplitudes Offset +6º TI = 1.0%

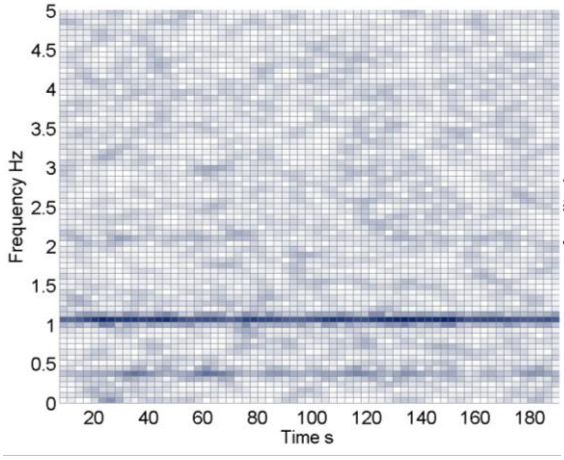

a3) Spectrogram Offset +6º TI = 2.0%

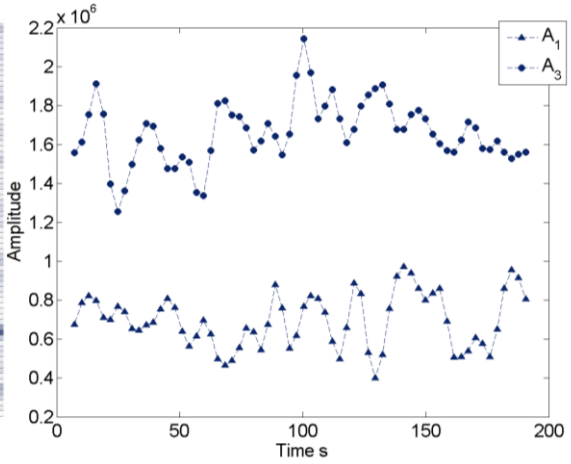

b3) Extracted Amplitudes Offset +6º TI = 2.0%

Figure 4.7: Spectrograms and extracted A_1 and A_3 amplitudes for the offset +6º fault setting and varying levels of turbulence.

4.5.2 EMD Feature Extraction

Figure 4.8 shows an instance of the application of the EMD amplitude extraction process outlined in Section 3.6.5. The figure shows the extracted IMFs corresponding to the amplitudes A_1 and A_3. The frequency spectrums for each observed for each IMF, which were utilised for appropriate IMF extraction, is also plotted. Figure 4.8 shows the results of the EMD amplitude extraction process were far less reliable than the results of the STFT process. Specifically the amplitudes observed for the A_3 amplitude were highly variable which would cause the monitoring criteria calculated via the EMD process to vary greatly.

The correct identification of the IMFS relating to the frequency content of interest was also an issue. This can be seen in Figure 4.8 b2 and Figure 4.8 b3 whereby the IMFs extracted corresponding to the A_3 amplitude are incorrect when considering the unexplained reduction of the amplitudes in the IMF spectrums at $3*\omega$. Furthermore the EMD process took longer to compute and resulted in a far larger data set which may be prohibitive for real world applications.

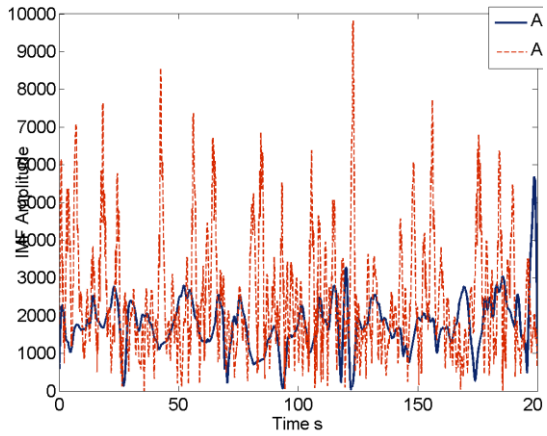

a1) Extracted IMFs Offset +6º TI = 0.5%

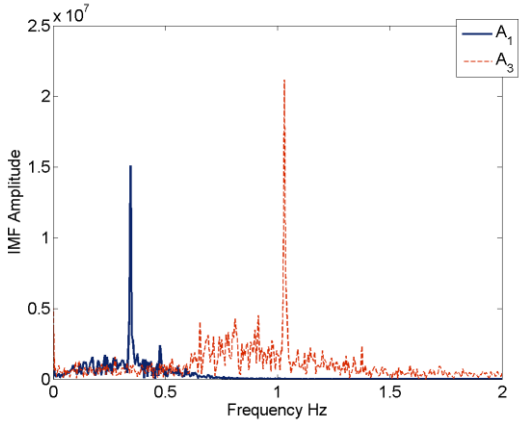

b1) Spectrum of IMFs Offset +6º TI = 0.5%

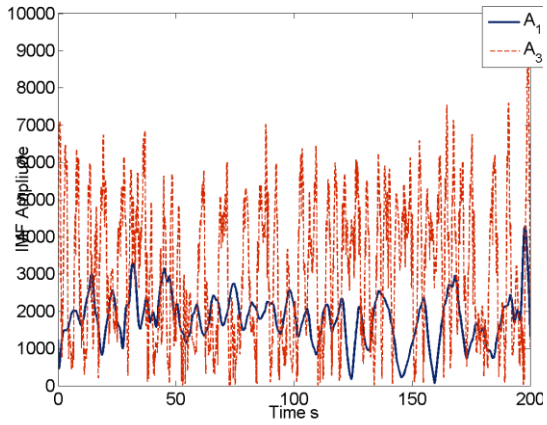

a2) Extracted IMFs Offset +6º TI = 1.0%

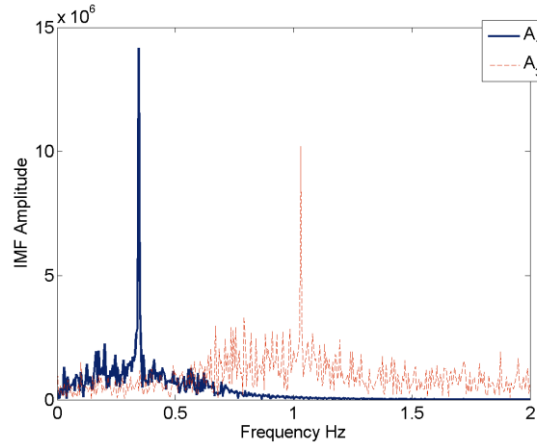

b2) Spectrum of IMFs Offset +6º TI = 1.0%

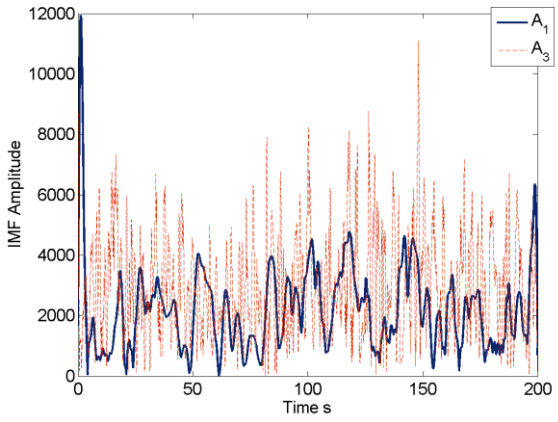

a3) Extracted IMFs Offset +6º TI = 2.0%

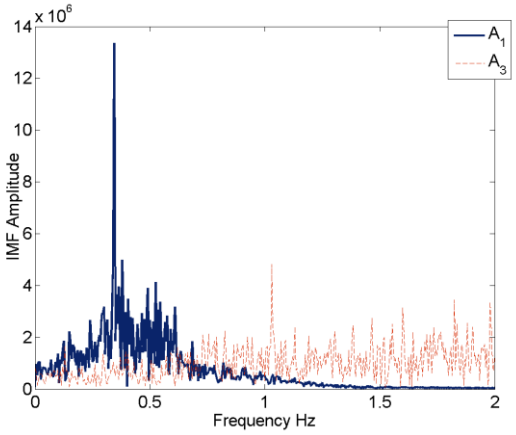

b3) Spectrum of IMFs Offset +6º TI = 2.0%

Figure 4.8: Extracted IMFs for A_1 and A_3 amplitudes with the amplitude spectrums plotted to show the appropriateness of IMF extraction via the algorithm outlined in section 4.3.3.

4.5.3 Fault Detection and Diagnosis Utilising STFT Extracted Amplitudes

Figure 4.9 shows the results of the application of the naïve Bayes classifier training process to the two monitoring criteria for each of the turbulence intensity cases and corresponds to C and C_l values extracted via the STFT. The pdf distributions shown relate to the normal or Gaussian family of pdfs fitted to the data for each fault case as discussed in Section 3.6.7. Figure 4.9 presents the probability of observing values of C and C_l for each of the rotor states. The classification results can be found in Appendix 10.2A in Tables A.1 to A.12, with the result classifications highlighted. It was found in the results of the application of NBC that the STFT based imbalance measures C and C_l could be used to successfully detect an anomalous rotor condition. In general the imbalance criterion was used to successfully classify the rotor fault severity. An exception to the successful classification of rotor fault severity was the single case of the C measure at turbulence intensity of 2%. Under these conditions the 0.5^o offset case was misclassified as the optimal case and the 6^o offset case was misclassified as the 3^o offset case, this can be seen in Table A.6. The C_l measure resulted in correct fault detection and diagnosis results for all conditions simulated. This suggests that the C_l imbalance criterion is more robust than the C criterion for the STFT feature extraction process.

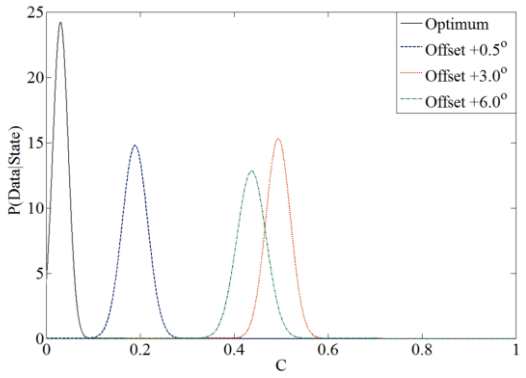

a1) Monitoring Criterion C TI = 0.5%

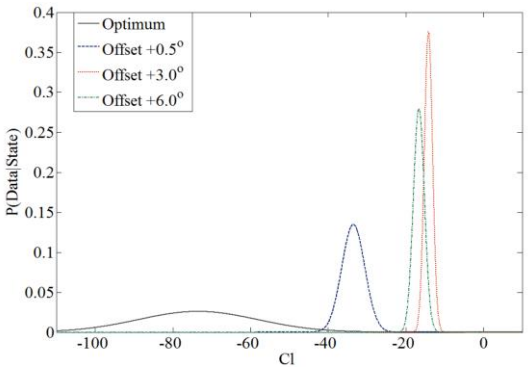

b1) Monitoring Criterion C_l TI = 0.5%

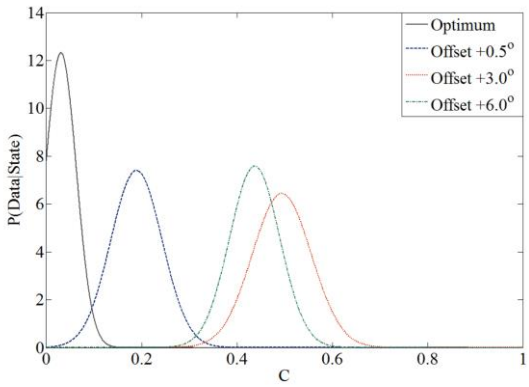

a2) Monitoring Criterion C TI = 1.0%

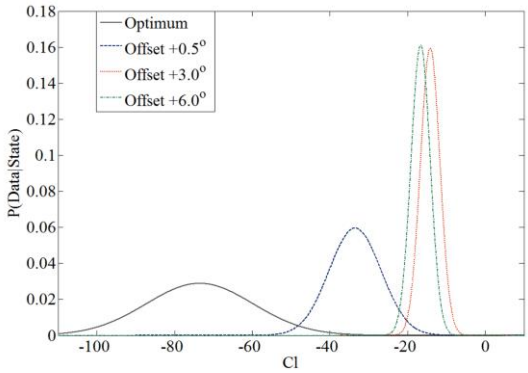

b2) Monitoring Criterion C_l TI = 1.0%

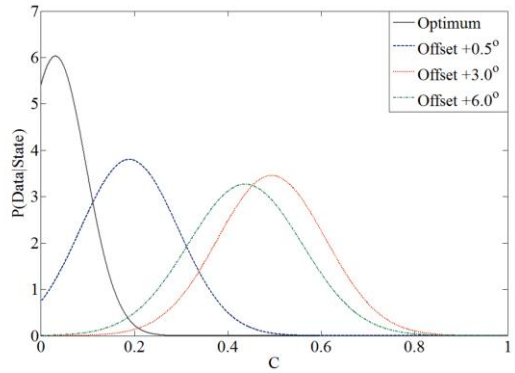

a3) Monitoring Criterion C TI = 2.0%

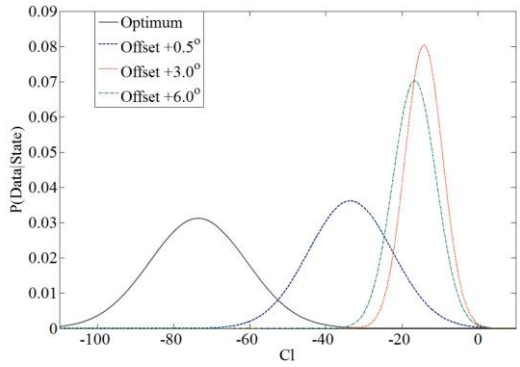

b3) Monitoring Criterion C_l TI = 2.0%

Figure 4.9: Normal probability distributions constructed via the 5 training datasets giving and estimate of P(Data|State) for varying levels of turbulence intensities for the STFT feature extraction process.

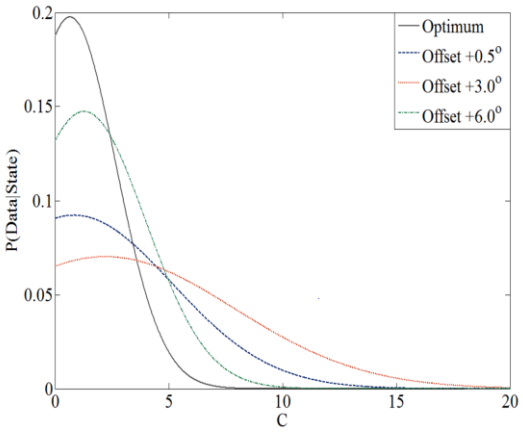

a1) Monitoring Criterion C TI = 0.5%

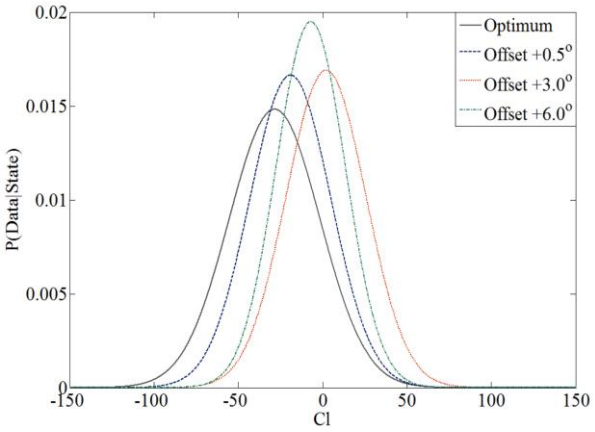

b1) Monitoring Criterion C_l TI = 0.5%

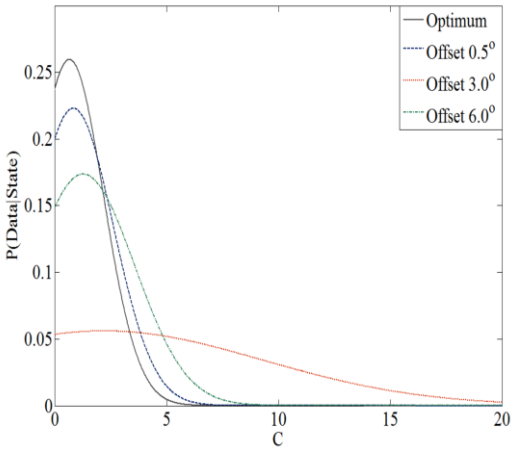

a2) Monitoring Criterion C TI = 1.0%

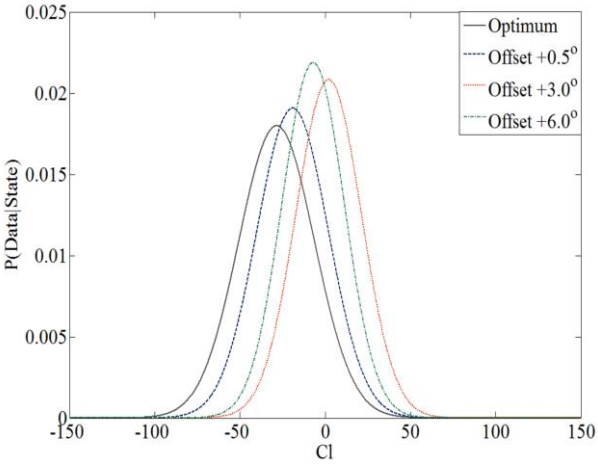

b2) Monitoring Criterion C_l TI = 1.0%

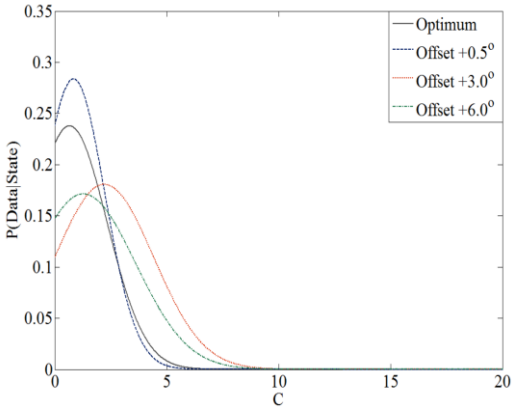

a3) Monitoring Criterion C TI = 2.0%

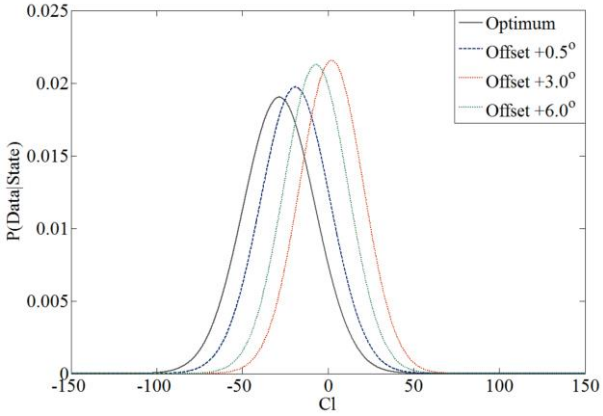

b3) Monitoring Criterion C_l TI = 2.0%

Figure 4.10: Normal probability distributions constructed via the 5 training datasets giving and estimate of P(Data|State) for varying levels of turbulence intensities for the EMD feature extraction process.

4.5.4 Fault Detection and Diagnosis Utilising EMD Extracted Amplitudes

Figure 4.10 shows that results of the same naïve Bayes classifier train process as discussed above for the EMD amplitude extraction process. It can be seen that in the case of the EMD extraction algorithm a negative result was found. Specifically large overlapping regions were observed for the probability of the data given the rotor state. These overlapping regions accordingly led to detections and diagnosis with unacceptable levels of uncertainty due to the similarities in the values observed for C and C_l under differing rotor condition. This can be seen in the NBC results presented in Appendix A in Tables A.13 to A.24.

4.6 Imbalance Algorithm Development

Based on the results of the above application of the proposed time-frequency monitoring processes a number of developments to the condition monitoring processes adopted were undertaken in order to improve the ability to detect and diagnose rotor fault conditions. The changes presented were then applied in-part to the experimental data captured (Section 6.4) and were further applied to the drive train simulations presented in Section 8.4. The proposed developments were as follows:

1. Inclusion of further monitoring criteria based on mean turbine operations in the form of non-dimensional turbine performance curves. Inclusion of any further metrics developed as a result of findings in Chapter 6.4. The goal here is to produce a fault vector in $\mathbb{R}^n$ rather than $\mathbb{R}^1$ in order to minimise uncertainty in detection and diagnostic processes.
2. Due to the limited success of the application IMF resulting from EMD for extraction of amplitudes A_1 and A_3 the EMD process utilised will be developed to produce the full Hilbert Huang Transform. The inclusion of this process was adopted as a method to overcome the Time-Frequency limitations of the STFT. In

reality this process is a development to the point of considering the instantaneous frequency of the IMF to give point estimates of the Spectrogram.

3. Due to the relatively transient nature of the calculated rotor imbalance criteria a smoothing operation will be applied to the outputted criterion time-series and compared with the unprocessed imbalance criteria time-series.
4. Lastly the monitoring criteria C_I was utilised for further testing due to the improved classification results.

5 Scale Flume Testing: Experimental Design.

5.1 Introduction

In order to further study the CM of TST rotors subjected to rotor imbalance faults a 1/20th scale flume testing campaign was under taken. The results of the experimental campaign were used in two ways: to further test the developed CM approaches outlined in Chapter 3 and to acquire data for a broader parameterisation of the rotor model outlined in Chapter 4. As discussed the CM approaches developed in Chapter 3 were done so based on frequency domain considerations of CFD results provided by co-researchers. The successful application of the CM approaches goes someway in showing the CFD modelling maybe a useful tool for developing CM approaches as well as providing more insight into how useful the CM approaches may be in practice.

The further parameterisation of the parametric rotor model is presented in Chapter 7; this process is informed by the results of the experimental campaign detailed within this chapter. The extended parameterisation was done to allow for non-steady state drive train simulations which were seen as a central requirement for the testing of the CM approaches developed.

This chapter goes on to describe the considerations made in developing the experimental approach. The chapter opens with a brief overview of the developed turbine used during the experimental campaign. The re-circulating flume used of the testing is briefly described followed by discussion of aspects of commissioning, calibration and setup. This is followed by a section considering the effects of Reynolds number on the experimental campaign. Lastly the testing procedure is outlined.

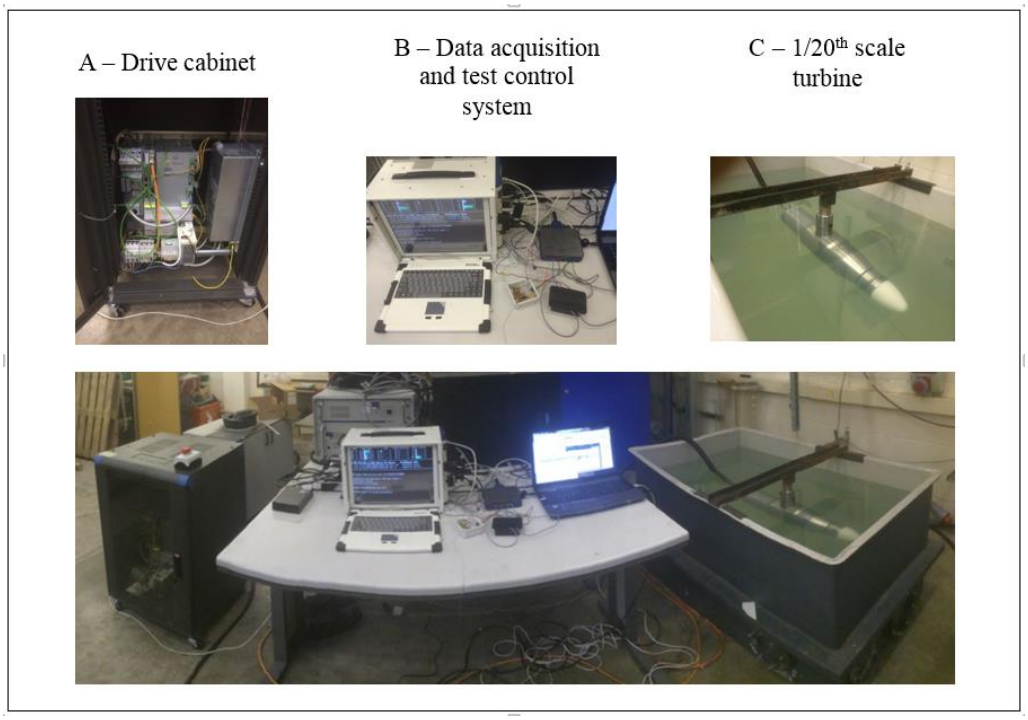

Figure 5.1: Overview of the 1/20th scale turbine test apparatus. A) Shows the motor drive cabinet, B) Shows the PXI system used for DAQ and test control and C) Shows the turbine without blades during tub testing.

5.2 1/20th Scale Turbine Design

Figure 5.1 shows an overview of the test rig during initial tub testing of the 1/20th scale turbine at Cardiff University. The TST test rig is made up of three main assemblies, namely, a drive cabinet (Figure 5.1a), a test control and data acquisition system (Figure 5.1b) and the 1/20th scale turbine (Figure 5.1c). Each of these assemblies is labelled and an overview of each is given in this section.

A schematic of the cross-section of the developed turbine is shown in Figure 5.2: Cross-section of the 1/20th scale turbine.. The rotor is directly coupled to a motor enclosed in a stainless steel nacelle. A nacelle mounting sleeve was used to attach the turbine to a supporting stanchion which is attached to a supporting beam via a load bearing block and support screws. The stanchion is instrumented with a force block measuring the thrust loading on the turbine.

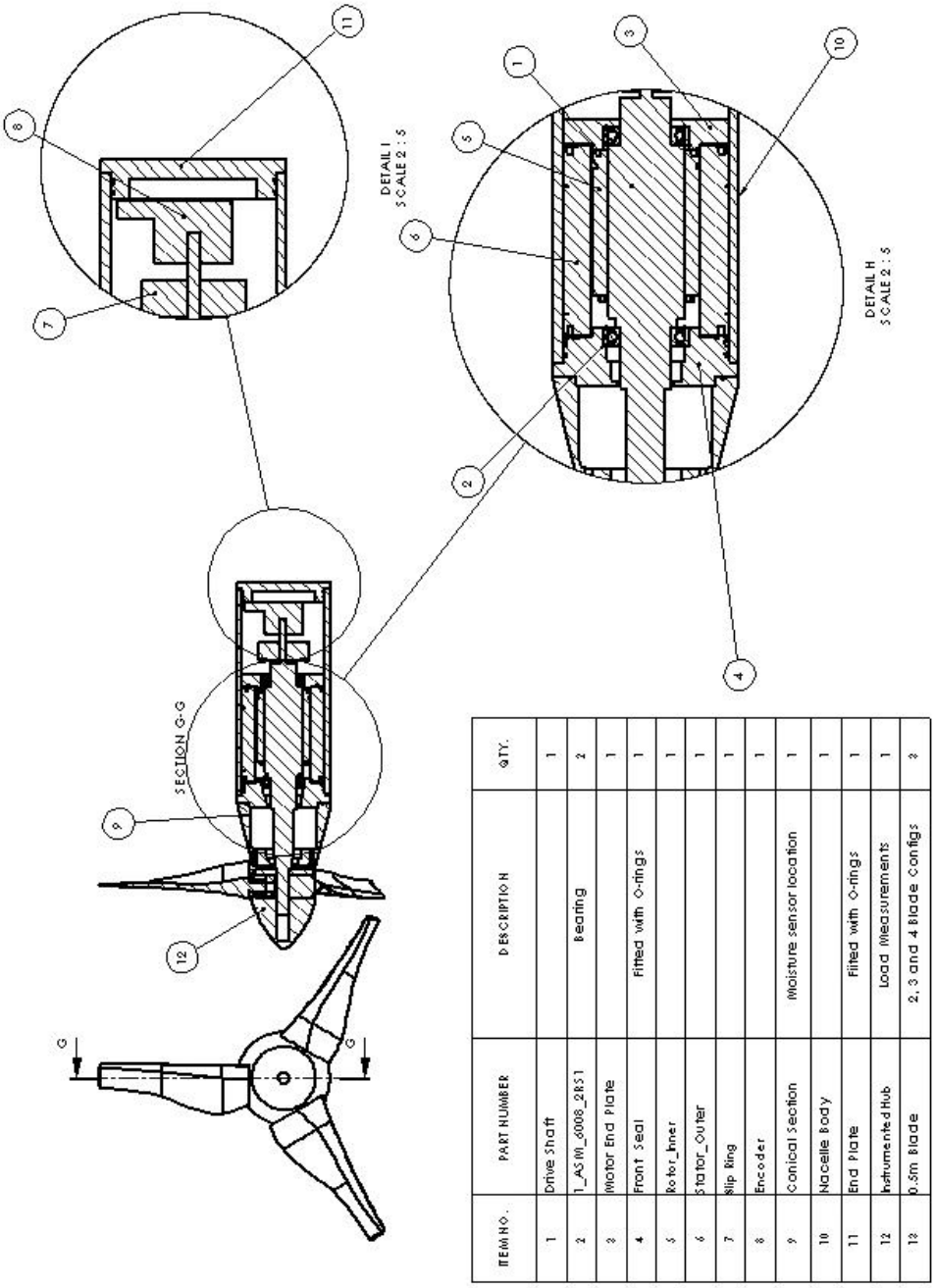

ITEM NO.	PART NUMBER	DESCRIPTION	QTY.
1	Drive Shaft		1
2	1_ASM_6008_2RS1	Bearing	2
3	Motor End Plate		1
4	Front Seal	Fitted with O-rings	1
5	Rotor_Inner		1
6	Stator_Outer		1
7	Slip Ring		1
8	Encoder		1
9	Conical Section	Moisture sensor location	1
10	Nacelle Body		1
11	End Plate	Fitted with O-rings	1
12	Instrumented Hub	Load Measurements	1
13	0.5m Blade	2, 3 and 4 Blade Configs	4

Figure 5.2: Cross-section of the 1/20th scale turbine.

The Bosh Rexroth synchronous torque motor was used to provide the breaking torque and turbine velocity control. The motor model was the MST130E-0035; the motor had a peak and rated torque values of 65 Nm and 22.5 Nm. The rated velocity was 350 RPM with a peak velocity of 700 RPM.

Moflon MUSB2121 USB slip ring with two addition lines was mounted behind the motor, in a third chamber, on the drive shaft, as shown in Figure 5.3A. This enables connectivity to the hub via the hollow drive shaft to provide communication between the Arduino and the turbine controller and data acquisition set-up. The motor encoder was mounted on the end of the turbine drive shaft. The power connections to the motor were also made in the chamber with the slip ring and motor encoder; this was done using solder sleeves. The turbine was sealed with a threaded end plate; the end plate used two O-rings to stop water ingress. The power leads and data leads were output through a hydraulic pipe threaded into the turbine end plate (Figure 5.3B).

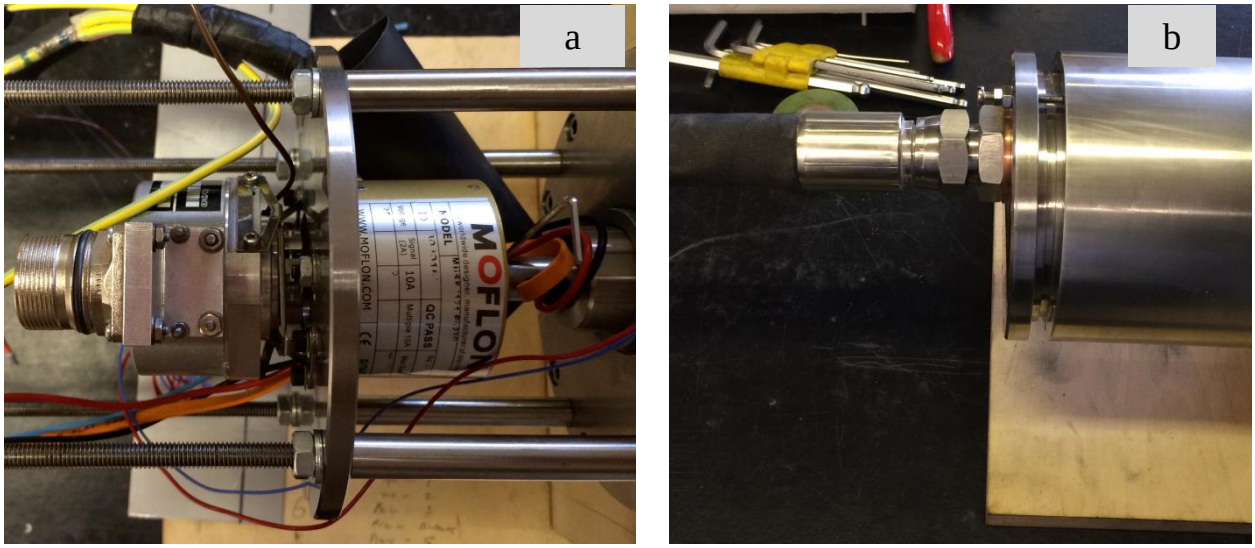

Figure 5.3: a) USB slip ring mounted at in the back turbine chamber for data communication and instrumentation power, b) Hydraulic hose attached to the turbine end plate through a threaded connection facilitating the motor and instrumentation cabling.

The turbine rotor houses an instrumented hub and a hollow nose cone. The instrumented hub had two strain gauged beams for measuring axial thrust and blade torque. The mechanical design of this element was undertaken by a co-researcher. The hub design allows the configuration of different blade arrangements, with 2, 3 or 4 blades being installed as required.

The data acquisition and processing functions were designed and implemented by the author and are detailed in this section. The supporting instrumentation circuitry was mounted within the hollow nose cone, with power, synchronising pulse train and serial communications leads fed through a hollowed drive shaft. On the back end of the turbine the drive shaft was terminated at an encoder for servo motor control and turbine velocity measurements. In this end section a USB slip ring is used for sending communications and power to the nose cone circuitry. Furthermore the required motor connections were made at this point.

Communication and power cables are fed into the nose cone via the hollow drive shaft. This drive shaft enters into the turbine body via a hole that has been closed with a PTFE seal. As a safety feature the initial section of the turbine body forms a sealed chamber. This provides the space needed for the possible future integration of a torque transducer. The section was equipped with a moisture sensor to monitor any seal failure and subsequently shut down the motor before water could cause any more serious damage. The braking motor is then located within a separate chamber. The turbine drive shaft was formed from the motor rotor. The motor stator was machined to closely fit within the turbine housing. Thus the two separate parts of the motor were integrated into the turbine, providing an elegant yet effective design.

The instrumented hub enabled the measurement of blade thrust and twist about the blade axis using two separate strain-gauged beams. In order to acquire and record the data from the strain gauged beams a circuit was designed by the author and a PCB was commissioned, as shown in Figure 5.4. The circuit, shown in Figure 5.5, was designed to achieve the desired sensitivity and accuracy from the beams while allowing data to be logged in real-time. The PCB design made use of an Arduino Nano for data logging and control, two bridge circuits

for the strain-gauged beams, two single rail instrument amplifiers, an ADXL 335 accelerometer and a serial connected SD card read/write board for data storage.

The effect of the water surrounding the hub housing the strain gauge beams meant that temperature compensation, usually achieved via a half-bridge setup, was thought to be unnecessary. This effect and consideration of the space constraints in the hub meant that a quarter-bridge configuration was considered suitable. The nominal resistance of the strain gauges was given by the manufacturer to be 119.8 Ω. The complimentary resistance on the same bridge was created using a 115 Ω fixed resistance in series with a 0-10 Ω range, 13 turn, variable resistor. This allowed the bridge to be balance easily at the high gain levels required. The other bridge arm was balanced to the required 2.5 V via two fixed resistors of 1 kΩ, which as well as balancing the bridge helped avoid currents running through the system above 500 mA. The output from each of the strain gauged beams was fed into a single-rail instrument amplifier (AD627), in the case of the thrust beam the input differential was taken relative to the circuit ground. In the case of the twist beam the differential input was taken relative to the midpoint of the measurement range of the ADC in the Arduino Nano, to accommodate the possibility of recording twist about the blade axis in both directions. To achieve this, a potential divider with two equal resistances with a 5 V potential was used and the output from this was fed into the instrument amplifier reference pin. Evidence for the bidirectional nature of the twist about the blade axis was taken from CFD models constructed within the research group. The CFD models were also used to give an estimate of the blade loading likely to be observed at differing turbine operating conditions. From this data the operating range of the axial thrust strained beam was set at 0 to 50 N and likewise on the blade twist strain gauged beam the range was considered to be -0.5 to 0.5 Nm. The gain for each amplifier was set via a fixed resistance of 180 Ω, producing a gain of 1,111. This was calculated via the equation given on the AD627 datasheet (Analog

Devices, 2013). The gain value was set after a number of calibration tests in order to maximise the signal-to-noise ratio for a desired sensitivity.

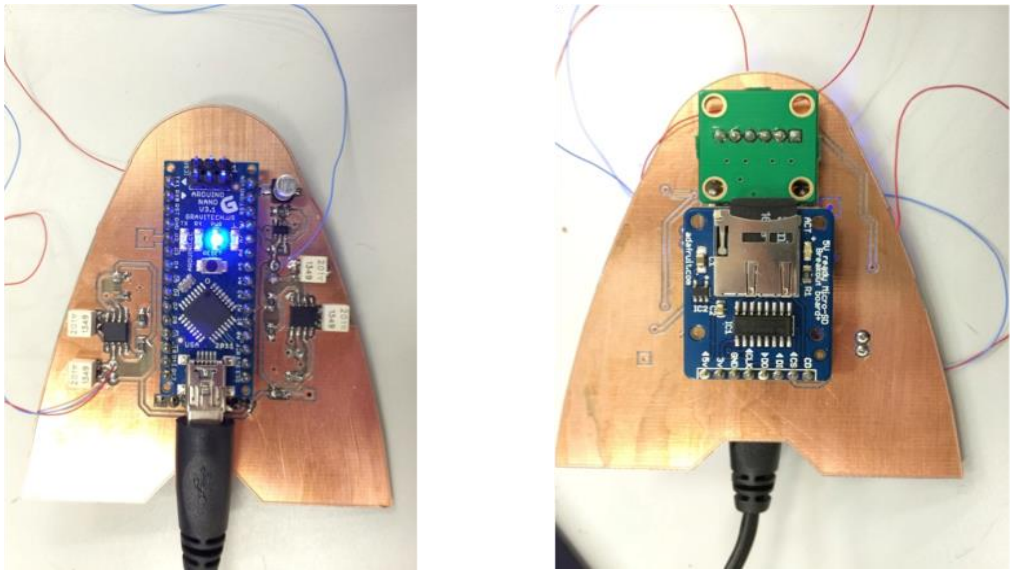

Figure 5.4: Nose cone circuitry used for signal conditioning and data acquisition via an SD for real-time data logging. Included in the circuitry is the ADXL 335 Accelerometer.

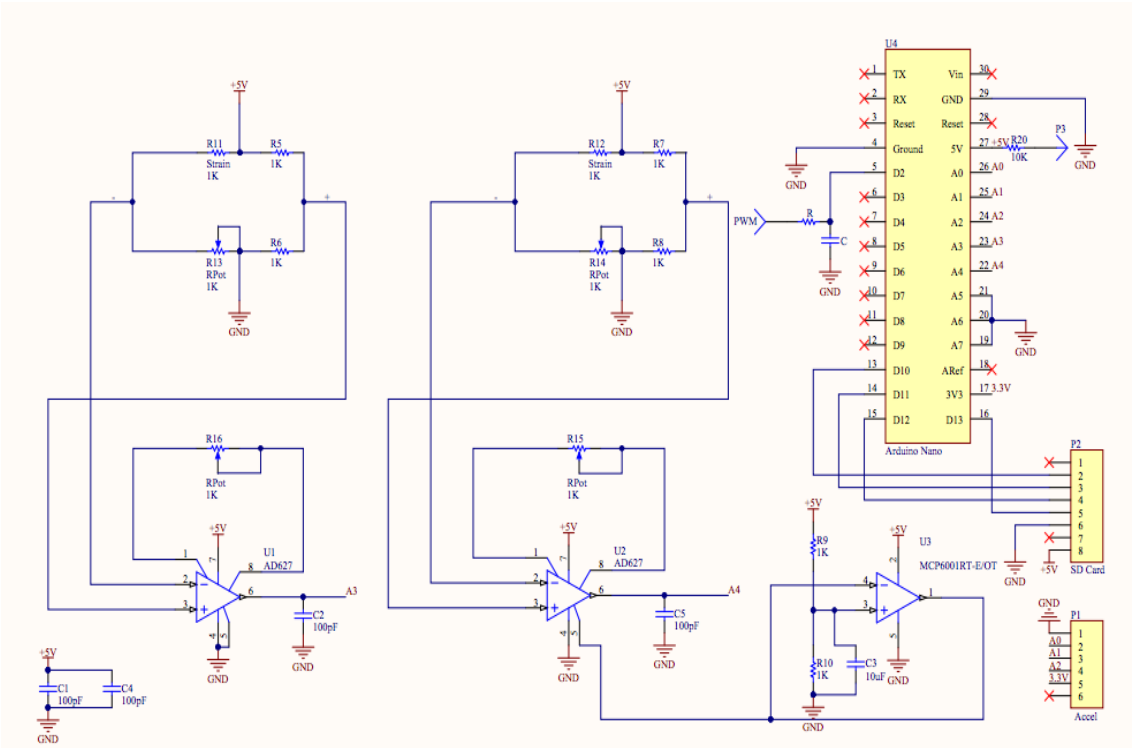

Figure 5.5: Circuit diagram of the instrumented hub PCB consisting of signal amplification and quarter bridge configuration signal conditioning circuitry.

5.3 Flume Facilities

The 1/20th scale testing undertaken as part of this research was conducted at the circulating flume tank facilities at the University of Liverpool. A schematic of the flume facilities is shown in Figure 5.6. The flume is operated via a 75 kW motor used to drive an impeller, the flow is pumped through flow straighteners prior to entering the working section. Previously detailed Laser Doppler Anemometry measurement have been taken and indicate that on average the TI observed within the flume is approximately 2% for fluid velocities between 0.5 ms^{-1} and 1.5 ms^{-1} (Tedds et al, 2013) . To ensure no velocity deficit at the free surface of the working section, due to the contraction into the working area, an energising jet is added to the flow – the jet injection speed were calibrated by the facility operators prior to testing (Mason-Jones et al, 2012; Tedds et al, 2013).

The working section is 3.7 m in length, 1.4 m in width and 0.84 m in depth. The turbine was mounted at the mid-point of the working section length and width. The turbine was mounted at a depth of 0.425 m at the turbine rotor centre, this gave a blockage ratio of 17%. The flume can generate up to 6 ms^{-1} flow speeds however for the associated 1/20th scale testing fluid velocities between 0.5 and 1.1 ms^{-1} were used leading to diameter based Reynold's Numbers between 249,000 and 495, 000. The effect of the ratio of inertial to viscous forces, captured by the Reynolds number, to allow for non-dimensional scaling using λ as a kinematic relationship is considered in Section 5.5.

A similar setup presented by Tedds et al (2013) was used for fluid velocity measurements – although in this case, as wake characteristics are not the object of the research, only the fluid flow upstream from the turbine was measured. The fluid velocity was measured using an Acoustic Doppler Velocimeter (ADV), specifically the Nortek Vectrino+ was used. ADV measurements provided x, y and z fluid velocity measurement with manufacturer calibrations quoting an uncertainty of 1% in measurements. The fluid velocity

measurements were sampled at 200 Hz and logged by the PXI. A full characterisation of the flume settings can be found in Tedds (2014).

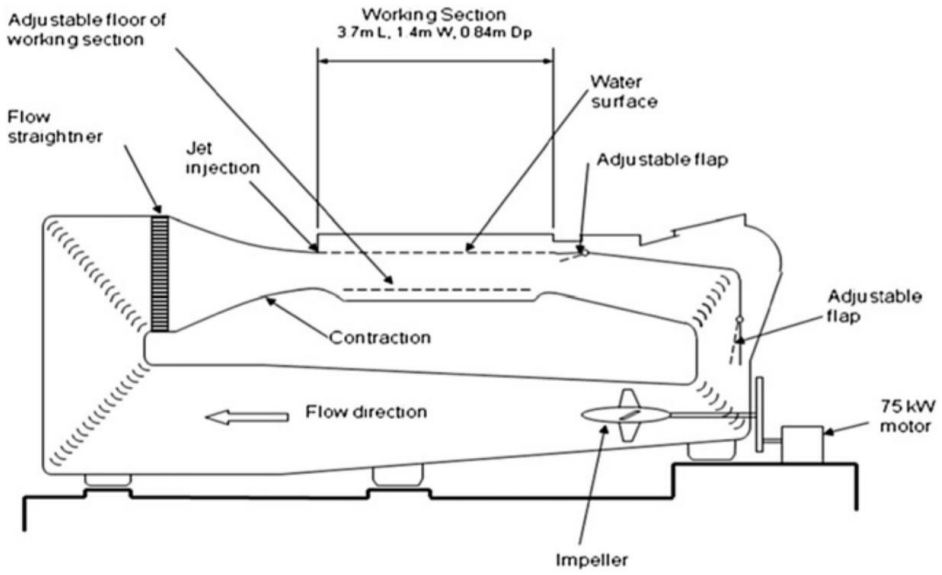

Figure 5.6: Schematic of the Liverpool of University test facilities used during 1/20th scale testing.

5.4 Commissioning

5.4.1 PMSM Calibration.

As the PMSM was used for drive shaft torque measurements as well as providing a resistive torque the manufacturer's specifications were tested via calibration. The calibration was undertaken by applying known moments to the turbine rotor in the clockwise direction – the direction of motion for the given blade setup. The moments were applied bout the centre of the turbine drive shaft by applying weights to a rod inserted in the blade housing holes. Using a process similar to that outlined in Section 5.6.3, the rod has held horizontal by the motor. The rod was loaded and unloaded with known weights at a known distance for the centre of the turbine drive shaft, specifically at 83.5 mm, to create a moment about the turbine drive shaft. The data was captured via the PXI system outlined above.

For each applied load 300 samples of the quadrature axis current (torque generating current) were measured via the motor drives over 30 seconds. This process was then repeated 5 times; the results for all 5 test are shown in Figure 5.7.

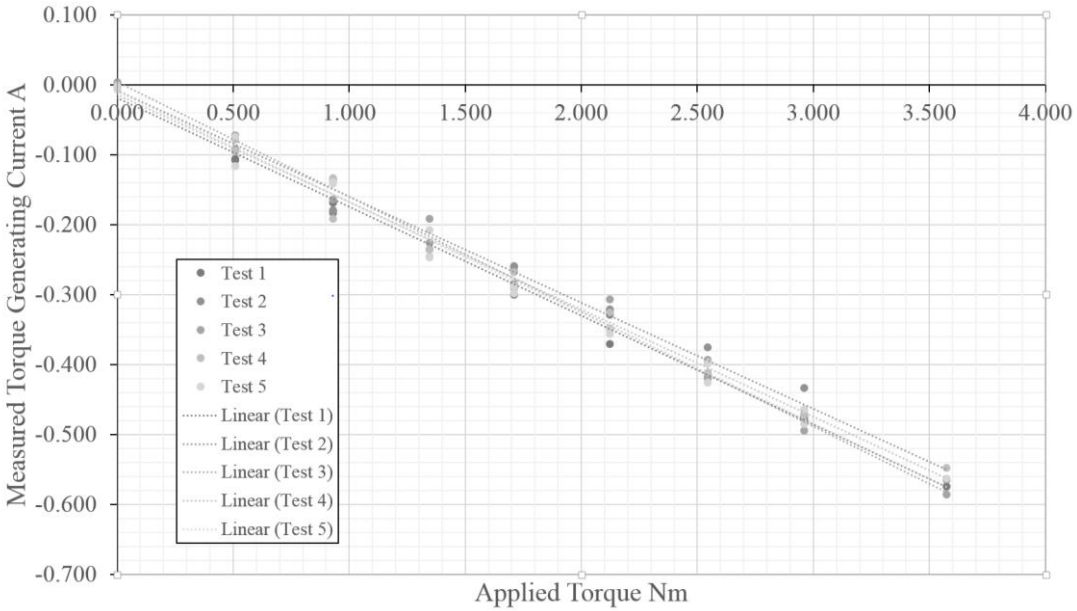

Figure 5.7: Calibration curves showing the relationship between applied moment and measured quadrature axis current.

As expected a linear trend was observed for each test case – the corresponding results of the linear regression are shown in Figure 5.7. Below

Table 5.1 shows the linear regression results. Minimal offset values were observed and an average slope of 6.390 was found. The regressions gave a minimum coefficient of determination value of 0.989 and mean value of 0.992. Using the uncertainty estimation

process outlined by Doman et al (2014) the overall (combining bias and precision uncertainties) uncertainty was found to be 0.07 Nm.

Table 5.1: Table showing the results of the linear regression to the PMSM calibration data.

Test No.	TGC Offset A	TGC Gradient Nm/A	TGC R^2
1	0.018	6.418	0.994
2	0.009	6.596	0.989
3	0.004	6.101	0.993
4	0.014	6.519	0.991
5	0.009	6.317	0.992
Mean	0.011	6.390	0.992
Standard Deviation	0.004	0.157	0.002

5.4.2 Frictional Losses Quantification

In order to accurately measure the torque developed at the turbine rotor due to the fluid flow the frictional losses in the turbine drive shaft had to be characterised. This is a clear requirement as the rotor torque will have to overcome shaft losses during testing and the motor will therefore measure the rotor torque minus the shaft losses observed. This was done in the lab by running the motor at various rotational velocities with no blades installed in the turbine nose cone. For each velocity setting 12000 readings of the power and torque required to maintain the rotational velocity of the turbine were measured. Polynomial functions were then fitted to the data and used to correct the torque and power values measured during flume

testing. Figure 5.8 shows the results of the shaft loss testing along with the polynomial functions fitted to the acquired data.

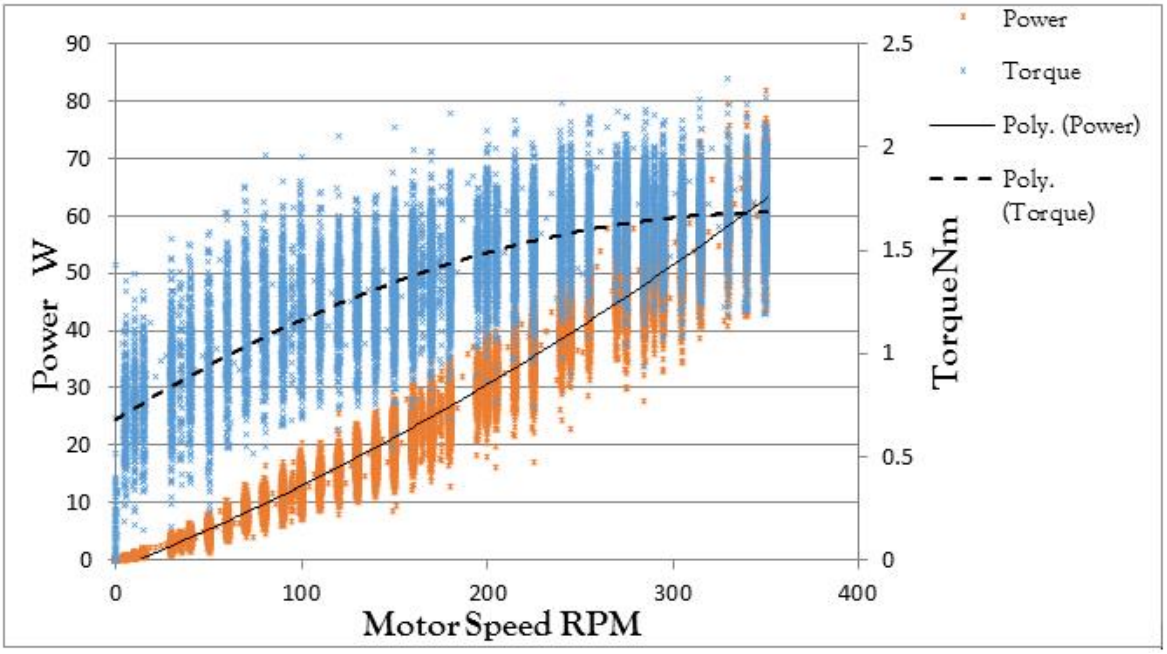

Figure 5.8: Shaft losses characterisation data taken under lab conditions with no blades installed in the turbine.

5.5 Reynolds Independence Testing

Upon commissioning and confirmation of the correct operation of the 1/20th scale model turbine Reynolds independence testing was undertaken. The testing was undertaken for a number of λ values and for 5 differing fluid velocities. This testing was done sequentially by setting the flume velocity to a given value and then setting the PMSM speed to a given value to achieve the λ of interest. Data was then captured for approximately 16 differing λ settings from freewheeling passed the stall region; at each point data was recorded for approximately 90 seconds. Once the data for each of the λ settings had been recorded the fluid velocity of the recirculating flume was increased to the next required velocity. The flume was allowed to settle for approximately 1 minute and the ADV measurements were checked to confirm the flume was operating at the correct speed. Once this was confirmed the process data capture process was repeated.

Figure 5.9 and Figure 5.10 show the power and torque curves developed during the Reynolds independence testing. As can be seen the testing was undertaken for fluid velocities between 0.7 ms^{-1} and 1.1 ms^{-1} in increments of 0.1 ms^{-1}. The point at which the power and torque coefficients observed became independent of the Reynold's number can be seen to be between 1.0 ms^{-1} and 1.1 ms^{-1}, as indicated by the close proximity of observed power and torque coefficients for each fluid velocity cases. Invariance of the non-dimensional turbine coefficients to Reynolds numbers simplifies the comparison of large scale CFD data with the 1/20th scale experimental data as similar turbine performance coefficients are expected for given kinematic scaling numbers, specifically for a given λ value. This finding is consistent with the work of Tedds et al (Tedds et al, 2011) where it was found that so-called Reynolds independence was observed for a 0.5 m diameter rotor in flow velocities above 1 ms^{-1}.

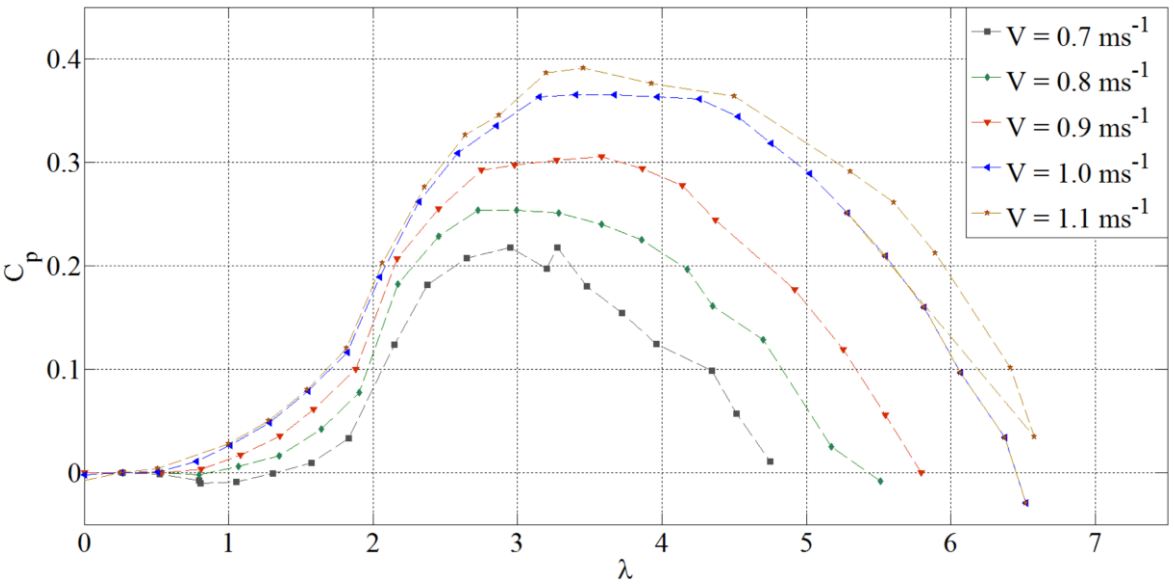

Figure 5.9: Power coefficient values observed for the Reynolds independence testing undertaken.

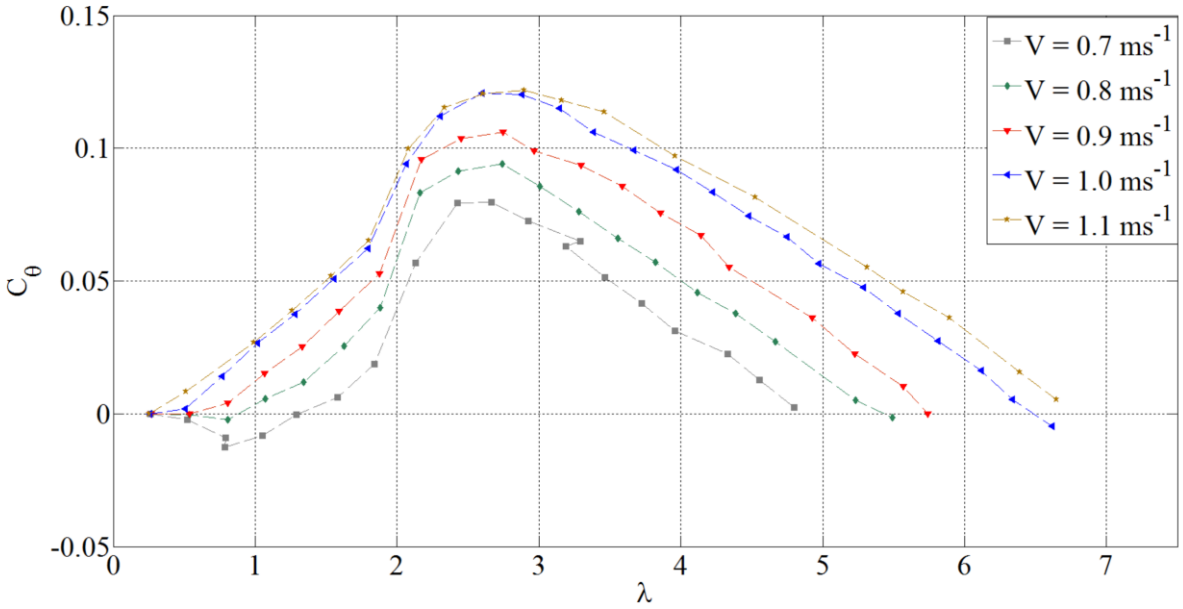

Figure 5.10: Torque coefficient values observed for the Reynolds independence testing undertaken.

5.6 Experimental Campaign

5.6.1 Turbine Control

For the set of tests undertaken as outlined in Section 5.6 it was considered that speed control of the PMSM would be the most suitable control approach. This was considered to be the case as the PMSM was used to undertake rotor torque measurements as well as provide a resistance to the rotor torque developed via the oncoming fluid flow. As outlined in Section 3.4.2 in order to accurately measure the rotor torque via the PMSM minimising the acceleration of the turbine rotor was required. As a result of the above reasoning all of the rotor imbalance test cases undertaken speed control of the PMSM was utilised in order to best measure the rotor transient characteristics.

5.6.2 Test Cases

The purposes of the flume testing campaign undertaken as part of the research activities were two-fold as noted in Section 5.1. In order to test CM approaches at the 1/20th scale and provide data for parametric model development an experimental campaign utilising testing at differing fluid velocities, turbine rotational velocities and with differing rotor conditions

was undertaken. Table 5.2 shows the rotor cases and the fluid velocities tested at the University of Liverpool; for each case five turbine rotational velocities were tested leading to λ values of: 1.5, 2.5, 3, 3.5, 4, 4.5 and 5.5. These test cases gave data relating to turbine operation at both differing diameter based Reynolds numbers and at differing kinematic scaling values – this allowed for transient relationships to be developed for turbine model development and to test the performance of monitoring approaches at a variety of turbine operating conditions.

Table 5.2: Outline of the rotor imbalance test cases simulated during the 1/20th scale testing along with the fluid velocities set.

Rotor Condition	Fluid Velocity
Optimum: All blades at 6^o pitch angle setting	0.9 ms^{-1}, 1.0 ms^{-1} and 1.1 ms^{-1}
Offset +3: Blade 1 at 9^o pitch angle, all others at 6^o	0.9 ms^{-1}, 1.0 ms^{-1} and 1.1 ms^{-1}
Offset +6: Blade 1 at 12^o pitch angle, all others at 6^o	0.9 ms^{-1}, 1.0 ms^{-1} and 1.1 ms^{-1}
Two Blades Offset: Blade 1 at 12^o, Blade 2 at 9^o, Blade 3 at 6^o.	0.9 ms^{-1}, 1.0 ms^{-1} and 1.1 ms^{-1}

In the considerations made for the testing campaign it was noted that the flume and turbine setups may exhibit some inherent imbalance as such the optimal case was included and the processing of condition monitoring approaches were compared with the optimal case. Furthermore considerable effort was made to reduce any unintentional imbalances introduced during the process of setting the blade pitch angles between tests as by necessity the turbine was removed to undertake this process. These provision are outlined in the following sections.

5.6.3 Instrumented Blade Position Setting

In order to set a consistent reference for the turbine rotor position relative to the stanchion, the encoder reference was set to 0^o when the instrumented blade was at top dead centre or pointing vertically parallel to the stanchion. This was done by exploiting the flat

surface which was created by the blade housing – this can be seen in Figure 5.11a. The flat surface highlighted on the figure was $90^o \pm 0.5^o$ to the blade orientation. A digital protractor - zeroed relative to the horizontal cross beam to which the turbine was mounted - was then used to confirm the blade housing was at the required angle namely, 0^o. This can be seen in Figure 5.11b. Once the position was correct the encoder reference was programmatically set to zero using the Bosch Rexroth IndraWorks software.

a b

Figure 5.11: Blade positioning setup, a) Blade Housing b) Setting the housing position using a digital protractor.

5.6.4 Blade Pitch Angle Setting

The process developed for setting the turbine blade pitch again utilised a digital protractor and the encoder reference set as outlined in the previous section. The turbine rotor was set such the blade undergoing the pitch setting was positioned horizontal relative to the turbine stanchion – in terms of the encoder reference the three angles which set the blades to the horizontal positon required were 90^o, 210^o and 330^o. Once the blade is horizontal, the pitch angle setting relative to the turbine rotational plane can be done relative to the vertical. To achieve this the digital protractor was zeroed relative to the turbine stanchion, which served as a useful vertical reference – see Figure 5.12a.

The digital protractor was then positioned across the turbine blade tip and the angle set. Once the angle was set the blade was secured via the grub screws – the angle was then checked and corrected if necessary. The digital protractor used had a resolution of 0.1^{o}, however due to human error the angles set were subjected to an error of ± 1^{o}. This was considered generating the test cases presented in Table 5.2: Outline of the rotor imbalance test cases simulated during the 1/20th scale testing along with the fluid velocities set.

a b

Figure 5.12: The blade pitch setting process, a) Zeroing the digital protractor relative to the vertical stanchion b) setting the blade pitch angel relative to the vertical.

5.6.5 Test Procedure

Testing was undertaken with care to ensure consistent results, specifically in terms of setting the turbine in place and allowing the flume to settle at the next fluid velocity or turbine rotational velocity. Once the 0^{o} zero position of the encoder was set the digital protractor zeroed vertically relative to the turbine stanchion. The process outlined above was then followed to set each blade pitch angle. Once the turbine blades were all set to the required pitch the turbine was moved into position with a crane. The turbine stanchion was

bolted to a cross beam mounted perpendicular to the flow direction across the recirculating flume – this was checked by measuring the distance of the cross beam from the flume inlet on either side of the flume. The recirculating flume was then set to the required fluid velocity, again, this was checked with ADV. The turbine, generally self-starting was allowed to freewheel for a minimum of 100 seconds. The turbine was then set to the required rotational velocity to achieve the desired λ value, again the turbine was allowed to rotate at this velocity for a minimum of 100s and then the data capture was initiated. Data was collected for 300 seconds and the next rotational velocity set. This process was repeated for each required λ value, as noted in Section 5.6.2. Once all the λ values for the fluid velocity setting were captured the flume was set to the next required flow velocity. This process was repeated for each setting outlined in Section 5.6.2.

6 Scale Turbine Flume-Testing Results

6.1 Introduction

This chapter presents key results from the flume based test campaign in order to provide an overview of the turbine performance under the differing operating conditions as well as to give an initial insight into the performance of condition monitoring algorithms under flume tank testing.

The chapter presents both mean value characteristics expressed in the usual performance coefficient curves and transient characteristics which were analysed in a variety of ways. Non-dimensional performance curves have been developed to confirm Reynold's independence during testing. These are used to compare recorded values with the previous values calculated via CFD computations. This is used to compare turbine operation under differing control schemes and rotor conditions. The non-dimensional turbine performance curves are supplemented by drive shaft torque transient results analysis. The transient results have been included in the appropriate sections for comparison of CFD calculated drive shaft torque transients. They also enable the consideration of turbine drive shaft torque transients observed under differing turbine control settings and thus highlight the effect of rotor condition on transient drive shaft torque characteristics. The latter considerations of the effect of rotor condition on drive shaft torque transients culminate in the frequency characterisation of the turbine rotor torque over a range of tip-speed ratios. These characterisations are then used to develop performance surfaces which are then utilised in two ways which are consistent with the goals of the research. Firstly, the surfaces are used

to provide ‘parameter surfaces’ for an empirical parametric rotor model presented in Chapter 7. They are further utilised in CM processes outlined in Chapter 3 and applied in Chapter 8.

The chapter ends with the presentation of the application of these CM algorithms the use of the developed surfaces.

6.2 Comparisons of flume data with CFD results

In order to validate CFD calculations and further confirm the expected rotor characteristics observed in previous test phases both the transient and steady state turbine characteristics were compared with CFD results. The data used for the comparison with the CFD values calculated were taken at a fluid velocity of 1 ms^{-1} for an optimum rotor setup. Figure 6.1 and Figure 6.2 show good agreement between the current experimental campaign and the legacy testing and simulations undertaken within the research group for the measured non-dimensional power and torque coefficients, respectively. Specifically, the non-dimensional power and torque coefficients observed passed the point of peak torque for the legacy data sets all fall within the 95 % (2 standard deviations) confidence interval of the data acquired as part of the research presented. This has been highlighted on both Figure 6.1 and Figure 6.2 by the error bars plotted.

At lower tip-speed ratios, at $\lambda \approx 1.5$, it was found that the power and torque coefficients observed during the current testing phase were in disagreement with the results generated via CFD calculations. This data set represents the first, taken by the research group, at lower tip-speed ratio values than the peak torque operating point. These measurements were made available by the more advanced motor control system which allowed for turbine speed control, as discussed in chapter 5. The data would suggest that the CFD calculations are over estimating the expected power output from the turbine at tip-speed ratios lower than the peak torque setting, at $\lambda \approx 2.1$. This suggests that the CFD calculations may need to be adapted when calculating the turbine performance in the stall region. As noted the diameter based

Reynolds Number for the test cases shown is 250,000 relative to 36,100,000 for the full scale rotor modelled using CFD. As the testing approached Reynolds independence at 1 ms^{-1} it was thought that, considering the relative velocity of the fluid given the turbine rotational velocity, the significance of viscous effects in the region of $\lambda \approx 2.1$ maybe the cause of the discrepancy. As such further testing is required to confirm why the discrepancies between the experimental data and CFD data exist in the stall region.

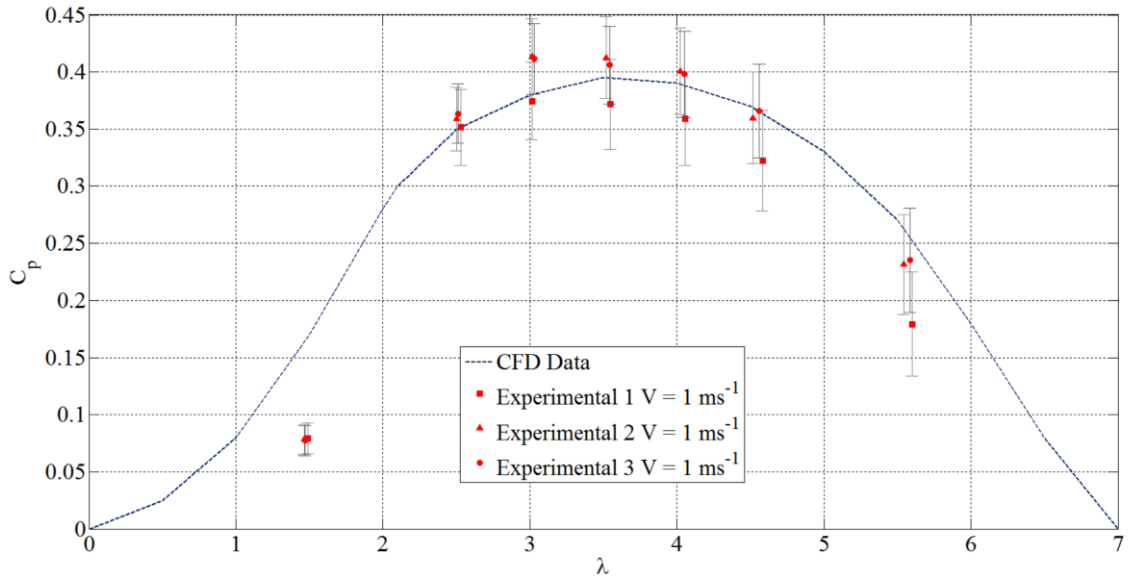

Figure 6.1: Power coefficient plot comparing the observed power curve from previous testing and simulation campaigns and the power curve observed during the current testing phase.

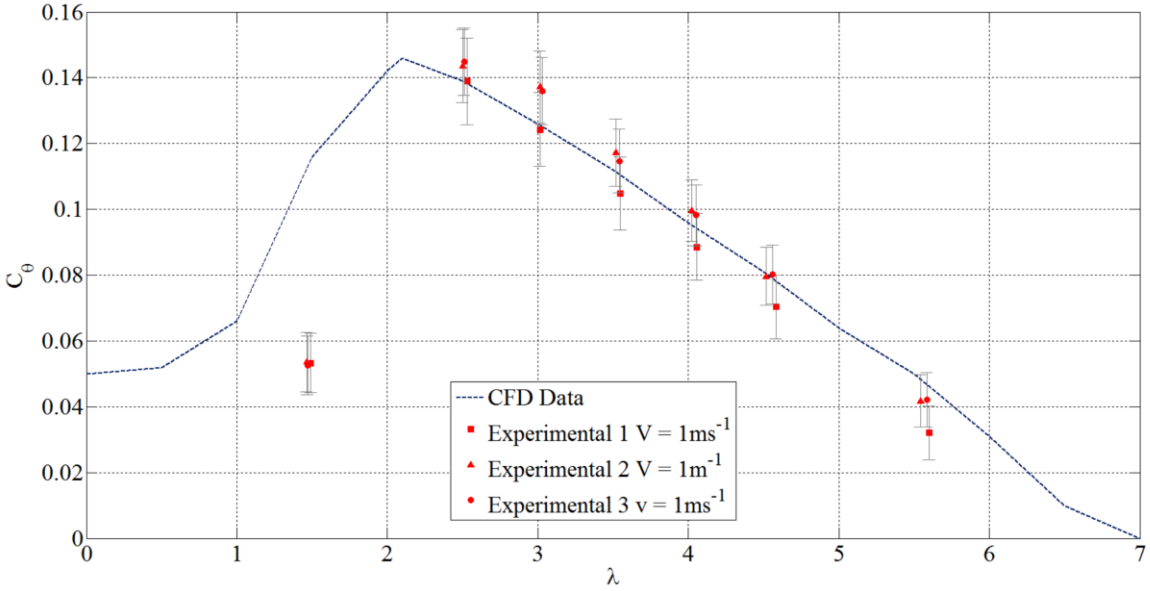

Figure 6.2: Torque coefficient plot comparing the observed power curve from previous testing and simulation campaigns and the power curve observed during the current testing phase.

Assure and progress the process of validating transient CFD calculations the spectrum of the calculated rotor torque via transient CFD simulation was compared with the spectrum observed for the turbine rotor torque measured during flume experimentation. The data used to undertake the validation exercise was again from testing at 1 ms^{-1} fluid velocity for optimum rotor condition at peak power ($\lambda \approx 3.5$). As CFD results were not available for the 0.5 m flume scale rotor so the comparison was made with the available CFD results for 5 m radius turbine at peak power operating condition for a fluid velocity of 3.086 ms^{-1}. Due to the difference in turbine scale the transient validation proceeded by using the amplitude spectrum observed in each case scaled by the mean torque value calculated or measured for the given case, referred to as relative amplitude herein. This was considered the most appropriate method for making the comparison of turbines of differing scales and was justified in that the structure of the observed spectra was of greater interest than the numerical values of the amplitudes observed.

Figure 6.3 shows a spectrum plot comparing the relative torque fluctuation amplitude at harmonic intervals up to the 8^{th} harmonic of the rotational velocity of the turbine. In the case of the flume testing the fundamental frequency was 2.23 Hz whereas for the CFD calculations the fundamental frequency was significantly lower at 0.33 Hz. As such the harmonic number was used for the frequency axis in order to make a meaningful comparison.

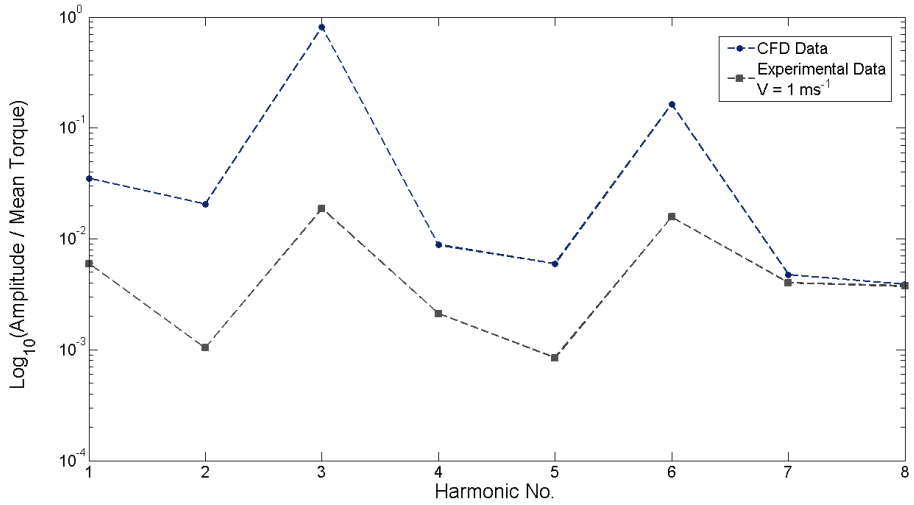

Figure 6.3: Spectrum plot comparing the observed transient torque characteristics calculated via transient CFD simulation campaigns and the transient torque characteristics observed during the current testing phase.

Although relative amplitudes have been considered to minimise the effects of the two differing turbine scales it can still be seen that the larger scale represented via the CFD has a significantly larger relative fluctuation amplitude up to the 7th harmonic of the turbine rotational velocity. Whilst there are undoubtedly inconsistencies between the two datasets the overall spectrum characteristics are similar, as characterised by the two peak amplitudes at the 3rd and 6th harmonics of the turbine rotational velocity. The amplitudes at these frequencies are associated with the torque rotor torque fluctuations introduced as each turbine blade passes the turbine stanchion. It was also noted that the flume testing rotor torque spectrum exhibited higher relative amplitude at the 1st harmonic when compared to the relative amplitude of the 3rd harmonic in the same data set.

6.3 Rotor Fault Simulations

As discussed in Section 3.3 and in-line with both the CFD and parametric simulations presented in Chapters 3 and 4, respectively, the turbine was set up to harbour rotor fault defects in the form of blade pitch errors. Specifically blade pitch errors of differing levels were applied to the instrumented blade, to further the scope of the study tests were also undertaken with blade pitch errors of differing degrees applied to two blades.

6.3.1 Scale turbine performance Curves

The first characterisation undertaken for the turbine rotor fault conditions was to study the effect of the rotor anomalies on the non-dimensional characteristic curves. Figure 6.4 and Figure 6.5 show the non-dimensional performance curves observed for each of the rotor conditions tested, the fluid velocity for the data presented was 1 ms^{-1}. Figure 6.4 shows the power coefficients, C_p and Figure 6.5 the torque coefficients, C_θ. In both figures it can be seen that significantly lower values of the non-dimensional coefficients where measured for each of the offset blade tests. In each case this decrease in the non-dimensional performance coefficients was expected. The greatest reduction was observed for the two-blade offset case followed by the offset +6 ^{o} case. The offset +3^o case whilst deviating significantly from the C_p and C_θ values observed for the optimum case at higher tip speed ratios showed negligible deviation from the optimum case in the peak power and peak torque neighbourhoods, i.e. for $1.5 \leq \lambda \leq 3.54$.

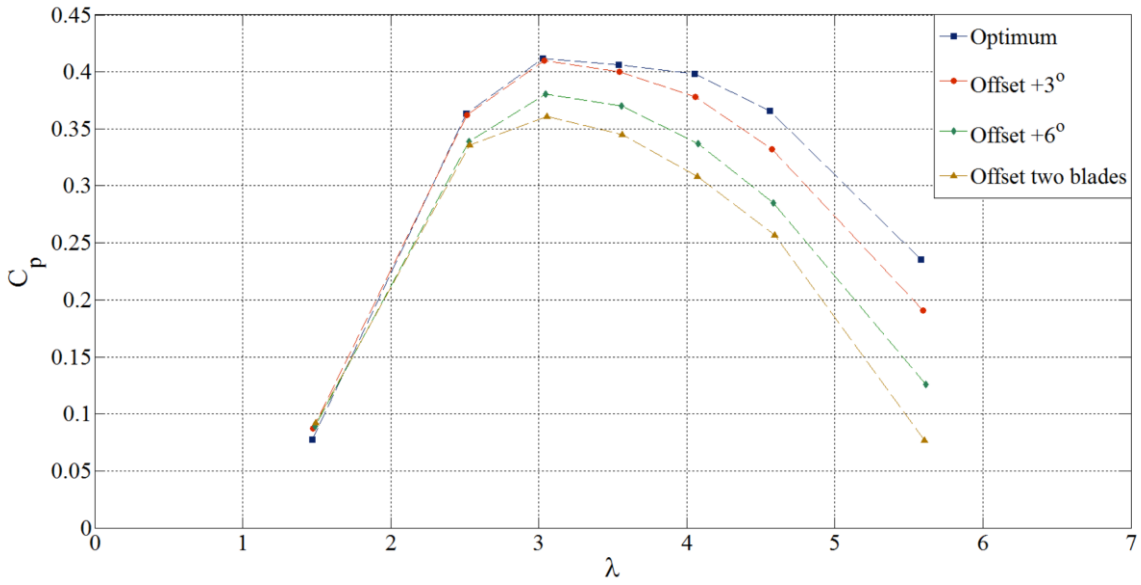

Figure 6.4: Non-Dimensional power curve for the rotor fault scenarios for a fluid velocity of 1 ms^{-1}.

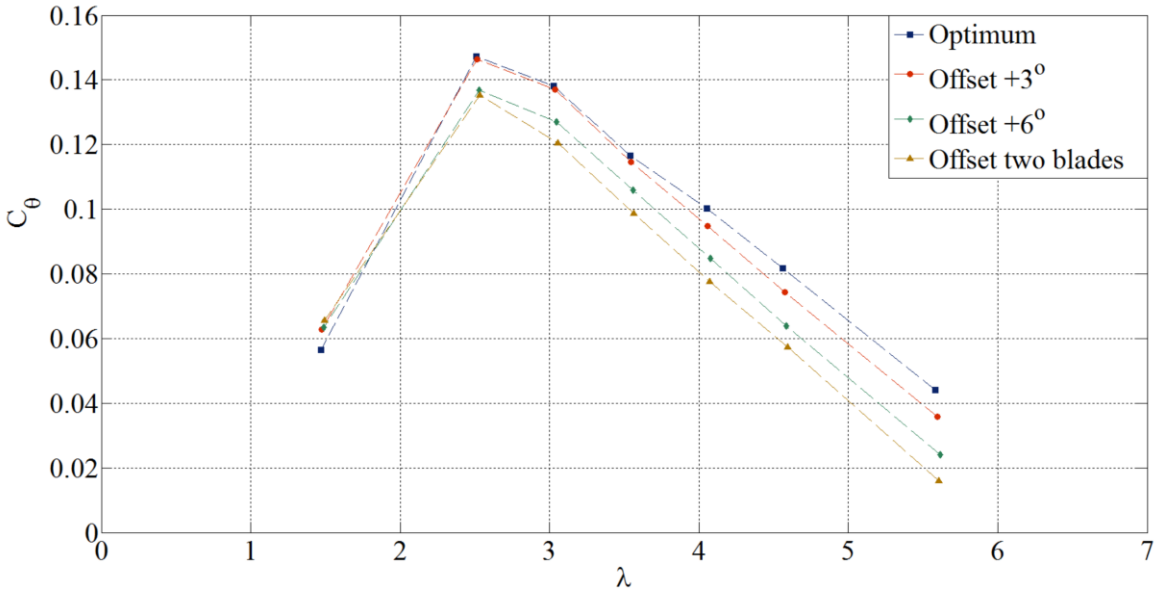

Figure 6.5: Non-Dimensional torque curve for the rotor fault scenarios for a fluid velocity of 1 ms^{-1}.

It was also noted that the spread in the values observed for the non-dimensional coefficients reduced towards peak torque ($\lambda \approx 2.1$) when moving from higher tip-speed ratios to lower tip-speed ratios. It was also observed that, at the tip-speed ratios lower than that of peak torque for which data was measured ($\lambda = 1.5$), the non-dimensional coefficients are in much closer agreement. Furthermore, it can be seen that at this λ value the non-optimum rotor conditions yield slightly higher C_p and C_θ values.

6.3.2 Time-Synchronous Averaging of Torque Data

Time synchronous averaging (TSA) as outlined in Section 3.5.1 was utilised to produce an estimate of the underlying torque transients in the data sets observed for differing rotor conditions. The process was utilised in this case for explorative analysis rather than as a CM algorithm. The TSA CM method will be utilised for subsequent datasets acquired via drive train simulations. The goal of the application of TSA was to highlight the average cyclic torque variations over a single rotation of the turbine. These average characteristics were then utilised to produce a more developed parametric rotor model as presented in Chapter 7.

Figure 6.6 and Figure 6.7 show the results of the TSA process for a fluid velocity of 1 ms^{-1} and a rotational velocity of approximately 134 RPM for the optimum and the offset +6° rotor cases, respectively. The figures show both the results of the data resampling process and the characteristics against the turbine rotation. The mean characteristic is represented by the thick black traces whereas the resampled data is indicated by the thin traces. The blade pass events are highlighted by the vertical lines with the specific blade number labelled above. The data was sampled at 1 kHz and resampled to 1 ° increments of the turbine rotor position, yielding 360 resample points.

It can be observed that the mean trace does indeed represent the average transient characteristics over a single rotation adequately. In both cases a reduction in torque output can be observed at each of the blade pass events.

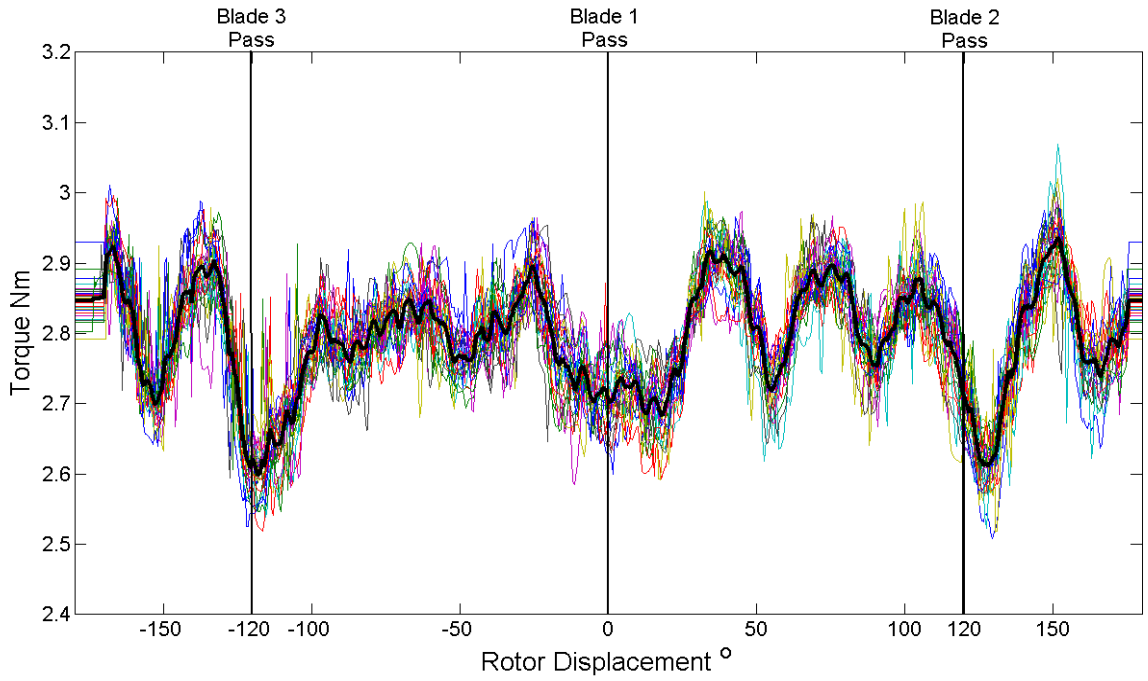

Figure 6.6: Time synchronous averaged data for the optimum rotor condition. The resampled data is plotted along with the process mean (thick line). Flume conditions 1ms^{-1} and rotational velocity 134 RPM.

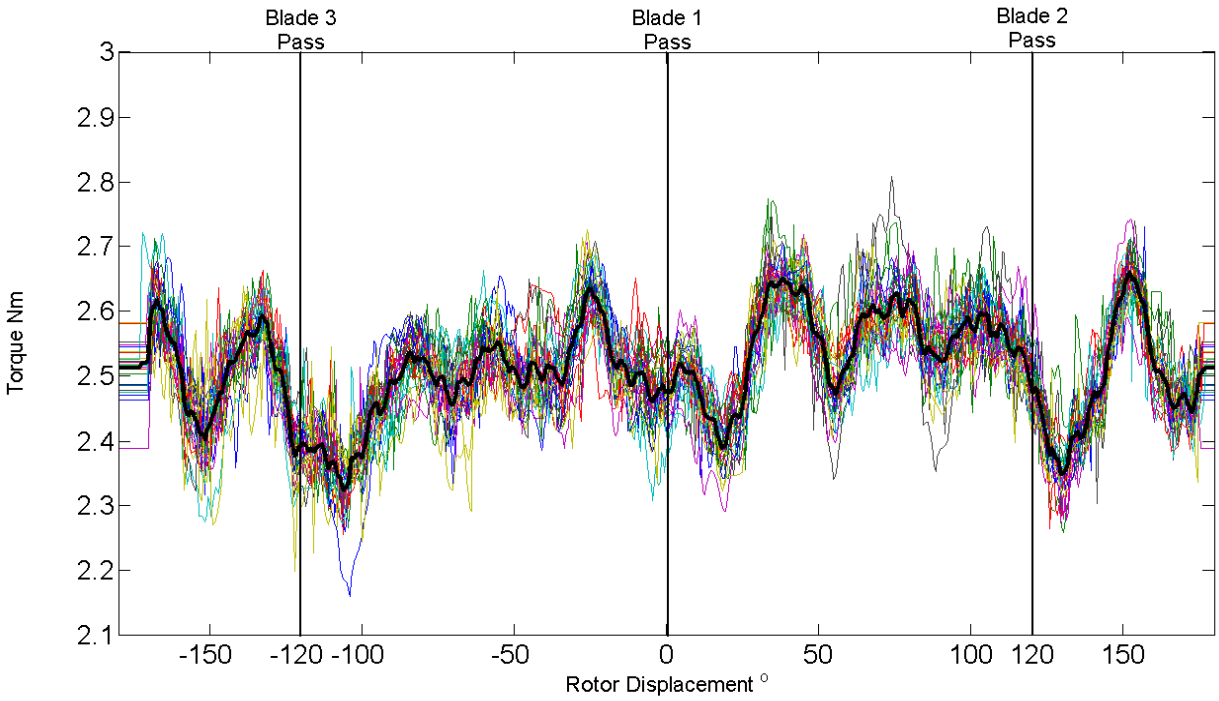

Figure 6.7: Time synchronous averaged data for the offset +6° rotor condition. The resampled data is plotted along with the process mean (thick line). Flume conditions 1ms-1 and rotational velocity 133 RPM.

However for the imbalanced rotor condition shown in Figure 6.7 the reduction in torque at the blade pass events has been distorted with both more variable torque reductions observed at each blade pass event and a shift in position of the local minima of the blade pass torque fluctuation by approximately +10°. Further cyclic variations were observed which occurred roughly ten times per rotation and were considered to be the effect of pole pass events associated with the PMSM operation.

In order to confirm that the mean of the process calculated via the TSA procedure was a suitable representation of the data the dispersion of data about the mean value at each resample point was considered. In order for the data to be adequately represented via the mean process a normal distribution of the data should be observed. This was expected as measurement data most often exhibits normal distribution characteristics. It was confirmed that normal characteristics were observed throughout the data sets recorded. This was

achieved using normal parameter estimation via the maximum likelihood method (Bishop, 2006). Figure 6.8 shows the results of fitting a normal distribution to the resampled data for varying rotor positions (90 º, 120 º and 240º) and for both the optimum (a) and offset +6º (b) cases.

In order to measure the effectiveness of the TSA procedure, and in particular to quantify the performance of the procedure under varying quantifies of data, the deviation of the dataset from the TSA mean was considered for datasets of differing sizes. The varying data set lengths were created by inclusion and exclusion of the measured flume data. The data set lengths were measured in number of rotations, i.e. the number of rotations worth of data included in the TSA result. The deviation was calculated by taking, at each resample point, the mean value of the magnitude of the raw data deviation from the TSA mean value for the given resample point. The mean of the deviations was then taken over the set of all 360 resample points.

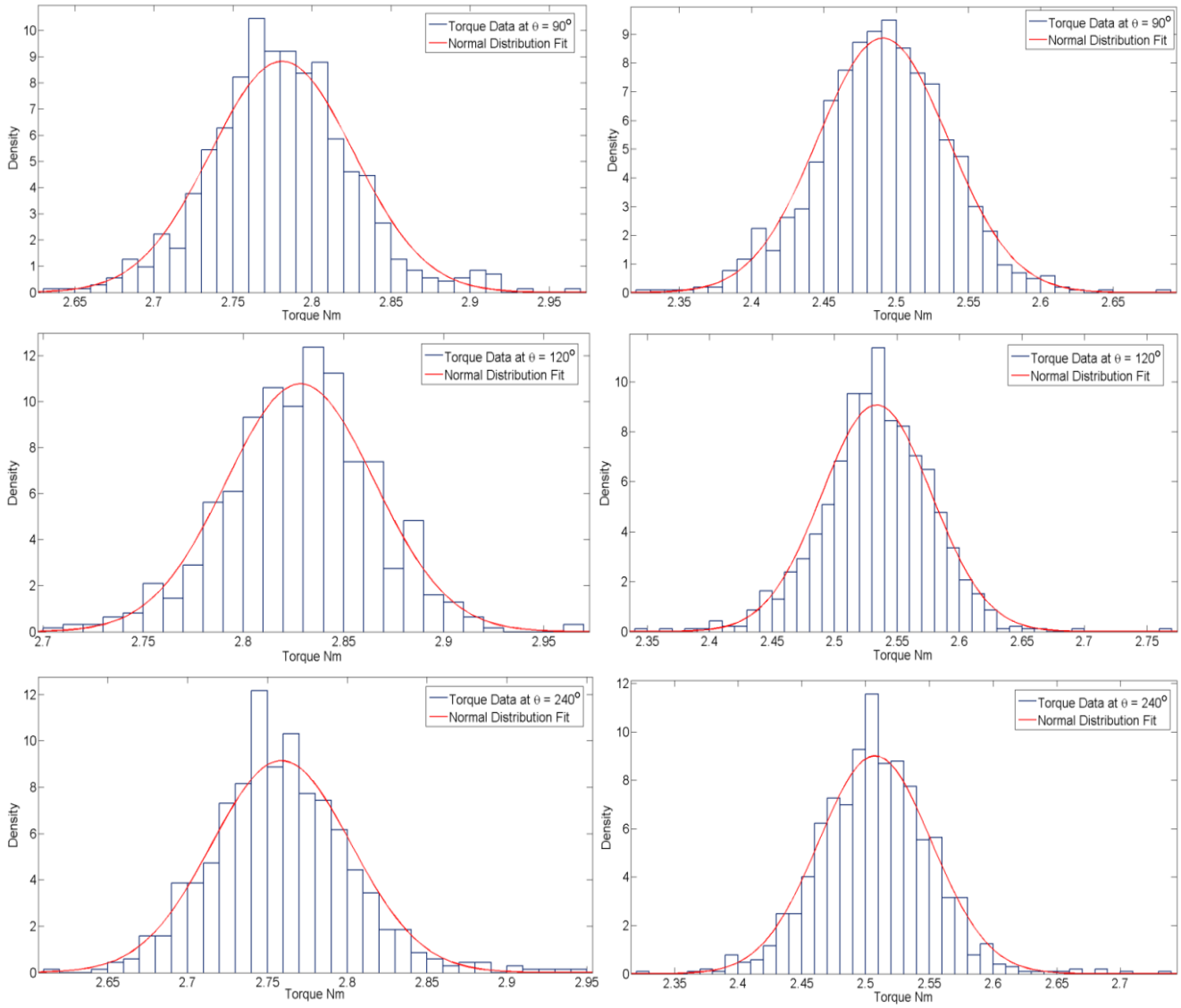

a) b)

Figure 6.8: Normal distribution fitting to the observed torque data sets after TSA re-sampling for differing rotor positions and for a) optimum rotor condition and b) Offset +6º rotor condition.

The results of the calculation are plotted in Figure 6.9. Referring to Figure 6.9 it was considered that the TSA process, when applied to more rotations, supplied a better estimate of the mean characteristics throughout a single turbine rotation as expected. As noted in the literature (Ha et al, 2015) this deviation shows an exponentially decaying tendency with the data set length. It was also considered that, due to this tendency and the reasonably fast

decay rate, the 20 rotations included in the process average calculation gave a good representation of the underlying transient torque characteristics. The asymptotic nature of the deviation from the TSA after 20 rotations suggests that improved process representation via the inclusion of more data would require much greater data set sizes which were impractical in during the course of the research. Figure 6.10 shows the deviation from the TSA process mean with turbine position for various data set sizes. Characteristic spikes in deviation due to rotor position were not observed further confirming the normal distribution of the data at each resample point and as such the validity of the TSA process applied to the data set.

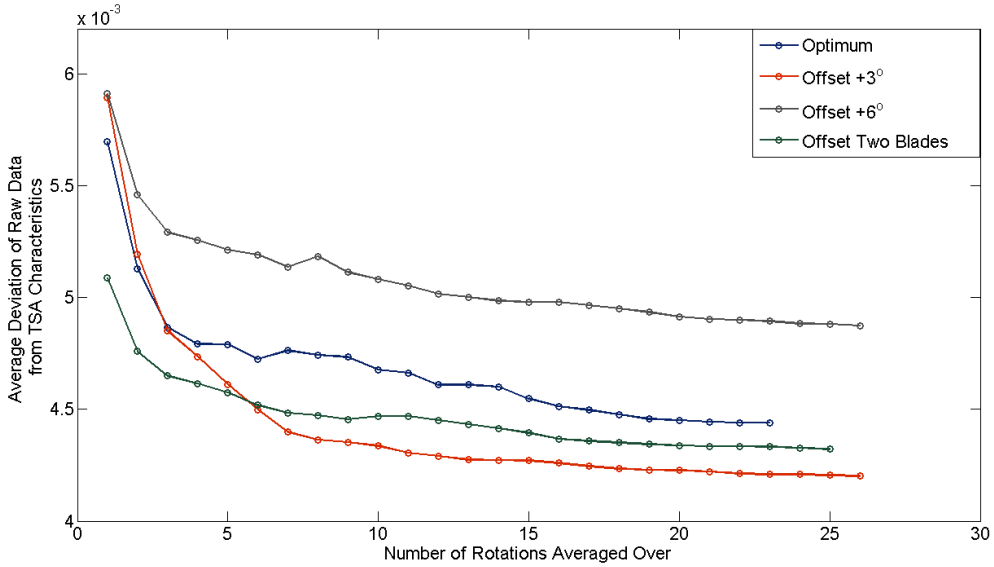

Figure 6.9: Reduction of the mean standard deviation of each entire data set for increasing inclusion of rotations in the TSA calculation for each rotor condition.

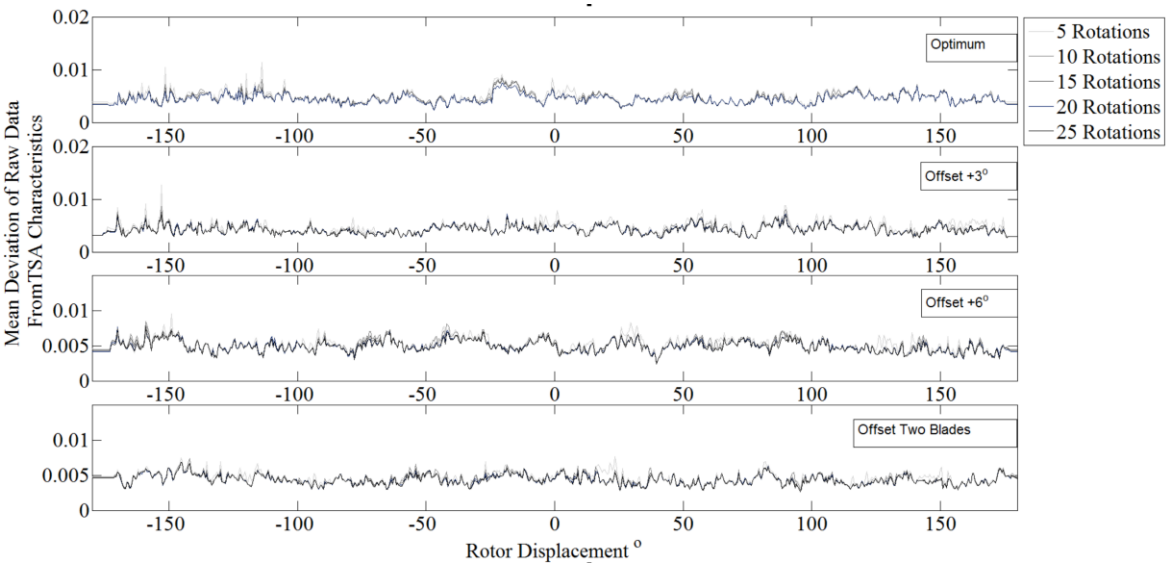

Figure 6.10: The figure shows the mean deviation from the process mean against the position index for increasing numbers of rotations.

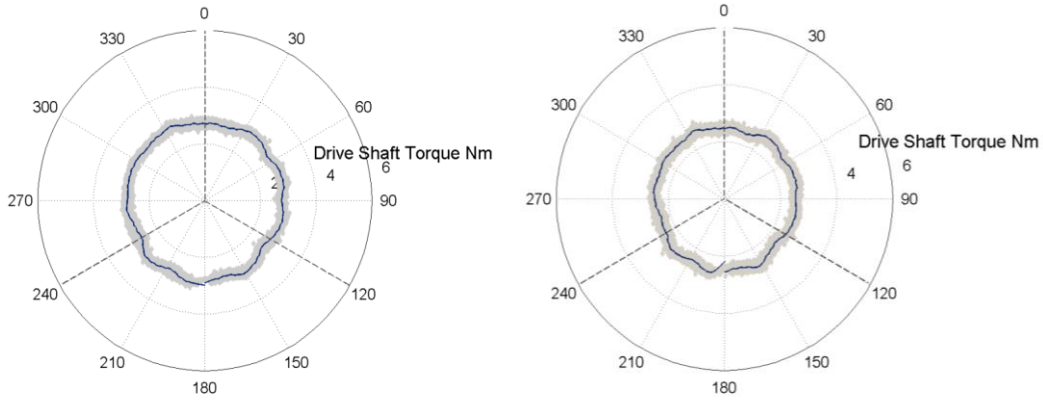

Figure 6.11: Polar plot showing the results of the TSA process for both the optimum and offset $+6^0$ cases. Showing the values observed during blade pass events.

Figure 6.11 shows the results of the TSA process in the form of polar plots for the same cases shown in Figure 6.6 and Figure 6.7, with the DC value of the torque preserved. The plots highlight the relative size of the fluctuation amplitudes with respect to the DC value. It can be seen that the torque fluctuations are minimal, in the order of 2 %, when compared with the mean torque value for the flume scale turbine.

The TSA process was applied to each of the datasets acquired during the flume testing. This was done to create a full transient characterisation of the turbine. Figure 6.12 shows the

results of the application of the TSA procedure to each operating point measured for the optimum rotor case at 1 ms^{-1}; this was repeated for each of the rotor cases at the same lambda values for fluid velocities of 0.9 ms^{-1}, 1.0 ms^{-1} and 1.1 ms^{-1}.

Figure 6.12 highlights the variety of transient characteristics observed for differing λ values. It was noted that a general trend could be observed when considering the prominence of the pole pass torque transient and that the prominence of such fluctuation was reduced with increasing turbine rotational velocity. Furthermore and perhaps related to the previous observation, it could be seen that the torque fluctuations attributed to the blade pass events was generally more observable at higher rotational velocities with the most prominent fluctuation in the measured torque occurring at freewheeling.

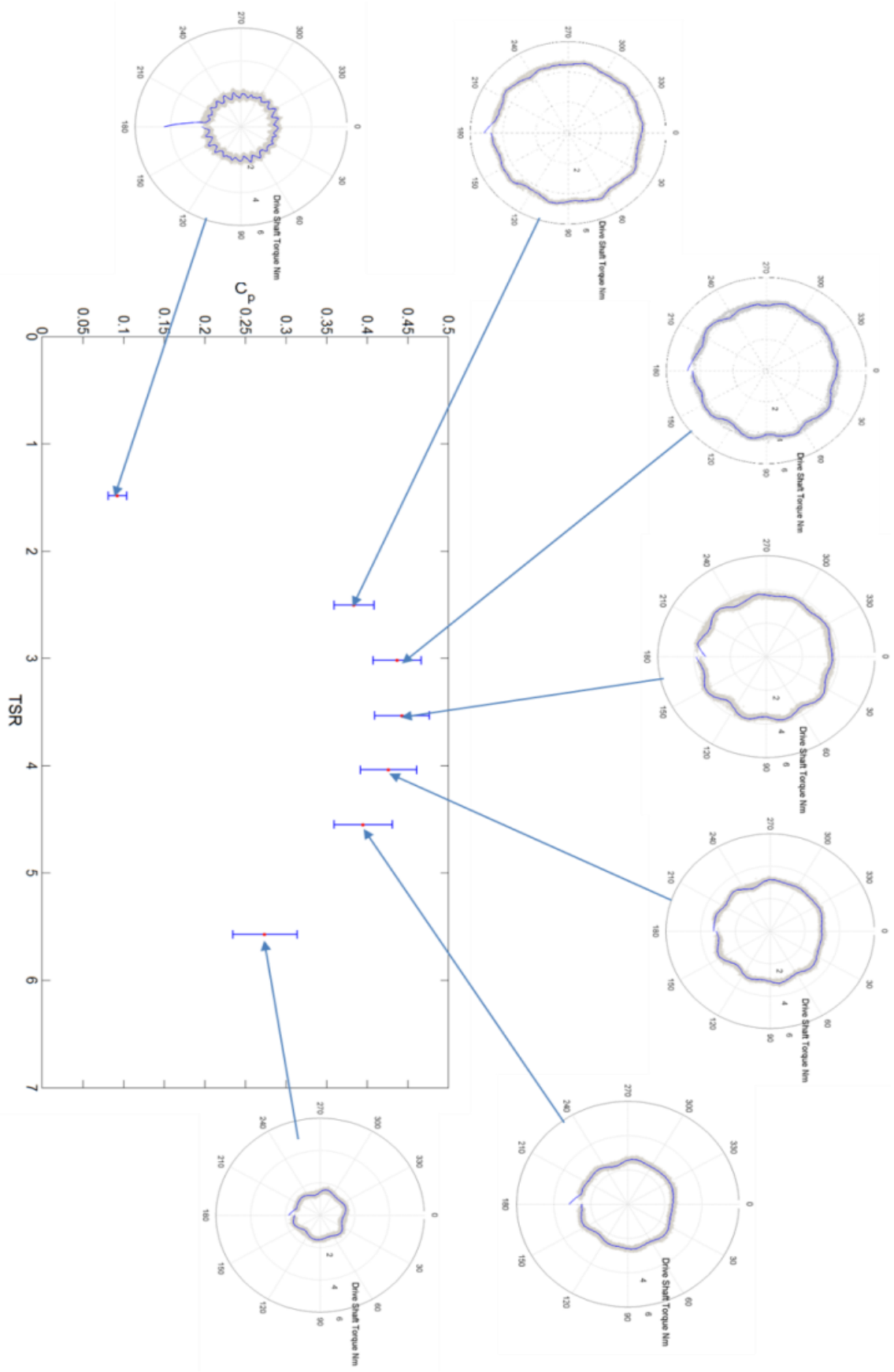

Figure 6.12: Application of the TSA process to data sets relating to differing operating λ values, for the optimum rotor setting and v = 1ms^{-1}

6.3.3 Frequency Characteristics

The results of the TSA procedure applied to the torque data observed during testing were then utilised for a more complete characterisation of rotor torque transients under the differing operating conditions. This characterisation was applied in the frequency domain within which the amplitudes considered were scaled by the mean torque value observed for the given time series. In order to confirm that the TSA procedure effectively preserved the frequency characteristics observed in the raw data sets, the spectrums of both the TSA and raw data sets were compared. Figure 6.13 and Figure 6.14 show the spectrums for the 1 ms^{-1} fluid velocity tests for a rotational velocity of approximately 134 RPM for the optimum and offset $+6^{o}$ rotor conditions, respectively. It is noted that due to the TSA process the frequency resolution for the TSA data was fixed at multiples of the rotational frequency of the turbine.

The figures show good agreement between the spectrums observed for the raw data sets and the TSA data sets. This was used as confirmation that the transient characterisation could proceed in the frequency domain utilising the output of the TSA procedure with a good level of validity. The spectrums show characteristic peaks at 1, 3, 6, 9 and 10 times the rotational frequency of the turbine. The peaks at 3, 6, 9 and 10 are observable under both rotor conditions however there is a marked increase in the amplitude of the 1^{st} harmonic observed in the offset $+6^{o}$ case as predicted. Between the harmonics of the rotational velocity the raw data sets exhibit no significant amplitudes, furthermore between these rotational harmonics the frequency content was considered to consist of low level noise.

A comparison of the spectrums observed for each of the rotor cases as calculated via CFD, presented in Section 3.6.1, and as measured during flume testing was also undertaken. The comparison was made both to validate the transient CFD modelling process and to confirm that development of monitoring approaches based on the CFD data were suitable.

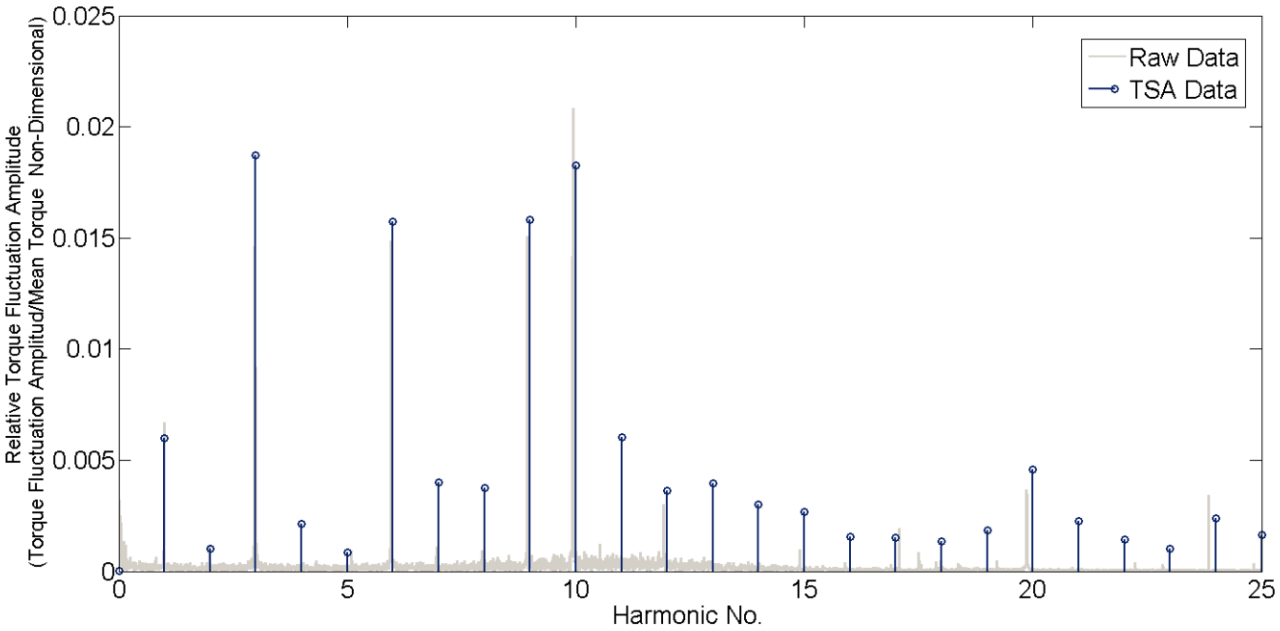

Figure 6.13: Comparison of the spectrum observed for the TSA data and the raw data for the optimum rotor case.

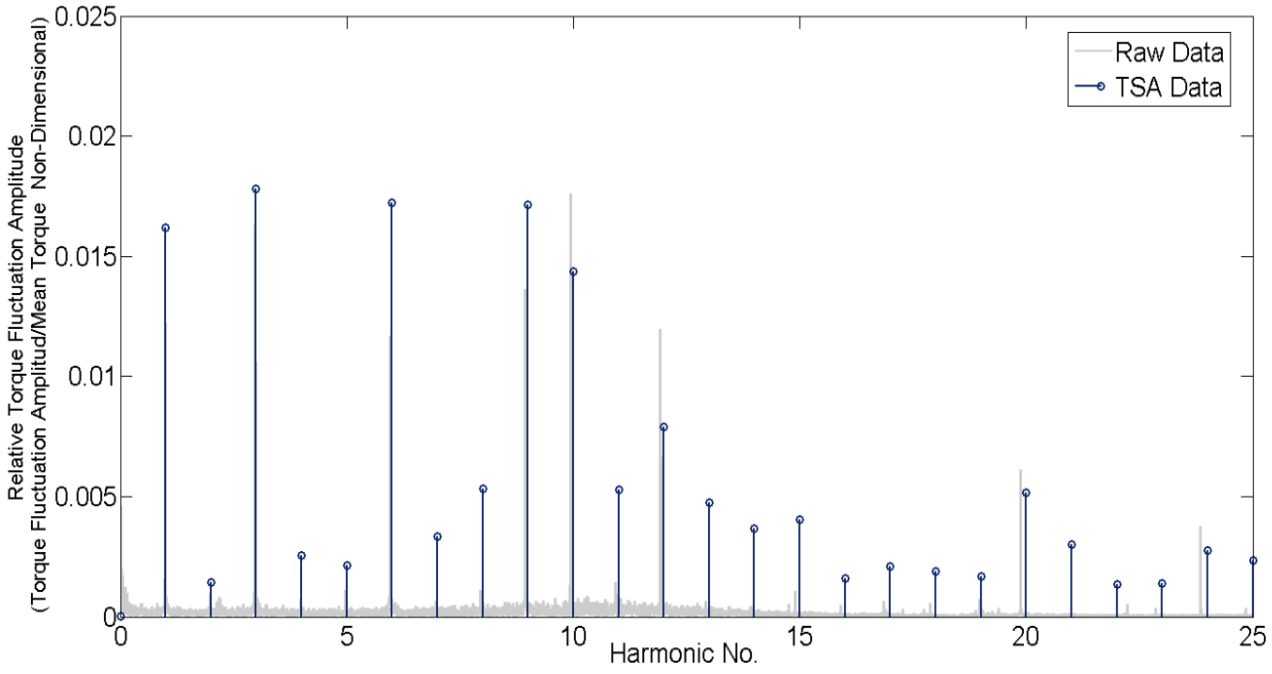

Figure 6.14: Comparison of the spectrums observed for the TSA data and the raw data for the offset +6° case.

Figure 6.15 shows the relative amplitude observed against harmonic number for three rotor conditions for the CFD data and the experimental data. It can be seen that, as in the

initial comparison with CFD results, considerably higher relative amplitudes were in general observed for the CFD data in comparison to the experimental data. However, similar overall characteristics can be observed when neglecting the difference in amplitude which may be due to the effect of turbine scale. Considering the observed amplitudes at the first harmonic of the turbine rotational frequency it can be seen that the amplitude is increased with increasing fault severity. It was also noted that at the 1st harmonic the experimental data showed higher amplitudes relative to subsequent harmonics this was attributed to the imperfect experimental setup relative to the geometrically correct CFD models. In both data sets peaks can be observed at the 3rd and 6th harmonics. It was considered that the general similarity between the two characteristics gave sufficiently good validation for both the CFD models and the process of developing monitoring approaches based on CFD data output.

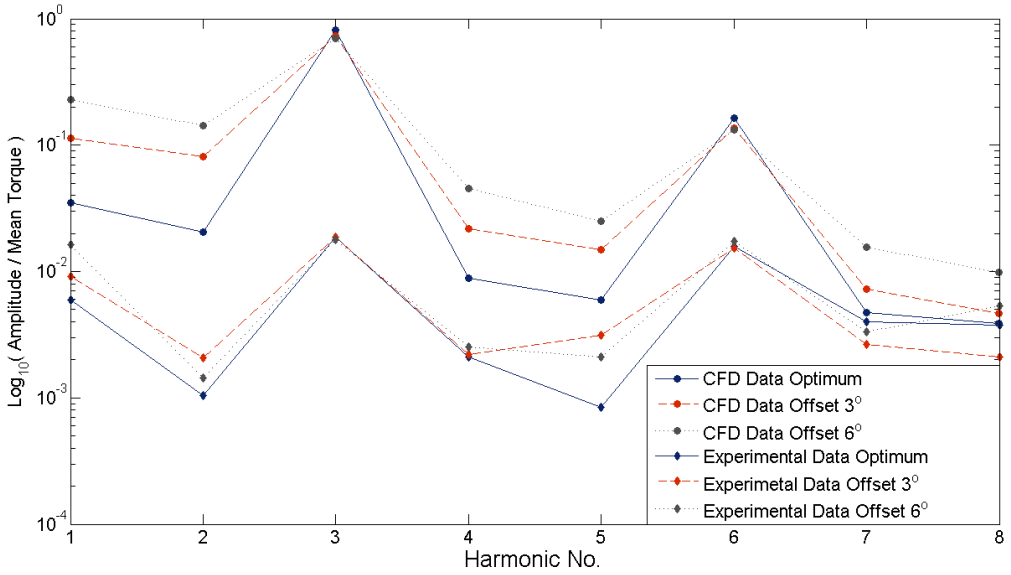

Figure 6.15: Comparison of the relative amplitudes observed in the flume data testing and the CFD data introduced in chapter 4.

Figure 6.16 shows the phase angle observed for a given harmonic number for three rotor conditions for the CFD data and the experimental data. The phase spectrum observed shows

a far more stochastic characteristic. At closer inspection it can be seen that the CFD data shows a fixed characteristic over the harmonics which has been shifted due to the differing rotor conditions. The experimental data shows an underlying trend over the harmonic values for the optimum and offset +6° cases. It can be noted that at the 4th harmonic the phase wrapping makes the phase angles appear more disparate than they are in reality. The offset +3° shows significant deviation from the trend observed for the previously mentioned rotor conditions. Whilst the CFD data and experimental data show little agreement in phase angles for a given harmonic two similarities were noted. The phase angles at the third harmonic were considered comparable and the greatest deviation in like data sources for differing rotor conditions were the same, namely the deviation between the optimum condition and the offset +3° condition.

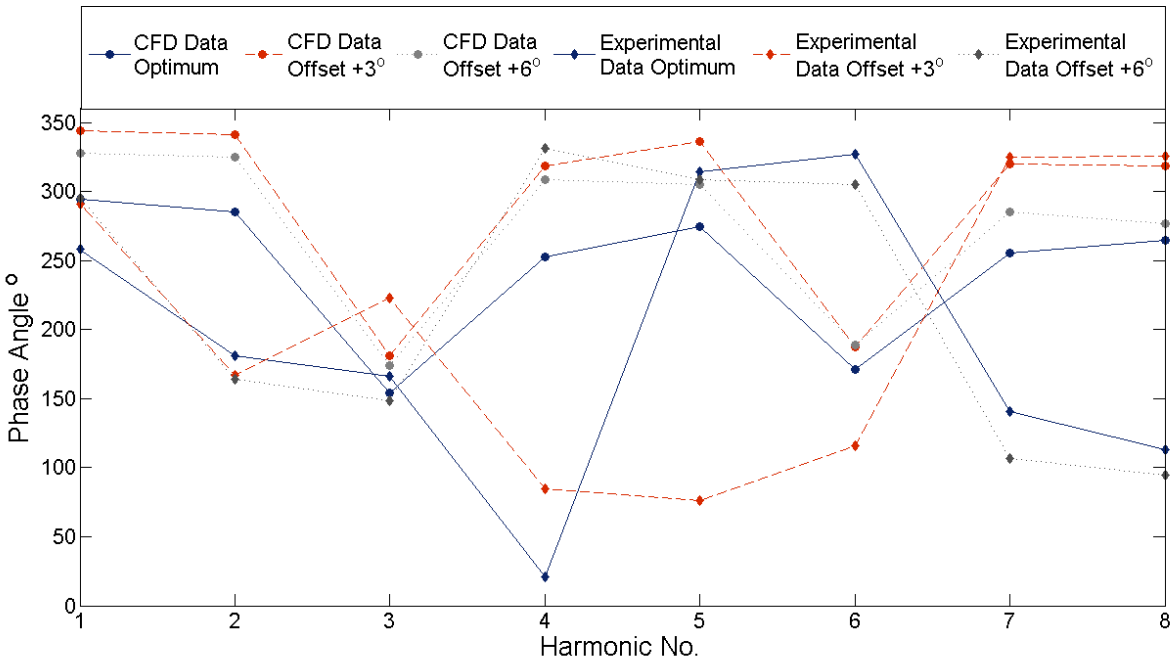

Figure 6.16: Comparison of the phase angles observed in the flume data testing and the CFD data introduced in chapter 4.

6.4 Application of Monitoring Algorithms

The remainder of the chapter considers the application of a variety of the CM approaches, outlined in Chapters 3 and 4, to the rotor fault data acquired during flume testing. The monitoring algorithms were applied to the 1 ms^{-1} case to datasets for each rotor fault scenario tested at the tip-speed ratio closest to peak power. The three algorithms presented in the remainder of the chapter are the performance curve monitoring process and two instances of the calculation of the rotor imbalance indicator, criterion "C" introduced in Section 3.6.3, utilising frequency feature extraction via the STFT and the HHT. In the context of the application of the rotor imbalance measurement algorithms the optimum data set is used to represent prior knowledge. It is applied in defining the correct turbine operational characteristics to which the blade fault cases are compared. For the power curve monitoring process all datasets are compared to the prior performance characteristics generated for the rotor during previous CFD modelling exercise and flume testing campaigns.

Lastly the chapter is concluded by presentation of the likelihood functions for a naïve Bayes classifier calculated in two-dimensional fault vector space, consisting of a fusion of outputs from the power curve monitoring process and rotor imbalance measurement process. As such two sets of likelihood functions are presented for each fault case tested, one utilising STFT frequency extraction method and the other utilising the HHT frequency extraction method.

6.4.1 Performance Curve Monitoring

Figure 6.17 shows λ versus C_p plots for 5 second intervals of the recorded flume data at 20 seconds and 50 seconds. On each figure the calculated non-dimensional values are plotted along with the expected non fault characteristics observed for the rotor design during

previous modelling and flume testing experiments (Mason-Jones, 2010; Mason-Jones et al, 2013). The no fault characteristics presented in the figures refers to the results of previous testing and simulation campaigns for the rotor utilised under optimum conditions. In this way the prior characteristics, in a real world application, represents knowledge of the rotor characteristic which have been characterised prior to installation or during initial data trending. The plotted results from this phase of flume testing then represent monitoring data taken in five second intervals at 1 kHz at some later time. It was observed that the optimum and offset +3° data closely matched the expected turbine characteristics. This was in contrast to the offset +6° and two-blade offset data which gave lower values for the non-dimensional power coefficient.

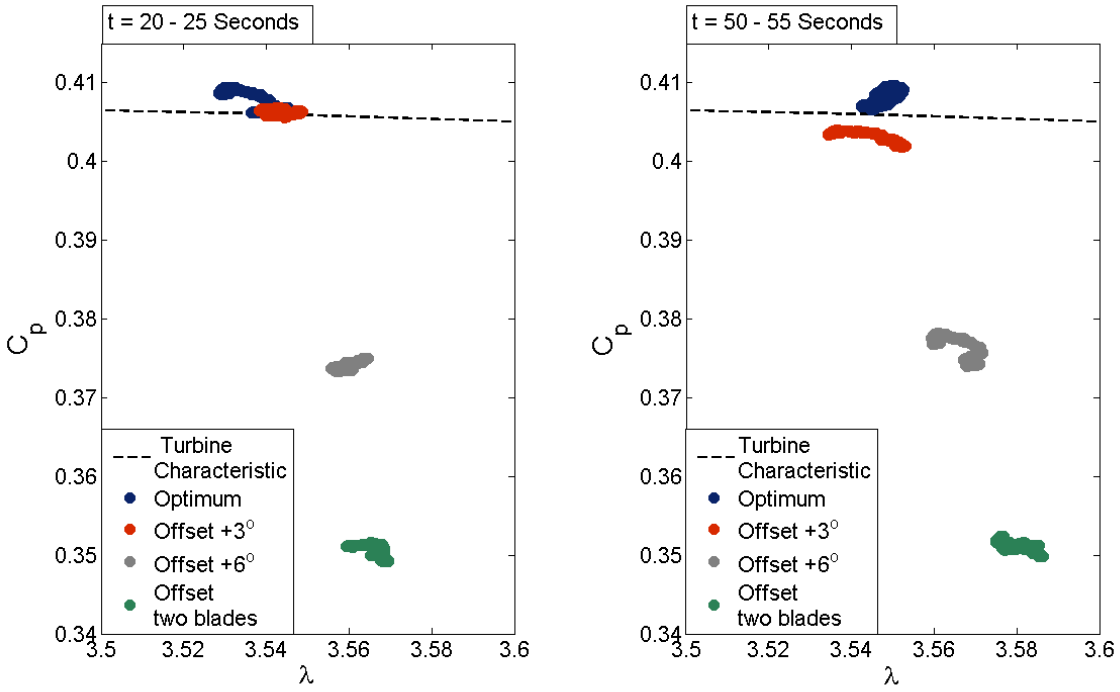

Figure 6.17: Illustration of the power curve monitoring process applied to 5 seconds worth of data at a) t = 20 secs and b) t = 50 secs.

Figure 6.18 shows the C_p error calculated for each dataset and plotted as a time series. It can be seen, as shown in Figure 6.17, that the C_p values calculated during flume testing for

the optimum rotor case was greater than the prior characteristic value for the given tip speed ratio value. This is represented in Figure 6.18 by the predominately negative trace. The same can be seen for the offset +3º case. It was also noted that the power curve monitoring was ineffective, due to the similarity of the error values observed for the optimum and offset +3º. This indicates the difficulty in descriminating between optimum conditions and a moderately damaged rotor state at $\lambda \approx 3.54$. However with reference to Figure 6.4 it can be expected this process would be more effective at higher tip speed ratios. It can be clearly seen in Figure 6.18 that diagnosis and detection of the offset +6º and two-blade offset would be feasibile using the power curve monitoring process.

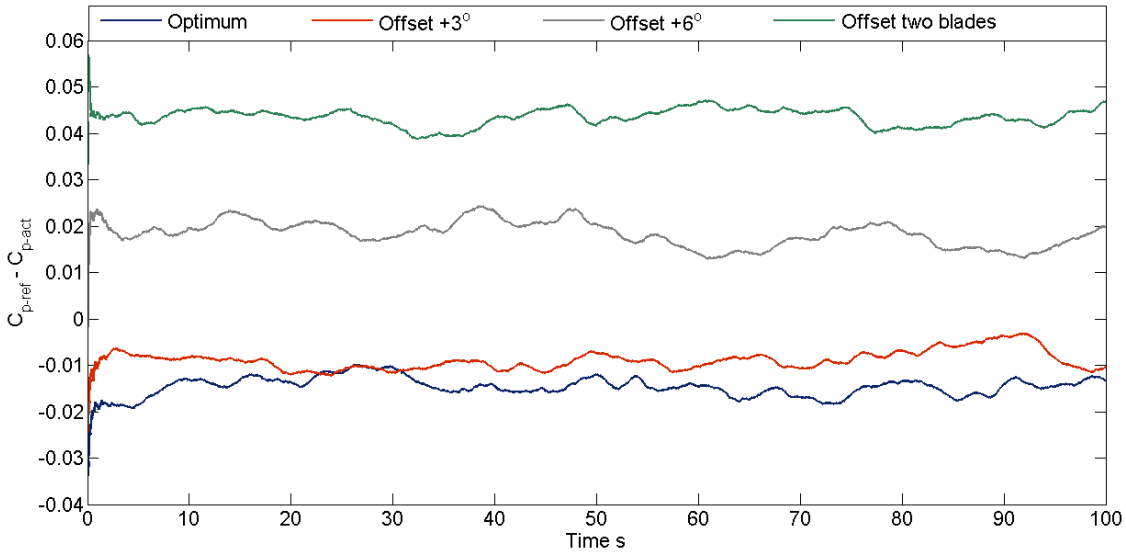

Figure 6.18: Discrepancy between the characteristic C_p values and the observed values under rotor fault testing plotted as a time series.

6.4.2 STFT frequency feature extraction

As in Chapter 4, the appraisal of the rotor imbalance measure algorithm would be undertaken with the aid of two pre-processing methods. This section corresponds to the use of the STFT frequency domain feature extraction as the pre-processing method. For the STFT a Hanning window of length of five rotations or 2^{11} samples was used with an overlap of 4 rotations (2^{11} – 450 samples). These settings gave good time-frequency resolution in

region of the 1st to 8th harmonics of the turbine rotational velocity as required for meaningful feature extraction. Figure 6.19 shows the spectrograms produced for the each of the rotor conditions, again for a fluid velocity of 1 ms^{-1} and a rotational velocity of 134 RPM.

The amplitude of the spectrograms was plotted as power spectral density in decibels and the frequencies of interest can be seen as the darker horizontal lines. For the feature extraction process the time series of the amplitudes for the first and third harmonic were extracted and applied to the calculation of the CM criterion C which is considered to be a measure of the turbine rotor imbalance.

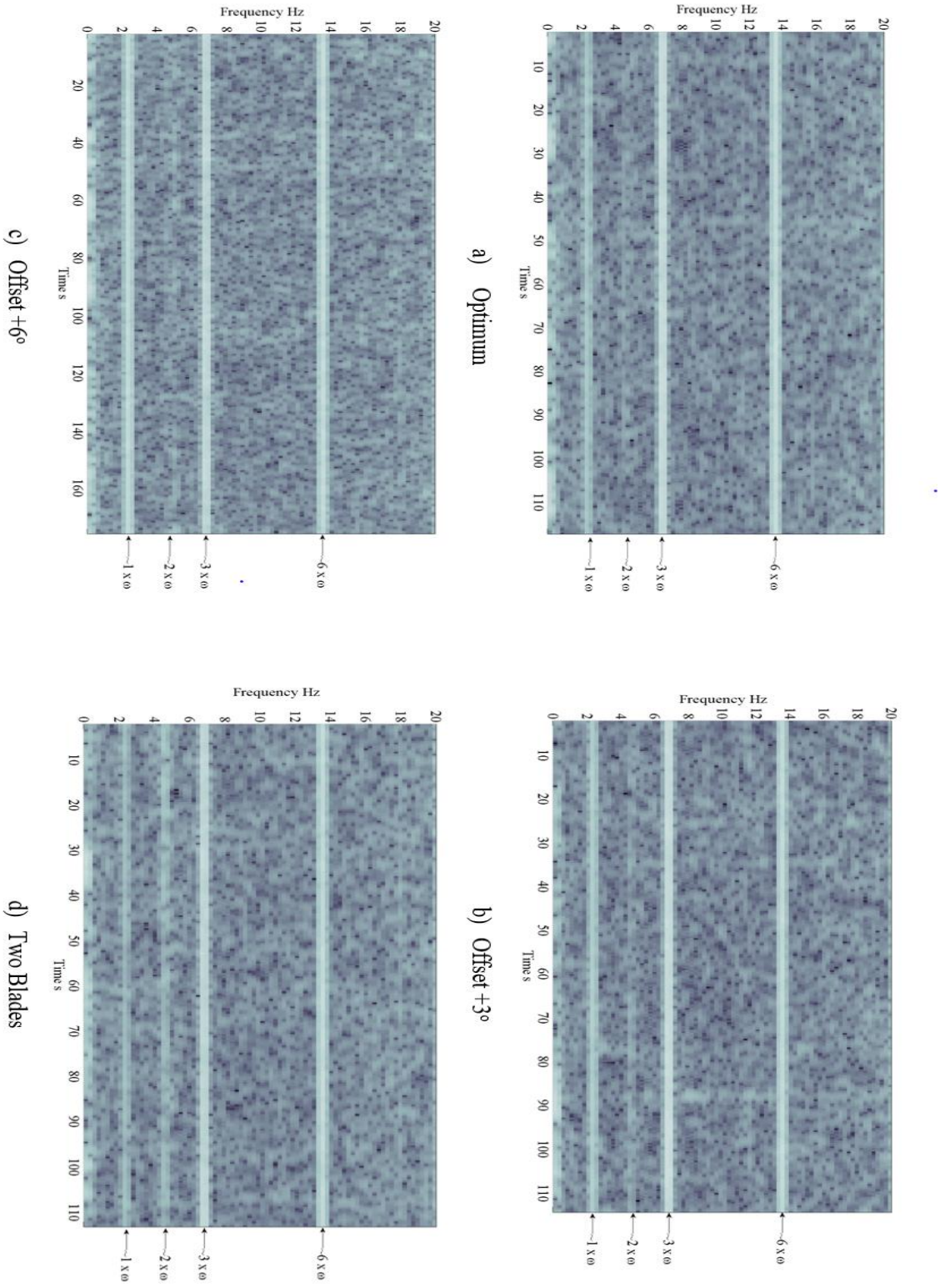

Figure 6.19: Spectrograms produced for each of the rotor conditions tested highlighting the time frequency characteristics of the rotor torque. a) Optimum b) Offset +3° c) Offset +6° and d) Two-blade offset

Figure 6.20 shows the mean values of the monitoring criterion C for each rotor condition at the previously specified operating conditions. The averages were taken over the entire time series extracted via the STFT. The plot shows that the mean the condition monitoring criterion could be effective for both fault detection and diagnosis.

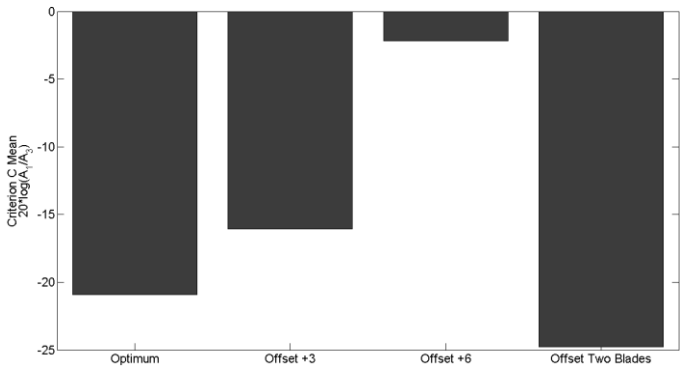

Figure 6.20: Mean values of the monitoring Criterion C for each of the rotor conditions tested the data for which was extracted via STFT calculations.

Figure 6.21 indicates that the time series of the condition monitoring criterion C shows a reasonable variation around the mean values observed in Figure 6.20. It was observed that, at multiple points in the time series, the condition monitoring criterion C for a given rotor condition overlaps with the criterion calculated for other rotor conditions. This is particularly prominent between the optimum, offset +3^{o} and two-blade offset cases.

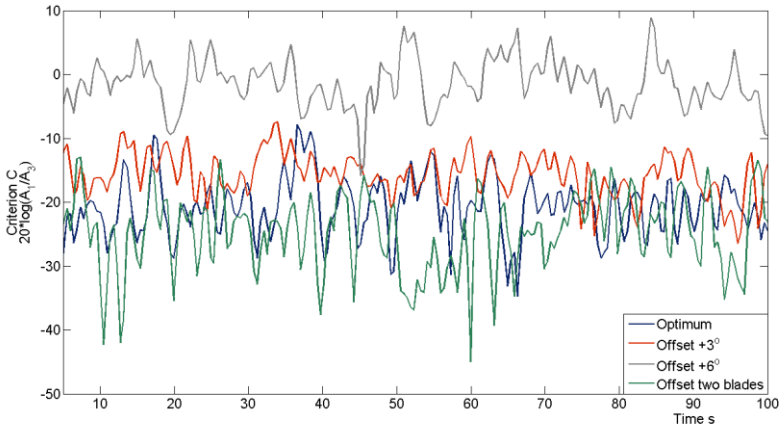

Figure 6.21: Time series of the condition monitoring criterion C for each rotor condition, the data for which was extracted utilising the STFT.

Figure 6.22 shows the time series after smoothing via convolution with a simple averaging function, equating to each sample being equal to the average of the four previous samples and the current sample. The effect of the averaging process reduced the overlap between the time series of differing rotor conditions leading to a more robust monitoring process. However a number of overlaps still remained in the data.

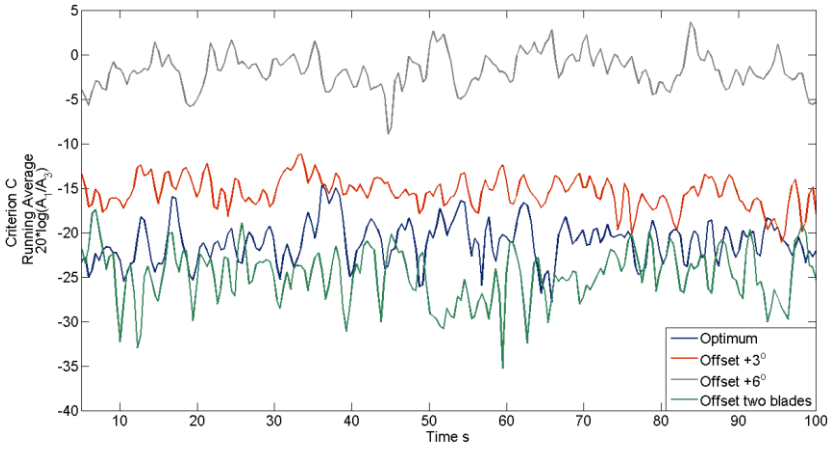

Figure 6.22: Smoothed time series plot of the condition monitoring criterion C, the data for which was extracted via the STFT and subsequently smooth via convolution with and averaging signal.

Tables A.25 to A.28 show the results of the NBC process as applied to both the smoothed and raw C_l time series data. The results show that the raw C_l data led to incorrect fault detection classification however correct fault severity classification was observed for the raw data. In comparison the smoothed data performed better under the classification process with correct detection and diagnostic classifications observed.

6.4.3 Hilbert-Huang Transform based frequency feature extraction

As with STFT and led to by considerations outlined in Chapter 4 the EMD process was developed into the HHT which was used for frequency feature extraction. This section outlines the results of the application of the frequency content extraction for the calculation of the CM criterion C.

The first step in conducting the HHT is to perform EMD on the measured rotor torque time-series to extract IMFs or monotonic functions. Using these the Hilbert transform can be applied for amplitude and instantaneous frequency estimation. Figure 6.23 shows the empirical mode decomposition process for the optimum rotor condition data set. The IMFs were used to reconstruct the original signal to highlight the effectiveness of the EMD algorithm used. The reconstructed signal successfully equated to the original signal as highlighted via the reconstruction error plot shown in Figure 6.23.

The IMF functions were then subjected to the Hilbert transform whereby the amplitude of the signal was extracted by taking the magnitude of the transform result. The instantaneous frequency was extracted by the derivative of the phase angle of the complex Hilbert transform result. The Hilbert transforms of IMFs were then interpolated over the frequency and time scales to build the Hilbert-Huang Transform. As the data led to point estimates of the frequency and amplitudes observed at each time step a Gaussian smoothing function was convolved with the surface. This highlights the uncertainty of the point estimates and gives a workable surface as an output.

Figure 6.24 shows the results of the HHT operation. The 1st rotational harmonic and the 3rd rotational harmonic, which are of interest, can be seen in each figure for each rotor condition. It can be seen that a greater time-frequency resolution is achieve by using the HHT as opposed to the STFT. Also the spectrograms obtained via the HHT show fluctuations in frequency content due to the slight non-stationarities in the signal resultant from the minimal acceleration and deceleration of the turbine.

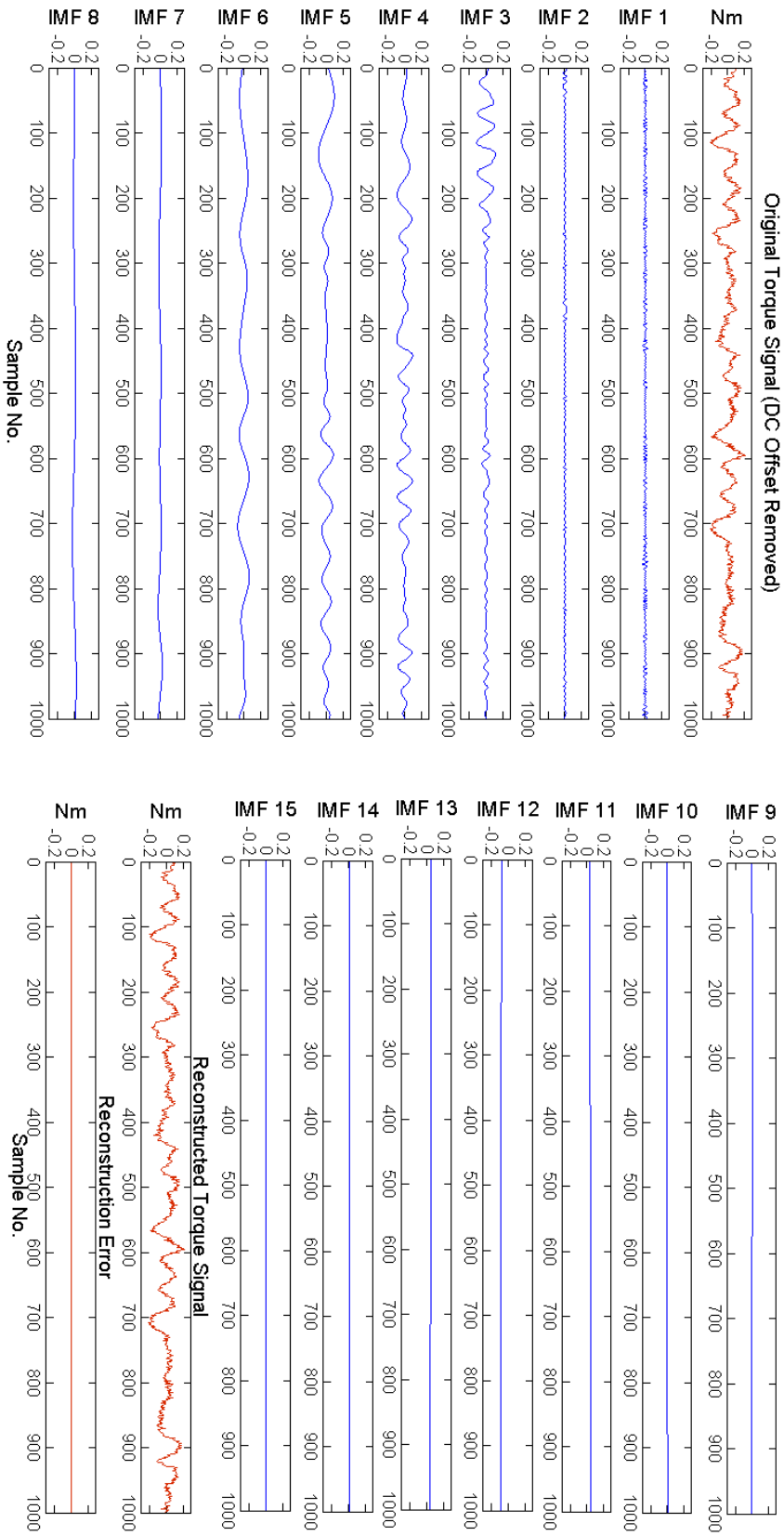

Figure 6.23: EMD of the torsional time series for the optimum rotor case at 1 ms^{-1} fluid velocity and a rotational velocity of 134 RPM. The figure shows the original signal, the extracted IMFs, the signal reconstructed via the IMFS and the reconstruction error (residual between original signal and the reconstructed signal.

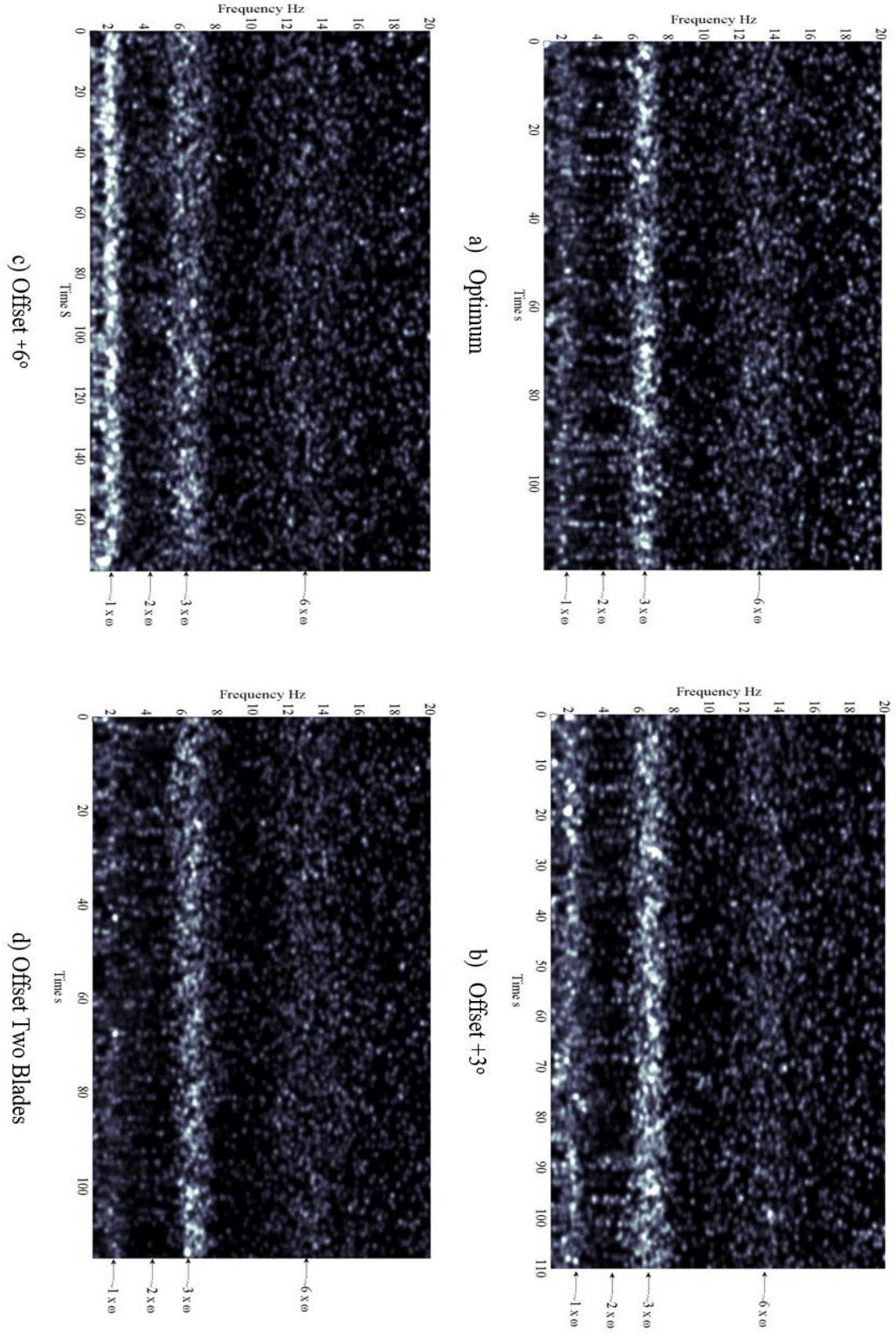

Figure 6.24: Hilbert-Huang Transform of the recorded flume data time series taken for a fluid velocity of 1ms-1 and a rotational velocity of 134 RPM. a) Optimum b) Offset +3º c) Offset +6º and d) Two-blade offset.

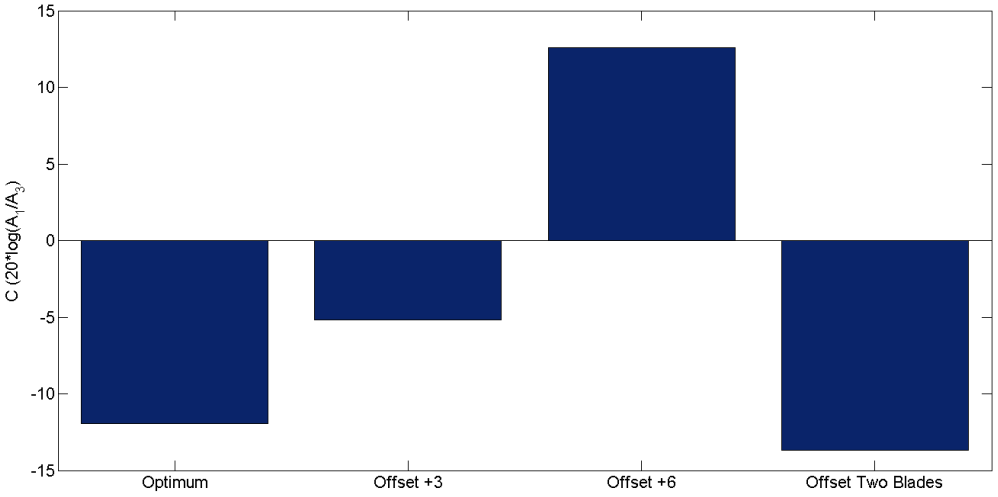

Figure 6.25: Mean values of the CM criterion C that for which was extracted via the HHT method.

Figure 6.25 shows the mean values of the CM criterion C for each of the rotor conditions tested at the operating point specified above. The figure shows that the HHT process of calculating the monitoring criterion C yields workable results for both detection and diagnosis processes. Whilst showing similar results to that of the STFT calculated monitoring criterion the HHT process yields less clear results.

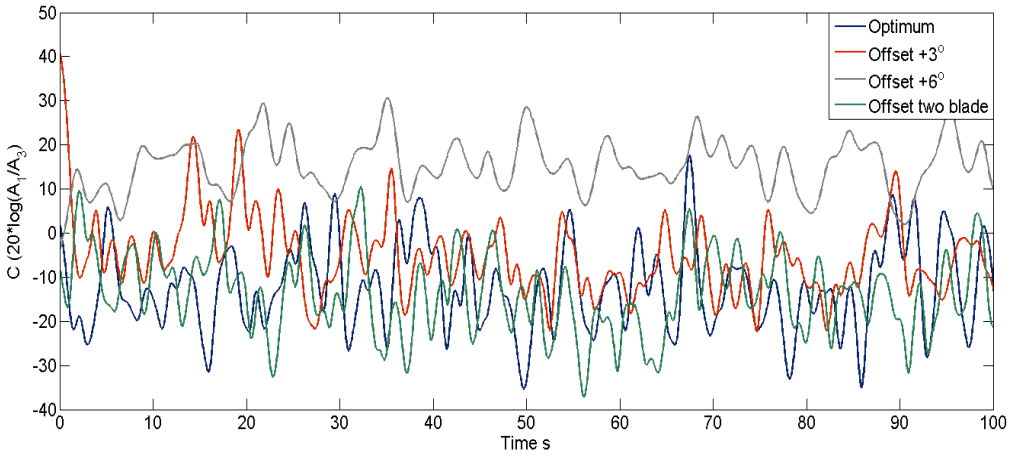

Figure 6.26: Time series of the CM criterion C the data for which was extracted via the HHT method.

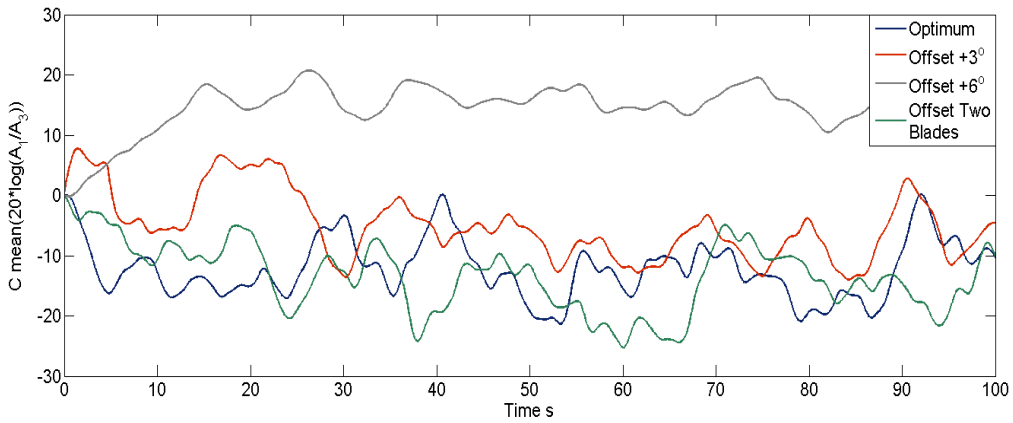

Figure 6.27: Smoothed time series of the CM criterion C the data for which was extracted via the HHT method and smoothed via convolution with an averaging function.

Figure 6.26 shows the time series of the CM criterion C calculated via the HHT process. As with the STFT extracted monitoring criterion, extensive overlap of the values exist between differing rotor conditions. Figure 6.27 shows the time series for the HHT extracted condition monitoring criterion C subjected to the same convolution averaging process as the STFT data. Again in this case the ability to distinguish between rotor conditions is improved. However, in this case significant overlap still exists between the optimum, offset +3^o and the two-blade offset case.

Appendix A tables A.29 to A.32 show the results of the NBC process applied to the HHT extracted C_I imbalance measure for both raw and smoothed data. In both cases false alarms are generated for the detection classification. In the case of the raw data the Offset 6^o and the two blades offset cases are correctly classified. The smoothed data gave comparatively better classification results with the classification of the two blade offset case as the no-fault case being the only observed misclassification.

6.4.4 Classification via performance curve and rotor offset measure feature fusion

Finally, the features extracted above from the flume test data for the four rotor conditions were used to as a ‘training data set’ in order to define the likelihood functions. This

establishes the probability of the data observed given the fault condition, which could be used in naïve Bayes classifier. The two sets of likelihood functions were generated in the form of 2 – dimensional multivariate Gaussian distributions fusing the power curve results and the monitoring criterion results. One set of likelihood functions utilised the STFT calculated monitoring criterion data whereas the other utilised the HHT calculated monitoring criterion.

Figure 6.28 and Figure 6.29 show contour plots of the multivariate Gaussian likelihood functions developed over the power curve monitoring data and the monitoring criterion data calculated via the STFT and the HHT methods, respectively. The figures highlight the effect of monitoring feature fusion characteristics for fault classification and shows reasonably good results. That is the probability distributions for each fault case are generally disjoint other than the slight overlap in the Optimum and offset +3^{o} cases.

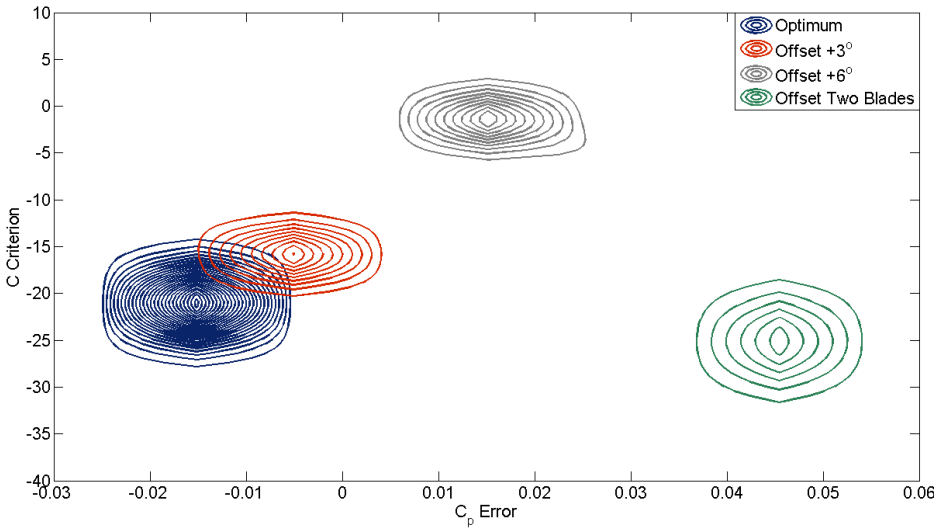

Figure 6.28: Contour plot of the likelihood function of the form of 2-dimensional multivariate Gaussian distributions over the input vector consisting of the performance monitoring data and the STFT based monitoring criterion.

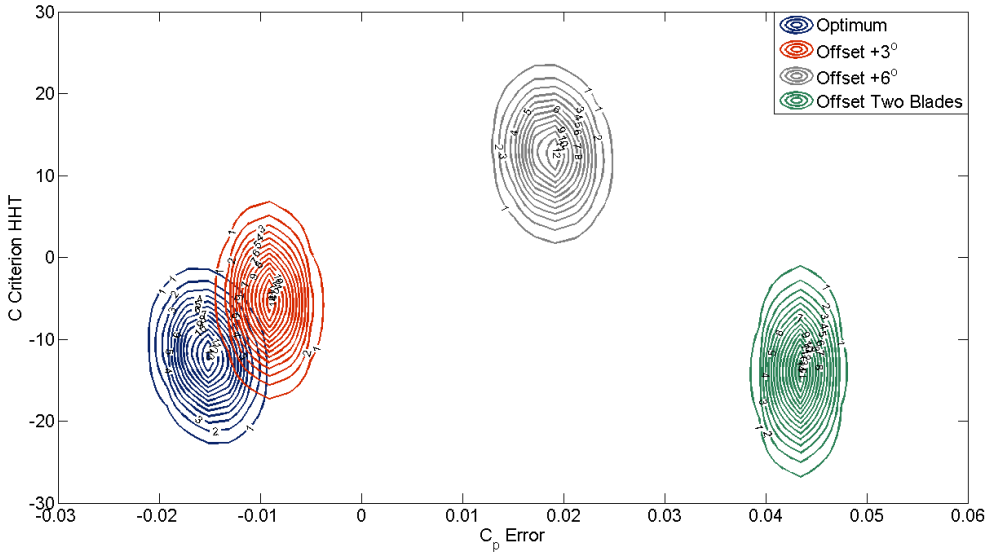

Figure 6.29: Contour plot of the likelihood function of the form of 2-dimensional multivariate Gaussian distributions over the input vector consisting of the performance monitoring data and the HHT based monitoring criterion.

Appendix A Tables A.33 to A.36 shows the results of the NBC process applied to the ensemble data. Although false alarms were observed for the detection classification for all cases other than the HHT extracted and smooth C_l measurement correct fault classification was observed throughout the data sets.

7 Drive Train Simulation Development

7.1 Introduction

This chapter extends the simulation and testing of CM processes under both steady state and non-steady state turbine operation. This follows from the recognition that in site turbine operation will inevitably vary from steady state operation to non-steady-state operation as defined by both the turbine design and the characteristics of the tidal resource. Details of the developed simulation approach are outlined herein. The specifics of a simulation campaign utilizing the outlined simulation process are presented in Chapter 8 along with the application of developed monitoring approaches to the acquired datasets.

7.2 Simulation Overview

The simulations presented in Chapter 4 assumed steady-state balances in equalising the rotor and generator feedback torque. In a similar sense the flume tank testing, reported in Chapters 5 and 6, was of steady-state operating conditions, with the turbine controlled to a constant angular velocity per test whilst the experimental driveshaft torque was measured.

In order to adequately develop and appraise the use of generator parameters as means for turbine rotor monitoring, as per the hypothesis developed in Chapter 3, an extension to more representative turbine operating conditions was required. A principal decision was to allow for such additional considerations via the addition of

both stochastic fluid flow artefacts and differing turbine control processes. The developed and extended simulation structure is described in detail in the rest of this chapter.

Figure 7.1 provides an overview and introduction to the simulation structure. The main observation is that the structure developed by the author allows the appraisal of turbine rotor torque at differing rotor displacements under a wide range of operating conditions. It is set up to use a one-dimensional stochastic fluid velocity model. The dynamic effects of tip-speed ratio based control to maintain the optimum power production operational conditions are also now included. The structure culminates in the ability to observe and test differing scenarios using a physical, scaled, drive train test rig.

Figure 7.1 accordingly provides a schematic point-of-reference of the simulation approach highlighting the interaction between the various developed models and control procedures. The resource model, presented in Section 7.3, provides flow velocity information to the parametric torque model and to the control actions, presented in section 7.5, to maintain a set-point tip speed ratio or fixed turbine velocity. The parametric model parameters are also set in an informed manner drawing on the scale model flume test results which were presented in Chapter 6 and developed upon herein. The form and parameterization process used for the model are presented in Section 7.4.

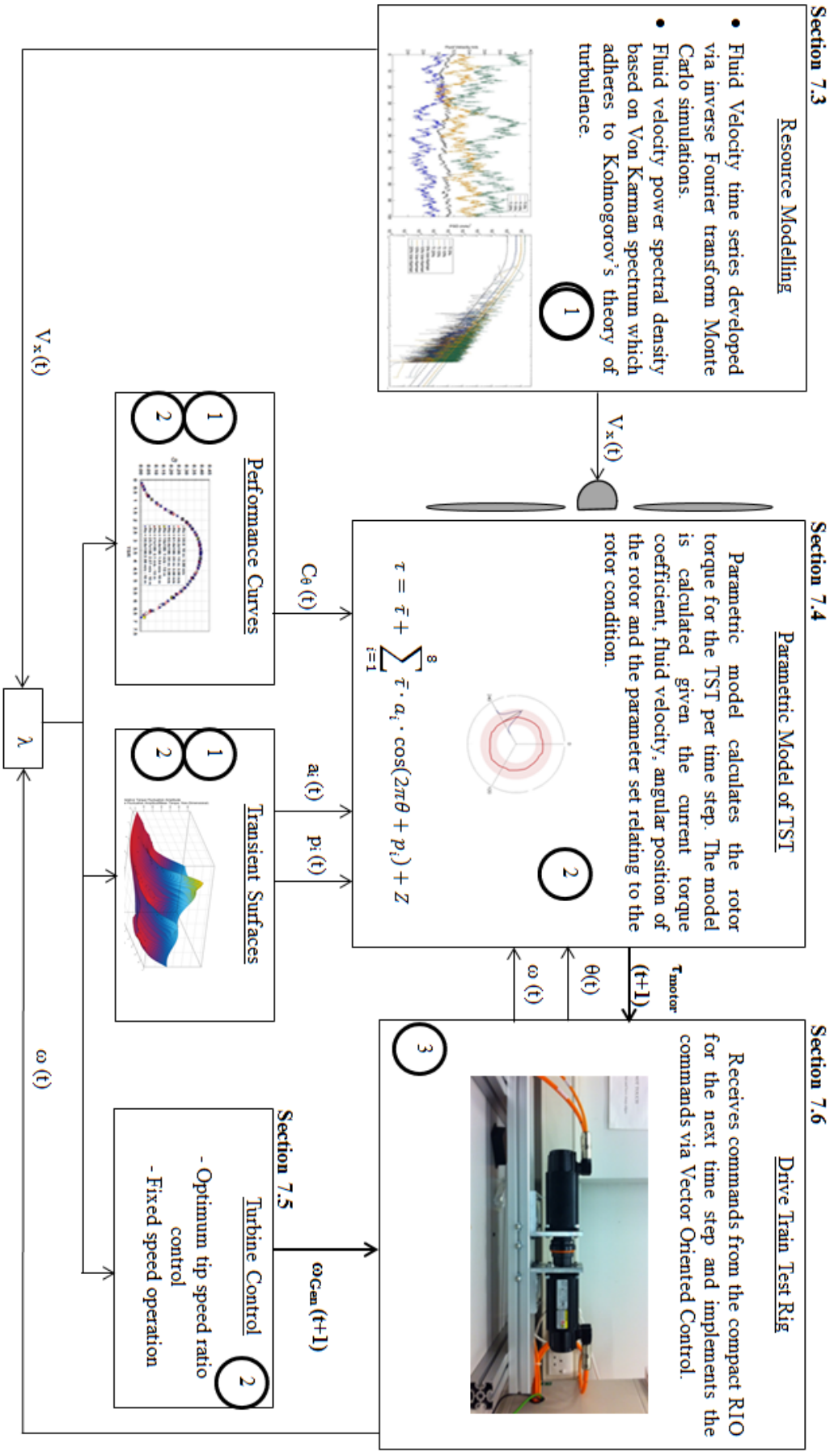

Figure 7.1: Schematic of the simulation process utilised in generating turbine simulations and scaled drive shaft emulator testing. The figure shows the 1/20th scale testing results as an input to the parametric rotor model along with the input of a resource simulation model

7.3 Tidal Resource Simulation

The simulations outlined in this chapter use the simplification that the turbine would be subjected to plug flow (non-profile flow) conditions. This simplification was necessary as this was the flow condition set for the CFD models and the approximate conditions for the flume testing. The plug flow assumption leads to a convenient representation of the flow conditions 'hitting' the turbine rotor. The flow is represented by:

$$U_x(t) = \overline{U_x} + u'_x(t) \tag{7.1}$$

where $U_x(t)$ is the fluid velocity at time t decomposed into a stationary mean fluid velocity $\bar{U}_x$ and a fluctuating component $u'_x(t)$ which is time varying with the x direction perpendicular to the turbine rotor plane. A natural model for representing the fluid flow given by the above is to model the fluid velocity fluctuations as a stationary process with given power spectral density characteristics. Furthermore utilising Kolomogrov's theory of turbulence the amplitude of the power spectrum should be proportional to $f^{-5/3}$ as $f \rightarrow \infty$. The von Kaman spectrum, as utilised by previous investigators (Val et al, 2014) for reliability simulations adheres to the above condition and can be written in the non-dimensional form:

$$\frac{fS_u(f)}{\sigma_u^2} = \frac{\frac{4fL}{\bar{U}}}{\left[1 + 70.78(\frac{fL}{\bar{U}})^2\right]^{\frac{5}{6}}} \tag{7.2}$$

where $S_u(f)$ is the spectral density function for the process, L is the length scale, σ_u is the standard deviation of the process $u'_x(t)$. In the above the x subscript has been omitted for brevity as the formulation outlined relates to a one-dimensional simulation.

The associated length scale of the turbulent process, L, for channel flows, has been shown to be approximately equal to 0.8 of the channel depth (Nezu et al, 1994). In the case of the CFD models this was taken to be 40 m and in the case of the flume testing it was 0.64 m. The standard deviation for the turbulent process is commonly normalised by the mean flow and is named the turbulence intensity. For flows greater than 1.5 m/s the expected range of turbulence intensities is between 0.05 and 0.1 (Osalusi, 2010). Here turbulence intensity is given by:

$$I_U = \frac{\sigma_u}{\bar{U}} \tag{7.3}$$

In order to generate time series of turbulent flow adhering to the above criteria the so-called inverse Fourier Monte Carlo simulation method was used as outlined by Grigoriu (Grigoriu, 2000). The method is reliant on the spectral representation theorem for weakly stationary processes (Grigoriu, 2000; Pourahmadi, 2001; Chatfield, 2004). Such a process can be modelled in the flowing manner:

$$U'_x(t) = \sum_{k=1}^{n} \sigma_k [A_k \cos(\omega_k t) + B_k \sin(\omega_k t)] \tag{7.4}$$

where:

$$\sigma_k^2 = \int_{\omega_k - \frac{\Delta\omega}{2}}^{\omega_k + \frac{\Delta\omega}{2}} S_u(\omega) \tag{7.5}$$

Where the frequency term in (6.2) gives:

$$\omega_k = 2\pi f \tag{7.6}$$

A_k and B_k are uncorrelated random variables. A realization of the process can be computed by sampling 2n random variables $\{A_k,B_k\}$ from a normal distribution with $\mu = 0$ and $\sigma^2 = 1$. The process can be considered simply as constructing a time series from a summation of sine and cosine functions evaluated at increasing frequencies with stochastic amplitudes scaled by the power spectral density function, represented as a von Karman spectrum, for the given frequency index *k*.

In order to generate the aforementioned fluid velocity time series a Matlab script was developed. The script constructs the time series given the inputs of required variance for a given turbulence intensity, the mean fluid velocity, length scale, integration resolution parameter and a frequency index. The output from the script is the constructed Von Karman spectrum with frequency index, the fluid velocity time series with time index and an estimate of the PSD of the constructed time series. The code was constructed via three functions. Namely, 'VonKarmanSpec.m', 'FluidTimeSeries.m' and the built in 'periodogram.m' function.

The 'VonKarmanSpec.m' function calculates a numerical approximation of the Von Karman spectrum by first converting the length scale parameter into Hz using the mean fluid velocity and then calculating the non-dimensional Von Karman spectrum directly using equation 7.2. The non-dimensional Von Karman spectrum is scaled by the variance parameter and the frequency index as per equation 7.2 to output the dimensional Von Karman spectrum. The spectrum is then input to 'FluidTimeSeries.m'.

The second function, 'FluidTimeSeries.m' then undertakes the Monte Carlo inverse Fourier transform process outlined in equations 7.4 to 7.6. To make this calculation the discrete approximation of the Von Karman spectrum generated via the previous function

is input along with the frequency index and integration resolution parameter. Firstly the frequency index is resampled and a numerical approximation of the integration in equation 7.5 is undertaken. The integration is performed via trapezoid numerical integration and has the limits of integration set by the resolution parameter, which specifies the number of points in the original frequency index to integrate over. Next the time-series index is constructed followed by sampling of the random parameters $\{A_k,B_k\}$. Lastly a discrete inverse Fourier transform is undertaken utilising equation 7.4 and the generated time series is output.

The last function utilised is the built-in Matlab function, 'periodogram' which can be used to generate an estimate of the PSD of the generated time-series. This was done to confirm that the generated time series' PSD adheres to an approximation of the Von Karman spectrum.

As the fluid velocity input to the parametric rotor model has been outlined the next section presents the formulation of the rotor model utilising the data captured from the $1/20^{th}$ scale testing campaign.

7.4 Parametric rotor model development and parameterisation based on flume testing results.

7.4.1 Model formulation

Chapter 4 outlines the development of a rotor torque model for a specific turbine rotor based on the results of a transient CFD modelling exercise. The model views the torque on the turbine drive shaft developed by the rotor as a composite of three blade contributions each deconstructed into a mean component and a fluctuating component. The mean component was calculated based on the turbine performance curves and the plug-flow fluid velocity at the rotor. The fluctuation component was represented as an 8-term Fourier series with amplitudes relative to the mean torque value appraised by the

angle of displacement of the turbine rotor. Each of the blade contributions were then summed for a given tip-speed ratio and rotor position to give the torque developed by the rotor, at the given position. Such a formulation, whilst incorporating many simplifications, was convenient for two reasons. Firstly, the turbine rotor torque could be appraised simply with knowledge of the turbine characteristic curves, the model parameters and the position of the turbine. Secondly, the process of constructing the model in itself gave insight into the frequency content of the drive shaft torque observed within the CFD models utilised. These insights then formed the basis of reasoning behind the CM algorithm used for rotor fault detection.

In this way a similar model structure is heralded for a more complete rotor model based on parameterisations from the flume data captured and outlined in chapter 6. However, a blade by blade deconstruction of the drive shaft torque is not convenient given the flume data content. As such the model form will be that of a mean component based on the turbine characteristic curves, a fluctuation component based on the frequency content of the drive shaft torque fluctuations measured and a stochastic component simulating experimental, measurement and chaotic effects associated with the experimental setup.

This model formulation was justified also by the convenience afforded during simulations. The knowledge of the current TSR, rotor position and model parameters was sufficient for the calculation of the rotor torque at a given rotor displacement. However the model parameters in this updated model required definition over a wider range of turbine operating conditions to allow for the use of the rotor model with the stochastic fluid velocity time series outlined above along with the turbine control processes outlined in the subsequent sections.

Having considered the strength of the previous formation and the updated requirements of the next generation model formation, the following rotor model was proposed:

$$\tau = \bar{\tau} + \sum_{i=1}^{x} \bar{\tau} \cdot a_i \cdot \cos(2\pi\theta + p_i) + Z \qquad (7.7)$$

where:

Z is a normally distributed strictly stationary random process with mean, $\mu = 0$ and standard deviation $\sigma = f(\lambda)$

x is highest harmonic considered in the model.

$\bar{\tau}$ is the mean torque developed by the rotor and is given by:

$$\bar{\tau} = C_\tau \cdot \rho \cdot A \cdot r \cdot U^2 \qquad (7.8)$$

a_i is the relative amplitude of fluctuations at various harmonics, 1 to x.

p_i is the phase angle at various harmonics , 1 to x.

θ is the position of the turbine rotor with 0^o defined as where blade 1 is at top dead centre.

The formulation of the model in this way required a number of assumptions and further investigation to confirm the structure of such a model. The assumptions and requirements are highlighted below and linked with the sections of this chapter in which they are addressed:

16. **Requirement:** the raw flume data will require appropriate processing to define the 'average' drive train torque fluctuation characteristics. The data is considered in Section 6.5.2 and this requirement is developed Section 7.4.2

17. **Requirement:** The highest harmonic number, *x*, considered within the model must be defined such that the fluctuations in rotor torque due to the underlying physical mechanism are adequately captured. This requirement is developed Section 7.4.3.

18. **Requirement:** in such a model to allow for the operation of the turbine over a range of TSR from 0 – 7, *a* and *p* must be defined over the harmonics *i* and the values of TSR, can then be considered to be represented as surfaces. This requirement is developed Section 7.4.4.

19. **Assumption:** in defining such surfaces it is assumed that a_i and p_i are not functions of the turbine rotational velocity nor the fluid velocity but only the non-dimensional quantity λ and the turbine position. This assumption is developed Section 7.4.5.

20. **Assumption:** to define *Z* as a normally distributed strictly stationary random variable with mean, $\mu = 0$ and standard deviation $\sigma \neq f(\Theta)$:

A. The raw flume data at various points should be stationary and normally distributed.

B. The standard deviation of the raw data throughout the rotation of the turbine should be approximately constant, as identified in Section 6.3.2. This requirement is developed Section 7.4.6.

21. **Requirement:** the variation of the standard deviation of *Z* should be defined over the required λ operating range, as identified in Section 6.3.2. This requirement is developed in Section 7.4.6.

7.4.2 Model structure relative to the flume Data

Pre-processing of the raw flume data to highlight the 'average' drive shaft torque fluctuation characteristics was undertaken and presented in Section 6.3.2. Figure 6.11 presented two polar plots of the flume data at 1 m/s flow velocities for the optimum blade pitch angle and the single blade 6^o offset pitch angle, respectively. These two polar plots represent the, 'training data' for the parametric model for a specific flow speed, rotational velocity and the resulting λ value.

Observing Figure 6.11 and the results outlined in Section 6.3.2 it can be seen that the TSA process can be used to capture the average or underlying fluctuations in drive shaft torque as a function of the turbine position. Furthermore it can be seen that the raw data plotted in the same figures, in grey, represents the distribution of torque values about a

mean given by the TSA trace. Viewing the raw data in this way led to the following consolidation of the model structure with the raw data: the drive shaft torque for a given position is a stationary process with mean defined by the above Fourier series and a distribution about this mean given by the standard deviation of the random variable, Z. This idea is shown conceptually in Figure 7.2. The mean value of the process is shown in the bold trace; the Gaussian distribution from which a 'realisation' of drive shaft torque is sampled is shown for the 240^o rotor position. The distribution of the process over the turbine position is shown in underlying shading. It is noted that the process shown conceptually in Figure 7.2 is equivalent to a maximum likelihood fitting of a Gaussian process to the data. This is the case as, for a Gaussian process, the maximum likelihood estimation of the process distribution is given by a Gaussian distribution with the mean given by the mean value of the data and the standard deviation given by the standard deviation of the data (Bishop, 2006)

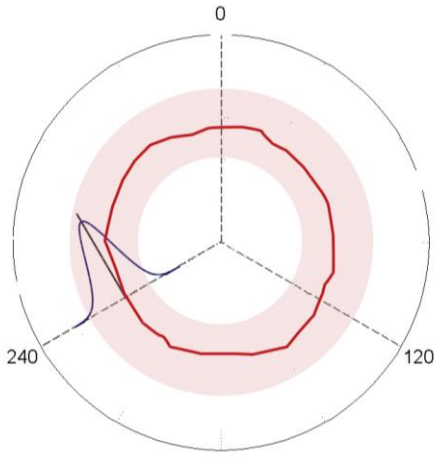

Figure 7.2: A diagrammatic representation of the structure of the rotor model as a realisation of a normal process with a mean (thick line) and data distribution (shaded region) with the normal distribution show at the 270^o rotor displacement.

The data captured during the flume based experimentation was representative of a variety of turbine operating conditions, i.e. for various values of λ composed of differing rotor velocities and fluid velocities. Utilising such data the torque fluctuations over a

turbine rotation were studied for a range of operating conditions; an example of the results of are presented for a flow velocity of 1 ms^{-1} in Figure 6.12. The analysis outlined below relating to the turbine rotor simulation development was applied to each of the turbine rotor conditions for flow velocities of 0.9, 1.0 and 1.1 ms^{-1}. By defining the torque fluctuations over a range of operating conditions the parametric model was extended to allow for variable speed turbine simulation. Flume data was taken for the following values of λ: 1.5, 2.5, 3.0, 3.5, 4.0, 4.5 and 5.5. The knowledge of the turbine characteristic at these points we used to interpolate and extrapolate to λ values ranging from 0-7.

7.4.3 Frequency content of the flume data

In order to further interrogate the data sets spectrums relating to each condition for both the raw and TSA data were calculated, as detailed in Section 6.3.3. From these results it was noted that the TSA processed data suitably represented frequency domain characteristics of the measured rotor torque during the flume testing campaign. This confirmed that the TSA data provides an accurate representation of the turbine characteristics and can therefore be used as parameterisation data in further developments.

Figure 7.3 shows the spectrum for the optimum setup relating to the polar plots shown in Figure 6.11 for the optimum. Figure 7.4 shows the spectrum for the six degree offset pitch angle case. In both figures the darker plots highlight the spectrum of the TSA data and the lighter plots shows that of the raw data. The frequency axis of each spectrum has been normalised by the mean turbine rotational velocity for each given dataset. The frequency content is thus presented in-terms of the harmonics of the rotational frequency of the turbine. Data for the time synchronous average processing and raw data were compared to confirm no spurious artefacts were introduced via the processing method.

In terms of the prominent amplitudes observed in the two spectrums, harmonic numbers 1, 3, 6, 9 and 10 show the greatest contribution to drive shaft torque fluctuations, relative to the mean torque. In order to parameterise the model effectively it was required that the model consider harmonics that relate only to torque fluctuations resultant from fluid-rotor interaction. Specifically harmonic amplitudes relating to the PMSM and the drive shaft bearings needed to be neglected or reduced to provide a more satisfactory rotor torque parametric model.

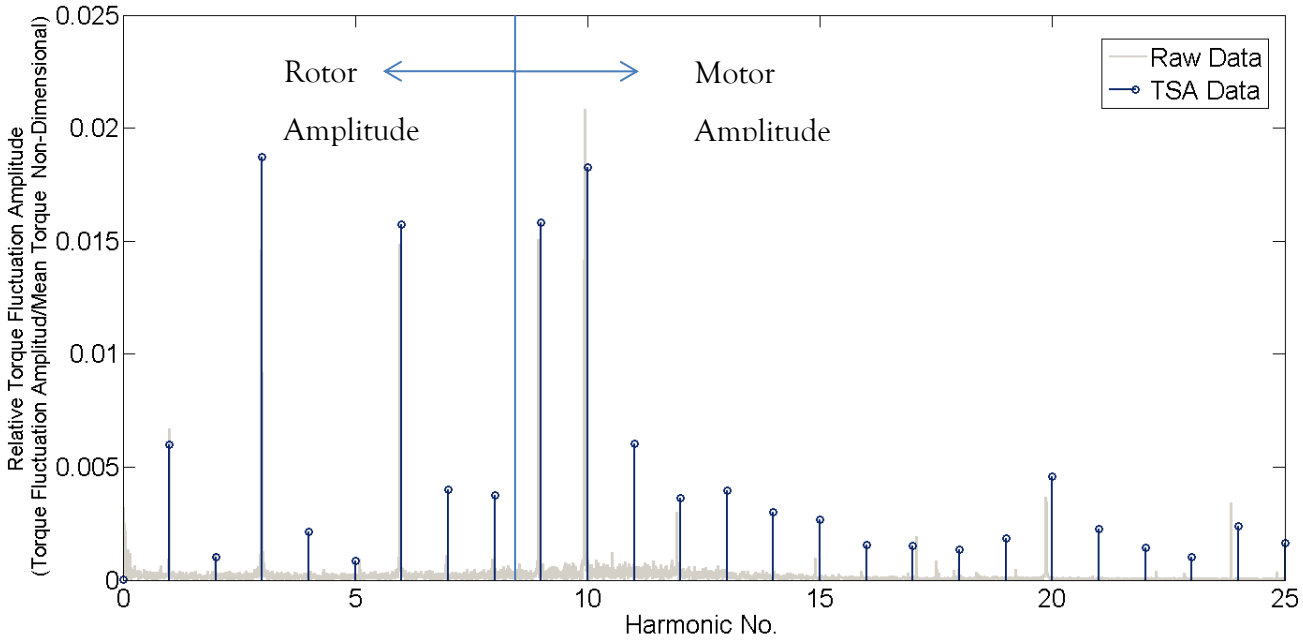

Figure 7.3: Amplitude spectrum of the drive shaft torque for the optimum rotor setting with a flow velocity of 1 m/s.

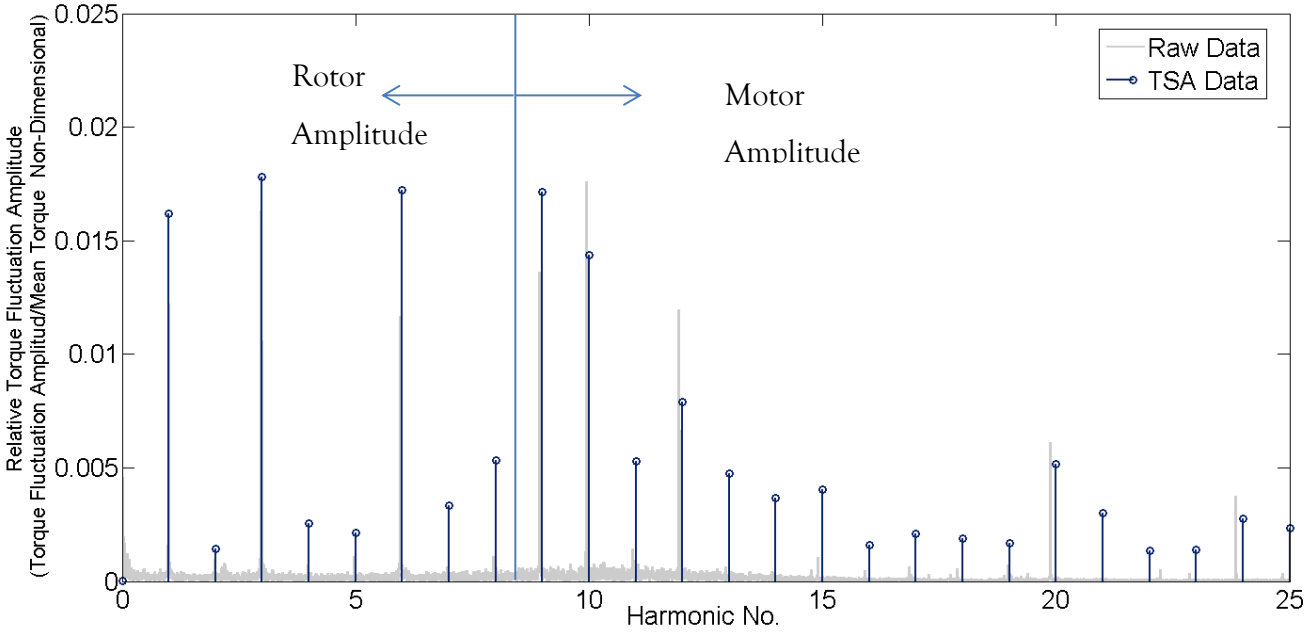

Figure 7.4: Amplitude spectrum of the drive shaft torque for the offset 12 rotor setting with a flow velocity of 1 m/s.

To make this judgement the harmonic characteristic observed in the CFD data were used as a guide. With reference to Figure 3.7: Drive shaft torque spectrum for optimum, offset +0.5o, offset +3o and offset +6o conditions. in Chapter 4 it can be noted that in the overall torque spectrum shown little significance in amplitude passed the eighth harmonic. Furthermore, and in agreement with this notion, it was considered that the 9th and 10th harmonic amplitudes were due to the pole passing frequency associated with the PMSM which had 10 pole pairs. This is further confirmed by the slight peak at the 20th harmonic also. This distinction has been highlighted in Figure 7.3 and Figure 7.4. The distinction between the lower frequency rotor artefacts and the higher frequency motor artefacts is also highlighted.

7.4.4 Parameter surface development

In Chapter 6, Figure 6.12 shows the results of applying the TSA pre-processing to data sets captured to differing λ values. The spectrums shown in Figure 7.3 and Figure 7.4 were calculated for each of the blade fault cases for each λ value, the spectrum data pertaining to the TSA data were then used throughout. The amplitudes were scaled by the

average torque $\bar{\tau}$ developed for the given operating condition. The surfaces were developed showing the fluctuation depth (relative amplitude surface) and phase of drive shaft torque over 8-harmonics and the 0-7 range for λ.

The surfaces were developed by inputting the known relative amplitudes and phase angles at the 8 harmonics considered and over the λ values measured in the flume experimentation as a 3-dimensional array into the Matlab curve fitting applet. The ranges of the surfaces for the harmonics were constrained between 1 and 8 with the range of the fit over λ constrained between 0 and 7. It should be noted that during the drive train experimentation data from the surfaces was output from Matlab and used as a look-up table within LabVIEW to minimise computational expense during real-time calculations, as outlined in Section 7.6.3.

In the case of the phase surface fit the phases were 'unfolded' empirically to minimise spurious surface gradients which arose from the phases being close to the -180^o and 180^o boundaries.

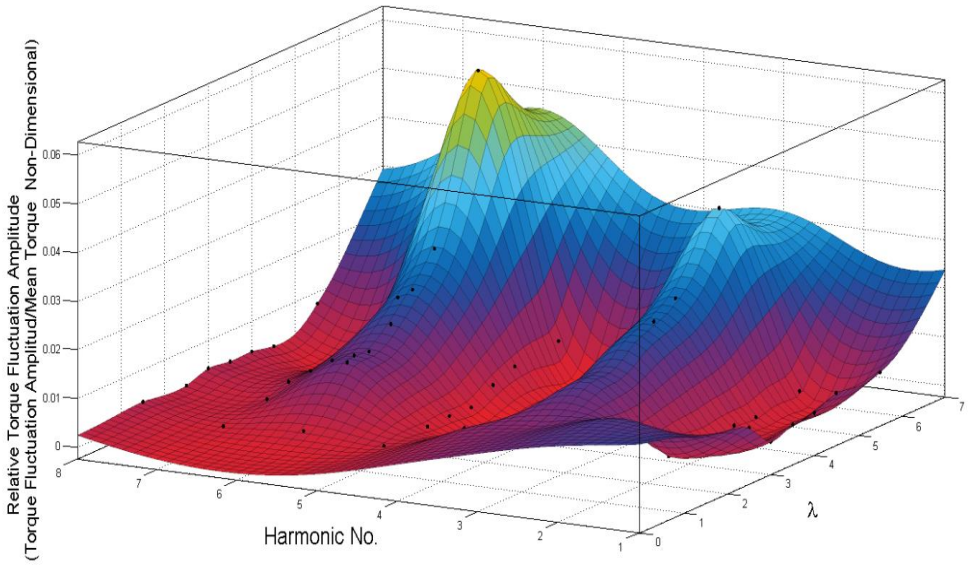

Figure 7.5: Amplitude surface generated via Bi-Harmonic Spline interpolation over harmonics and λ values of turbine operation, for 1 m/s fluid velocity and optimum rotor condition.

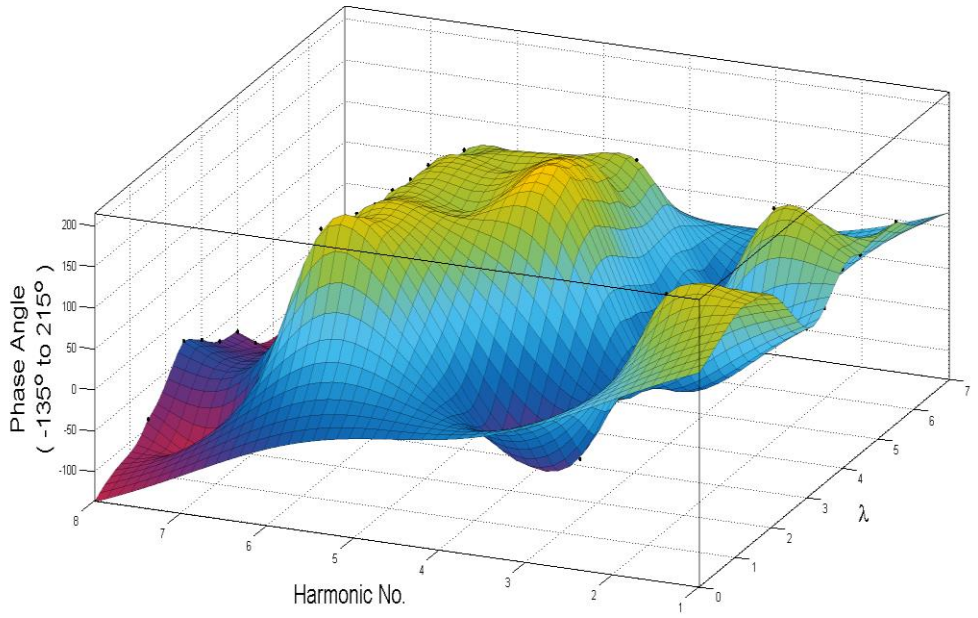

Figure 7.6: Phase surface generated via Bi-Harmonic Spline interpolation over harmonics and λ values of turbine operation, for 1 m/s fluid velocity and optimum rotor condition.

Examples of the surfaces generated are shown in Figure 7.5 and Figure 7.6. The figure show the relative amplitude and phase surfaces for the optimum case at a flow velocity of 1 ms^{-1}, respectively. Figure 7.7 and Figure 7.8 show the corresponding surfaces for a blade fault case of offset 6^{o}. It can be observed that a similar surface structure was found for both relative amplitude and phase surface for the two cases. This was consistent over all the flume data cases used to develop the surfaces. Furthermore it is highlighted in the developed surfaces that an increase in relative amplitude for the 1^{st}, 3^{rd} and 6^{th} harmonics correspond with increasing values of λ. In the case of the phase surfaces the phase wrapping used is highlighted on the phase axis.

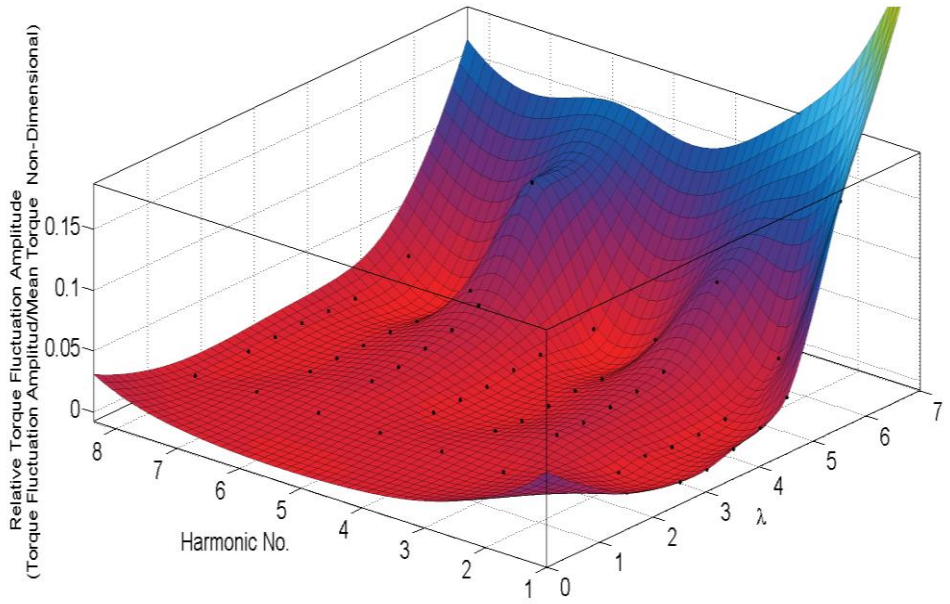

Figure 7.7: Amplitude surface generated via Bi-Harmonic Spline interpolation over harmonics and λ values of turbine operation, for 1 m/s fluid velocity and Offset 6º rotor condition.

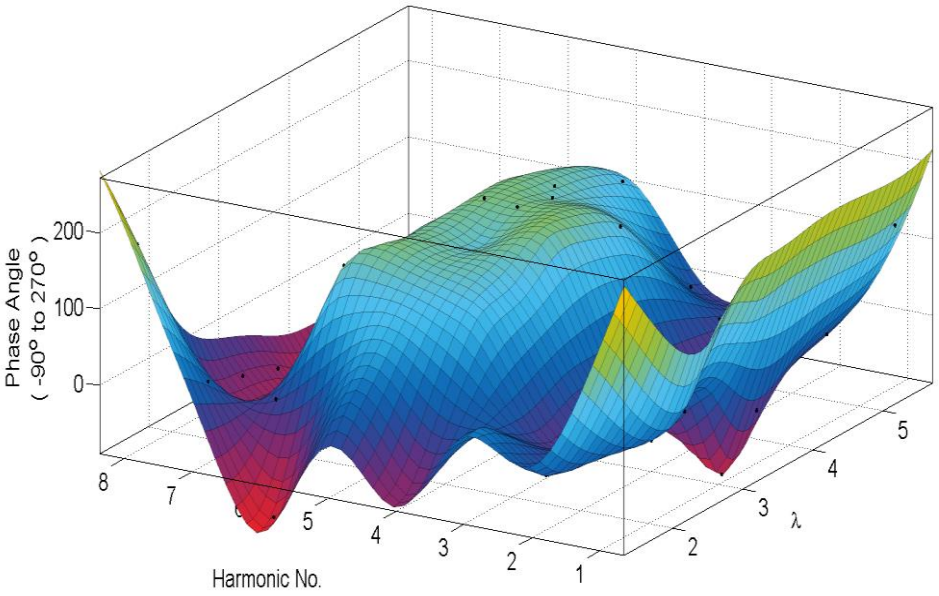

Figure 7.8: Phase surface generated via Bi-Harmonic Spline interpolation over harmonics and λ values of turbine operation, for 1 m/s fluid velocity and Offset 6º rotor condition.

It can be noted that conceptually the drive shaft torque fluctuations can be viewed as a set of 8 data points on the surface aligned with the 8 harmonics and during variable speed simulations are moving along the λ axis as the fluid velocity changes and the turbine control system tries to maintain peak power.

7.4.5 Torque distribution characteristics vs tip-speed-ratio.

In this section consideration is given to the use of the developed surfaces for varying fluid velocities which will be utilised as outlined to provide more realistic turbine simulations. In order to verify that the rotor model under development could be utilised for varying fluid velocity levels both the relative amplitude and phase spectrums were plotted for each value of λ for the three fluid velocity values tested within the flume testing campaign. Figure 7.9 and Figure 7.10 show the relative amplitude spectrums and phase spectrums, respectively, for the optimum rotor turbine setup. The figures present the data used to construct the surface presented above – they represent the surface values for differing harmonics for each given λ value.

It is clear that the relative amplitude spectrums for each of the three fluid velocities in general show good agreement, with the exception of the spectrum observed for λ equal to 1.5. This suggests that for λ values above 1.5 the relative drive train torque fluctuations are a function of the non-dimensional quantity and not the specific flow speed and rotational velocity used to calculate said non-dimensional value. Therefore the rotor torque simulation method proposed can be utilised for variable speed turbine operation, if limited to operation above a λ value of 1.5. This restriction, it should be noted, was considered to have little impact on the proposed simulations as, due to the optimal λ control schemes utilised, the operating range of λ expected would be, $2 < \lambda < 4$.

The phase spectrums show an altogether more complicated relationship over the λ values studied. There does seem to be agreement between the phase spectrums for λ greater than 3.5. Furthermore, it is worthwhile noting that the phase angles seem to be consistent and in good agreement for the 1st, 3rd and 6th harmonics. Specifically it was observed that the 1st harmonic occurs between the 70^{o} and 90^{o} phase angles. Between 350^{o} (-170 ^{o}) and 380^{o} (+160^{o}) were generally observed for the 3rd harmonic and phase values of between 150^{o} and 180^{o} were observed for the 6th harmonic. As such it was

considered suitable to assume a single surface structure for the range of fluid velocities utilised in the simulations.

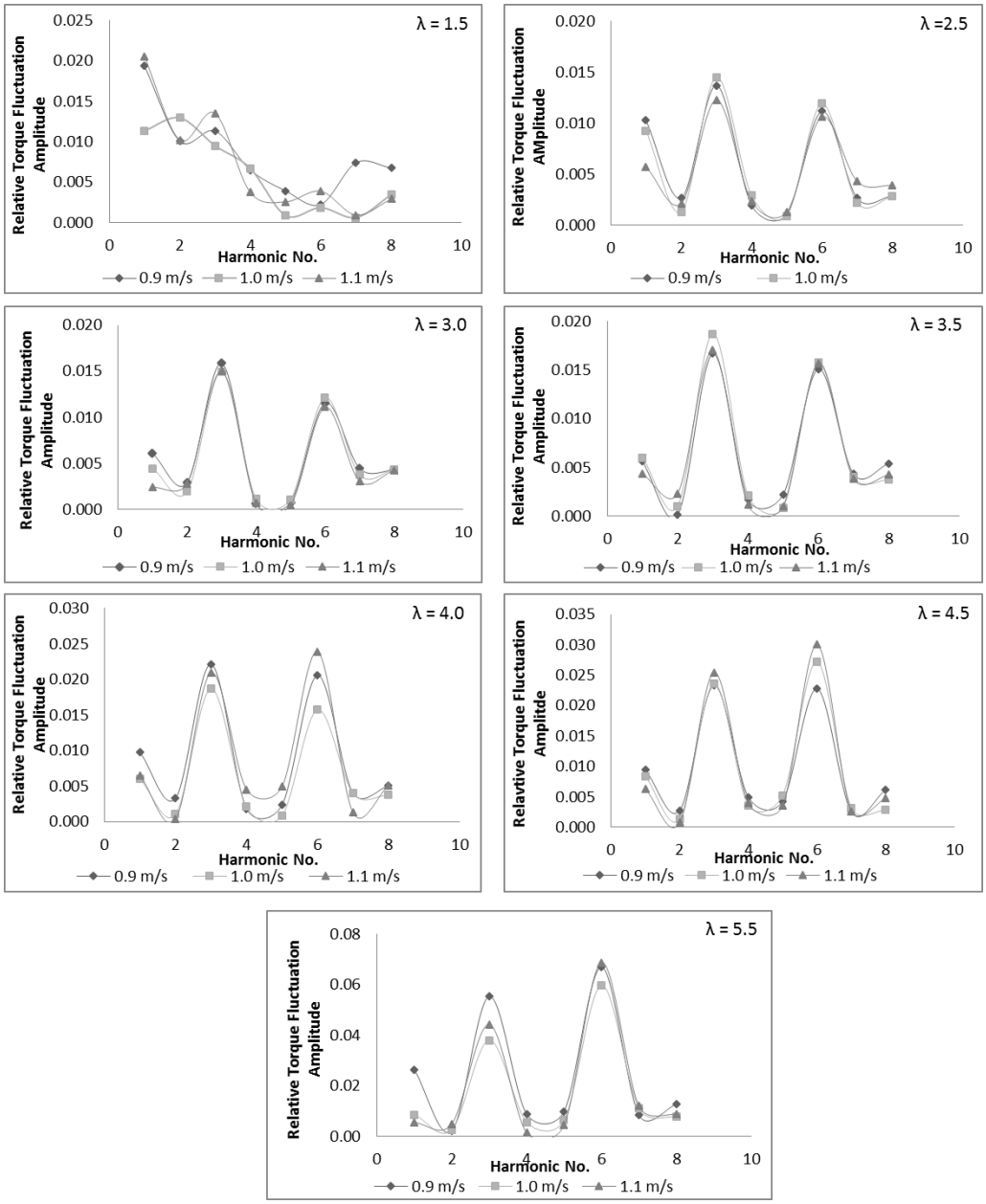

Figure 7.9: The amplitude spectrum for the 1/20th scale turbine driveshaft torque at varying λ values comparing the relative fluctuation depth for flow velocities: 0.9 m/s, 1 m/s and 1.1 m/s, the rotor setting for the case shown is optimum.

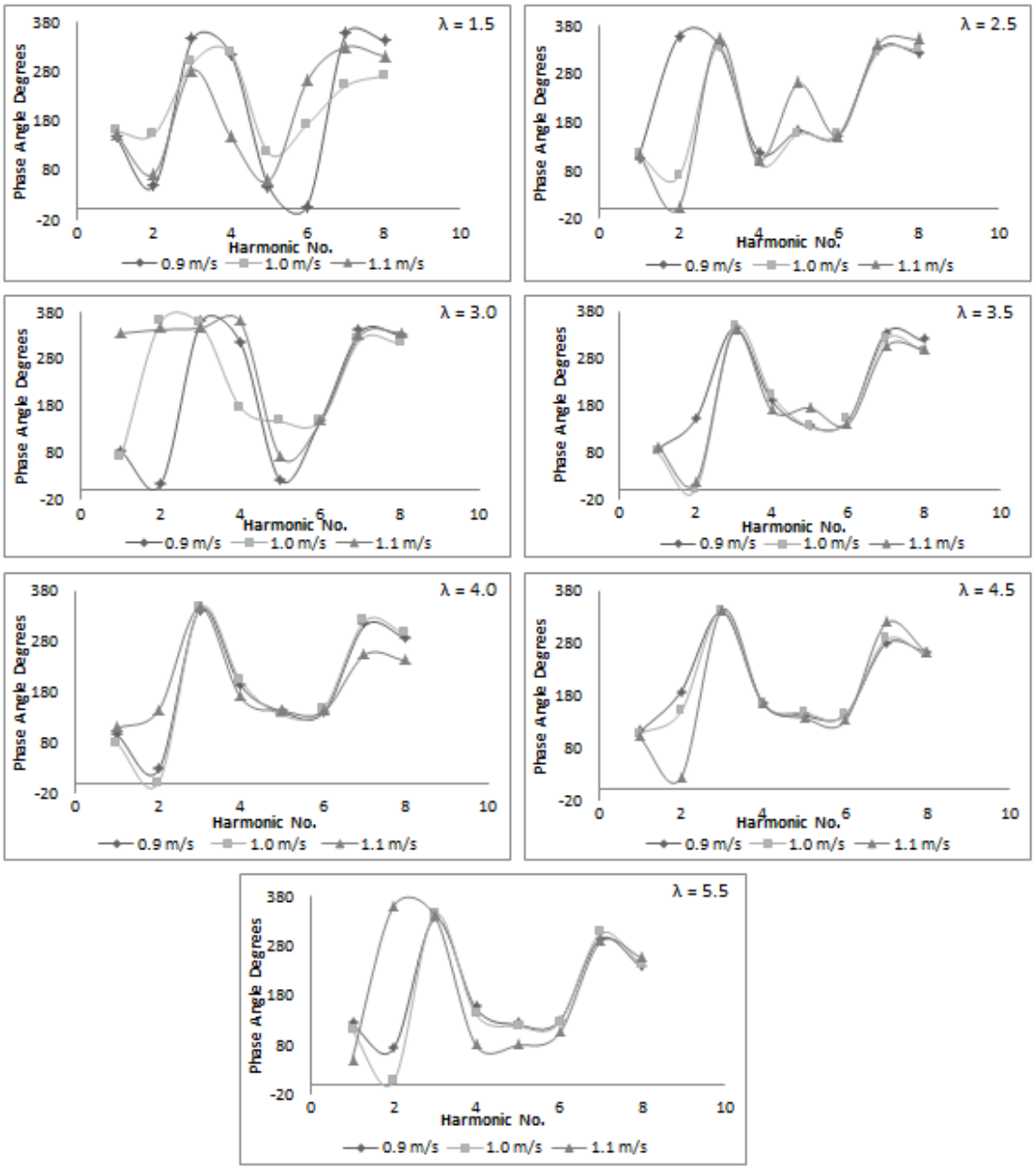

Figure 7.10: The phase spectrum of the 1/20th scale turbine driveshaft torque at varying tip-speed-ratio values comparing the phase angles for flow velocities: 0.9 m/s, 1.0 m/s and 1.1 m/s. The rotor case is that of the optimum rotor condition.

7.4.6 Consideration of the distribution of the raw data

The generation of the above surfaces and the associated considerations outlined formed the development of Fourier series based process mean calculation. As specified in the model formulation, however, the actual torque value for a single 'realisation' for a given turbine position would be sampled from a normal distribution with the mean defined by the aforementioned Fourier series and the standard deviation of the

distribution defined by study of the raw flume data. Specifically it was required to show that the raw data for a given turbine rotor position was distributed normally and that the standard deviation of the process was consistent overall turbine rotor positions. This was shown to be true in Section 6.3.2.

It was also required to study the effect of the turbine operating conditions on the spread of the raw torque data. To this end the standard deviation of torque data was calculated for each of the λ values measured. In order to study the effect of the turbine operating conditions on the torque data distribution from the process mean the standard deviation relative to the mean torque developed was plotted for each rotor condition and for each flow velocity measured during the flume testing. Figure 7.11: Plot showing the SD of the raw data over varying λ values for each of the rotor cases. shows an example of the variation in standard deviation of the raw data with λ value. This is indicative of the variation for each of the fluid velocity values. It was concluded that for convenience due to the relative consistancy of these variations a single second order polynomial in terms of the λ value could be utilised to represent the process distribution from the mean. Figure 7.11 highlights the second order polynomial fitted to the standard deviations obsereved for varying λ values. Below the curve fit and data values the residuals between the fitted polynomial and the training data are shown. As can be seen insignificant residuals were obsereved over the range λ values considered.

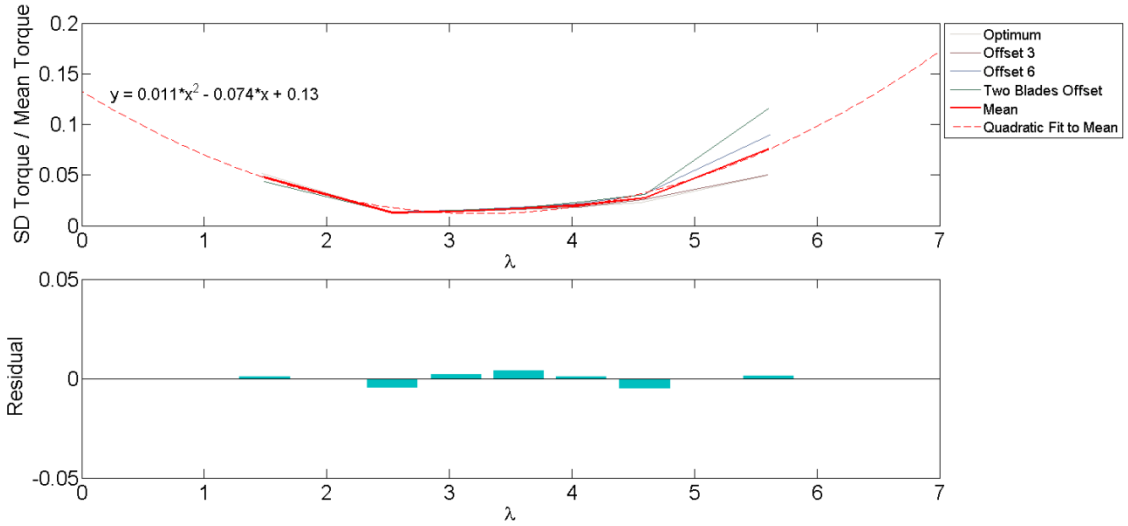

Figure 7.11: Plot showing the SD of the raw data over varying λ values for each of the rotor cases.

7.4.7 Final model outline

The formulations developed over the previous sections were used to define the inputs into the model resulting in the final model form as given in equation 7.9.

$$\tau = \bar{\tau} + \sum_{i=1}^{8} \bar{\tau} \cdot a_i \cdot \cos(2\pi\theta + p_i) + Z \qquad (7.9)$$

where:

Z is a normally distributed strictly stationary random process with mean, $\mu = 0$ and standard deviation:

$$\sigma = 0.011\lambda^2 - 0.074\lambda + 0.13 \qquad (7.10)$$

$\bar{\tau}$ is the mean torque developed by the rotor and is given by (7.8).

a_i is the relative amplitude of fluctuations at various harmonics, i to 8 – represented as a surface.

p_i is the phase angle at various harmonics , i to 8 – represented as a surface.

The simulation and drive train testing results are presented fully in chapter 8. However, to illustrate the output of the model formulated and to compare it with the

flume data used to parameterise the model, two instances of steady-state simulation are shown below. Specifically Figure 7.12 shows the model data calculated for 50 turbine rotations with a fixed fluid velocity of 1 ms^{-1}. The TSA of the 50 rotations is shown along with the TSA data from the flume testing for comparison. A more detailed discussion of the results will be provided in subsequent chapters however, it seems that the proposed rotor model adequately captures the lower frequency content of the flume data as was the desired outcome.

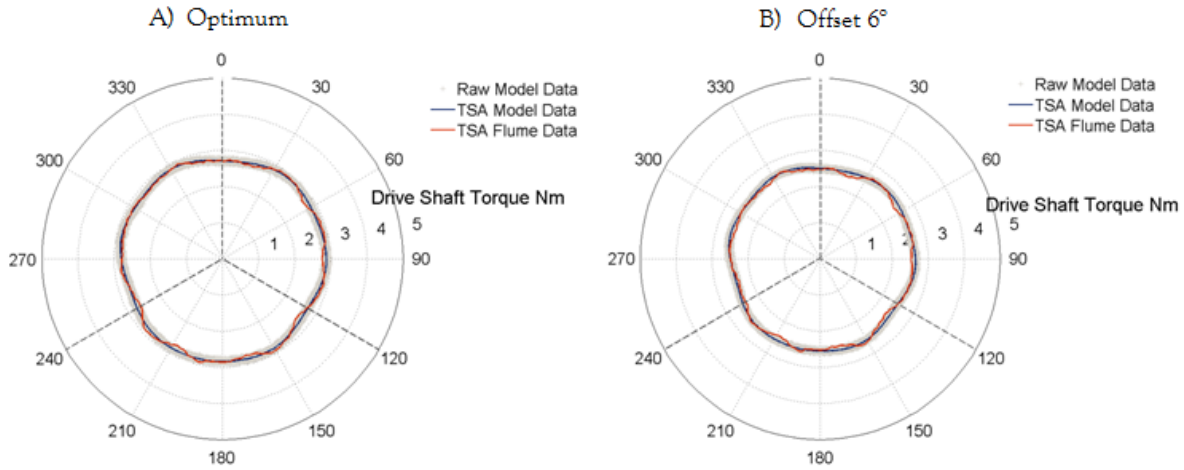

Figure 7.12: Model output under fix fluid velocity operation. Raw and TSA data are shown along with the TSA flume data for comparison. A) Shows the optimum rotor case. B) Shows the offset 6° rotor case.

7.5 Tidal Stream Turbine Control

As detailed the simulations implemented via the drive train test rig, were created to emulate variable speed turbine and fixed speed turbine control. Details relating to turbine topology and control were presented during in Section 3.4.1 and as such only the details directly relevant to the simulations are discussed herein.

7.5.1 Fixed-speed turbine control

Fixed speed turbine control has been included in the simulation capability to allow for comparison between flume results and drive train test rig results. It was also considered that the fixed speed operation under higher turbulence intensities will provide simulations which have similar characteristics to slow acting turbines with higher inertia drive trains. Lastly it was considered as an additional turbine setup to which the turbine CM approaches could be applied for testing and development. The fixed speed operation of the turbine will be achieved by setting the turbine rotational velocity to the value that corresponds to the λ value for peak power operation given the mean fluid velocity over the entire simulation.

7.5.2 Optimal λ Control

To simulate turbine dynamics in a rigorous and representative manner variable speed turbine control was utilised for the experimental simulations. This was included to allow for adequate appraisal of CM hypotheses based on the simulation results. The variable speed turbine control scheme used was that of optimal tip-speed ratio control. The method involved taking fluid velocity and turbine rotational velocity measurements required to define the turbine operating tip speed ratio. The measured operating point is compared with a set-point tip speed ratio, known prior to operation to give maximum power output under continuous turbine operation. The error value is passed to a controller to regulate the generator load to achieve the torque required to minimise the tip speed ratio error. Figure 7.13 shows the control diagram for the optimal tip speed ratio tracking control system used during the experimental simulations [Abdullah et al, 2012].

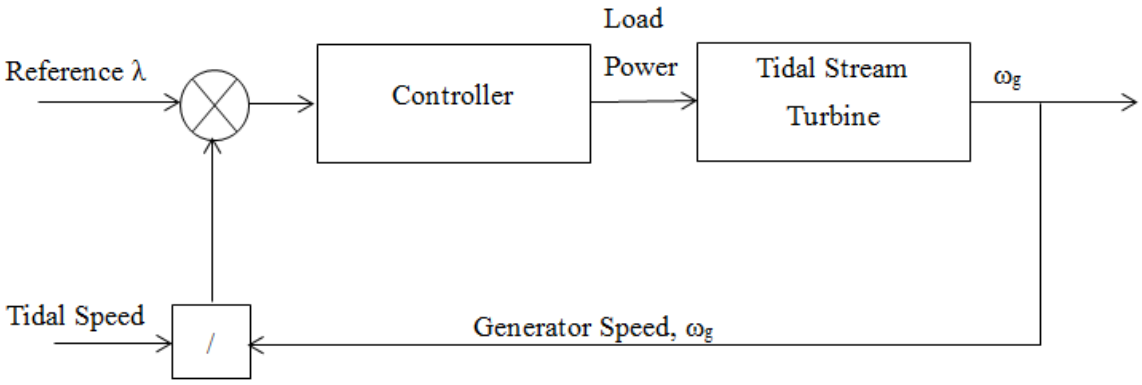

Figure 7.13: An example of optimal λ (TSR) control scheme as presented by (Abdullah et al, 2012).

It can be seen that the essential element in controlling the generator feedback torque and hence rotational velocity is controlling the load power output via the power converter apparatus. During the experimental simulations the torque set point command was input to the motor drive used and the internal control structure was used which is outline in Section 7.6.2.

7.6 Drive train test rig implementations

7.6.1 Overview of hardware

Figure 7.14 shows the drive train test bed developed for tidal stream turbine simulations. The test bed motor can be controlled to replicate the turbine rotor input to the drive train. In this case the motor is directly coupled to a generator for power extraction thereby effectively enabling the simulation of both a direct-drive and geared tidal stream turbine equipped with a permanent magnet synchronous generator. To allow for flexibility the two rotating machines are of the servo type with on board encoders measuring the rotor velocity and position for feedback control. The machines are Bosch Rexroth IndraDyn MSK 050Cs and are synchronous permanent magnet machines rated with a maximum velocity of 4300 RPM and a maximum torque of 9 Nm. A proprietary flexible coupling was used to connect the machine's drive shafts.

The motor drives setup is shown in Figure 7.15. The drives used were the Indradrive Cs which were set-up as master and slave utilising the SERCOS III communication protocol. The master drive was then connected via Modbus TCP/IP to a National Instruments Compact RIO. The TST model and maximum power point tracking control loops were implemented using the Real-Time operating system in the Compact RIO and the rotor and generator commands were sent to the motor drives via the Modbus link. The motor drives utilised close-loop vector oriented control to implement the commands sent from the Compact RIO. For the simulations undertaken the speed of the turbine was set by commanding the rotational velocity of the generator which was achieved via load output regulation. The motor was control to replicate torque commands output form the parametric model given the current parameters and simulation data.

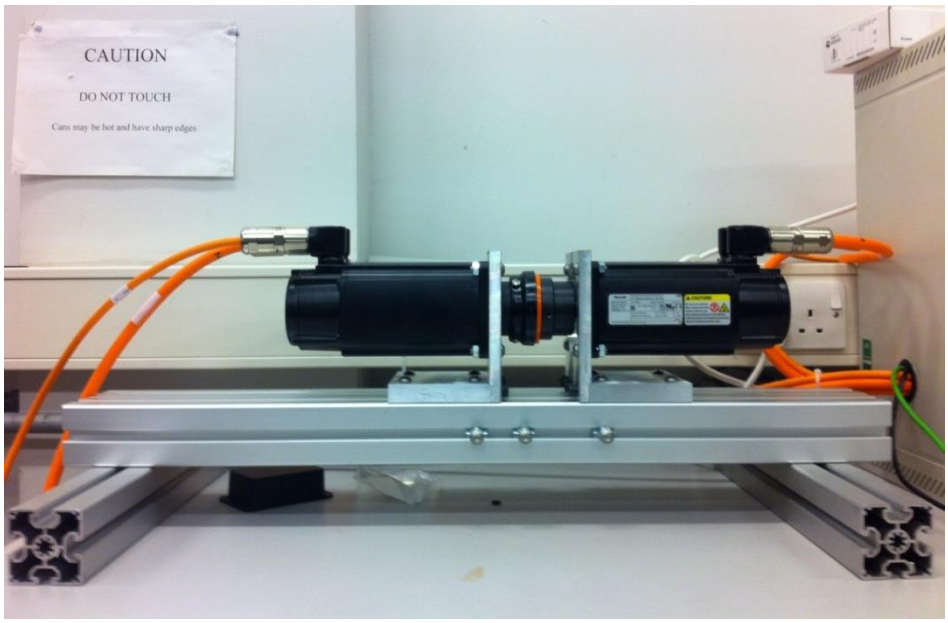

Figure 7.14: The drive train test rig which was utilised for scale turbine drive train simulations.

Figure 7.15: Motor drives and Compact RIO arranged in the drive cabinet.

Figure 7.16 shows a schematic of the test rig indicating the interaction between each of the hardware elements. The figure also shows the flow of information highlighting the use of measured data for recursive simulation calculations and the storing of data for further analysis. The numbers circled within each of the elements relate the elements of the overall simulation schematic presented in Figure 7.1 to the hardware schematic in Figure 7.16. Specifically the calculation of each numbered element is undertaken via the hardware labelled with the corresponding number in Figure 7.16.

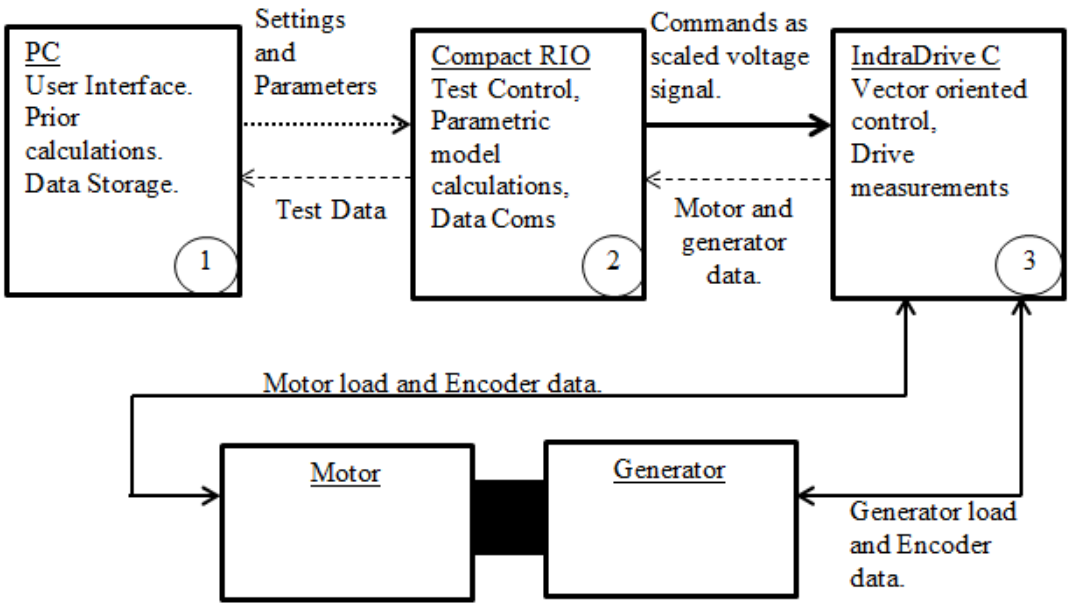

Figure 7.16: Schematic of the interacting hardware elements and the distribution of functionalities across the hardware platforms.

7.6.2 Vector Oriented Control of PMSM.

The PMSM utilised for the test rig setup were setup to implement vector oriented control (VOC). In the case of the motor the goal of the VOC was to operate the motor in a similar fashion to a TST via the application of appropriate torsional loads which are calculated via the outlined rotor model. The goal of the VOC for the generator is to control the generator load in order to realise optimal TSR control.

The idea of vector oriented control has been previously utilised for motor and generator control. Its use in relation to tidal stream turbine control has been reported (Liang and Whitby, 2011). The process related to applying this to wind turbine control has also been reported (Anaya-Lara, 2009). In the case of a PMSG, this is done by noting that under normal operation the i_d current in Equation 3.8 is weakening the magnetic flux producing the generator feedback torque and can therefore be set to zero, this gives:

$$\tau_e = \frac{2}{3} \cdot p \cdot \varphi \cdot i_q \qquad (7.11)$$

For a set-point torque required to accelerate or decelerate the turbine velocity to the required optimal rotational velocity the reference direct and quadrature currents are given by:

$$i_{dref} = 0 \tag{7.12}$$

$$i_{qref} = \frac{3}{2}\frac{T_{sp}}{p \cdot \varphi} \tag{7.13}$$

The required voltage in the direct and quadrature axis can be found be re-arranging (7.13) and (7.14).

$$v_{dref} = Ri_d + \omega_r L_q i_q \tag{7.14}$$

$$v_{qref} = -Ri_{dq} - \omega_r L_d i_d + \omega_r \varphi \tag{7.15}$$

The voltage reference signal is then input into a PWM module which generates the switching sequence for the IGBT to regulate the phase voltages of the generator to give the required generator feedback torque which will result in the set-point λ value required for peak power extraction. The VOC control scheme was implemented in the drive systems of the PMSMs and was developed by Bosch Rexroth as a standard control system for the machines utilized. A schematic of the control process implemented via three cascaded control loops is shown in Figure 7.17 (Bosch Rexroth AG, 2011).

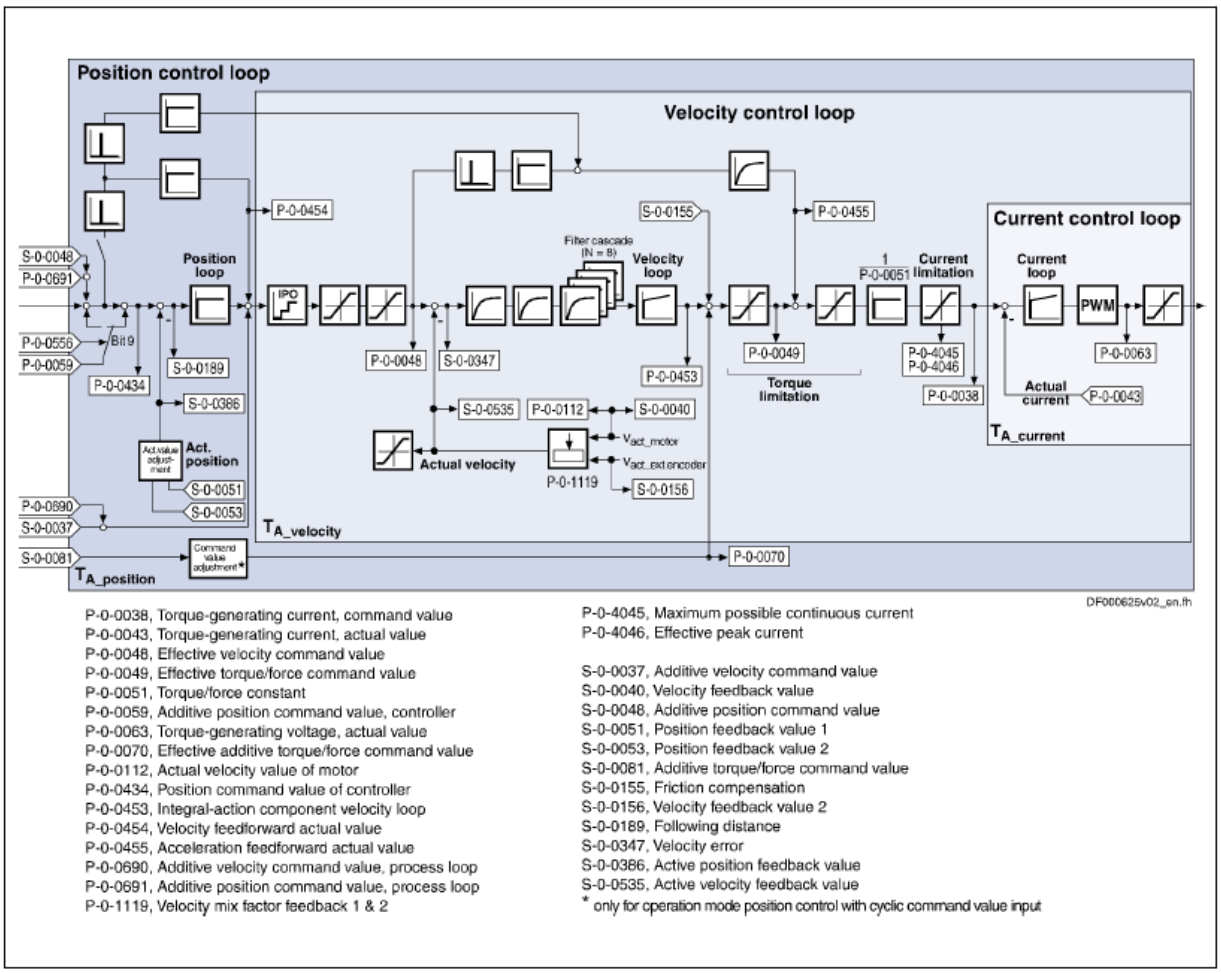

P-0-0038, Torque-generating current, command value
P-0-0043, Torque-generating current, actual value
P-0-0048, Effective velocity command value
P-0-0049, Effective torque/force command value
P-0-0051, Torque/force constant
P-0-0059, Additive position command value, controller
P-0-0063, Torque-generating voltage, actual value
P-0-0070, Effective additive torque/force command value
P-0-0112, Actual velocity value of motor
P-0-0434, Position command value of controller
P-0-0453, Integral-action component velocity loop
P-0-0454, Velocity feedforward actual value
P-0-0455, Acceleration feedforward actual value
P-0-0690, Additive velocity command value, process loop
P-0-0691, Additive position command value, process loop
P-0-1119, Velocity mix factor feedback 1 & 2

P-0-4045, Maximum possible continuous current
P-0-4046, Effective peak current

S-0-0037, Additive velocity command value
S-0-0040, Velocity feedback value
S-0-0048, Additive position command value
S-0-0051, Position feedback value 1
S-0-0053, Position feedback value 2
S-0-0081, Additive torque/force command value
S-0-0155, Friction compensation
S-0-0156, Velocity feedback value 2
S-0-0189, Following distance
S-0-0347, Velocity error
S-0-0386, Active position feedback value
S-0-0535, Active velocity feedback value
* only for operation mode position control with cyclic command value input

Figure 7.17: Control structure implemented in the Bosch Rexroth drive utilising VOC for torque (current), velocity and position control of the PMSM (Bosch Rexroth AG, 2011).

7.6.3 Software Implementations

In order to implement the parametric simulation method constructed by the author various software elements had to be incorporated. Specifically the author wrote software routines for each of the platforms highlighted in Figure 7.16. The PC and Compact RIO ran software routines constructed in LabVIEW which were constructed as a single software project distributed between the Windows operating system (Host PC) and the NI Real-Time operating system (Compact RIO). The IndraDrive Cs systems ran software routines which were implemented via structured text. The majority of the software implemented was engineered to allow data capture and sharing between the various platforms as required. Furthermore software was implemented to allow for user interface functionalities and for the input of test settings, fluid velocity time-series and

parameter surfaces. The main element of the software was the parametric model implementation, presented below.

The model calculation is made as highlighted on Figure 7.18. The three main aspects of the calculations are using the motor measurements and fluid velocity value for the given time step to calculate the current operating tip-speed ratio. In the same stage the tip-speed ratio is used to interpolate the turbine non-dimensional torque curve and parameter surfaces to obtain the torque coefficient, C_θ, the amplitude parameters, a_i, and lastly the phase angle parameters p_i. In the next step the parameters set outlined, rig measurements and the fluid velocity value for the time step are used to calculate the turbine rotor torque. The calculation is made using the formulation outline in Section 7.4 and as discussed returns a realisation of the process for the given rotor position and simulation settings. A new 'realisation' is returned each time step and time steps corresponding to equal rotor displacements and fluid velocity settings will not necessarily return equal torque values. However, the process mean for a given displacement and fluid velocity value will be equal to the value calculated via equation 7.9 with the random variable Z set to zero.

The last step calculates the set point rotational velocity for either optimal TSR control or for fixed velocity control. The generator velocity and the motor torque commands are output as scaled voltages, in the range 0 V - 10 V, which are input to the built-in analogue inputs on the IndraDrives Cs. The new measurements from the motor and generator are acquired and used to update the turbine state. The updated variables or turbine state is then used for the next execution of the calculation loop.

In order to undertake the first iteration of the model calculations outlined above the first fluid velocity value must be read and the generator set to the required velocity. This is done during a 30 second period allowing the rig to reach the required velocity and to successfully send data to the Compact RIO. At the end of the 30 second period the final

measurements of motor and generator parameters are input to the model for the first iteration.

Prior to the simulation start and run-in period the software is controlled via user input. Under this state the user is able to select the fault states to be simulated and if there is to be a change in turbine characteristics during the simulations. In order to set the turbine characteristics the user loads files in to the software containing the turbine non-dimensional torque curve, amplitude surface and phase surface. Furthermore the user can upload a fluid velocity time series generated via the process outlined in Section 7.3 prior to simulation. Lastly, it is worthwhile noting that the author made efforts to create highly modular software whereby changes to the simulation approach can be easily achieved. Chapter 8 presents the results of a CM study made based on the outlined simulation approach. The simulations considered fixed speed and optimal TSR turbine operations and the impact of such turbine operation on the use of generator signals for rotor fault detection and diagnosis are further investigated.

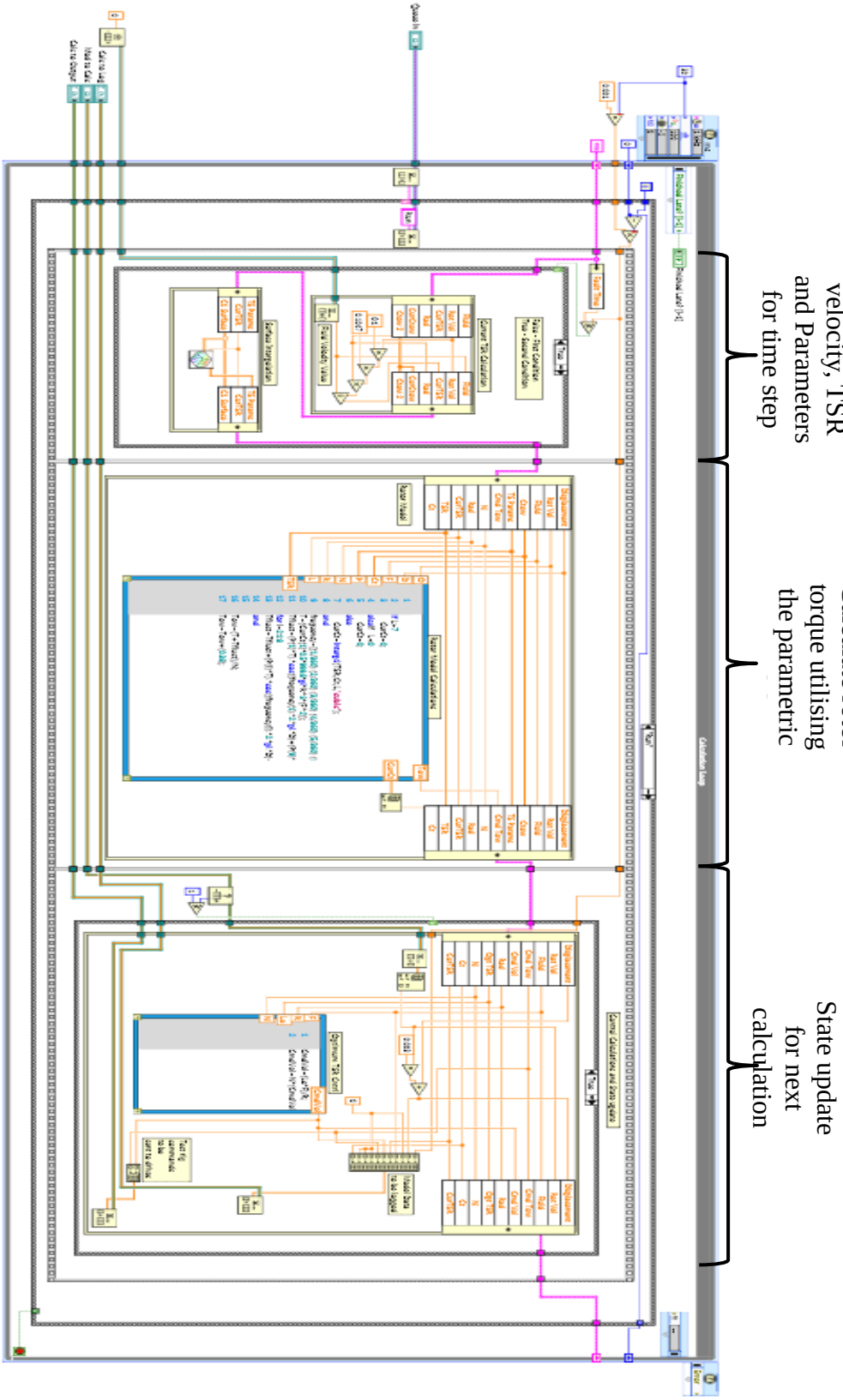

Figure 7.18: Screen shot of the LabVIEW code implementation of the parametric rotor model and turbine control processes discussed throughout this chapter.

8 Drive Train Simulation Results

8.1 Overview of simulation

This chapter outlines the results and findings of the drivetrain test rig based TST simulations. The goal was to further develop and test the applicability of various fault detection and diagnosis algorithms under differing turbine operating scenarios. The datasets developed to appraise the effectiveness of the CM algorithms are outlined in the test matrix shown in Table 8.1. Simulations were undertaken at a variety of tip speed ratio values for the optimum turbine setup in order to develop monitoring surfaces. The fault conditions were then simulated at a value close to peak power, specifically at $\lambda = 3.6$.

Table 8.1: Drive train simulation test matrix.

Rotor Setting: Optimum. *Test Type:* Steady State. $\overline{U}$ = 1 ms^{-1}. λ = 3.0, 3.6 and 4.2. *TI* = 0 %.	*Rotor Setting:* Optimum. *Test Type:* Optimum TSR Tracking. $\overline{U}$ = 1 ms^{-1}. λ = 3.0, 3.6 and 4.2. *TI* = 10 %	*Rotor Setting:* Optimum. *Test Type:* Fixed Speed Control. $\overline{U}$ = 1 ms^{-1}. ω = 229 RPM, 275 RPM and 352 RPM. *TI* = 10 %.
Rotor Setting: Offset +3º. *Test Type:* Steady State. $\overline{U}$ = 1 ms^{-1}. λ = 3.6. *TI* = 0 %.	*Rotor Setting:* Offset +3º. *Test Type:* Optimum TSR Tracking. $\overline{U}$ = 1 ms^{-1}. λ = 3.6. *TI* = 10 %	*Rotor Setting:* Offset +3º. *Test Type:* Fixed Speed Control. $\overline{U}$ = 1 ms^{-1}. ω = 275 RPM. *TI* = 10 %.
Rotor Setting: Offset +6º. *Test Type:* Steady State. $\overline{U}$ = 1 ms^{-1}. λ = 3.6. *TI* = 0 %.	*Rotor Setting:* Offset +6º. *Test Type:* Optimum TSR Tracking. $\overline{U}$ = 1 ms^{-1}. λ = 3.6. *TI* = 10 %	*Rotor Setting:* Offset +6º. *Test Type:* Fixed Speed Control. $\overline{U}$ = 1 ms^{-1}. ω = 275 RPM. *TI* = 10 %.
Rotor Setting: Two Blades. *Test Type:* Steady State. $\overline{U}$ = 1 ms^{-1}. λ = 3.6. *TI* = 0 %.	*Rotor Setting:* Two Blades. *Test Type:* Optimum TSR Tracking. $\overline{U}$ = 1 ms^{-1}. λ = 3.6. *TI* = 10 %	*Rotor Setting:* Two Blades. *Test Type*: Fixed Speed Control. $\overline{U}$ = 1 ms^{-1}. ω = 275 RPM. *TI* = 10 %.

8.2 Initial results and test rig limitations

The initial intention of the author was to undertake simulations which related to the operation of a turbine of similar characteristics to the one developed and utilised for flume testing. However the drive train test rig hardware had two limitations which required modification of these simulations. It was found that the measurement system (PLC) feedback to the real-time operating system (PXI) in which the turbine model calculations took place was of too low a sample rate. Specifically the position, torque and rotational velocity measurements used to undertake the hardware in the loop simulation had an effective sample rate of 20 Hz due to the Modbus TCP/IP communication method used to send the PMSM measurements back to the real-time operating system. This was problematic when simulating turbine rotor transient characteristics based on the harmonic structure of the observed rotor contribution to the turbine drive shaft torque, as detailed in Chapter 7. Secondly the regeneration characteristics of the PMSM utilised for the simulations were found to be inconsistent with the required regeneration characteristics required to carry out such simulations. Specifically the required torque values necessary for representative regeneration characteristics were unobtainable at the rotational velocities required to adhere to the turbine scale and operational characteristics.

These limitations made the goal of simulating the operational characteristics of a TST unachievable without changing the test rig setup. The approach adopted meant undertaking the simulations which included the drive shaft torque at the high speed shaft of an indirect drive turbine. As well as the inclusion of a ‘virtual gear box’ in the simulations the power and torque levels had to be scaled to allow for simulations to be undertaken utilising the available hardware i.e. within the speed vs torque characteristics of the PMSMs.

The reasoning behind the changes undertaken was to allow for the simulation of a larger diameter turbine which would be feasible given the limitations of the measurement system communication rate. This feasibility was afforded as a turbine of greater diameter would by

necessity rotate at a lower rotational velocity than the 0.5 m diameter turbine initially proposed. The slower rotational velocity meant that the model calculations could be undertaken without aliasing of the harmonic content of the simulated rotor contribution to the turbine drive shaft torque. The inclusion of the 'virtual gear box' and torque scaling was then undertaken so that the motor input to the simulated drive train resulted in achievable power output characteristics from the generator. The specific adaptations to the simulation are shown in Table 8.2.

Table 8.2: Adaptions made to the proposed.

Characteristic	Lab Scale Turbine	Simulated Turbine
Diameter	0.5 m	2.5 m
Mean Flow Rate, $\bar{U}$	1 ms^{-1}	1 ms^{-1}
Peak Power TSR, λ_{max}	3.61	3.61
Rotor Velocity at Peak Power and mean flow rate, $\omega_{max,\ 1\,ms^{-1}}$	14.4 $rads^{-1}$	2.88 $rads^{-1}$
Maximum model harmonic frequency, f_{max}.	18.33 Hz	3.66 Hz
Gear Ratio, n	1:1	1:10
High Speed Shaft Velocity, at Peak Power and mean flow rate, $\psi_{max,\ 1\,ms^{-1}}$	14.4 $rads^{-1}$, 138 RPM	28.9 $rads^{-1}$, 260 RPM
Peak Power at mean fluid velocity, P	39 Watts	981.9 Watts
Power Scaling Factor	1	1/25
Peak Torque at mean fluid velocity and λ = 3.61	2.70 Nm	340 Nm
Torque Scaling Factor	1	1/125

The adaptations to the simulated turbine also impacted on the amplitudes of the harmonic content of the rotor torque. Specifically, the introduction of the 'virtual gearbox' and the artificial torque scaling meant that the torque output of the rotor model had to be scaled by

the inverse of the gear ratio utilised and a factor required to allow for safe operation using the given hardware. This scaling was also applied to the amplitudes of the torque fluctuation harmonics included in the turbine rotor model. This scaling of the torque harmonic amplitude became problematic as the resultant amplitude of torque fluctuation after the scaling process was of the same scale as the noise of the system. As such the amplitudes of the simulations were also scaled to increase the resultant torque fluctuation amplitudes by a factor of 20. This allowed the torque fluctuation amplitudes to be observed in the motor input to the drive train simulations.

8.3 Simulation Results

8.3.1 Fluid velocity simulations

Figure 8.1 shows a single realisation of the 20 fluid velocity simulations created using the process outlined in Section 7.3. The fluid velocity simulations developed were 150 seconds in length, had a mean fluid velocity of 1ms^{-1} and a turbulence intensity of 10%.

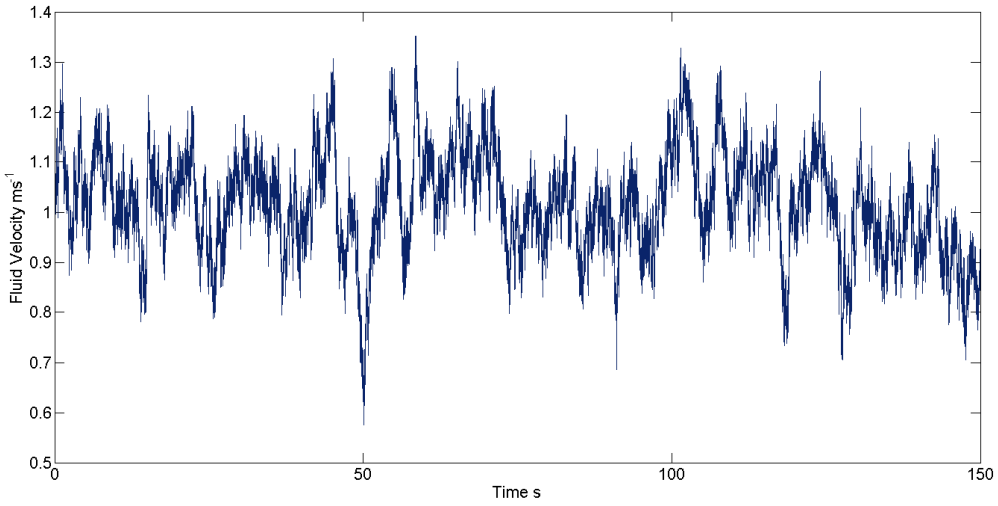

Figure 8.1: Example of the generated fluid velocity time series for a mean fluid velocity 1 ms^{-1} and a turbulence intensity of 10 %.

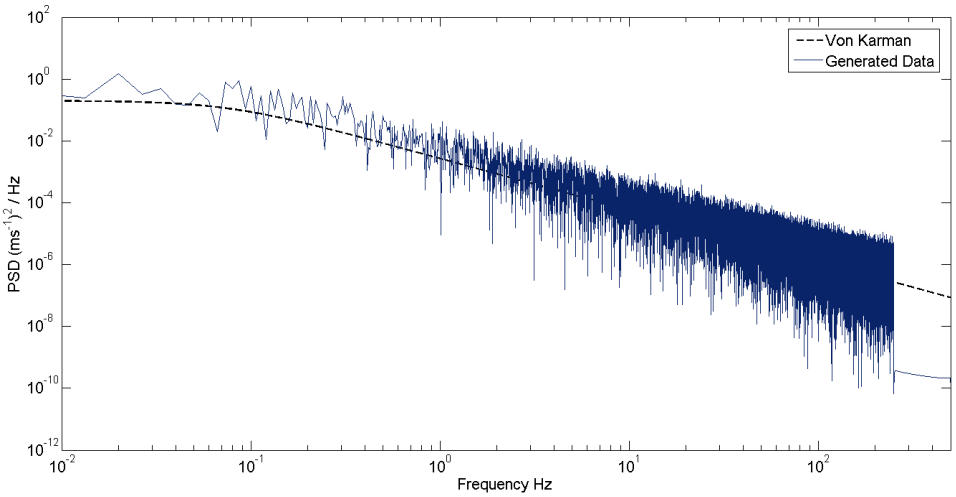

Figure 8.2: Comparison of the Von Karman spectrum and the spectrum observed for a single instance of the fluid velocity time series generated for a mean fluid velocity of 1ms-1 and a turbulence intensity of 10%.

Figure 8.2 indicates that the fluid velocity time-series simulated exhibited the required Von Karman power spectrum characteristics. This was seen as confirming that the simulation method was successful in generating fluid velocity time series with the required spectral properties.

Figure 8.3 is a histogram of the observed mean fluid velocities for the 20 resulting fluid velocity time series. The means observed range between 0.98 ms^{-1} to 1.04 ms^{-1} which was suitable for the simulations being undertaken.

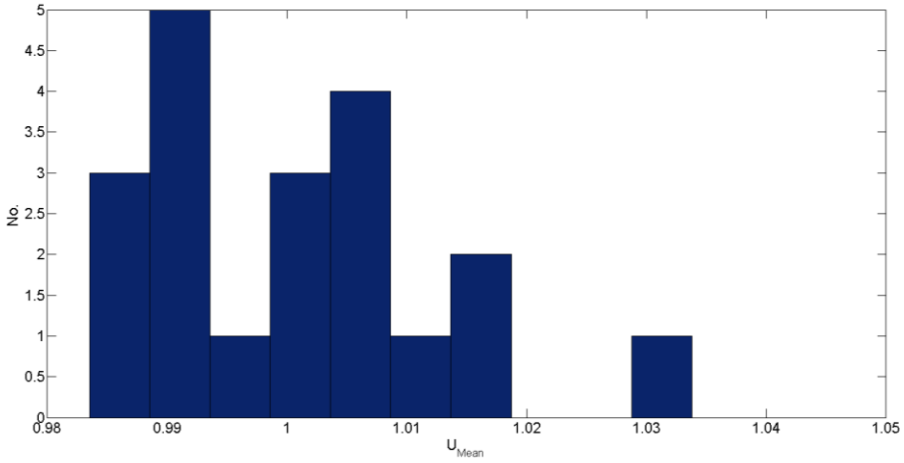

Figure 8.3: Histogram showing the range of mean fluid velocities generated for the 20 time series created for the drive train testing campaign for a specified mean fluid velocity of 1 ms-1.

Figure 8.4 then shows a histogram of the observed turbulence intensity values of the 20 simulated fluid velocity time series. The histogram confirms that the simulations resulted in time series of approximately 10% turbulence intensity as required. The observed turbulence intensities ranged from 8.5 % to 10.5 %.

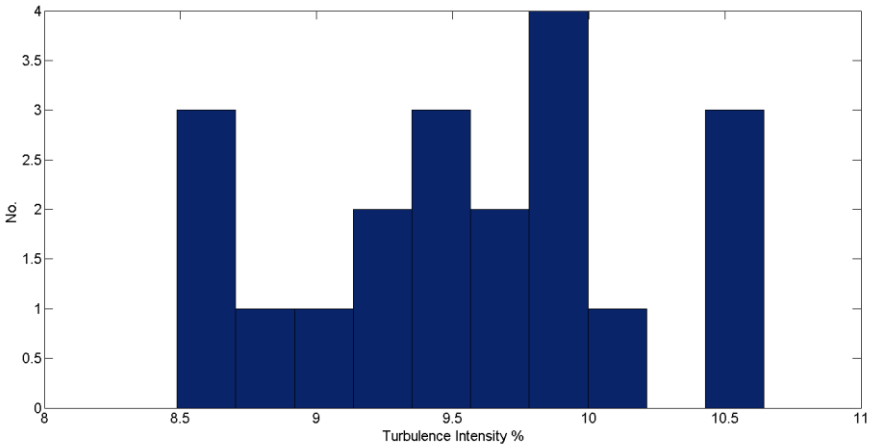

Figure 8.4: Histogram showing the range of turbulence intensities generated for the 20 time series created for the drive train testing campaign for a specified mean fluid velocity of 1 ms-1 and TI of 10%

Figure 8.5 shows the effect of the frequency resolution used during the inverse-Fourier transform Monte Carlo simulation method. It can be observed that generally as the frequency resolution is increased the obtained time series approach the required turbulence intensity.

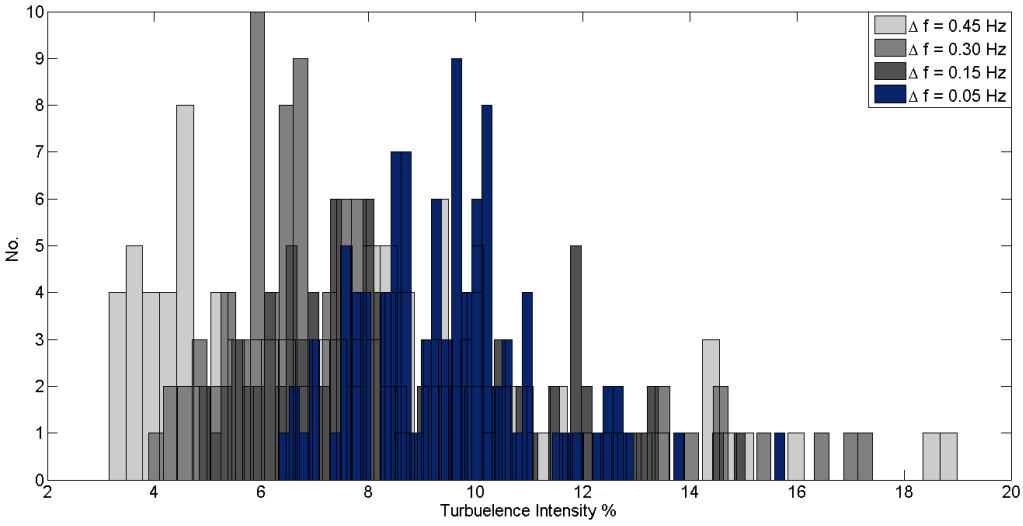

Figure 8.5: Histogram showing the effect of varying the frequency resolution (integration limits in equation) on the observed turbulence intensity of 20 generated fluid velocity time series.

It can be seen in Figure 8.5 that as the frequency resolution used for the simulation is increased the spread of turbulence intensities observed for a given frequency resolution decreases. This goes some way to explaining the spread of turbulence intensities observed in the 20 fluid velocity time series used for drive train test rig simulations. The fluid velocity time series were generated using a frequency resolution of 0.05Hz, which in referring to Figure 8.5 still exhibits some spread in the observed turbulence intensities. The frequency resolution utilised was applied because the computational time required for greater frequency resolution simulations became increasingly prohibitive.

8.3.2 Real-time model output

Figure 8.6 and Figure 8.7 show examples of the resulting data sets from the drive train simulations undertaken following the process outlined in Chapter 7 along with adaptations outlined in Section 8.2. Figure 8.6 shows the results of steady state simulations undertaken with a fixed fluid velocity. As a result one can see the fixed rotational velocity set point command resulting from the optimal TSR control system. Furthermore the figure shows the imparted torsional fluctuations incorporated into the simulations to account for the transient characteristics of the rotor behaviour observed during flume testing. The torque fluctuations can be seen in the quadrature axis current of the generator and the power output of the generator. The power output of the generator PMSM is negative following the motor convention and thus signalling operation of the PMSM as generator extracting energy from the system. Lastly the effect of the introduction of the ‘virtual gearbox’ can also be seen in the position measurements of the rotor and generator.

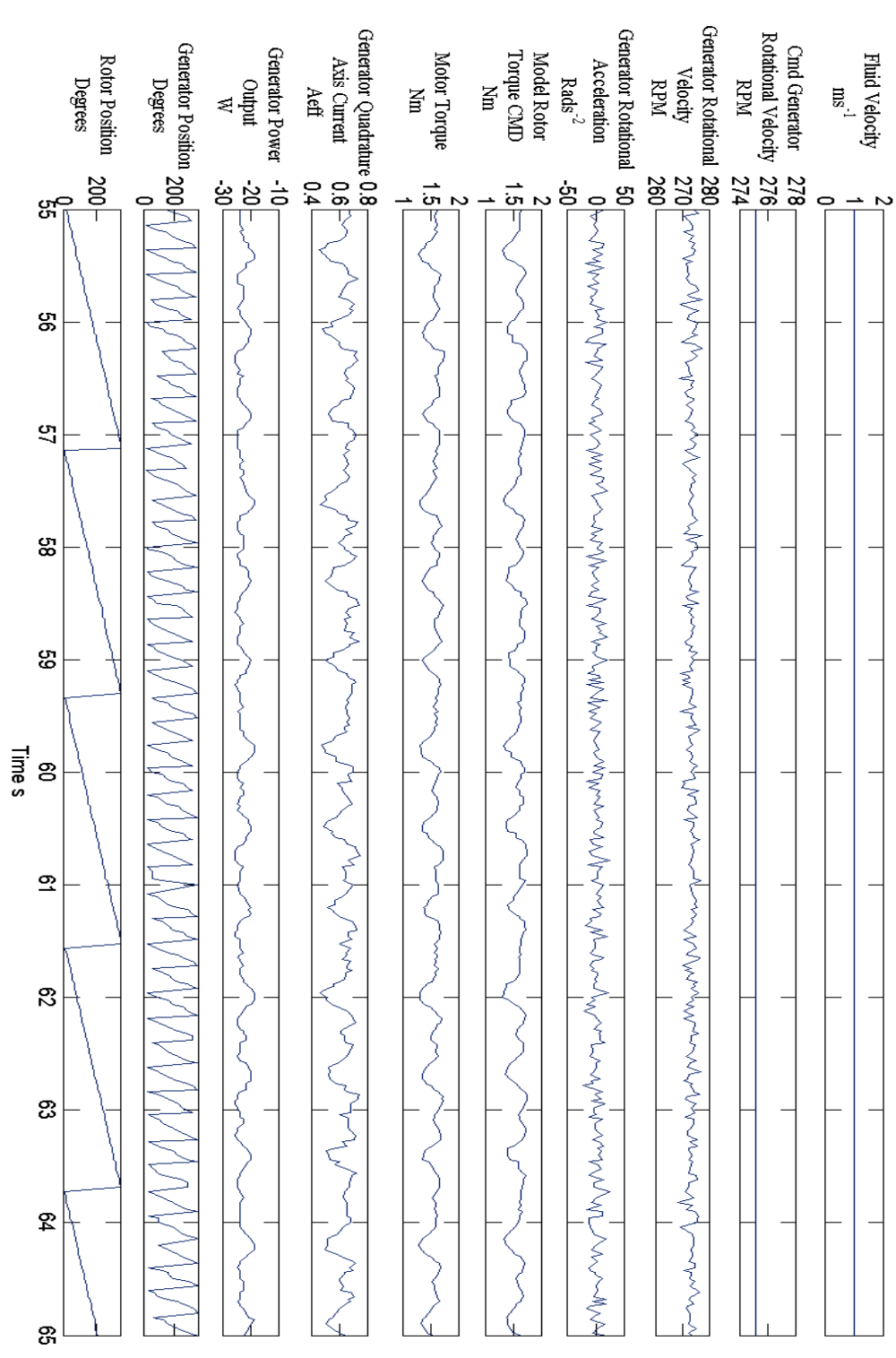

Figure 8.6: Results from the real-time drive train simulations, the case shown is the optimum rotor case with TI = 0%.

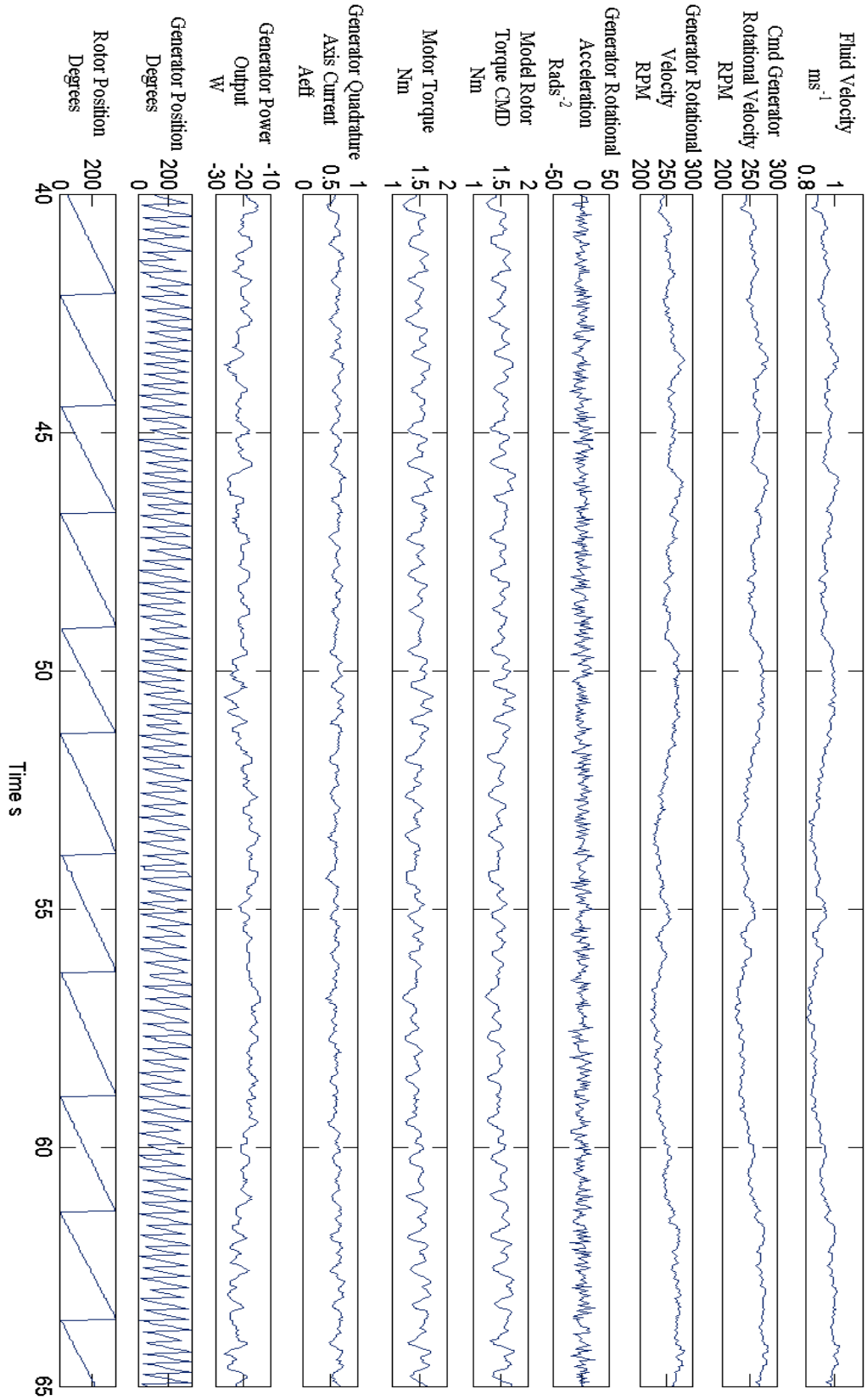

Figure 8.7 : Results from the real-time drive train simulations, the case shown is the optimum rotor case with TI = 10% with optimal TSR control utilised.

Figure 8.7 shows the results of non-steady state simulations with the inclusion of the turbulent fluid velocity time series discussed in Section 8.3.1. Accordingly it can be seen that fluid velocity fluctuations are included in the simulations and as a result of the optimal TSR control scheme adopted rotational velocity fluctuations of the turbine can also be seen. Furthermore due to the change in fluid velocity additional fluctuations can be seen in the torsional input of the motor simulating the high speed shaft output from the 'virtual gearbox'. These additional fluctuations are also evident in traces for power output and quadrature axis current measured via the generator PMSM control system.

To confirm the correct operation of the turbine rotor model utilising the generator position and velocity measurement feedback, the spectrums input via the amplitude surfaces utilised for the model calculation were compared with the spectrums observed for the motor torque command value and the achieved motor input torque values. In order to make the comparison the data used related to the steady state simulations allowing the surface spectrum to be calculated simply by indexing the input amplitude surface at the fixed tip-speed ratio value for the simulations.

Figure 8.8 and Figure 8.9 show the model amplitude parameters during steady state simulations and observed at the various points in the simulations. Figure 8.8 and Figure 8.9 show the structure of the torque spectrums calculated and observed at differing points in the turbine model. The top plot in both figures shows the model surface values, the second plot then shows the torque command spectrum output via the rotor model in real-time. The plot at the bottom of both figures shows the motor input to the test rig and as required closely matches the command values shown in the plots above.

As can be seen in both Figure 8.8 and Figure 8.9 the simulation methodology allowed adequate simulations of the outlined harmonic content of the rotor torque input, this can be seen in the similarity between the spectrums shown in both Figure 8.8 and Figure 8.9.

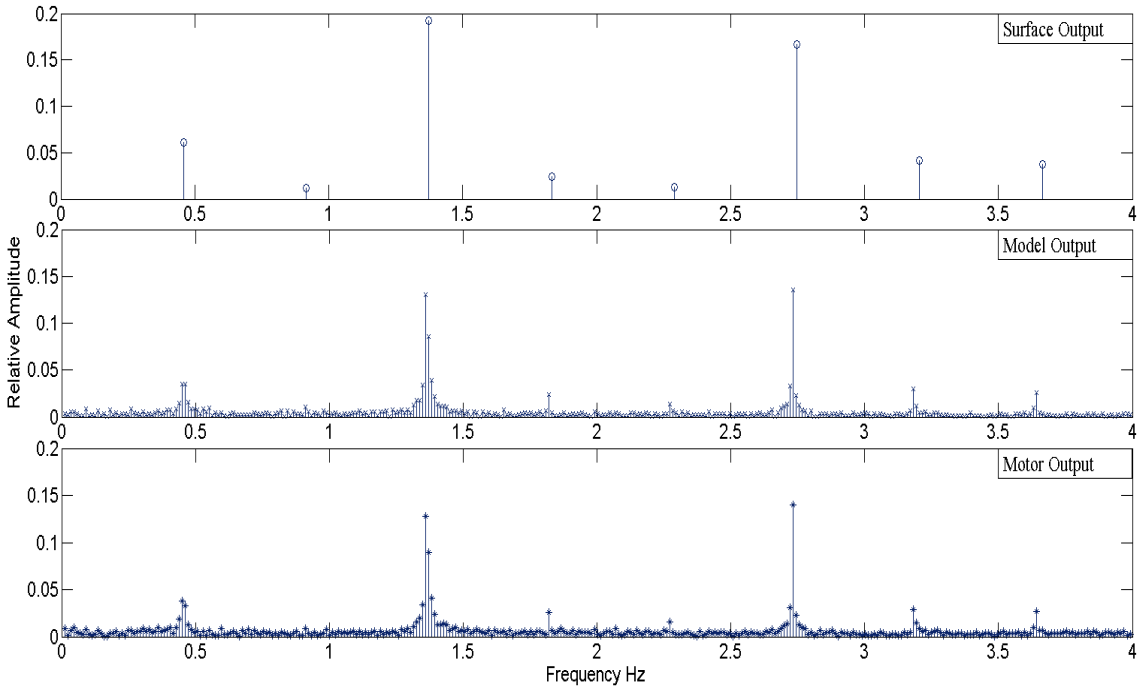

Figure 8.8: Model amplitude parameters input for the optimum rotor setting.

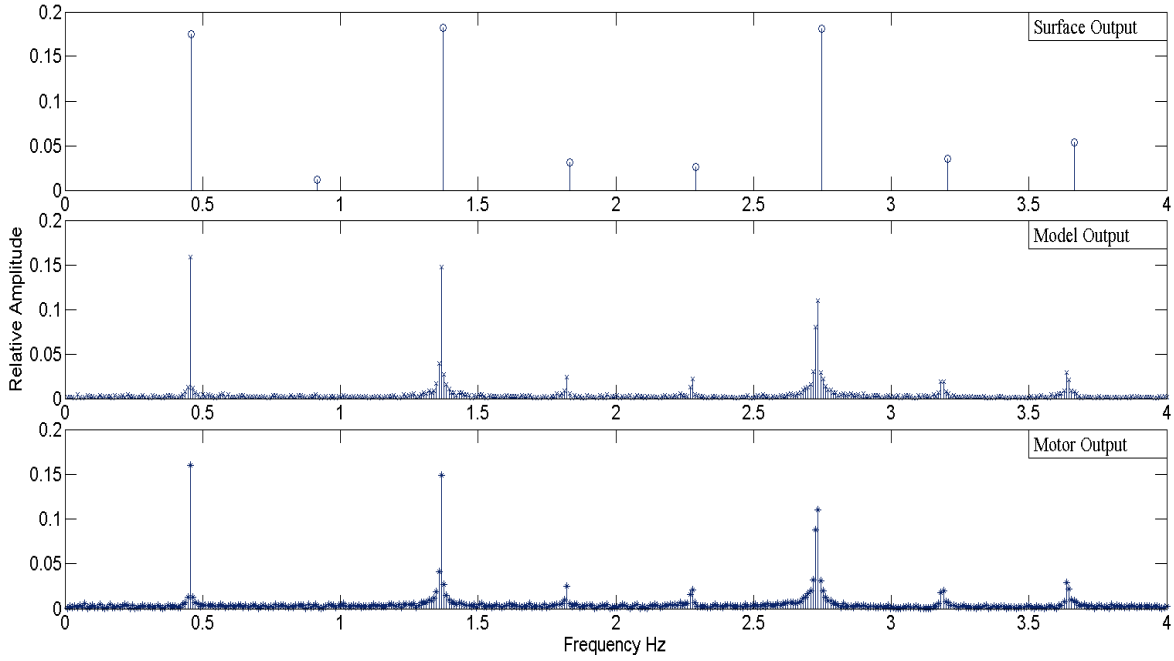

Figure 8.9: Model amplitude parameters input for the offset +6° rotor setting.

8.4 CM algorithm application

8.4.1 STFT imbalance criterion calculation

The rotor imbalance measurement algorithms utilised in Chapter 6 as applied to the measurements undertaken during flume testing were also applied to the drive train simulation datasets generated. This was done to gauge the effectiveness of the rotor imbalance algorithm for fault detection and diagnosis under differing turbine control scenarios. In this section the results of the STFT based rotor imbalance measurement algorithm are presented. Figure 8.10 to Figure 8.12 show the spectrums extracted from the quadrature axis time series developed for each the fault cases and control types.

The four figures labelled as Figure 8.10 show the spectrums relating to the steady state simulations undertaken with fixed fluid velocity. Figure 8.11 and Figure 8.12 then show the four spectrums developed from the quadrature axis current measurement for the optimum lambda control datasets and the fixed speed control datasets, respectively. It can be seen that the spectrums developed for the steady state simulations clearly show the harmonics inputted via the turbine rotor model outlined in Section 7.4. This can be seen by the higher amplitudes (brighter areas on the surface) observed at the rotational frequency of the turbine and its harmonics.

Figure 8.10 1 to 4 the effect of the fixed speed turbine control along with the fluid velocity time series of turbulence intensity of 10% can be seen. As the rotational velocity of the turbine is not changing the harmonics are fixed similar to that of steady state case. It can be observed however that the prominence of such harmonic amplitudes in fixed speed control case are reduced relative to the steady state case. Furthermore in both sets of Figure 8.11 and Figure 8.12 it can be seen that significant harmonic energy at very low frequencies can be observed. This effect was considered to be due to the fluctuation of the fluid velocity time

series generated for the simulations and was more visible in the case of the fixed speed turbine velocity control case (Figure 8.12)

Figure 8.13a to Figure 8.13c show histograms of the generated monitoring criteria C_l for each of the simulation cases. It can be seen that the effect of the inclusion of turbulence intensity on the simulations was to reduce the ability of the monitoring criteria C_l to discriminate between the differing fault cases, shown by the increasing level of overlap in the values for C_l observed for the given cases. However the ability of the monitoring criteria C_l to detect the offset $+6^o$ case was consistent throughout the simulated datasets.

Appendix A Tables A.41 to A.48 show the results of the detection and diagnostic applications of the NBC process. The STFT based C_l measure resulted in both false alarm generation and false negative results for the fault detection classification but gave reasonable results when applied to the diagnostic classification. Although reasonable results were found for the diagnostic classifications under optimal λ control the two blade offset case was misclassified as the no fault case. Furthermore under the fixed speed control case the non-fault condition was misclassified as the two blade offset case.

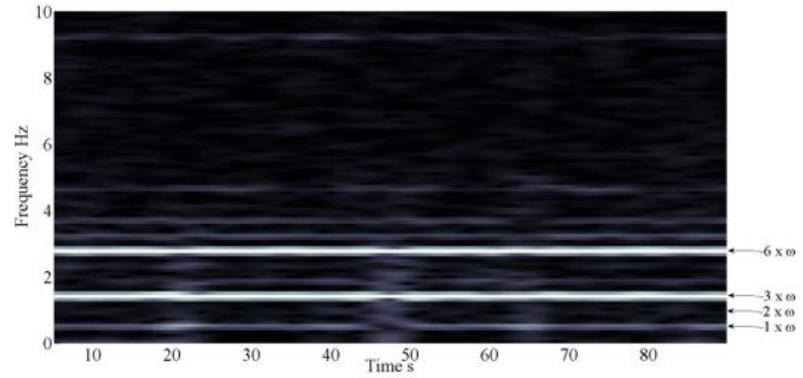

a) Optimum

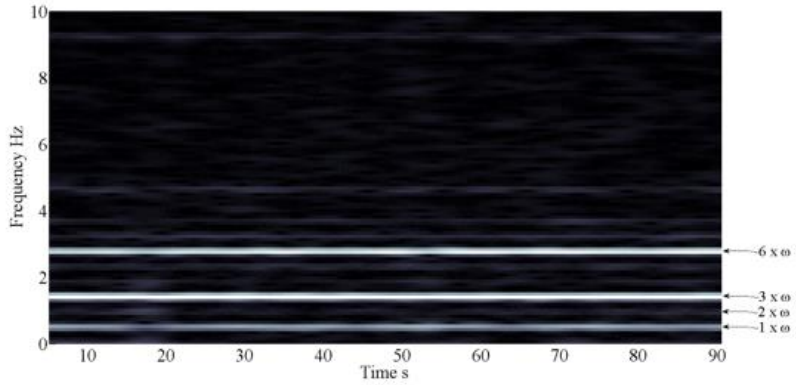

b) Offset +3°

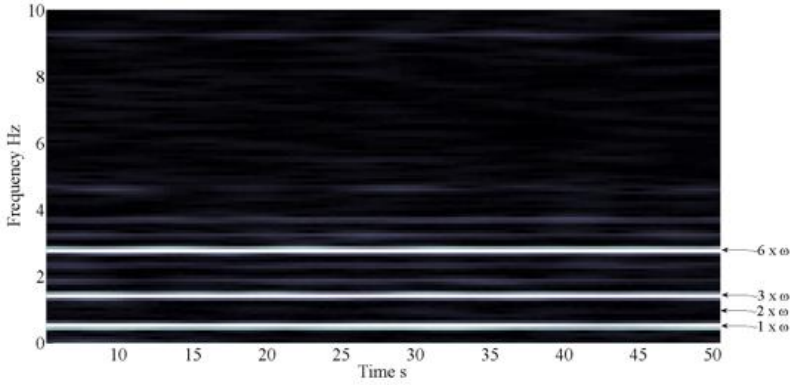

c) Offset +6°

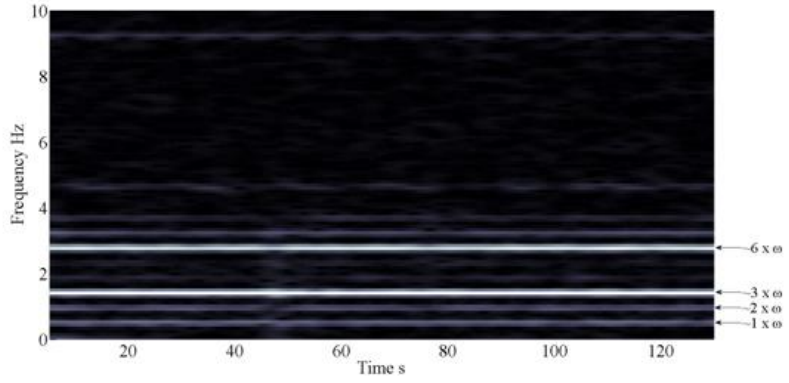

d) Offset Two Blades

Figure 8.10: Spectrums developed via STFT for steady state simulations for each of the differing rotor conditions.

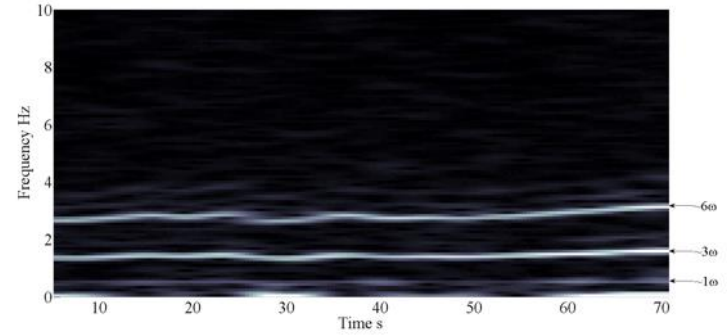

a) Optimum

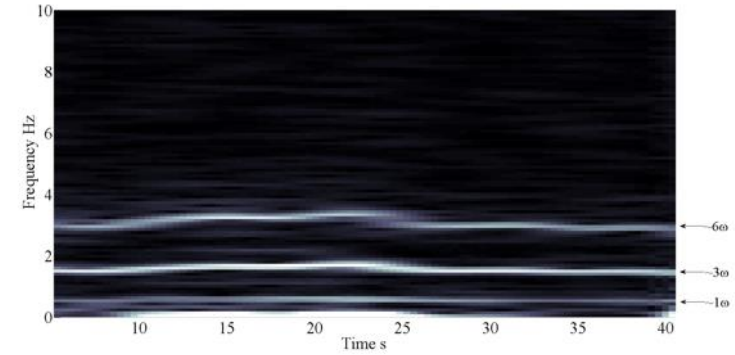

b) Offset +3°

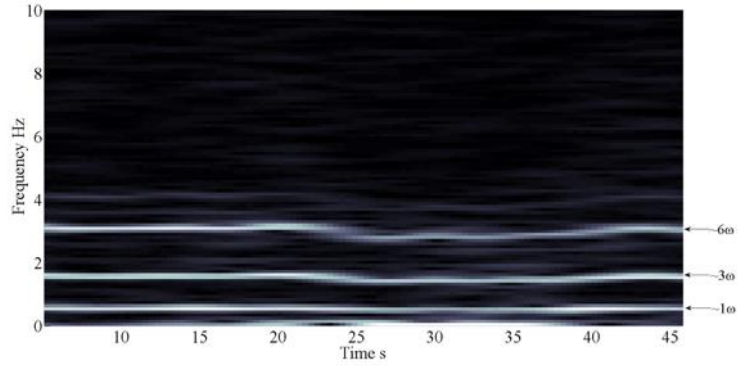

c) Offset +6°

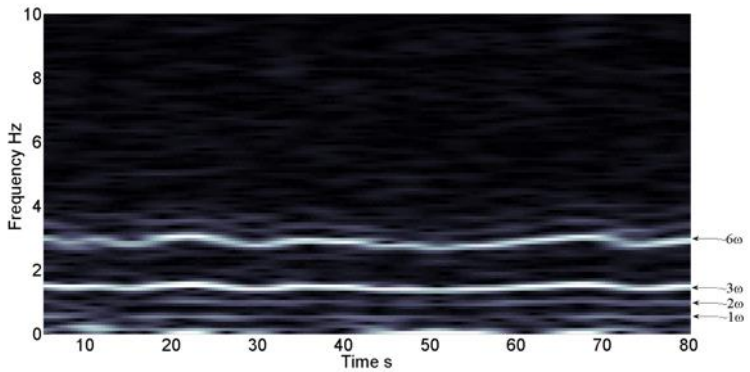

d) Offset Two Blades

Figure 8.11: Spectrums developed via STFT for λ control simulations for each of the differing rotor conditions.

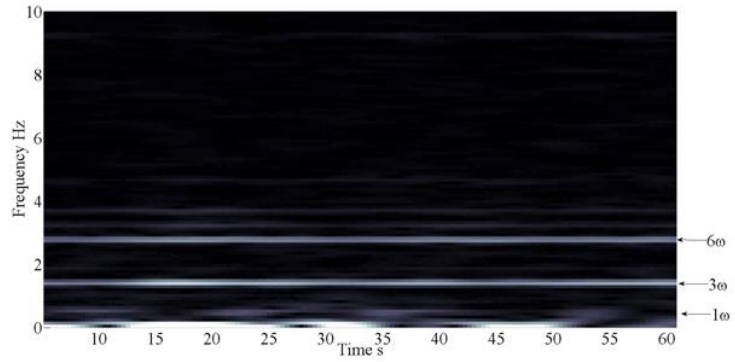

a) Optimum

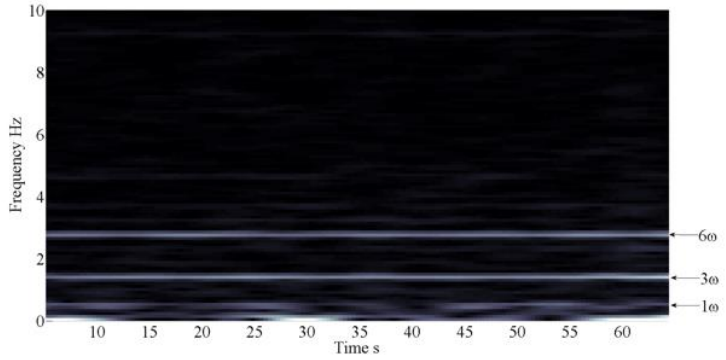

b) Offset +3°

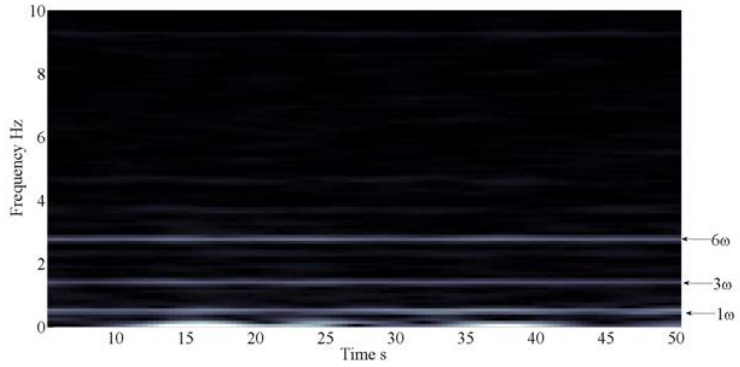

c) Offset +6°

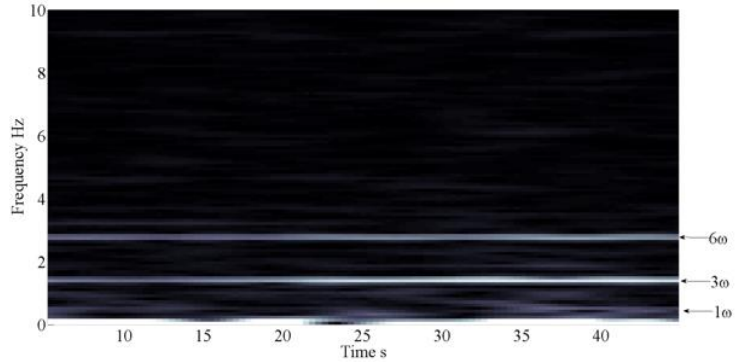

d) Offset Two Blades

Figure 8.12: Spectrums developed via STFT for fixed speed control simulations for each of the differing rotor conditions.

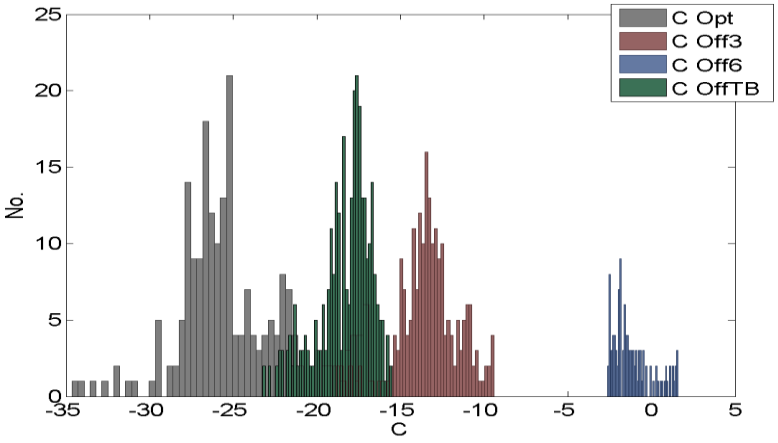

a: Steady State

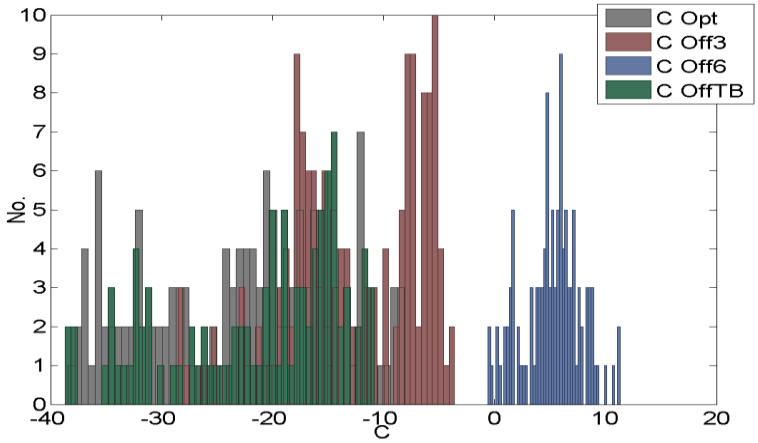

b: Lambda Control

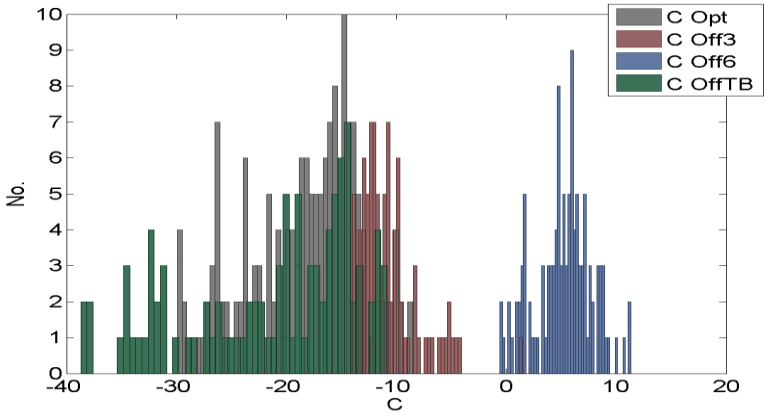

c: Fixed Speed Control

Figure 8.13: Histograms of the values of the monitoring criterion cl calculated via the STFT for differing turbine control scenarios.

8.4.2 HHT imbalance criterion calculation.

In the final element of this work the rotor imbalance measurement utilising the Hilbert-Huang transform was also applied to the simulated turbine datasets. This was done to consider the effectiveness of the HHT based algorithm for rotor fault detection and diagnosis. Figure 8.14 to Figure 8.16 show the developed spectrums of the measured quadrature axis current for the differing simulation settings. Figure 8.14 show the results for the steady state simulations whereas Figure 8.15 and Figure 8.16 show the spectrums developed for the optimal TSR control and fixed speed control datasets, respectively. It can be immediately viewed that the Hilbert spectrums developed show very good time frequency resolution. However it can be seen that the Hilbert spectrum developed show far more chaotic spectrum structures than the STFT counter parts. Within the spectrums the prominent harmonics of interest, namely those at harmonic frequencies of the turbine rotational velocity, can be detected to some degree by eye. However, the prominence of the 6^{th} harmonic of the rotational frequency of the turbine is greatly reduced and the clarity with which the amplitudes of interest can be seen if generally reduced due to the chaotic nature of the spectrum structures.

Figure 8.17 show the calculated monitoring criterion C_I calculated via the amplitudes extract form the Hilbert spectrums as described in chapters 4 and 8. The histograms show a high degree of overlap between the observed values of the monitoring criterion C_I for differing rotor conditions. The degree of overlap of the monitoring criterions C_I is exacerbated by the inclusion of the turbulence intensity in the simulations. This can be seen as Figure 8.17b and a shows a greater degree of overlap that Figure 8.17a.

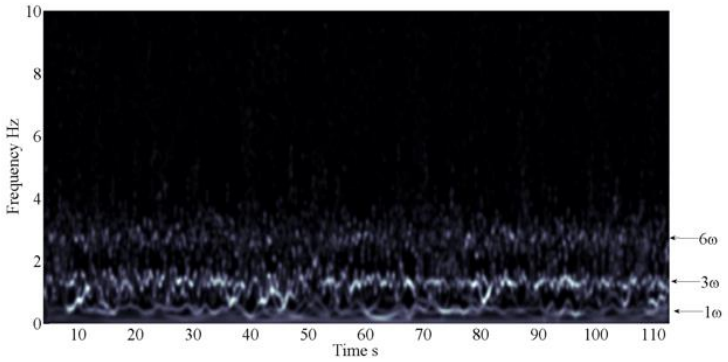

a) Optimum

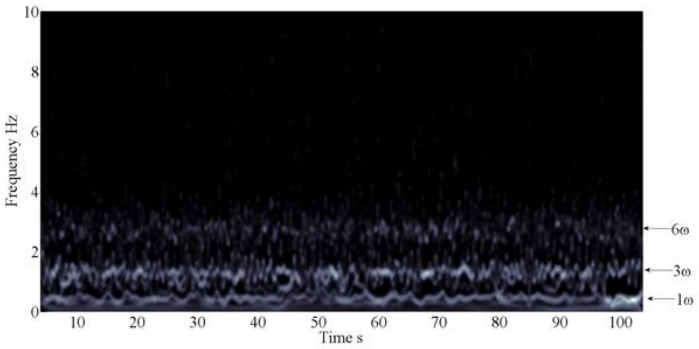

b) Offset +3°

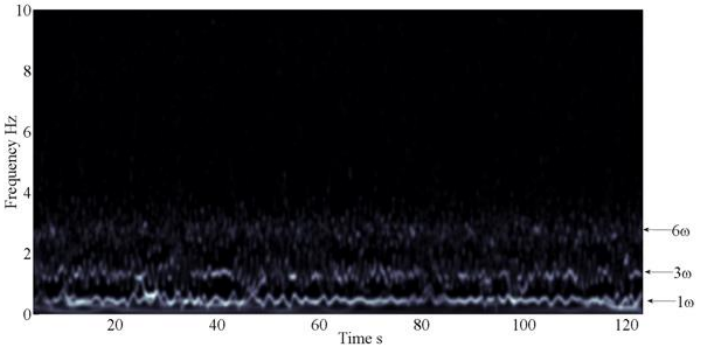

c) Offset +6°

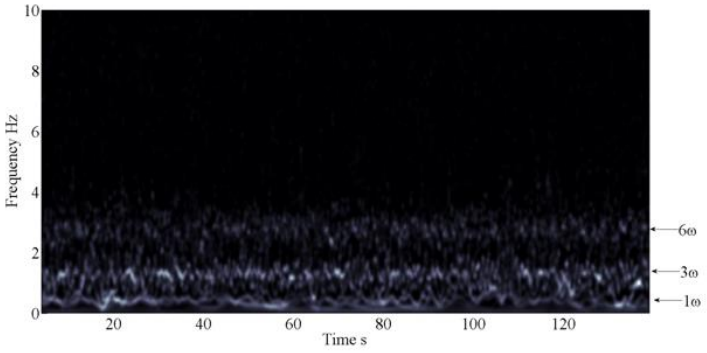

d) Offset Two Blades

Figure 8.14: Hilbert spectrums calculated for each of the rotor fault conditions and steady-state simulations.

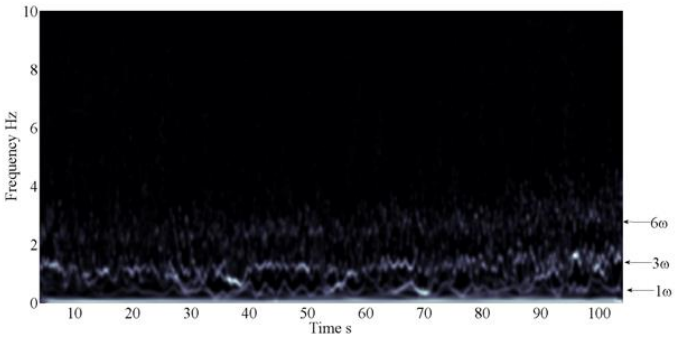

a) Optimum

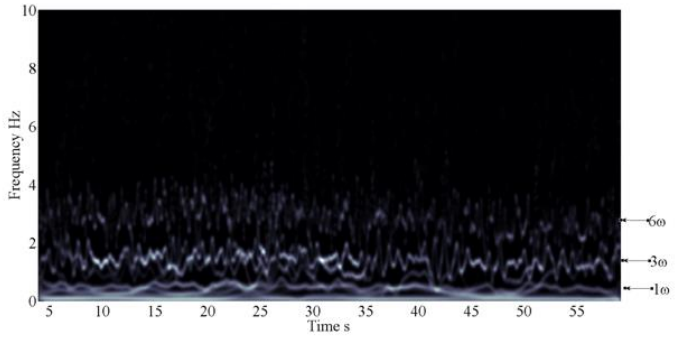

b) Offset +3°

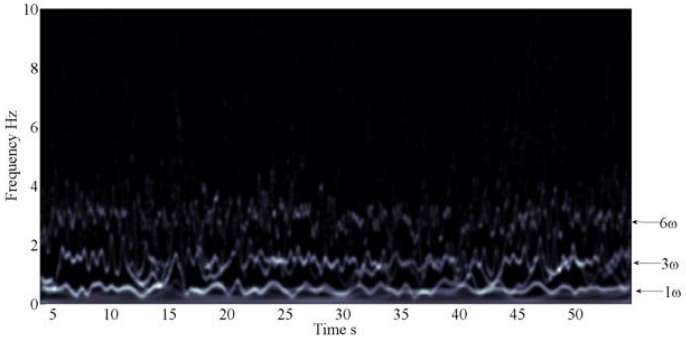

c) Offset +6°

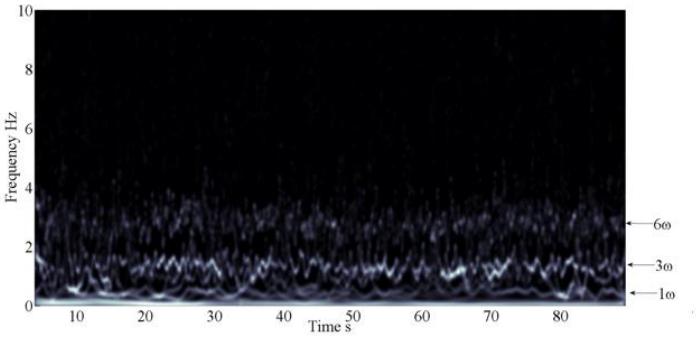

d) Offset Two Blades

Figure 8.15: Hilbert spectrums calculated for each of the rotor fault conditions and optimal λ turbine control scenarios.

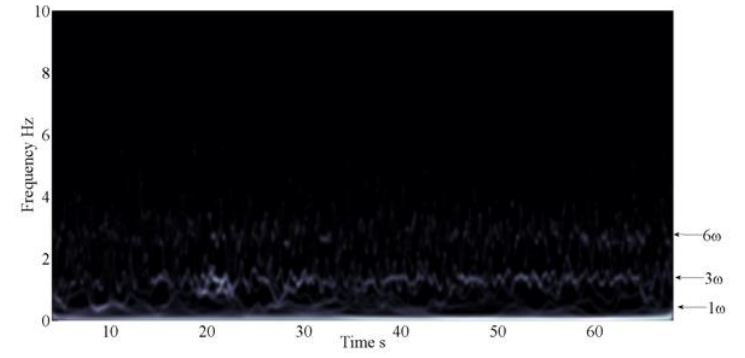

a) Optimum

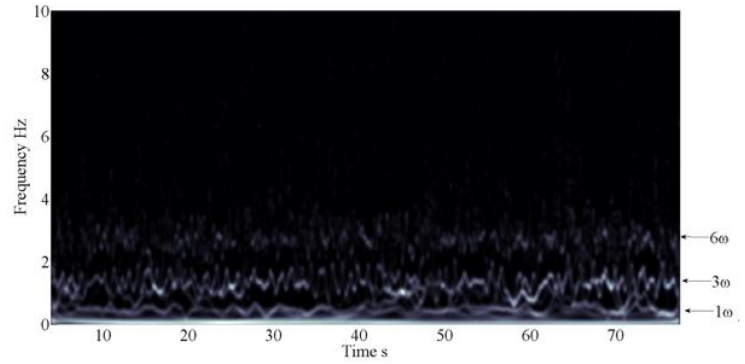

b) Offset +3°

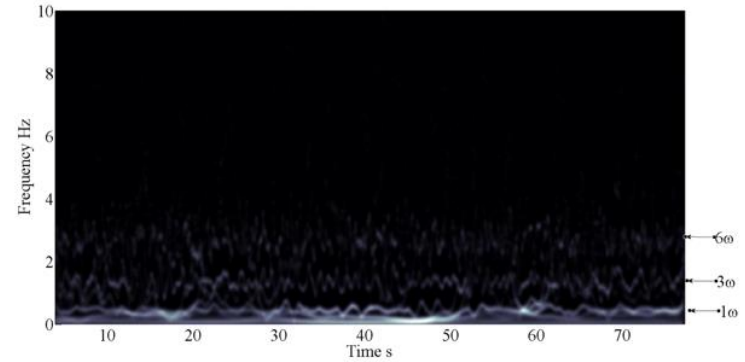

c) Offset +6°

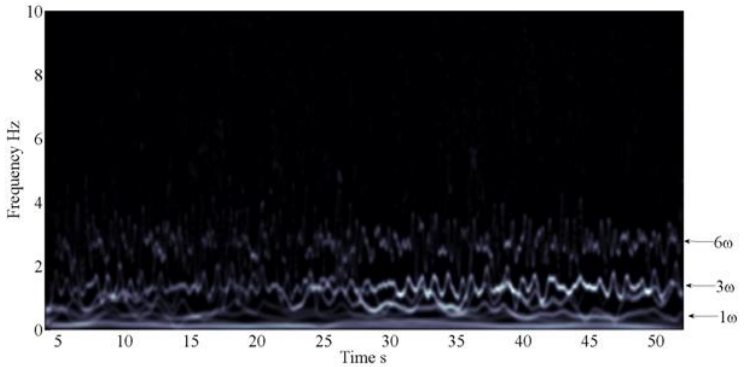

d) Offset Two Blades

Figure 8.16: Hilbert spectrums calculated for each of the rotor fault conditions and fixed speed turbine control scenarios.

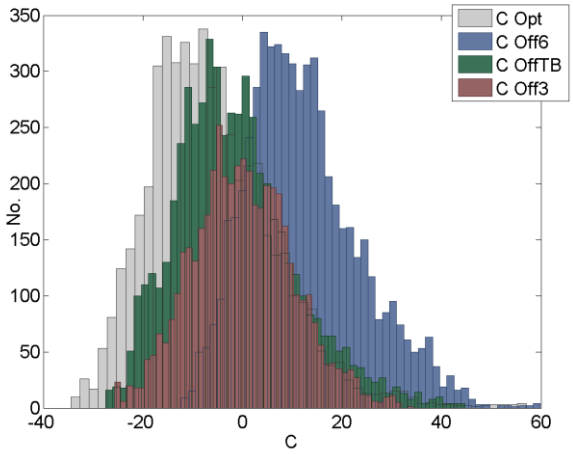

a: Steady State

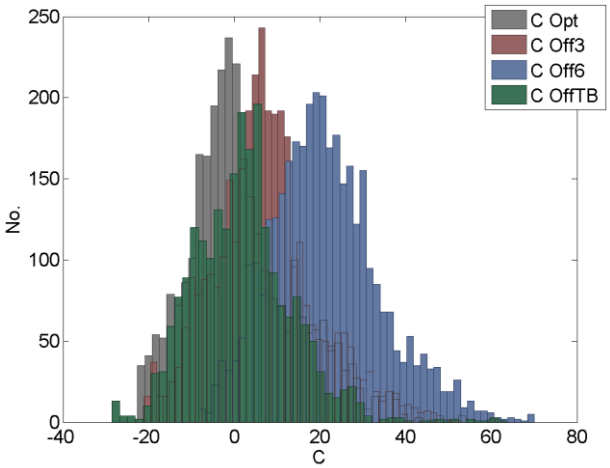

b: Lambda Control

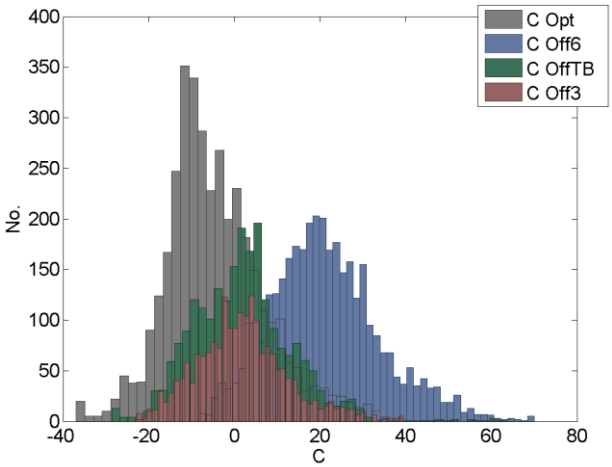

c: Fixed Speed Control

Figure 8.17: Histograms of the values of the monitoring criterion cl calculated via the HHT for differing turbine control scenarios.

The HHT based C_I measure resulted false alarm generation under the fixed speed control case but gave correct detection classification under optimal λ control. Numerous misclassification of the fault type or severity were found for both the optimal λ control and the fixed speed control cases.

8.4.3 Transient Monitoring Surface generation – steady state conditions

Figure 8.18 and Figure 8.19 show the results of the surface generation process for the steady-state simulations. In these cases the fluid velocity for the simulations was held constant (1 ms^{-1}) and the simulated turbine was set to a fixed rotational velocity to achieve a fixed λ value for the simulation. Simulations were undertaken at three differing λ values to create a portion of the monitoring surface. Specifically the values of λ used for the simulations were of 3.0, 3.6 and 4.2.

The surface construction followed the process outlined in Section 3.6.8. The surface points were created for each test relating to a fixed λ value by applying the TSA process to the raw simulation data; the spectrum of the TSA process output was calculated and added to the surface at the relevant harmonic numbers and λ value. Figure 8.18 shows the effect of the TSA process on the generator quadrature-axis current a) displacement series and b) spectrum. In both parts of this figure the effect of the inclusion of data relating to a greater number of rotations in the TSA process is highlighted. It can be seen in Figure 8.18a that the TSA process smooth's the data with increasing severity with the inclusion of a greater number of data sets. This can also be seen in the spectrums shown in Figure 8.18b whereby the energy in higher harmonics is reduced with an increase in the number of rotations included in the averaging process.

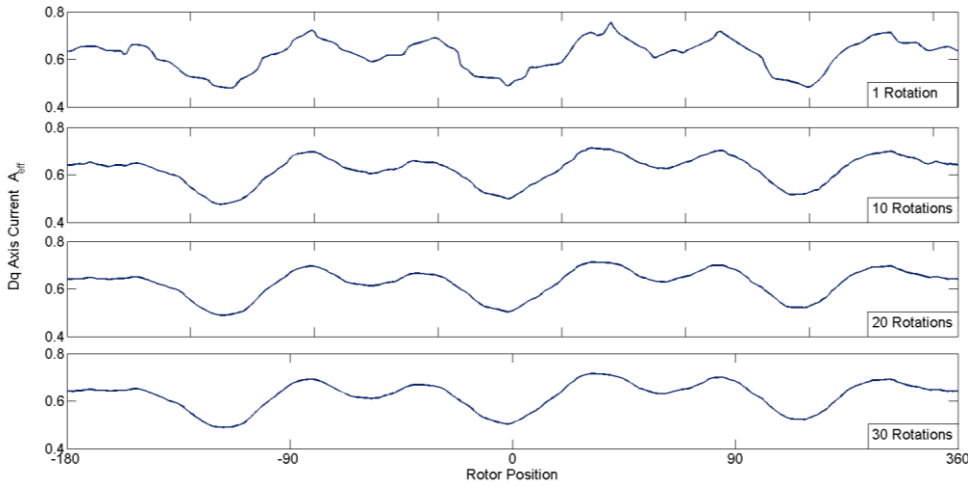

a)

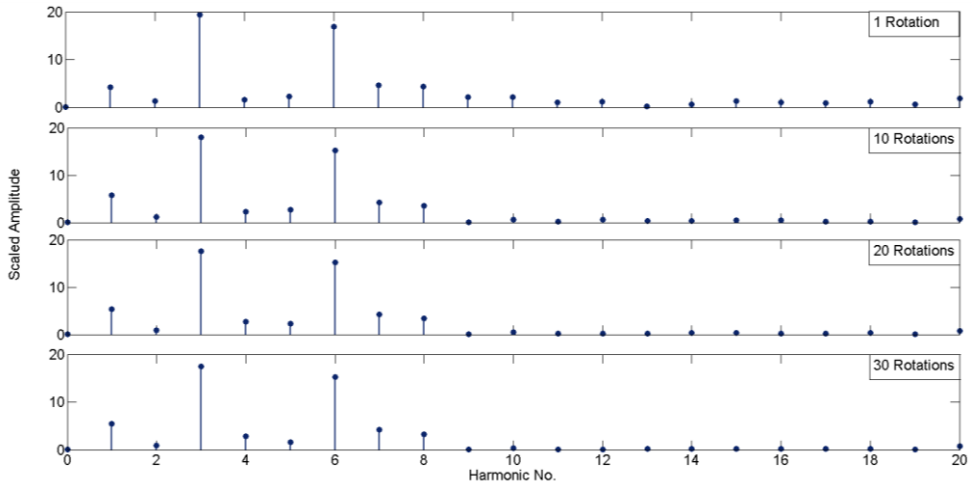

b)

Figure 8.18: The effect of the TSA process on the observed generator quadrature axis current A) in the time domain and B) in the frequency domain.

Figure 8.19 shows the surface generation process for the 3 values of λ simulated. Figure 8.19 a shows the results of the TSA process for each of tip-speed ratio value tested. The plots show the mean value observed for the full data set and the resampled data from each of the rotations within the dataset. The figure highlights the suitability of TSA mean as representing the underlying process. Figure 8.19b shows the resultant spectrums observed for the TSA process means for each λ value simulated. Finally, Figure 8.19c shows the constructed amplitude surface. This surface can then be considered to be the 'normal' operating condition output surface for the turbine simulated.

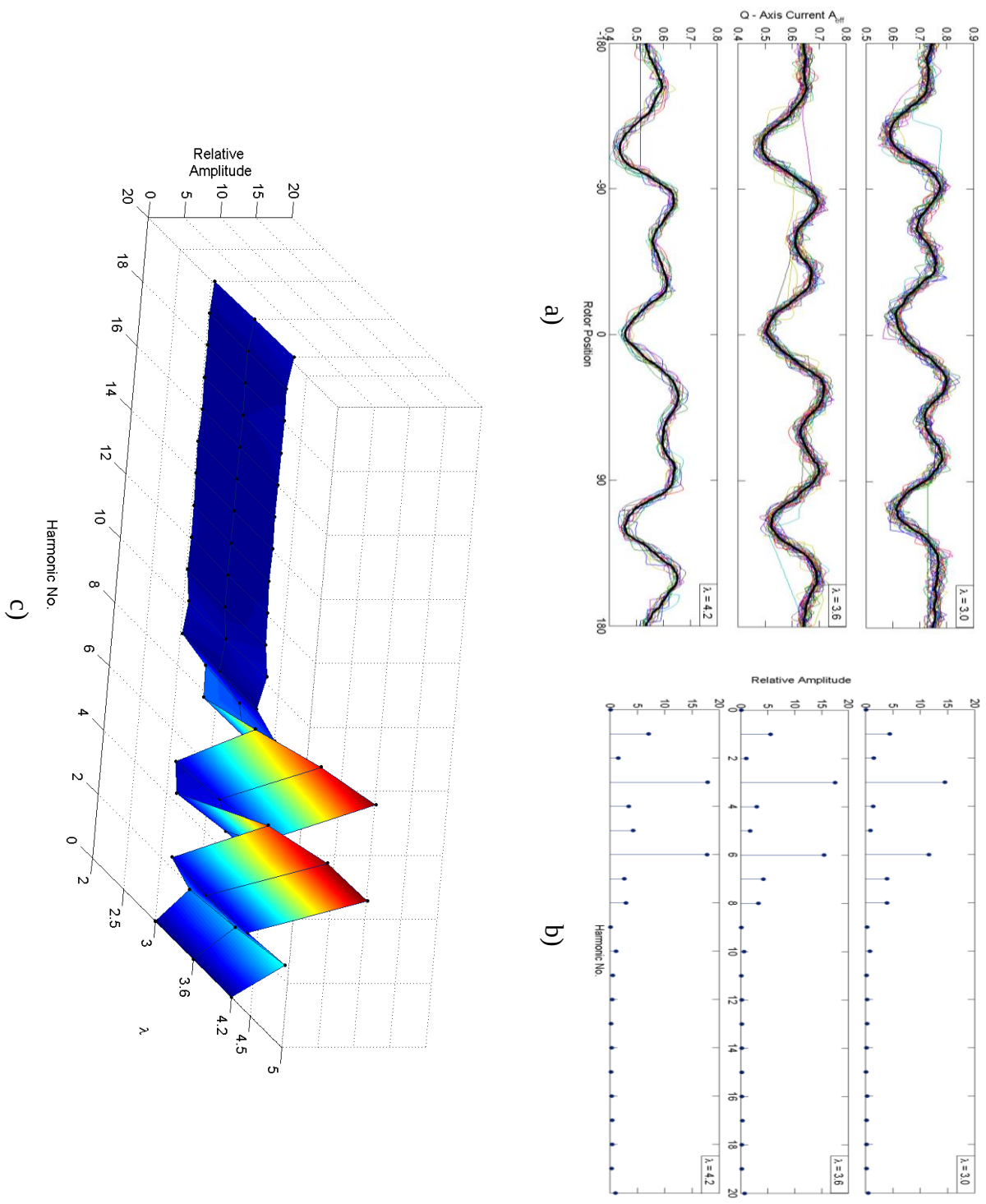

Figure 8.19: Output monitoring surface generation process of the Optimum fixed rotational and fluid velocity simulations. A) Shows the TSA process, B) shows the amplitude extraction process and C) shows the output portion of the monitoring surface for normal operational conditions

8.4.4 Transient Monitoring Surface generation – Set Point λ Control.

This section presents the results of the TMS generation for simulations undertaken utilising set-point λ control. The results here relate to a simulated fluid velocity time series with a turbulence intensity of 10%. The process of generating the TMS follows the same procedure outlined in Section 3.6.8. However in this case the mean torque or generator current component used to normalise the data was not fixed and fluctuated due to the turbulent fluid velocity time series utilised within the simulations. To develop a method for effectively normalising the quadrature-axis current data to allow for the comparison of data recorded under differing fluid velocities and turbine rotational velocities the structure of the turbine rotor model was considered. Generally the structure of the rotor torque model utilised to construct the simulations used the following general form:

$$\tau(t) = \bar{\tau} + \bar{\tau} \cdot A \qquad (8.1)$$

Where *A*, in the case of the turbine rotor model, was a Fourier series representing the fluctuating component of the turbine drive shaft torque. In the current model structure the fluctuating components are related to turbine rotor operation and more specifically to the effect of turbine stanchion interactions and rotor imbalance. Accordingly the fluctuating components captured in *A* are explicitly a function of the turbine rotational displacement. They are also implicitly a function of time due to the rotational velocity of the turbine and the effect of the varying fluid velocity and the relationship between the two quantities. This has been captured by the scaling of *A* by the mean torque value, $\bar{\tau}$. In the generation and use of the model until this point, the data sets considered generally adhered to the condition that, $\bar{\tau} = constant$. This was a simplifying condition which resulted from consideration of steady – state turbine operation. However, in the current non steady-

state operation $\overline{\tau} = f(t)$. Furthermore as the generator output is being considered, as discussed in chapter 3, the turbine drive shaft torque is estimated using the generator quadrature axis current i_q. Considering that the generator quadrature current is being utilised and that due to the non-steady-state turbine operation the mean current will be a function of time, equation 8.1 becomes:

$$i_q(t) = \bar{\imath}_q(t) + \bar{\imath}_q(t) \cdot A. \tag{8.2}$$

It then readily follows that the quadrature axis current observed can be normalised in the following manner to give an estimate of A, which as proposed relates specifically to turbine operational effects:

$$A = \frac{i_q(t) - \bar{\imath}_q(t)}{\bar{\imath}_q(t)} \tag{8.3}$$

This normalisation method allows for the development of the monitoring surface which relates to relative fluctuation amplitudes that are resultant from the turbine operational characteristics of interest, such as any rotor imbalance and the stantion shadowing effect. However, in utilising such a method, it should be considered, that the quantity $\bar{\imath}_q(t)$ cannot be measured directly and therefore will need to be estimated by some other means.

To estimate $\bar{\imath}_q(t)$ as it was considered that the mean component of the torque developed by the turbine rotor is proportional to the square of the fluid velocity impacting upon the turbine rotor as presented in Equation (1.12). This gives:

$$\bar{\tau}(t) \propto U(t)^2 \tag{8.4}$$

By the proportionality developed in section 3.4.2 the generator quadrature axis current will also be proportional to the square of the upstream fluid velocity.

$$\bar{\iota_q}(t) \propto U(t)^2 \tag{8.5}$$

Furthermore, under set point λ control the fluid velocity is proportional to the turbine rotational velocity as can be seen in Equation (1.13). Therefore the proportionality in equation (8.5) can be expressed as,

$$\bar{\iota_q}(t) \propto U(t)^2 \propto \omega(t)^2 \tag{8.6}$$

It follows from the above considerations that the rotational velocity may be useful in normalising the observed generator q-axis current to extract *A.* This will also further support the building of a surface which is could be more robust under non-steady state conditions. Lastly, it was considered that the fluctuation in the two quantities are of orders of magnitude apart. Due to process of calculating *A* this would lead to incorrect distortions of the observed signal. To find the constant of proportionality the ratio of the mean values of the observed quantities was used,

$$\frac{mean(\omega(t)^2)}{mean\left(\bar{\iota_q}(t)\right)} = c \tag{8.7}$$

Finally the normalisation is under taken by:

$$A = \frac{i_q(t) - C \cdot \omega(t)^2}{C \cdot \omega(t)^2} \tag{8.8}$$

Where

$$\bar{\iota_q}(t) \approx C \cdot \omega(t)^2 \tag{8.9}$$

Figure 8.20 shows the effect of normalising the generator q-axis current data on the TSA process used to construct the output monitoring surfaces. The figure shows the deviation of the recorded data from the TSA characteristic with increasing numbers of rotations included in the TSA process. The figure shows that normalising the generator output data as described above results in better convergence to an underlying TSA characteristic. This was found for each of the λ values simulated. It can be seen that minimal convergence to an underlying TSA process was observed for the non-normalised simulation data. Furthermore the figure also shows greater deviation from the calculated TSA characteristics for the higher tip-speed ratio values.

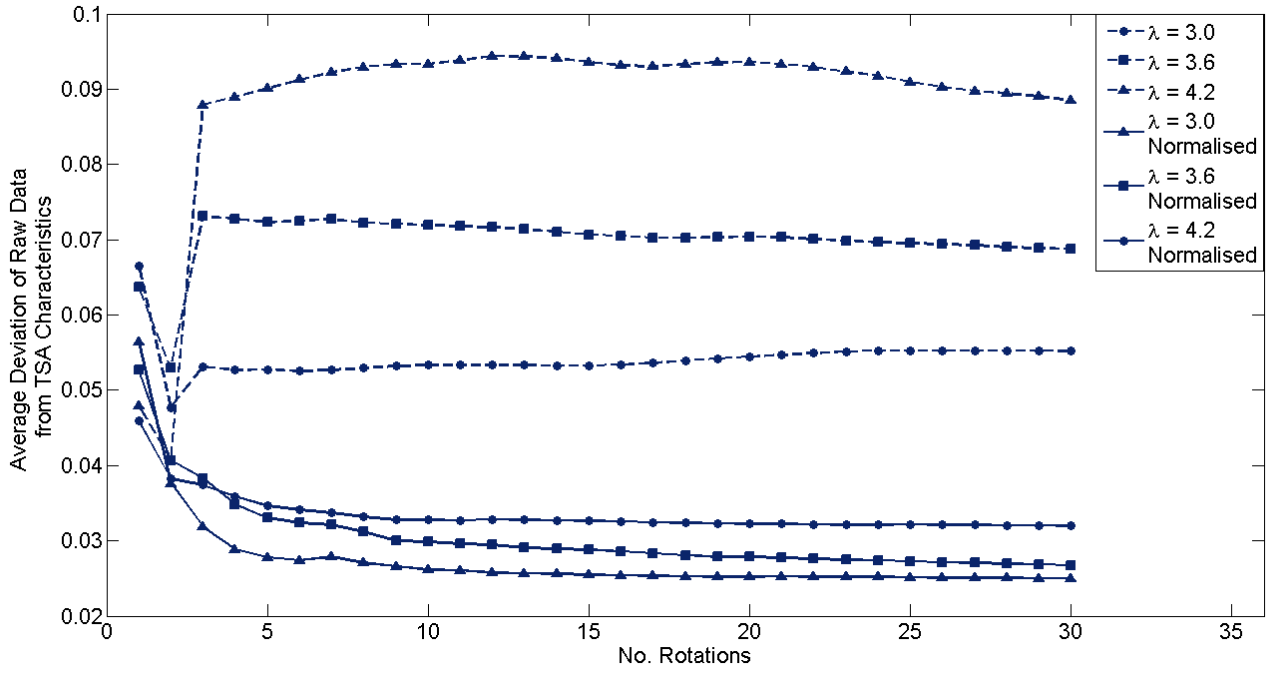

Figure 8.20: Deviation of the generator quadrature axis datasets form the TSA means characteristics for normalised and non- normalised datasets and various TSR values.

Figure 8.21 shows the surface generation process for the 3 values of λ simulated. Figure 8.21a shows the results of the TSA process for each of tip-speed ratio value tested. The plots show the mean value observed for the full data set and the resampled data from each of the rotations within the dataset. The figure highlights the suitability of TSA mean as representing the underlying

process. Figure 8.21b shows the resultant spectrums observed for the TSA process means for each λ value simulated. Finally, Figure 8.21c shows the constructed amplitude surface. This surface can then be considered to be the 'normal' operating condition output surface for the turbine simulated.

8.4.5 TMS generation under fault conditions – optimal λ control.

In order to use the developed TMS as a fault detection or diagnosis method the surface development method described previously was utilised on the rotor imbalance simulation cases. The rotor imbalance simulations were undertaken for the three fault cases for a single set-point tip speed ratio value of 3.6 (peak power for the simulated turbine). The surfaces developed for each of the fault conditions were then compared with the characteristic surface developed for the normal operating case, Figure 8.21c.

In order to give a numerical measurement of the discrepancies between the characteristic surfaces developed for the differing turbine conditions the SOSE error measurement presented in Section 3.6.8. Figure 8.22 shows the development of the surface error as more rotations are included in the surface characterisation. To compare the standard error observed during comparison of the developed normal operating surface with new data relating to normal operating conditions a second simulation relating to normal operating conditions was under taken. This data set was used to develop a subsequent surface to compare the sum of surface error for the optimum conditions with the values observed for the fault conditions.

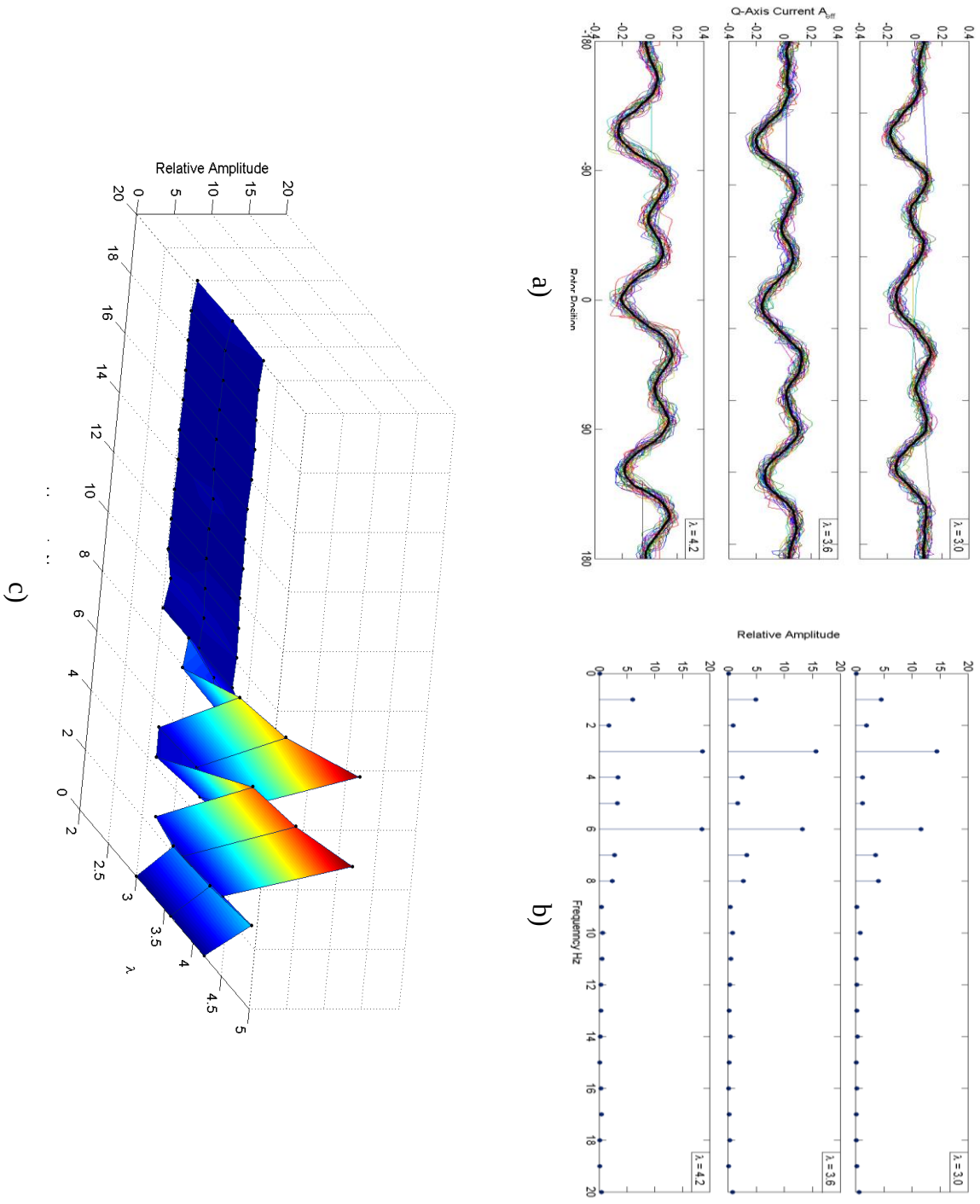

Figure 8.21: Output monitoring surface generation process of the Optimum for optimal TSR turbine control with fluid velocity of TI = 10%. A) Shows the TSA process, B) shows the amplitude extraction process and C) shows the output portion of the monitoring surface for normal operational conditions.

Figure 8.22 shows that initially, before approximately 5 rotations are included in the surface generation process, the sum of surface error measurement is relatively large for all cases. As more rotations are included in the surface generation process the sum of surface error measurement reduces in all cases. This indicates that the turbine is more accurately characterised by increasing amounts of data. As more data is included in the surface construction the figure shows that sum of surface error starts to converge to a given value for each fault condition. The two blade offset condition sum of surface error measurement is the lowest of the fault conditions, this followed by the 3° offset case with the largest sum of surface error observed for the 6° offset case.

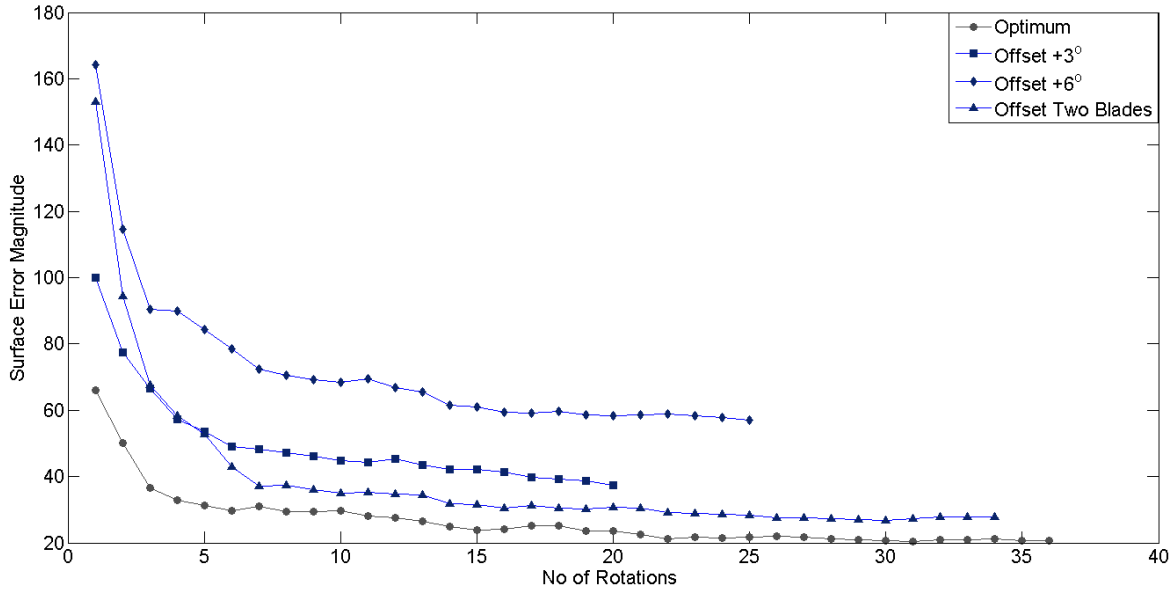

Figure 8.22: Development of the Sum of Surface error value observed for differing rotor conditions plotted against the number of rotations included in the surface generation process.

8.4.6 TMS generation – fixed speed control

Here the process of TMS training as applied to the fixed speed control datasets is presented. The dataset utilised here are from three differing tests undertaken with differing set-point rotational velocity settings and with a fluid velocity of 1 ms^{-1} with a turbulence intensity of 10 %. The rotational velocities utilised were 229 RPM, 275 RPM and 352 RPM

leading to datasets captured with average λ values of 3.0, 3.6 and 4.2, respectively. As with the set point λ control datasets relating to the 10 % fluid velocity case the process of generating monitoring surfaces for the fixed speed control data required an approach specific to the control type. Whereas in the set point λ control tests the normalising of the TMS data posed significant challenges the fixed speed control data set posed a challenge regarding the λ indexing of the surface. Specifically as the control specification for these data sets were set point rotational velocities the fluctuating fluid velocity resulted in fluctuating λ values, again by Equation (1.13). This meant that the processing methods used above could not be leveraged for this control case as the data sets did not relate to a single λ value. As such an indexing method had to be developed in order to construct the appropriate output monitoring surface.

To overcome problems associated with the λ indexing a method was developed in which the data collected was categorised into so called, 'λ bins'. To undertake such a categorisation the instantaneous value of λ was calculated for each measured sample in the data sets. The instantaneous λ values were calculated using the Equation (1.13) formula from the measured rotational velocity of the turbine as well as the simulated fluid velocity value for the given sample point. The calculated λ values were then categorised into discrete bins. The bin sizes were given by 2 x Δλ and were centred on the λ values used as the surface index. During the categorisation process λ bins with less than 150 samples associated with them were discarded. For each bin with more than 150 samples associated with it the corresponding turbine position and torque generating current measurements were stored.

The categorisation process led to the each λ bin having samples associated with it from various points in the overall dataset where the calculated λ value fell within the λ bin width. As the turbine rotational velocity was constant due to the set point control the fluid velocity values associated with the measurements in each bin were approximately constant. The data

sets for each λ bin were then compiled to provide composite rotational data sets. The datasets of varying numbers of rotations were then input into the TSA algorithm as above and processed as described.

Figure 8.23 shows the composite samples and the resultant time synchronous average for the data set relating to the set point turbine velocity of 275 RPM. It can be seen that this process was to a degree successful in generating smaller datasets from the overall simulation time series which relate to specific λ values. Furthermore, the data sets were then successfully used to characterise the drive shaft torque fluctuations (via the proportionality with the measured quadrature axis current) used to develop the monitoring output surfaces.

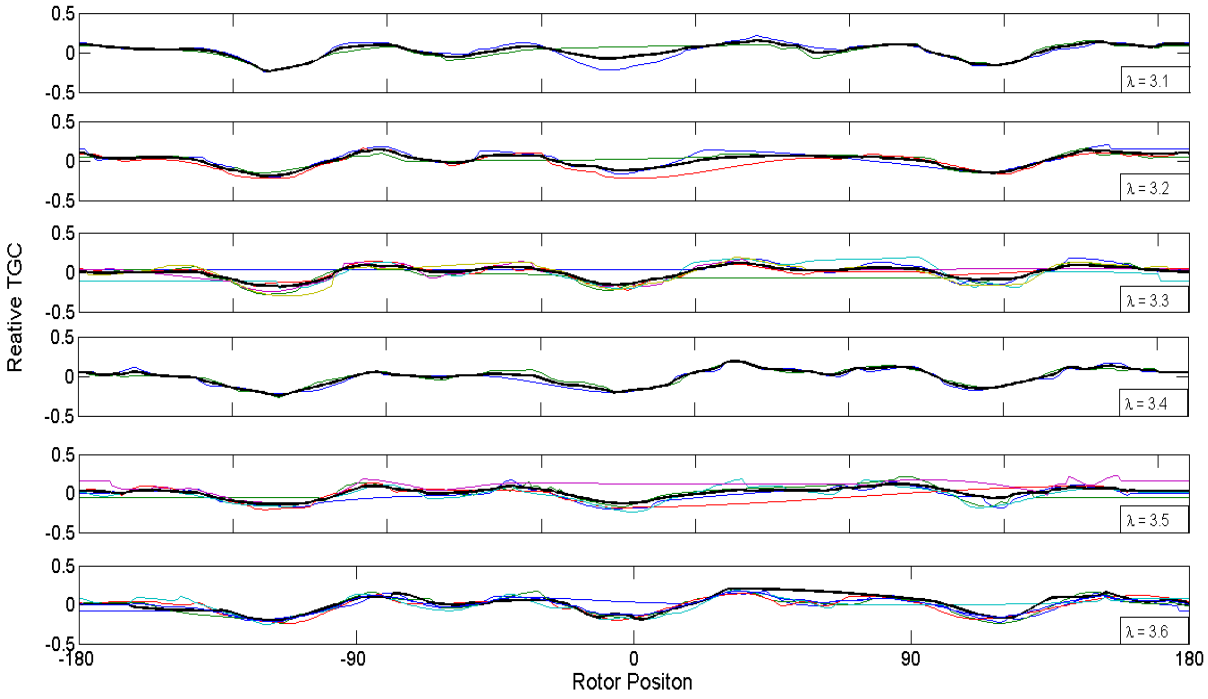

Figure 8.23: Extracted data for differing λ bin values utilised to create TSA characteristics for differing λ values.

It should be noted that the outputted TSA data used to characterise the average turbine behaviour was clearly less representative than the two previous control cases as in some instances only 1 or 2 rotations could be constructed for a given λ bin. As a result the TMS

developed by taking the spectrum of the TSA output data, shown in Figure 8.24, was more erratic in nature the surfaces developed for the previously outlined control scenarios.

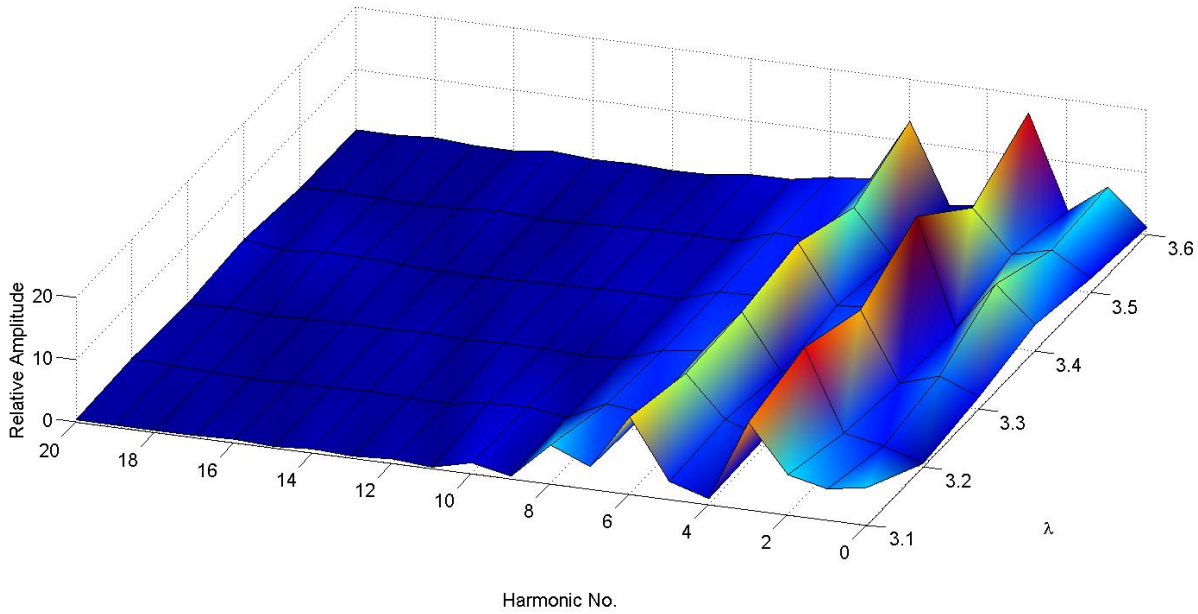

Figure 8.24: Monitoring output surface created using the TSA characteristics calculated for differing lambda values. The surface shown is for the optimum rotor case with a set-point turbine rotational velocity value of 320 RPM.

However it can be seen in Figure 8.24 the inputted harmonic structure to the simulations in the developed output surface. Specifically the prominence of the 3rd and 6th harmonics can be easily identified over all TSR indexes. Lastly it was noted that data sets of greater length could be used to develop an output surface which was more representative of the underlying turbine characteristics.

8.4.7 TMS Generation under Fault Conditions – Fixed Speed Control.

As in the case of the optimal TSR control datasets and the associated monitoring surfaces the sum of surface error relative to the trained normal operating condition surface was considered to test the validity of using such characteristic surfaces as monitoring tools. Figure 8.25 shows the developed monitoring surfaces for each of the turbine conditions. Figure 8.25a and Figure 8.25b both show instances of the developed normal operating

condition surfaces. The first of these was used as the surface with which others were compared and the second to study the degree of error for surfaces of like conditions. Figure 8.25c, Figure 8.25d and Figure 8.25e show the surfaces generated for the offset by 3^{o}, the offset by 6^{o} and the two blades offset case. The process of taking the sum of the absolute error between observed surface harmonics was conducted as outlined in Section 8.4.3. Here however, due to the index scheme outlined in the last section, with the data available, only a single value of the sum of surface error could be calculated. Figure 8.26 and Figure 8.27 show the calculated sum of surface errors. Figure 8.26 shows the un-weighted values of the sum of surfaces error, for which differing levels of error were observed for differing fault conditions. Figure 8.27 shows the sum of surfaces errors weighted by the number of rotations used in the calculation of the surface – this scheme was used to observe the effect of considering the degree of belief in the surface value given the number of observations used in creating the surface. It can be seen that the effect of this weighting is to reduce the error associated with the offset $+6^{o}$ case due to the relative few samples used to construct the surface for this case.

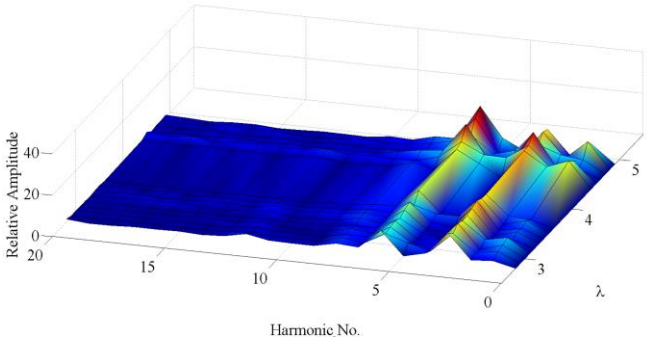

a) Optimum Training

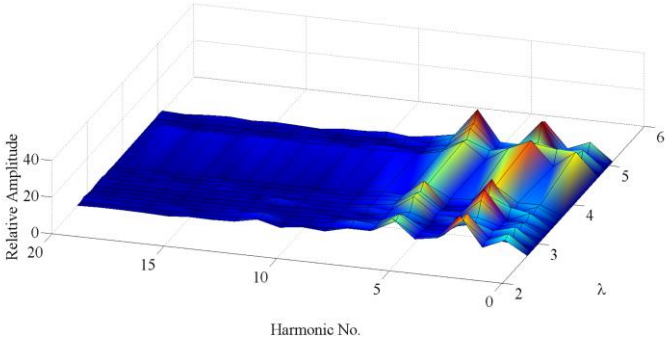

b) Optimum Test

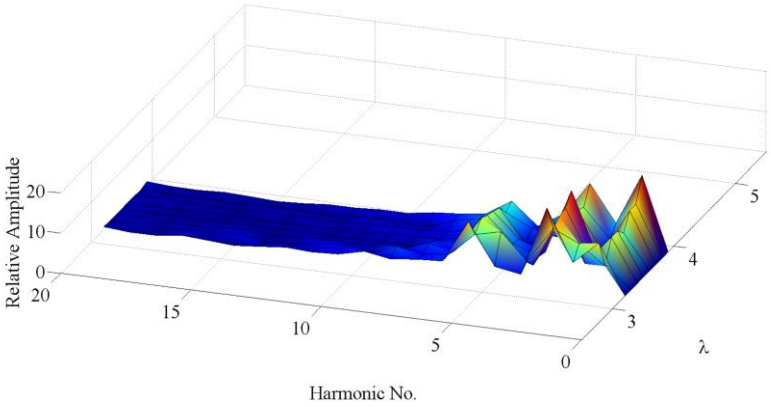

c) Offset +3º

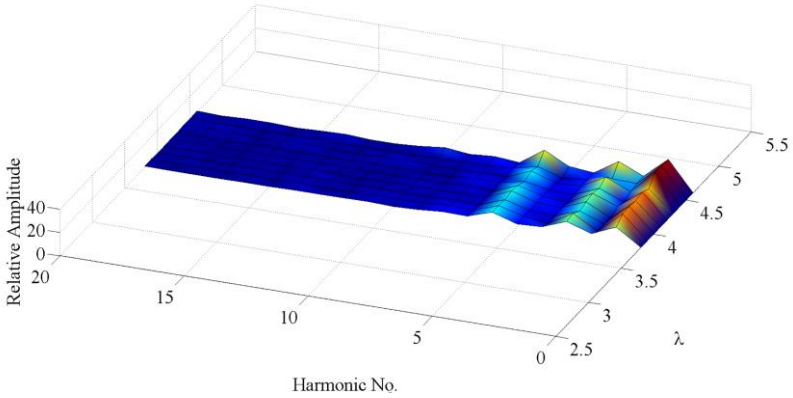

d) Offset +6º

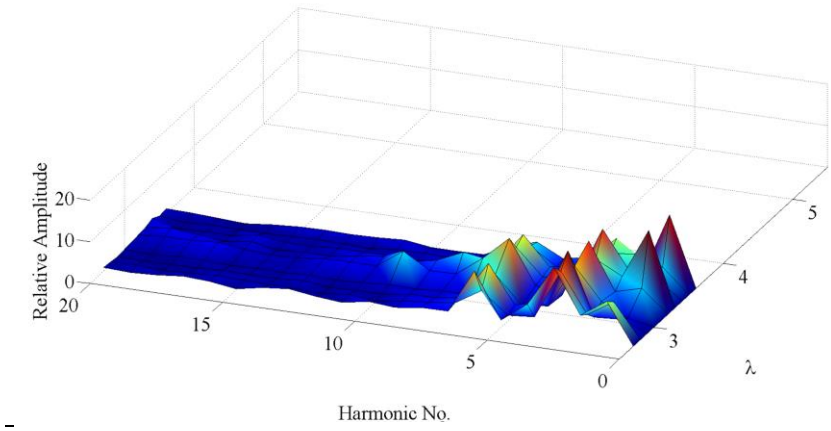

e) Offset Two Blades

Figure 8.25: Set Monitoring Surfaces generated for differing rotor conditions developed utilising the process outlined in Section 8.4.6.

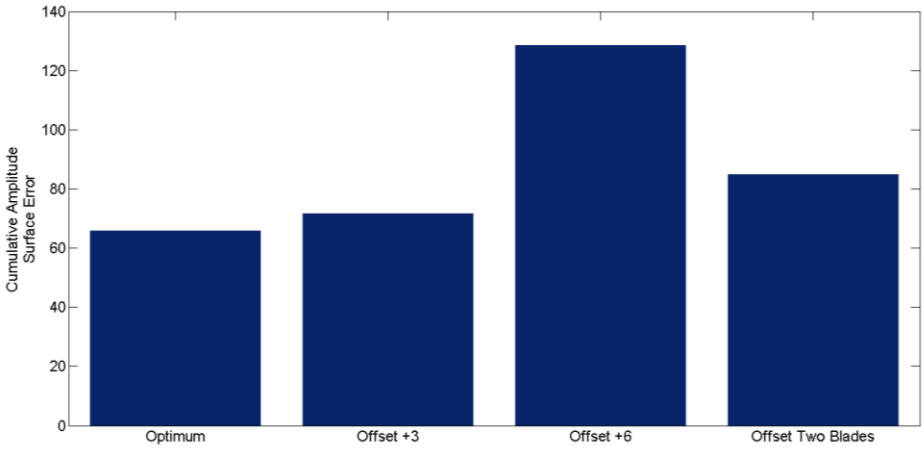

Figure 8.26: Non-weighted sum of surface error values for each of the rotor cases simulated.

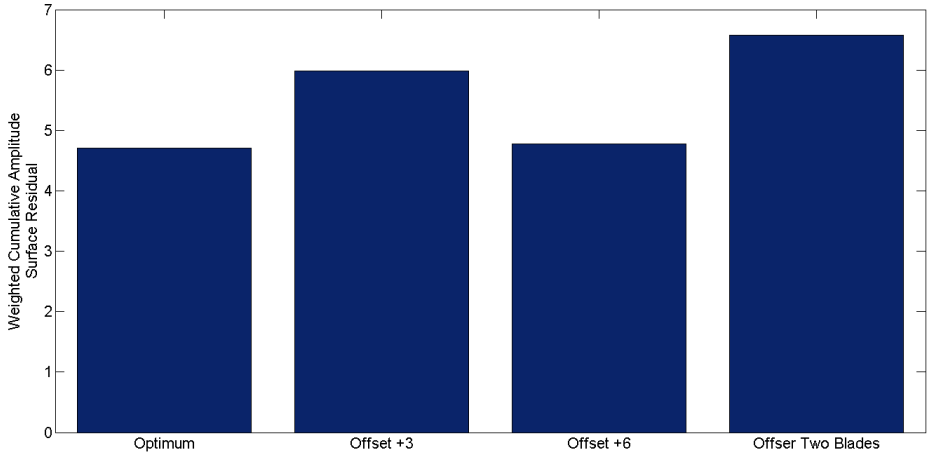

Figure 8.27: Calculated sum of surface error values weighted by the number of rotations used to generate the monitoring surface.

9 Discussion

9.1 Introduction

The research presented in this thesis had the main aim of adding to the understanding and application of TST CM. One objective of the research was to produce more realistic scenarios under which to test the monitoring approaches highlighted. In this way the thesis develops both simulation and testing approaches after each phase of research. This has involved the consideration of the design and application of algorithms to enable TST rotor fault detection and classification. Accordingly the discussion of the work undertaken is presented in a sequential manner considering the impacts of the main features presented in each chapter. This includes considerations of how the solutions generated can impact on the wider research community.

9.2 Methodology

Chapter 3 presents an overview of processes utilised in the testing and development of methods and approaches to rotor faults detection and diagnosis. The experimental methodology was based on the combination of CFD modelling, scale turbine testing and drive train simulation to help appraise the applicability of the outlined methods for rotor fault detection and diagnosis. Following this the chapter presents specific elements of the techniques and approaches researched for rotor fault detection purposes. The techniques and considerations presented were developed based on the research available at that time. Physical considerations of the turbine setup and how these impact on the ability of the generator signals to be used in rotor fault detection were made. Many of the pre-processing and feature extraction approaches utilised throughout the research were presented. The function of the work in Chapter 3 was to present the overall methodology adopted in conducting the research in this thesis. The chapter thus presents many of the mathematical

formulations of processes utilised throughout the body of research conducted. These processes are then developed and applied in various formats throughout the simulation and testing phases outlined in Section 3.2.

Chapter 3 also presents the data output from CFD models created by members of the CMERG research group to represent the effects of rotor defects. In doing so the chapter presents the non-dimensional performance curves and details of the rotor being studied throughout the research.

The work shows that CFD data can be used to develop preliminary CM approaches; in this case a rotor imbalance measure was developed via consideration of the torque spectra observed under differing rotor conditions. The chapter presented two rotor imbalance measures which could be calculated via extraction of the $A_{1\omega}$ and $A_{3\omega}$ harmonic amplitudes. It was shown using the CFD results that the imbalance measure could well be an effective rotor fault indicator

The chapter informs the wider research community by presenting a methodology that could be utilised by other researchers in developing TST CM strategies. The outlining of the simulation and experimental procedures utilised throughout the research provides an illustrative example of utilising CFD modelling, flume testing and bench top testing to develop condition monitoring approaches. This approach can be adopted by other researchers and developed for use in research relating to many TST CM problems. It was also shown that CFD modelling can serve as a useful tool in developing condition monitoring systems. Whilst a specific instance was shown here further approaches based on models of higher complexity and with the inclusion of differing sub-assemblies and flow conditions could well serve as a useful starting point in generating condition monitoring approaches.

9.3 Initial Steady State Simulations.

Chapter 4 demonstrates the use of observed spectra of the torsional time-series along with the non-dimensional curves for a given turbine rotor the CFD data was used to create a parametric rotor model. The model was then used to create more general and stochastic torque time series which could be used to test the applicability of the proposed CM techniques as applied to more general and less steady state time series.

The use of STFT and EMD signal processing methods was outlined for use in the harmonic amplitude extraction. The algorithms for creating rotor imbalance measures using the two differing signal processing techniques were presented. The results of applying the rotor imbalance measure to the generated torsional time series provided an indicator as to how useful the rotor imbalance measure may be when utilised on more realistic turbine rotor torque measurements. This work was a pre-cursor to the use of generator signal monitoring as the generator signals were effectively utilised to estimate the drive shaft torque observed.

In terms of the body of research conducted the work presented in Chapter 4 impacted on the subsequent research in two main ways. Firstly, the monitoring approaches developed were applied to the data generated in the two subsequent experimental campaigns. Secondly the rotor simulation process presented was utilised and developed for drive train test rig simulations. The form of the model outlined was altered slightly but the approach was developed by considering the strengths and weakness of the approach as applied to the initial steady state simulations.

The process of utilising a set of steady state CFD results to parameterise a turbine rotor model was also considered to impact on the wider research field. The ability to parameterise the model utilising simplified results and then using the parametric model to generate more realistic results could serve as a useful tool for many TST researchers.

In terms of condition monitoring output from the work presented in the initial steady state simulations chapter, it was found that the rotor imbalance measure as developed via the CFD results showed potential as a condition monitoring feature. This was especially true of the rotor imbalance measure calculated via the STFT process. The use of EMD was less successful but also gave rise to the development of utilising the HHT to overcome some of the limitation of using EMD procedure. Furthermore by considering some of the reasons behind the weakness of the EMD base rotor imbalance measure the chapter serves to guide further research into the use of EMD for TST condition monitoring purposes.

9.4 Flume based Turbine Development

Chapter 5 presented an overview of the development process undertaken to create a fully integrated model scale test turbine. The work covered many aspects of the implementation of a condition monitoring system for TSTs, albeit on a lab testing scale. The software for the flume-scale turbine was developed and integrated using three differing platforms. The central test control software was developed using NI LabVIEW 2013 and implemented using a PXI running the NI real-time operating system. The turbine nose cone measurement system was developed for control, data acquisition, storage and communication. As part of this work a PLC program was developed for turbine control and generator data acquisition. The software required for the integration of the three nodes or elements of the test setup was also undertaken. Communication between the nodes was implemented via both serial and Modbus TCP/IP protocols. Furthermore the measurement system was also developed to allow for synchronised sampling from each of the differing elements as well as the inclusion of the lower sample rate measurements sent via the Modbus TCP/IP link between the central control unit, the PXI, and the motor drives.

The process of creating an embedded nose cone measurement system with on-board storage was critical to the work undertaken in developing the lab-scale turbine. The circuitry for data capture, signal processing and storage were all developed by the author and

implemented via a designed PCB. The on-board storage was seen as an effective method of capturing measurement in an environment hampered by electric noise. Specifically the on board storage negated the need to send measurements back to the central control system since the path of the data cabling by necessity would have to have been through the centre of the turbine generator. Understandably this would result in unusable measurements and the local storage successfully allowed data capture from the turbine nose cone without significant distortion of the captured signals.

The effectiveness of adopting a nodal condition monitoring structure was addressed within Chapter 5. The chapter discussed the application aspects of a nodal system approach highlighting the use of a central processing unit to co-ordinate the system's actions. The design of this system was considered as an application of the nodal architecture approach, albeit on a smaller scale than for general turbine deployment. Whilst no condition monitoring actions were conducted many of the supporting requirements were enabled and much of the data captured during the flume testing campaigns was intended to facilitate condition monitoring research.

The ability to create working condition monitoring platforms may be considered to have been demonstrated through the successful deployment of the scale turbine testing system. This provided an example of a fully developed nodal architecture instance, albeit on a small scale. In terms of the impact on the research conducted as part of this thesis the development of the lab-scale turbine and the results captured by the completed system allowed of further testing of condition monitoring algorithms and developments to the parametric rotor model presented in Chapter 4. The turbine as piece of research apparatus has also helped to facilitate the research of other colleagues within CMERG and has also be used of collaborative research between institutions.

The wider impact of the outlined scale turbine development was considered to be the formation of some good practices in implementing scale turbine setups. The process of on

board data capture and storage was, as mentioned, considered to be a highlight of the scale turbine implementations and the process was thought to inform the research community in its implementation. Other successful aspects of the scale turbine development were considered to be the adoption of the nodal structure in the development process and the synchronisation of various measurement sources. Furthermore the application developed was considered to aid in further research conducted within CMERG as the application serves as a baseline application which could well be developed to reflect the needs of further research projects. This was considered to be the case the system developed adhered to the nodal architecture approach advocated resulting in modular code which can be updated and maintain with relative efficiency.

9.5 Flume Based Rotor Fault testing

Chapter 6 presents the results of the rotor fault flume based testing. Tests were undertaken at various turbine operating points and for differing rotor conditions; the use of offsetting turbine blades was considered to be an effective and economical method for simulating rotor damage. The chapter presents the non-dimensional characterisation of turbine performance under differing rotor conditions. It was found that greater discrepancies between the observed non-dimensional values for power and torque were observed at higher tip speed ratios. Also the level of discrepancy between the expected and observed non-dimensional values increased with increasing fault severity.

The TSA process outlined in Chapter 3 was used to characterise rotor torque transients for differing rotor conditions at a various λ-values. It was found that the TSA process was successful in characterising the observed rotor transients for the steady state flume testing. This was presented in a novel diagram, Figure 6.11, highlighting the calculated TSA characteristics along with the observed raw data across differing portions of the non-dimensional power curve observed for the given rotor. This was considered to add to the

research knowledge by providing a repeatable method for characterising rotor transient torques for differing turbine operating conditions.

Spectral analysis of the rotor torque transients in raw data form and of the TSA outputs showed that the TSA output could be analysed in the frequency domain to provide adequate characterisations of the lower frequency content of the rotor torque transients. Comparison of the TSA developed spectra and the spectra observed for the CFD data presented in Chapter 4 showed similar characteristics. The amplitude spectra were shown to be in good agreement in structure but exhibited difference in the scaling of amplitudes. This similarity in spectra structure confirmed that CFD data could be utilised to construct condition monitoring processes but further validation and testing is required.

A number of condition monitoring approaches were also applied to the captured experimental data. Promising results were observed for non-dimensional performance monitoring in spite of only taking a point measurement of the upstream fluid velocity. The application of the rotor imbalance measure calculated both via the STFT and the HHT were effective in highlighting differing rotor conditions. Smoothing of the rotor imbalance criteria was applied in both instances and improved the clarity of the results. In the extreme the mean value of the imbalance criteria calculated over the entirety of the captured dataset gave the clearest results. Fusion of the rotor imbalance measure and the non-dimensional performance curve monitoring results provided further clarity in fault detection and identification. The process of fitting a two-dimensional normal distribution showed that classification of the rotor fault condition based on the two measures was feasible with further research.

The chapter provided a number of results and the details of processes which could be of value to the TST research community. The process of the characterising rotor torque transients over a range of λ-values provided a non-dimensional transient characterisation of the observed rotor torque. This could well be a useful method of making comparisons of the

transient nature of the rotor torque observed for differing rotor configurations. As mentioned it was also shown that utilising CFD data for condition monitoring hypothesis generation could well be a useful tool for condition monitoring researchers. The results were also considered to show the effectiveness of the rotor imbalance measure for rotor anomaly detection. This could well provide a novel and fruitful area for further research. Lastly the fusion of two fault indicator metrics was shown to increase fault clarity of fault diagnosis and this too should prompt further research into fault indicator fusion.

9.6 Drive Train Simulation Development

The research extending the parametric TST rotor model to facilitate non-steady state drive train simulations was presented in Chapter 7. This included developing a Matlab script to create more representative plug flow fluid velocity time series. The script developed was based on the work of (Val et al, 2015) and was created to output fluid velocity time series which exhibited Von Karman spectral properties and the variance levels in line with turbulence intensities required. The process in itself was not novel but was required to consider the impact of the more representative fluid velocity spectral properties on the application of the condition monitoring procedures.

The chapter also presents the development of the parametric rotor torque model structure which was developed in the form of a single 8-term Fourier series plus a DC offset value. This model was appraised via the input of the model parameters, turbine position, rotation velocity, fluid velocity and related non-dimensional torque coefficient. The development allowed the inputting of model parameters for a variety of tip-speed-ratio values thus allowing non-steady-state simulations. By the very nature of testing of monitoring approaches under non-steady state conditions this development also allowed the original assertion of the applicability of utilising the generator quadrature axis current as a measure of the developed turbine torque to be studied. In developing the model structure it was also shown that for the rotor under consideration the relative amplitudes of the rotor torque

spectra for a given rotor condition and tip-speed-ratio were in close proximity for differing fluid and rotation velocity values.

In regard to the development of the turbine model, modifications were made to allow for implementation of the rotor model in hardware-in-the-loop simulations. These modifications included developing turbine control approaches for speed and tip speed ratio control. The developments also meant the adaption of the original Matlab script developed for real-time implementation undertaken via the NI Compact RIO platform. The real time calculation of the model required the development of drive control processes and parameter look-up in real time.

In terms of the impact of this work on the research community it was considered that the approach developed could be utilised for a variety of differing fault scenarios. The surfaces used for parameter lookup may be extended to included transients introduced by differing drive train sub-assemblies. In this way the approach can be utilised in a number of ways including the simulation of bearing and gearbox fault conditions. The developed simulation can also be extended to incorporate a number of differing rotor fault conditions to further supplement the research presented. As such the system developed was considered to form the first instance of an integrated fault simulation test bench which could be utilised for testing and development of a number of differing TST condition monitoring approaches.

This work also highlights the strength in the overall strategy of allowing differing experimental and simulation campaigns to impact upon each other. The model structure was developed utilising CFD data and then refined using acquired flume experimentation data. This process allowed for significant time savings when compared to generating such information via flume testing or CFD modelling alone. Creating the parametric surfaces was based on intuition or from full scale deployment data. With a minimal amount of further development the simulation process can be utilised for turbine control research. In such

research the test rig setup and simulation process can be utilised to understand the differing trade-offs between various control strategies.

9.7 Drive Train simulation results

Chapter 8 outlined the differing turbine control scenarios, rotor conditions and fluid velocity characteristics simulated via the drive train test rig setup. Based on the results of preliminary testing the required changes to the simulation setup were presented. These took into account the regeneration characteristics of the PMSMs utilised to create the simulations as well as the real-time data feedback rate from the drive set and the impact this had on the simulations. The changes made required the simulation of a larger diameter turbine with the integrated motor in the test rig simulating the transient torque structures output from a 'virtual gearbox' with a gear ratio of N = 10. The inclusion of such changes was seen as a successful approach to implementing condition monitoring research using the drive train test rig.

The results of the fluid velocity time-series generation process outlined in Chapter 7 are also presented. The results highlight the suitability of the mean, variance and spectral characteristics of the fluid velocity time-series generated via the Monte Carlo inverse Fourier transform simulation method. The time series generated were considered to allow for more realistic appraisal of the application of the outlined monitoring techniques as well as realistic application of newly developed techniques based on the surface development process outlined in Chapter 7. An overview of the results generated under a number of turbine control settings for the optimal rotor setup were also presented to give the reader an overview of the datasets created utilising the simulation approach. The datasets developed, after some cleaning, were particularly suitable for CM analysis due to synchronised data capture from each of the two drives for each of the quantities measured. Furthermore the output of the real-time model calculations were also synchronised with those measured for the PMSMs.

Calculating the torque spectra at various points in the simulation process also confirmed the correct simulation of torsional transients via the hardware-in-the-loop simulation setup.

In Chapter 8 the results of using the STFT amplitude extraction method were presented as histograms of the observed values of the rotor imbalance criteria for each of the turbine control cases. It was observed that, as already shown in Chapter 4, the imbalance criteria produced positive results for both detection and diagnosis of the fault cases considered for the steady state simulations. The considerations outlined above relating to the degree of success of the approach and the mechanisms behind the observed results were considered to apply to this application of the imbalance criterion to the steady state simulations and as such and for brevity are not discussed any further. Of greater significance are the results of the imbalance criteria observed for the non-steady state simulation cases.

The histogram of rotor imbalance criteria observed for the optimal λ control non-steady state case, Figure 8.13b, shows a marked reduction in the effectiveness of the method for minor fault detection under the given control scheme and fluid velocity characteristics. Whilst the offset $+6^{o}$ can readily be detected utilising the rotor imbalance criteria the distributions of the monitoring criteria for the optimum and remain fault cases exhibit prohibitively large degrees of overlap. In consideration of the relatively un-successful application of the rotor imbalance criteria to the optimal λ control non-steady state simulations two main aspects of the process were considered. Firstly it was though that the process of extracting the amplitudes from the spectrums generated for these simulation cases posed difficulties. Whereas in the steady state simulations the fluctuation of the turbine rotational velocity was minimal in the case of optimal λ control far greater fluctuations occurred. The fluctuation in turbine rotational velocity meant that frequencies which were harmonics of the rotational velocity were varying far more significantly than in the steady state case.

In terms of extraction of the amplitudes relating to the rotational harmonics of interest a more involved and less well defined method was required. In this case the rotational velocity time series for each case was used. For each time sample of the observed spectrograms the greatest amplitude observed over a range of frequencies centred at the harmonic of interest was extracted and stored to generate either the A_1 or A_3 time series. This method is prone to inaccuracies as were other methods considered. Inaccuracies arose from the incorrect identification of the amplitude to be extracted, due to the averaging of the spectrum over periods when the turbine velocity is fluctuating (windowing) and choosing the correct rotational frequency value for the spectrogram time step.

The second perceived shortcoming of the rotor imbalance measure was the non-existence of the required steady-state conditions for reasonable approximation of the turbine drive shaft torque via the generator quadrature axis current. This was known to be the case prior to the application of the process to the simulation data. The goal was to consider how effective detection and diagnostic processes dependent on the steady-state assertion were under non-steady state conditions. Lastly, it was also considered that the spectral characteristic of the simulated turbulent characteristics impacted on the low frequency amplitudes of interest as was considered to be the case in the flume testing setup, albeit to a lesser degree.

The application STFT based rotor imbalance criteria to the fixed speed turbine control simulations exhibited similar results to those of the optimal λ control. The results were similar in that the imbalance criteria was successful in identification of the $+6^o$ offset rotor fault case but a prohibitively high degree of overlap between the distributions of the rotor imbalance criteria for each of the other rotor fault cases was observed. Whereas the problems arose in the optimal λ case due to the fluctuating rotational velocity of the turbine these problems were considered to not embody the causes of the reduced effectiveness of the rotor imbalance measurement for the fixed speed control case. In the fixed speed control case the

reduced effectiveness of the process was attributed to the impact of the spectral characteristics of simulated fluid velocity time series on the observed quadrature axis spectrograms. Specifically the low frequency content of the simulated fluid velocity time series strongly impacted on the ability to extract the features in A_1 that are solely resultant from the effects of rotor imbalance. The low frequency fluctuation in the simulated turbulent fluid velocity time series impacts on the ability to extract the imbalance features in A_1 in two ways. From the standard set of equations presented in Chapter 1 it can be seen that the torque developed via the turbine rotor is proportional to the square of the fluid velocity at the turbine rotor. Furthermore, due to the constant rotational velocity of the turbine the changes in fluid velocity result in fluctuating tips speed ratios which in turn impact on the torsional constant in Equation (1.11).

Similar results in both cases were found for the HHT case. However in general the ability to detected and diagnose turbine rotor anomalies was reduced when using the HHT process for feature extraction.

The chapter then goes on to describe the results of the novel TMS condition monitoring approach based on the surface generation process outlined in Chapter 7. The creation of the surfaces for the steady-state test scenarios was straightforward but further normalisation and indexing schemes required for application of the process to non-steady state turbine operating scenarios were outlined and developed with some degree of success. In terms of the optimal λ control scenarios the TMS generation process was undertaken via a novel normalisation process as applied to the measured generator quadrature axis current. The normalisation process made use of the proportionality between the observed drive shaft torque and the square of the rotor velocity as imposed by the optimal TSR control strategy. In this way data segments feed into the TSA process required to create the monitoring surfaces could be normalised to compare the TSA outputs for a given λ value at differing

fluid velocities and turbine rotational velocities. This was considered to be a strong aspect of the monitoring surface technique as applied to the optimal λ control scheme data sets.

Developing the TMS generation process to a condition monitoring procedure was undertaken by considering the distortion of the monitoring surfaces under anomalous rotor condition relative to the generated surface for optimal rotor conditions. This was achieved by considering the SOSE between the surfaces generated under anomalous conditions and optimal conditions. It was found that varying fault conditions gave varying sum of surface error values. Also it was found that as greater numbers of rotations were utilised in constructing the surfaces for each differing condition the sum of surface error relative to the normal operating surface seemed to converge to a given value. This was considered to help provide stability and avoid false alarms when generating detection and diagnostic reasoning based on the approach. The relative success and stability of the method in spite of fluctuating fluid velocities and rotational velocities was seen as a significant result. This result indicates that the method utilised was sound when faced with non-steady state turbine operation and optimal TSR turbine control. Another aspect of the process that was seen as an asset was that the method didn't rely on fluid velocity measurements in order to construct the normalised monitoring surfaces. This was considered to allow for the application of the method to a variety of optimal TSR turbine control schemes, such as hill climb and optimal torque turbine control.

The TMS construction for the fixed speed turbine control case required a more involved indexing approach as a result of the fluctuations in λ values brought about by the simulated turbulent fluid velocity time series used for the simulations. This more involved approach involved segmenting the simulation into so called, λ–bins. The data within each bin was then used to create the TSA output for the given λ value with the results of the TSA process used to create the monitoring surface. This approach is novel and represents as a successful contribution to the TST condition monitoring research field.

The process showed a degree of success; however, due to the nature of the method only a point estimate of the sum of surface error was output for each dataset. Whilst differing levels of SOSE for differing rotor conditions were observed further validation tests are required to make any definite claims as to the effectiveness of the method. Whilst no real validation of the effectiveness of the method was able to be given the application of the process gave rise to some important considerations. The categorisation into λ-bins required knowledge of the fluid velocity and rotational velocity of the turbine for each data point categorised. As mentioned the process of acquiring fluid velocity measurements for each data point maybe difficult to obtain. Furthermore, the use of a point estimate of the fluid velocity to characterise the nature of the fluid field passing the turbine rotor could also lead to inaccuracies in the process. This was seen to be a drawback in using the developed method but more research will need to be conducted to fully quantify the effects of fluid velocity measurements on the surface generation process.

The research presented in Chapter 8 highlights a number of promising condition monitoring approaches. The results reported show varying degrees of successful implementation but was seen as providing a starting point for more in-depth research. Developments and further testing of both the imbalance criteria and the 'monitoring surface' development process can be undertaken based on the research presented to more fully realise the application of such techniques. The successful simulation of 1-dimensional fluid velocity values which yielded results with the desired mean, variance and spectral characteristics as part of the overall simulation process was also considered to be of interest to TST condition monitoring research as a whole. Again the results provide support for the methodology adopted in generating condition monitoring knowledge based on the application of information from three supporting sources. Specifically the effectiveness of the proposed algorithms has been successfully appraised in more realistic scenarios generated via a combination of the insights draw from each stage of simulation and experimentation.

10 Conclusions

10.1 Conclusions

The following conclusions and contributions to the field were generated by the research presented:

- An approach to the testing and development of CM processes applied to rotor imbalance monitoring of TSTs was created and detailed. Specifically, the research presented a process of utilising data from CFD simulations, parametric model simulations, flume testing and drive train testing to both test and develop the proposed CM processes. A similar approach can be followed by other researchers in the community based on the details presented.
- A parametric modelling procedure was created to simulate expected drive train torque transient characteristics. The process was developed to be flexible and was successfully parameterised using CFD data calculated for a single operating condition and flume data measured over a range of operating conditions.
- The parametric model was created to allow for flexibility in inputted fluid velocity time series. Uses of a naïve approach and a more representative approach to fluid velocity simulation coupled to the parametric model were demonstrated.
- The parametric modelling process was successfully adapted for real-time hardware in the loop simulations. This process was central to testing CM approaches under more realistic TST operating scenarios. The process was also a convenient method for creating representative drive train simulations from CFD data and experimental data which otherwise would be difficult to incorporate in real-time simulations. This also

holds for the output of BEMT modelling exercises and can service a useful process for a variety of researchers due to the convenience in model parameterisation and real-time implementation.

- The measurement, data acquisition and control systems for a scale model turbine were developed as part of the research activities undertaken by this researcher. The development included the successful implementation of both central and turbine nose cone level data capture. The development process can be used by the research community to aid in future turbine development activities.
- A number of CM processes were developed and tested based on turbine generator signal monitoring. Three classes of CM processes were developed based on generator signal measurement, namely: Cp monitoring, rotor imbalance criterion monitoring and transient characteristic surface monitoring. In the case of the rotor imbalance criteria algorithms the effectiveness of such approaches was appraised using naïve Bayes classifiers.
- The Cp monitoring approach was applied to data captured during flume based experiments under a number of operating λ. The results of the Cp monitoring approach were promising and were also successfully incorporated into an ensemble rotor imbalance indicator when coupled with the rotor imbalance measure presented.
- A rotor imbalance measure was developed using legacy CFD data. The process considered the ratio of 1^{st} to 3^{rd} harmonic amplitudes of the rotational velocity of the turbine. The imbalance measures presented were successfully calculated using a number of amplitude extraction processes, namely STFT, EMD and HHT. Furthermore the process of applying the measurement to drive shaft torque data and generator quadrature axis current measurements was demonstrated.

- The rotor imbalance measure was successfully applied to data from a variety of sources. The processes were initially applied to steady-state turbine simulation data; the results of this application gave input into the development of the imbalance measure criterion approaches. The developed approaches were then tested using data from a flume testing campaign. Lastly the imbalance measures were applied to non-steady state turbine simulations including two differing turbine control implementations.
- The imbalance measures showed a high degree of success when applied to near steady state TST operation data. The process of the imbalance measure was less successful when applied to the non-steady state data sets.
- A set of approaches to turbine transient characterisation, based on the development of TMSs, were applied to the non-steady state data. The approaches were data intensive and gave promising but non-conclusive results. Further testing these processes is required to understand if the normalisation and characteristic surface generation process are effective.
- An ensemble rotor imbalance condition indicator was developed via the combination of the Cp monitoring and imbalance criterion monitoring data. The indicator applied to the flume testing data and gave promising results. Further work should be conducted to test the differing approaches to ensemble condition indictors. Furthermore work looking into the performance of such indicators under non-steady state turbine operation should be undertaken.

10.2 Further work.

The research presented outlines a novel approach to efficient and flexible simulation of TST rotor torque and presents some CM approaches based on both flume scale testing and CFD simulations. As with any research presenting novel approaches a variety of pathways

for continuing the research and developing its applicability exist. Further work is recommended in the following areas:

- Development and testing of spectrogram based extraction of the monitoring criterion C. The presented shows what could be considered the first non-trivial approach to calculating a monitoring criterion C. As was seen in Chapter 8 the monitoring criterion C performed poorly under non-steady state conditions - development of each process in the calculation of the condition monitoring criteria C could improve this performance.
- Testing of developed monitoring criteria, C, at differing turbine scales. The monitoring criterion C was applied to $1/20^{th}$ scale test data and to $1/5^{th}$ scale drive train simulations under specific control strategies. In order to gauge the applicability of this approach across the TST industry the approach would have be proven at differing turbine scales – ideally the scales should be dictated by the rotor sizes currently or foreseen as being used within the industry.
- The condition monitoring criteria, C, could also be tested under more dynamic flow conditions including profiled flows, flows of higher turbulence intensities than 10% with differing integral length scales and flows subjected to waves.
- The use of the TMS will should be tested further at the conditions outlined within the thesis gain further insight into their application. The TMS surfaces if proved to be useful can then be subjected to all the above considerations. Lastly, the discretisation of the harmonic index of the TMS surface could be increased subject to great volumes of data. Likewise the range of harmonics captured by the surfaces could be increased. This would allow for the study of the usefulness of the TMS to detect other drive train faults.

- In all cases more realistic rotor faults could be simulated and used to test the CM approaches against.
- The parametric model developed can be extended to include higher frequencies allowing the simulation of further drive train faults if correctly parameterised.
- Lastly, the parametric model approach should be developed for more dynamic sea conditions. This may require the inclusion of more sinusoids in the model or possibly frequency or amplitude modulation terms. This work could be of great importance and may allow turbine developers to simulate device behaviour under numerous sea conditions for both development and CM generation approaches.

References.

Abouhnik, A., Albarbar, A., 2012. Wind turbine blades condition assessment based on vibration measurements and the level of an empirically decomposed feature. Energy Conversion and Management, IREC 2011, The International Renewable Energy Congress 64, 606–613. doi:10.1016/j.enconman.2012.06.008

Alan Tan, 2008. Hilbert-Huang Transform - File Exchange - MATLAB Central [WWW Document]. URL http://de.mathworks.com/matlabcentral/fileexchange/19681-hilbert-huang-transform (accessed 6.29.16).

Allmark, M., Grosvenor, R., Byrne, C., Anayi, F., Prickett, P., 2013. Condition Monitoring of a Tidal Stream Turbine: Development of an Experimental Methodology. Presented at the 9th European Wave and Tidal Energy Conference, Aalborg.

Alstom completes the acquisition of Tidal Generation Limited (TGL) from Rolls-Royce plc [WWW Document], n.d. URL http://www.alstom.com/press-centre/2013/1/alstom-completes-the-acquisition-of-tidal-generation-limited-tgl-from-rolls-royce-plc/ (accessed 6.29.16).

Anaya-Lara, O. (Ed.), 2009. Wind energy generation: modelling and control. John Wiley & Sons, Chichester, U.K.

Antoniadou, I., Dervilis, N., Papatheou, E., Maguire, A.E., Worden, K., 2015. Aspects of structural health and condition monitoring of offshore wind turbines. Philosophical Transactions of the Royal Society of London A: Mathematical, Physical and Engineering Sciences 373, 20140075. doi:10.1098/rsta.2014.0075

Atlantis Resources Limited - AR1000 [WWW Document], n.d. URL http://atlantisresourcesltd.com/turbines/ar-series/ar1000.html (accessed 6.29.16).

Atlantis Resources Limited - AS series [WWW Document], n.d. URL http://atlantisresourcesltd.com/turbines/as-series.html (accessed 6.29.16).

Bahaj, A.S., 2011. Development of marine current turbines for electricity production, in: 2011 IEEE Power and Energy Society General Meeting. Presented at the 2011 IEEE Power and Energy Society General Meeting, pp. 1–4. doi:10.1109/PES.2011.6039067

Bahaj, A.S., Molland, A.F., Chaplin, J.R., Batten, W.M.J., 2007. Power and thrust measurements of marine current turbines under various hydrodynamic flow conditions in a cavitation tunnel and a towing tank. Renewable Energy 32, 407–426. doi:10.1016/j.renene.2006.01.012

Balageas, D., Fritzen, C.-P., Güemes, A., 2006. Structural health monitoring. Wiley Online Library.

B Osgood, 2007. The Fourier Transform and its Applications. Stanford Open Courseware.

Beaujeany, P.P., Khoshgoftaar, T.M., Sloan, J.C., Xiros, N., Vendittis, D., 2009. Monitoring ocean turbines: A reliability assessment. Presented at the Proceedings - 15th ISSAT International Conference on Reliability and Quality in Design, pp. 367–371.

Betz, "Das Maximum der theoretisch möglichen Ausnützung des Windes durch Windmotoren," *Zeitschrift für das gesamte Turbinenwesen*, vol. 26, no. 307–309, p. 8, 1920.

Bishop, C.M., 2006. Pattern recognition and machine learning, Information science and statistics. Springer, New York.

Black and Veatch, 2011. UK Tidal Current Resource & Economics. Carbon Trust, London.

Black and Veatch, 2005. Phase II UK Tidal Stream Energy Resource Assessment. London: Carbon Trust. Carbon Trust, London.

Bouno, T., Yuji, T., Hamada, T., Hideaki, T., 2005. Failure forecast diagnosis of small wind turbine using acoustic emission sensor. KIEE International Transactions on Electrical Machinery and Energy Conversion Systems 5, 78–83.

Byrne, C., Cherrett, W., Grosvenor, R., Mason-Jones, A., Morris, C., O'Doherty, D., O'Doherty, T., Prickett, P., n.d. An Investigation into the Possible Effects of Cavitation on a Horizontal Axis Tidal Turbine.

Caselitz, P., Giebhardt, J., 2005. Condition monitoring and fault prediction for marine current turbines, in: International Conference Ocean Energy; from Innovation to Industry. pp. 1–8.

Chen, B., Zappalá, D., Crabtree, C.J., Tavner, P.J., 2014. Survey of commercially available SCADA data analysis tools for wind turbine health monitoring.

Clarke, J.A., Connor, G., Grant, A.D., Johnstone, C.M., 2007. Design and testing of a contra-rotating tidal current turbine. Proceedings of the Institution of Mechanical Engineers, Part A: Journal of Power and Energy 221, 171–179. doi:10.1243/09576509JPE296

Crabtree, C.J., Zappalá, D., Tavner, P.J., 2014. Survey of commercially available condition monitoring systems for wind turbines.

Crown Estate, 2012. UK Wave and Tidal Key Resource Areas Project Summary Report.

Current Builds Behind Tidal Energy Take-off [WWW Document], n.d. URL http://www.renewableenergyworld.com/articles/print/volume-16/issue-2/ocean-energy/current-builds-behind-tidal-energy-take-off.html (accessed 6.29.16).

de Jesus Henriques, T.A., Botsari, A., Tedds, S.C., Poole, R.J., Najafian, H., Sutcliffe, C.J., Owen, I., n.d. The Effects of Wave-Current Interactions on the Performance of Horizontal Axis Tidal-Stream Turbines, in: 2 Nd Oxford Tidal Energy Workshop. p. 37.

Delorm, T.M., 2014. Tidal stream devices: reliability prediction models during their conceptual & development phases. Durham University.

Delorm, T.M., Zappala, D., Tavner, P.J., 2011. Tidal stream device reliability comparison models. Proceedings of the Institution of Mechanical Engineers, Part O: Journal of Risk and Reliability 1748006X11422620.

D. A. Doman, R. E. Murray, M. J. Pegg, K. Gracie, C. M. Johnstone, and T. Nevalainen, "Tow-tank testing of a 1/20th scale horizontal axis tidal turbine with uncertainty analysis," *Int. J. Mar. Energy*, vol. 11, pp. 105–119, 2015.

Donoho, D.L., 1995. De-noising by soft-thresholding. Information Theory, IEEE Transactions on 41, 613–627.

Duhaney, J., Khoshgoftaar, T.M., 2013. Multi-class classification for ocean turbine state detection. Presented at the Proceedings - 19th ISSAT International Conference on Reliability and Quality in Design, RQD 2013, pp. 240–244.

Duhaney, J., Khoshgoftaar, T.M., Napolitano, A., 2012a. Studying the effect of class imbalance in ocean turbine fault data on reliable state detection. Presented at the Proceedings - 2012 11th International Conference on Machine Learning and Applications, ICMLA 2012, pp. 268–275. doi:10.1109/ICMLA.2012.53

Duhaney, J., Khoshgoftaar, T.M., Sloan, J.C., 2011a. Feature level sensor fusion for improved fault detection in MCM systems for ocean turbines. Presented at the Proceedings of the 24th International Florida Artificial Intelligence Research Society, FLAIRS - 24, pp. 15–20.

Duhaney, J., Khoshgoftaar, T.M., Sloan, J.C., 2011b. Feature selection on dynamometer data for reliability analysis. Presented at the Proceedings - International Conference on Tools with Artificial Intelligence, ICTAI, pp. 1012–1019. doi:10.1109/ICTAI.2011.173

Duhaney, J., Khoshgoftaar, T.M., Wald, R., 2012b. Applying feature selection to short time wavelet transformed vibration data for reliability analysis of an ocean turbine. Presented at the Proceedings - 2012 11th International Conference on Machine Learning and Applications, ICMLA 2012, pp. 330–337. doi:10.1109/ICMLA.2012.62

Duhaney, J., Khoshgoftaar, T.M., Wald, R., Beaujean, P.P., 2012c. Fusion of wavelet transform features for reliable fault detection within an ocean turbine MCM system. Presented at the Proceedings - 18th ISSAT International Conference on Reliability and Quality in Design, pp. 23–27.

Elasha, F., Teixeira, J.A., 2014. Condition Monitoring Philosophy for Tidal Turbines. International Journal of Performability Engineering 10, 521.

Eriksson, S., Bernhoff, H., Leijon, M., 2008. Evaluation of different turbine concepts for wind power. Renewable and Sustainable Energy Reviews 12, 1419–1434.

"European Commission : CORDIS : Projects & Results Service : Demonstration of a Condition Monitoring System for Tidal Stream Generators. Tidal Sense, 2009." [Online]. Available: http://cordis.europa.eu/project/rcn/102179_en.html. [Accessed: 12-Jan-2017].

"European Commission : CORDIS : Projects & Results Service : Development of a condition monitoring system for tidal stream generator structures. TidalSenseDemo, 2011." [Online]. Available: http://cordis.europa.eu/project/rcn/107809_en.html. [Accessed: 12-Jan-2017].

Faudot, C., Dahlhaug, O.G., Holst, M.A., 2013. Tidal turbine blades in runaway situation: experimental and numerical approaches, in: Proceedings of the 10th European Wave and Tidal Energy Conference (EWTEC13), Aalborg, Denmark.

Feng, Z., Liang, M., Chu, F., 2013. Recent advances in time–frequency analysis methods for machinery fault diagnosis: A review with application examples. Mechanical Systems and Signal Processing, Condition monitoring of machines in non-stationary operations. 38, 165–205. doi:10.1016/j.ymssp.2013.01.017

Frost, C., Morris, C.E., Mason-Jones, A., O'Doherty, D.M., O'Doherty, T., 2015. The effect of tidal flow directionality on tidal turbine performance characteristics. Renewable Energy 78, 609–620. doi:10.1016/j.renene.2015.01.053

Gardels, D.J., Qiao, W., Gong, X., 2010. Simulation studies on imbalance faults of wind turbines, in: IEEE PES General Meeting. Presented at the IEEE PES General Meeting, pp. 1–5. doi:10.1109/PES.2010.5589500

Giebhardt, J., 2007. Condition Monitoring for Wind Turbines "State of the Art" Report as Deliverable 7.1. 1. WP7, March.

Gong, X., Qiao, W., 2012. Imbalance Fault Detection of Direct-Drive Wind Turbines Using Generator Current Signals. IEEE Transactions on Energy Conversion 27, 468–476. doi:10.1109/TEC.2012.2189008

Grigoriu, M., 2000. A spectral representation based model for Monte Carlo simulation. Probabilistic Engineering Mechanics 15, 365–370. doi:10.1016/S0266-8920(99)00038-7

Grosvenor, R.I., Prickett, P.W., Frost, C., Allmark, M.J., 2014. Performance and condition monitoring of tidal stream turbines. Presented at the 2nd European Conference of the Prognostic Health Management Society, PHM Society, Nantes.

Ha, J.M., Park, J., Oh, H., Youn, B.D., 2015. Vibration-based Fault Diagnostics of Planetary Gearbox Using Time Synchronous Averaging with Multiple Window Functions. Presented at the Annual Conference of the Prognostics and Health Management Society 2015.

Hameed, Z., Ahn, S.H., Cho, Y.M., 2010. Practical aspects of a condition monitoring system for a wind turbine with emphasis on its design, system architecture, testing and installation. Renewable Energy 35, 879–894. doi:10.1016/j.renene.2009.10.031

Hameed, Z., Hong, Y.S., Cho, Y.M., Ahn, S.H., Song, C.K., 2009. Condition monitoring and fault detection of wind turbines and related algorithms: A review. Renewable and Sustainable energy reviews 13, 1–39.

Han, S.-H., Park, J.-S., Lee, K.-S., Park, W.-S., Yi, J.-H., 2013. Evaluation of vertical axis turbine characteristics for tidal current power plant based on in situ experiment. Ocean Engineering 65, 83–89.

Hashin, Z., 1980. A reinterpretation of the Palmgren-Miner rule for fatigue life prediction. Journal of Applied Mechanics 47, 324–328.

Heaviside, O,. “XXXIX. On the electromagnetic effects due to the motion of electrification through a dielectric,” *The London, Edinburgh, and Dublin Philosophical Magazine and Journal of Science*, vol. 27, no. 167, pp. 324–339, 1889.

Hu, Z., Du, X., 2012. Reliability analysis for hydrokinetic turbine blades. Renewable Energy 48, 251–262.

Huang, N.E., Shen, Z., Long, S.R., Wu, M.C., Shih, H.H., Zheng, Q., Yen, N.-C., Tung, C.C., Liu, H.H., 1998. The empirical mode decomposition and the Hilbert spectrum for nonlinear and non-stationary time series analysis, in: Proceedings of the Royal Society of London A: Mathematical, Physical and Engineering Sciences. The Royal Society, pp. 903–995.

IEEE SA - 1588 WG - Precise Networked Clock Synchronization Working Group [WWW Document], n.d. URL http://standards.ieee.org/develop/wg/1588_WG.html (accessed 6.29.16).

ISO 10816-8:2014 - Mechanical vibration -- Evaluation of machine vibration by measurements on non-rotating parts -- Part 8: Reciprocating compressor systems [WWW Document], n.d. . ISO. URL http://www.iso.org/iso/catalogue_detail.htm?csnumber=56782 (accessed 6.29.16).

ISO 13374-1:2003 - Condition monitoring and diagnostics of machines -- Data processing, communication and presentation -- Part 1: General guidelines [WWW Document], n.d. . ISO. URL http://www.iso.org/iso/catalogue_detail?csnumber=21832 (accessed 6.29.16).

J. Duhaney, T. M. Khoshgoftaar, A. Napolitano, 2012a. Studying the Effect of Class Imbalance in Ocean Turbine Fault Data on Reliable State Detection, in: Machine Learning and Applications (ICMLA), 2012 11th International Conference on. Presented at the Machine Learning and Applications (ICMLA), 2012 11th International Conference on, pp. 268–275. doi:10.1109/ICMLA.2012.53

J. Duhaney, T. M. Khoshgoftaar, J. C. Sloan, 2011a. Feature Selection on Dynamometer Data for Reliability Analysis, in: 2011 IEEE 23rd International Conference on Tools with Artificial Intelligence. Presented at the 2011 IEEE 23rd International Conference on Tools with Artificial Intelligence, pp. 1012–1019. doi:10.1109/ICTAI.2011.173

J. Duhaney, T. M. Khoshgoftaar, J. C. Sloan, B. Alhalabi, P. P. Beaujean, 2011b. A Dynamometer for an Ocean Turbine Prototype: Reliability through Automated Monitoring, in: High-Assurance Systems Engineering (HASE), 2011 IEEE 13th International Symposium on. Presented at the High-Assurance Systems Engineering (HASE), 2011 IEEE 13th International Symposium on, pp. 244–251. doi:10.1109/HASE.2011.61

J. Duhaney, T. M. Khoshgoftaar, R. Wald, 2012b. Applying Feature Selection to Short Time Wavelet Transformed Vibration Data for Reliability Analysis of an Ocean Turbine, in: Machine Learning and Applications (ICMLA), 2012 11th International Conference on. Presented at the Machine Learning and Applications (ICMLA), 2012 11th International Conference on, pp. 330–337. doi:10.1109/ICMLA.2012.62

Jo, C.H., Lee, J.H., Kim, D.Y., Lee, K.H., 2013. Performance of a Horizontal Axis Tidal Current Turbine with Blade Deformation. Presented at the 10th European Wave and Tidal Enery Conference.

Khan, M.J., Bhuyan, G., Iqbal, M.T., Quaicoe, J.E., 2009. Hydrokinetic energy conversion systems and assessment of horizontal and vertical axis turbines for river and tidal applications: A technology status review. Applied Energy 86, 1823–1835.

Kumar, D., Sarkar, S., 2016. A review on the technology, performance, design optimization, reliability, techno-economics and environmental impacts of hydrokinetic energy conversion systems. Renewable and Sustainable Energy Reviews 58, 796–813.

Kusnick, J., Adams, D.E., Griffith, D.T., 2015. Wind turbine rotor imbalance detection using nacelle and blade measurements. Wind Energ. 18, 267–276. doi:10.1002/we.1696

Lee, K., Aihara, A., Puntsagdash, G., Kawaguchi, T., Sakamoto, H., Okuma, M., 2016. Feasibility study on a strain based deflection monitoring system for wind turbine blades. Mechanical Systems and Signal Processing.

Li, H., Hu, Z., Chandrashekhara, K., Du, X., Mishra, R., 2014. Reliability-based fatigue life investigation for a medium-scale composite hydrokinetic turbine blade. Ocean Engineering 89, 230–242.

Liang, J., Whitby, B., 2011. Field Oriented Control of a Permanent Magnet Synchronous Generator for use in a Variable Speed Tidal Stream Turbine, in: Universities' Power Engineering Conference (UPEC), Proceedings of 2011 46th International. Presented at the Universities' Power Engineering Conference (UPEC), Proceedings of 2011 46th International, pp. 1–6.

Liu, P., Veitch, B., 2012. Design and optimization for strength and integrity of tidal turbine rotor blades. Energy 46, 393–404.

Liu, W.Y., Tang, B.P., Han, J.G., Lu, X.N., Hu, N.N., He, Z.Z., 2015. The structure healthy condition monitoring and fault diagnosis methods in wind turbines: A review. Renewable and Sustainable Energy Reviews 44, 466–472.

Losi, J., Becker, E., 2009. Imbalance: a danger to components. Erneuerbare Energien.

Magagna, D., MacGillivray, A., Jeffrey, H., Hanmer, C., Raventos, A., Badcock-Broe, A., Tzimas, E., 2014. Wave and tidal energy strategic technology agenda. SI Ocean 44.

Manwell, J.F., McGowan, J.G., Rogers, A.L., 2009. Wind energy explained theory, design and application. Wiley, Chichester, U.K.

Makaya, K., Burnham, K., Campos, C., 2011. Assessment of defects in wind and tidal turbine blades using guide waves. Engineering Structural Integrity Assessment: from plant and structural design, manufacture to disposal, EMAS 2011.

Mason-Jones, A., 2010. Performance assessment of a Horizontal Axis Tidal Turbine in a high velocity shear environment. (phd). Cardiff University.

Mason-Jones, A., O'Doherty, D.M., Morris, C.E., O'Doherty, T., Byrne, C.B., Prickett, P.W., Grosvenor, R.I., Owen, I., Tedds, S., Poole, R.J., 2012. Non-dimensional scaling of tidal stream turbines. Energy, Integration and Energy System Engineering, European Symposium on Computer-Aided Process Engineering 2011 44, 820–829. doi:10.1016/j.energy.2012.05.010

Mjit, M., Beaujean, P.-P.J., Vendittis, D.J., 2011. Comparison of fault detection techniques for an ocean turbine. Presented at the Proceedings of the Annual Conference of the Prognostics and Health Management Society 2011, PHM 2011, pp. 123–133.

Mjit, M., Beaujean, P.-P.J., Vendittis, D.J., 2011. Smart Vibration Monitoring System for an Ocean Turbine, in: High-Assurance Systems Engineering (HASE), 2011 IEEE 13th International Symposium on. IEEE, pp. 252–260.

Mjit, M., Beaujean, P.-P.J., Vendittis, D.J., 2010. Fault detection and diagnostics in an ocean turbine using vibration analysis. Presented at the ASME International Mechanical Engineering Congress and Exposition, Proceedings (IMECE), pp. 535–543. doi:10.1115/IMECE2010-40963

Morris, C., 2014. Influence of solidity on the performance, swirl characteristics, wake recovery and blade deflection of a horizontal axis tidal turbine. PhD Thesis. Cardiff University.

Mycek, P., Gaurier, B., Germain, G., Pinon, G., Rivoalen, E., 2014a. Experimental study of the turbulence intensity effects on marine current turbines behaviour. Part I: One single turbine. Renewable Energy 66, 729–746. doi:10.1016/j.renene.2013.12.036

Mycek, P., Gaurier, B., Germain, G., Pinon, G., Rivoalen, E., 2014b. Experimental study of the turbulence intensity effects on marine current turbines behaviour. Part II: Two interacting turbines. Renewable Energy 68, 876–892. doi:10.1016/j.renene.2013.12.048

Mycek, P., Gaurier, B., Germain, G., Pinon, G., Rivoalen, E., 2013. Numerical and experimental study of the interaction between two marine current turbines. International Journal of Marine Energy 1, 70–83. doi:10.1016/j.ijome.2013.05.007

N. Waters, P. P. Beaujean, D. Vendittis, 2012. Detection, localization, and identification of bearing faults on an ocean turbine, in: 2012 Oceans. Presented at the 2012 Oceans, pp. 1–8. doi:10.1109/OCEANS.2012.6404832

Nezu, I., Nakagawa, H., Jirka, G.H., 1994. Turbulence in open-channel flows. Journal of Hydraulic Engineering 120, 1235–1237.

Nicholls-Lee, R.F., 2011. Adaptive composite blades for horizontal axis tidal turbines. University of Southampton.

Osalusi, E., 2010. Analysis of wave and current data in a tidal energy test site. Heriot-Watt University.

Pereira, G., Mikkelsen, L.P., McGugan, M., 2015. Embedded Fibre Bragg Grating Sensor Response Model: Crack Growing Detection in Fibre Reinforced Plastic Materials, in: Journal of Physics: Conference Series. IOP Publishing, p. 12115.

Pourahmadi, M., 2001. Foundations of time series analysis and prediction theory, Wiley series in probability and statistics. Wiley, New York.

Prickett, P., Grosvenor, R., Byrne, C., Jones, A.M., Morris, C., O'Doherty, D., O'Doherty, T., 2011. Consideration of the Condition Based Maintenance of Marine Tidal Turbines, in: 9th European Wave and Tidal Energy Conference. pp. 5–9.

Pyrhönen, J., Jokinen, T., Hrabovcová, V., Wiley InterScience (Online service), 2008. Design of rotating electrical machines. Wiley, Chichester, U.K.

Qiao, W., Lu, D., 2015a. A Survey on Wind Turbine Condition Monitoring and Fault Diagnosis; Part I: Components and Subsystems. IEEE Transactions on Industrial Electronics 62, 6536–6545. doi:10.1109/TIE.2015.2422112

Qiao, W., Lu, D., 2015b. A Survey on Wind Turbine Condition Monitoring and Fault Diagnosis; Part II: Signals and Signal Processing Methods. IEEE Transactions on Industrial Electronics 62, 6546–6557. doi:10.1109/TIE.2015.2422394

Qiao, W., Zhang, P., Chow, M.-Y., 2015. Condition Monitoring, Diagnosis, Prognosis, and Health Management for Wind Energy Conversion Systems. Industrial Electronics, IEEE Transactions on 62, 6533–6535.

Renewable energy directive - Energy - European Commission [WWW Document], n.d. . Energy. URL https://ec.europa.eu/energy/en/topics/renewable-energy/renewable-energy-directive (accessed 6.29.16).

Renewable UK, 2011. Wave and Tidal Energy in the UK.

Rilling, G., Flandrin, P., Goncalves, P., others, 2003. On empirical mode decomposition and its algorithms, in: IEEE-EURASIP Workshop on Nonlinear Signal and Image Processing. NSIP-03, Grado (I), pp. 8–11.

Schubel, P.J., Crossley, R.J., Boateng, E.K.G., Hutchinson, J.R., 2013. Review of structural health and cure monitoring techniques for large wind turbine blades. Renewable Energy 51, 113–123. doi:10.1016/j.renene.2012.08.072

Sloan, J.C., Khoshgoftaar, T.M., Beaujean, P.-P., Driscoll, F., 2009. Ocean turbines - A reliability assessment. International Journal of Reliability, Quality and Safety Engineering 16, 413–433. doi:10.1142/S0218539309003472

Smith, S.W., 1997. The scientist and engineer's guide to digital signal processing, 1st ed. ed. California Technical Pub, San Diego, Calif.

Stallard, T., Feng, T., Stansby, P.K., 2014. Experimental study of the mean wake of a tidal stream rotor in a shallow turbulent flow. Journal of Fluids and Structures. doi:10.1016/j.jfluidstructs.2014.10.017

s-test-rig-at-the-EMEC-tidal-test-site-Image-Mike-Brookes-Roper.jpg (800×545) [WWW Document], n.d. URL http://www.emec.org.uk/wp-content/uploads/2013/10/s-test-rig-at-the-EMEC-tidal-test-site-Image-Mike-Brookes-Roper.jpg (accessed 6.29.16).

Sustainable Marine Energy [WWW Document], n.d. . Sustainable Marine Energy. URL http://www.sustainablemarine.com/ (accessed 6.29.16).

Tavner, P., Qiu, Y., Korogiannos, A., Feng, Y., 2010. The correlation between wind turbine turbulence and pitch failure. UK.

Tavner, P., Ran, L., Penman, J., Sedding, H., 2008. Condition Monitoring of Rotating Electrical Machines. IET, The Institution of Engineering and Technology, Michael Faraday House, Six Hills Way, Stevenage SG1 2AY, UK.

Tedds, S,C. 2014. Scale Model Testing of Tidal Stream Turbines: Wake Characterisation in Realistic Flow Conditions. PhD Thesis, University of Liverpool.

Tedds, S.C., Poole, R.J., Owen, I., Najafian, G., Bode, S.P., Mason-Jones, A., Morris, C., O'Doherty, T., O'Doherty, D.M., 2011. Experimental investigation of horizontal axis tidal stream turbines, in: 9th European Wave and Tidal Energy Conference (EWTEC). Southampton, UK. p. 13.

Tian, Z., Jin, T., 2011. Maintenance of wind turbine systems under continuous monitoring, in: Reliability and Maintainability Symposium (RAMS), 2011 Proceedings - Annual. Presented at the Reliability and Maintainability Symposium (RAMS), 2011 Proceedings - Annual, pp. 1–6. doi:10.1109/RAMS.2011.5754488

Tidal devices : EMEC: European Marine Energy Centre, n.d.

"TidalSense." [Online]. Available: http://www.tidalsense.com/. [Accessed: 12-Jan-2017].

Tidal Energy Ltd – Tidal Power, Renewable Energy » WALES' FIRST FULL-SCALE TIDAL ENERGY GENERATOR UNVEILED AHEAD OF ITS INSTALLATION IN WELSH WATERS [WWW Document], n.d. URL http://www.tidalenergyltd.com/?p=2191 (accessed 6.29.16).

UK renewable energy roadmap: 2011 - Publications - GOV.UK [WWW Document], n.d. URL https://www.gov.uk/government/publications/renewable-energy-roadmap (accessed 6.29.16a).

UK renewable energy roadmap: 2012 update - Publications - GOV.UK [WWW Document], n.d. URL https://www.gov.uk/government/publications/uk-renewable-energy-roadmap-update (accessed 6.29.16b).

UK renewable energy roadmap: 2013 update - Publications - GOV.UK [WWW Document], n.d. URL https://www.gov.uk/government/publications/uk-renewable-energy-roadmap-second-update (accessed 6.29.16c).

Vachtsevanos, G.J., Lewis, F.L., Roemer, Mi., Hess, A., Wu, B., 2006. Intelligent fault diagnosis and prognosis for engineering systems. Wiley, Hoboken, N.J.

Val, D.V., 2009. Aspects of reliability assessment of tidal stream turbines, in: Proceedings of the 10th International Conference on Structural Safety and Reliability (ICOSSAR), Osaka, Japan. pp. 13–17.

Val, D.V., Chernin, L., Yurchenko, D.V., 2014. Reliability analysis of rotor blades of tidal stream turbines. Reliability Engineering & System Safety 121, 26–33. doi:10.1016/j.ress.2013.07.011

Walker, J.M., Flack, K.A., Lust, E.E., Schultz, M.P., Luznik, L., 2014. Experimental and numerical studies of blade roughness and fouling on marine current turbine performance. Renewable Energy 66, 257–267. doi:10.1016/j.renene.2013.12.012

Walker, J.M., Flack, K.A., Lust, E.E., Schultz, M.P., Luznik, L., 2013. The effects of blade roughness and fouling on marine current turbine performance, in: 10th European Wave and Tidal Energy Conference. pp. 1–10.

Waters, N., Beaujean, P.-P., Vendittis, D.J., 2013. Targeting faulty bearings for an ocean turbine dynamometer. International Journal of Prognostics and Health Management 4.

Weller, S.D., Thies, P.R., Gordelier, T., Johanning, L., 2015. Reducing Reliability Uncertainties for Marine Renewable Energy. Journal of Marine Science and Engineering 3, 1349–1361. doi:10.3390/jmse3041349

Whitby, B., Ugalde-Loo, C.E., 2014. Performance of Pitch and Stall Regulated Tidal Stream Turbines. IEEE Transactions on Sustainable Energy 5, 64–72. doi:10.1109/TSTE.2013.2272653

Wolfram, J., 2006. On Assessing the Reliability and Availability of Marine Energy Converters: The Problems of a New Technology. Proceedings of the Institution of Mechanical Engineers, Part O: Journal of Risk and Reliability 220, 55–68. doi:10.1243/1748006XJRR7

World-leading tidal energy system achieves 5GWh milestone [WWW Document], n.d. URL http://www.marineturbines.com/News/2012/09/05/world-leading-tidal-energy-system-achieves-5gwh-milestone (accessed 6.29.16).

Xie, L., 2013. A new method for failure modes and effects analysis and its application in a hydrokinetic turbine system.

Yang, W., 2014. Condition Monitoring the Drive Train of a Direct Drive Permanent Magnet Wind Turbine Using Generator Electrical Signals. Journal of Solar Energy Engineering 136, 21008.

Yang, W., Jiang, J., Tavner, P.J., Crabtree, C.J., 2008a. Monitoring wind turbine condition by the approach of Empirical Mode Decomposition, in: International Conference on Electrical Machines and Systems, 2008. ICEMS 2008. Presented at the International Conference on Electrical Machines and Systems, 2008. ICEMS 2008, pp. 736–740.

Yang, W., Tavner, P.J., Crabtree, C.J., Wilkinson, M., 2010. Cost-Effective Condition Monitoring for Wind Turbines. Industrial Electronics, IEEE Transactions on 57, 263–271. doi:10.1109/TIE.2009.2032202

Yang, W., Tavner, P.J., Wilkinson, M., 2008b. Condition monitoring and fault diagnosis of a wind turbine with a synchronous generator using wavelet transforms, in: 4th IET Conference on Power Electronics, Machines and Drives, 2008. PEMD 2008. Presented at the 4th IET Conference on Power Electronics, Machines and Drives, 2008. PEMD 2008, pp. 6–10.

Yang, W., Tavner, P.J., Wilkinson, M.R., 2009. Condition monitoring and fault diagnosis of a wind turbine synchronous generator drive train. IET Renewable Power Generation 3, 1–11. doi:10.1049/iet-rpg:20080006

Za Hyers, R.W., Mc Gowan, J.G., 2006. Condition monitoring and prognosis of utility scale wind turbine. Energy Material 1, 187–203.

Zeng, J., Lu, D., Zhao, Y., Zhang, Z., Qiao, W., Gong, X., 2013. Wind turbine fault detection and isolation using support vector machine and a residual-based method, in: American Control Conference (ACC), 2013. IEEE, pp. 3661–3666.

Zhang, X.-P., Zeng, P., 2013. Marine Energy Technology. Proceedings of the IEEE 101, 862–865. doi:10.1109/JPROC.2013.2244735

A. Appendix: Naïve Bayes Classification Results.

A1. Initial Steady State Simulations

Table A.1: Naïve Bayes classifier results for rotor fault detection for the STFT C imbalance criteria, TI = 0.5%.

Condition (Class) / Condition (Data)	No Fault	Fault
No Fault	1	0
Offset 0.5°	0	1
Offset 3°	0	1
Offset 6°	0	1

Table A.2: Naïve Bayes classifier results for rotor fault diagnosis for the STFT C imbalance criteria, TI = 0.5%.

Condition (Class) / Condition (Data)	No Fault	Offset 0.5°	Offset 3°	Offset 6°
No Fault	1	0	0	0
Offset 0.5°	0	1	0	0
Offset 3°	0	0	0.86	0.14
Offset 6°	0	0	0.20	0.80

Table A.3: Naïve Bayes classifier results for rotor fault detection for the STFT C imbalance criteria, TI = 1%.

Condition (Class) / Condition (Data)	No Fault	Fault
No Fault	0.92	0.08
Offset 0.5°	0.05	0.95
Offset 3°	0	1
Offset 6°	0	1

Table A.4: Naïve Bayes classifier results for rotor fault diagnosis for the STFT C imbalance criteria, TI = 1%.

Condition (Class) / Condition (Data)	No Fault	Offset 0.5°	Offset 3°	Offset 6°
No Fault	0.93	0.07	0	0
Offset 0.5°	0.05	0.95	0	0
Offset 3°	0	0	0.58	0.42
Offset 6°	0	0.01	0.20	0.79

Table A.5: Naïve Bayes classifier results for rotor fault detection for the STFT C imbalance criteria, TI = 2%.

Condition (Class) / Condition (Data)	No Fault	Fault
No Fault	0.76	0.24
Offset 0.5°	0.35	0.65
Offset 3°	0	1
Offset 6°	0	1

Table A.6: Naïve Bayes classifier results for rotor fault diagnosis for the STFT C imbalance criteria, TI = 2%.

Condition (Class) / Condition (Data)	No Fault	Offset 0.5°	Offset 3°	Offset 6°
No Fault	0.84	0.15	0	0.01
Offset 0.5°	0.43	0.42	0.05	0.10
Offset 3°	0.01	0.08	0.66	0.25
Offset 6°	0	0.20	0.44	0.36

Table A.7: Naïve Bayes classifier results for rotor fault detection for the STFT C_l imbalance criteria, TI = 0.5%.

Condition (Class) / Condition (Data)	No Fault	Fault
No Fault	1	0
Offset 0.5°	0.02	0.98
Offset 3°	0	1
Offset 6°	0	1

Table A.8: Naïve Bayes classifier results for rotor fault diagnosis for the STFT C_l imbalance criteria, TI = 0.5%

Condition (Class) / Condition (Data)	No Fault	Offset 0.5°	Offset 3°	Offset 6°
No Fault	1	0	0	0
Offset 0.5°	0.04	0.96	0	0
Offset 3°	0	0	0.88	0.12
Offset 6°	0	0	0.21	0.79

Table A.9: Naïve Bayes classifier results for rotor fault detection for the STFT C_l imbalance criteria, TI = 1%.

Condition (Class) / Condition (Data)	No Fault	Fault
No Fault	0.93	0.07
Offset 0.5°	0.05	0.95
Offset 3°	0	1
Offset 6°	0	1

Table A.10: Naïve Bayes classifier results for rotor fault diagnosis for the STFT C_l imbalance criteria, TI = 1%

Condition (Class) / Condition (Data)	No Fault	Offset 0.5°	Offset 3°	Offset 6°
No Fault	0.92	0.08	0	0
Offset 0.5°	0.04	0.96	0	0
Offset 3°	0	0	0.60	0.40
Offset 6°	0	0.03	0.23	0.74

Table A.11: Naïve Bayes classifier results for rotor fault detection for the STFT Cl imbalance criteria, TI = 2%.

Condition (Class) / Condition (Data)	No Fault	Fault
No Fault	0.63	0.37
Offset 0.5°	0.23	0.77
Offset 3°	0.00	1.00
Offset 6°	0.00	1.00

Table A.12: Naïve Bayes classifier results for rotor fault diagnosis for the STFT Cl imbalance criteria, TI = 2%

Condition (Class) / Condition (Data)	No Fault	Offset 0.5°	Offset 3°	Offset 6°
No Fault	0.62	0.37	0.00	0.02
Offset 0.5°	0.22	0.60	0.07	0.11
Offset 3°	0.00	0.06	0.71	0.23
Offset 6°	0.00	0.14	0.51	0.34

Table A.13: Naïve Bayes classifier results for rotor fault detection for the EMD C imbalance criteria, TI = 0.5%.

Condition (Class) / Condition (Data)	No Fault	Fault
No Fault	0.46	0.54
Offset 0.5°	0.19	0.81
Offset 3°	0.03	0.97
Offset 6°	0.00	1.00

Table A.14: Naïve Bayes classifier results for rotor fault diagnosis for the EMD C imbalance criteria, TI = 0.5%.

Condition (Class) / Condition (Data)	No Fault	Offset 0.5°	Offset 3°	Offset 6°
No Fault	0.97	0.00	0.01	0.01
Offset 0.5°	0.95	0.00	0.01	0.03
Offset 3°	0.76	0.00	0.07	0.17
Offset 6°	0.86	0.00	0.04	0.09

Table A.15: Naïve Bayes classifier results for rotor fault detection for the EMD C imbalance criteria, TI = 1%.

Condition (Class) / Condition (Data)	No Fault	Fault
No Fault	0.15	0.85
Offset 0.5°	0.07	0.93
Offset 3°	0.02	0.98
Offset 6°	0.03	0.97

Table A.16: Naïve Bayes classifier results for rotor fault diagnosis for the EMD C imbalance criteria, TI = 1%.

Condition (Class) / Condition (Data)	No Fault	Offset 0.5°	Offset 3°	Offset 6°
No Fault	0.90	0.00	0.02	0.08
Offset 0.5°	0.88	0.00	0.02	0.10
Offset 3°	0.57	0.00	0.09	0.34
Offset 6°	0.79	0.00	0.04	0.17

Table A.17: Naïve Bayes classifier results for rotor fault detection for the EMD C imbalance criteria, TI = 2%.

Condition (Class) / Condition (Data)	No Fault	Fault
No Fault	0.15	0.85
Offset 0.5°	0.23	0.77
Offset 3°	0.03	0.97
Offset 6°	0.06	0.94

Table A.18: Naïve Bayes classifier results for rotor fault detection for the EMD C imbalance criteria, TI = 2%.

Condition (Class) / Condition (Data)	No Fault	Offset 0.5°	Offset 3°	Offset 6°
No Fault	0.01	0.90	0.02	0.07
Offset 0.5°	0.00	0.93	0.01	0.05
Offset 3°	0.02	0.72	0.05	0.21
Offset 6°	0.02	0.79	0.04	0.15

Table A.19: Naïve Bayes classifier results for rotor fault detection for the EMD C_l imbalance criteria, TI = 0.5%.

Condition (Class) / Condition (Data)	No Fault	Fault
No Fault	0.45	0.55
Offset 0.5°	0.19	0.81
Offset 3°	0.03	0.97
Offset 6°	0.00	1.00

Table A.20: Naïve Bayes classifier results for rotor fault diagnosis for the EMD C_l imbalance criteria, TI = 0.5%.

Condition (Class) / Condition (Data)	No Fault	Offset 0.5°	Offset 3°	Offset 6°
No Fault	0.65	0.14	0.06	0.15
Offset 0.5°	0.44	0.17	0.15	0.25
Offset 3°	0.09	0.18	0.47	0.26
Offset 6°	0.05	0.23	0.36	0.36

Table A.21: Naïve Bayes classifier results for rotor fault detection for the EMD C_l imbalance criteria, TI = 1%.

Condition (Class) / Condition (Data)	No Fault	Fault
No Fault	0.14	0.86
Offset 0.5°	0.07	0.93
Offset 3°	0.02	0.98
Offset 6°	0.03	0.97

Table A.22: Naïve Bayes classifier results for rotor fault diagnosis for the EMD C_l imbalance criteria, TI = 1%.

Condition (Class) / Condition (Data)	No Fault	Offset 0.5°	Offset 3°	Offset 6°
No Fault	0.29	0.18	0.20	0.33
Offset 0.5°	0.15	0.13	0.28	0.43
Offset 3°	0.05	0.02	0.70	0.23
Offset 6°	0.07	0.09	0.44	0.40

Table A.23: Naïve Bayes classifier results for rotor fault detection for the EMD C_l imbalance criteria, TI = 2%.

Condition (Class) / Condition (Data)	No Fault	Fault
No Fault	0.14	0.86
Offset 0.5°	0.21	0.79
Offset 3°	0.02	0.98
Offset 6°	0.05	0.95

Table A.24: Naïve Bayes classifier results for rotor fault detection for the EMD C_l imbalance criteria, TI = 2%.

Condition (Class) / Condition (Data)	No Fault	Offset 0.5°	Offset 3°	Offset 6°
No Fault	0.41	0.22	0.24	0.13
Offset 0.5°	0.53	0.18	0.21	0.09
Offset 3°	0.11	0.12	0.38	0.39
Offset 6°	0.26	0.13	0.31	0.30

A2. Flume Testing

Table A.25: Naïve Bayes classifier results for rotor fault detection for the STFT based C_l imbalance criteria.

Condition (Class) / Condition (Data)	No Fault	Fault
No Fault	0.10	0.90
Offset 3°	0.03	0.97
Offset 6°	0.00	1.00
Offset Two Blades	0.10	0.90

Table A.26: Naïve Bayes classifier results for rotor fault diagnosis for the STFT based Cl imbalance criteria.

Condition (Class) / Condition (Data)	No Fault	Offset 3°	Offset 6°	Offset Two Blades
No Fault	0.60	0.18	0.00	0.22
Offset 3°	0.27	0.66	0.00	0.07
Offset 6°	0.00	0.03	0.97	0.00
Offset Two Blades	0.34	0.20	0.00	0.47

Table A.27: Naïve Bayes classifier results for rotor fault detection for the STFT based C_l imbalance criteria after smoothing.

Condition (Class) / Condition (Data)	No Fault	Fault
No Fault	0.77	0.23
Offset 3°	0.09	0.91
Offset 6°	0.00	1.00
Offset Two Blades	0.40	0.60

Table A.28: Naïve Bayes classifier results for rotor fault diagnosis for the STFT based Cl imbalance criteria after smoothing.

Condition (Class) / Condition (Data)	No Fault	Offset 3°	Offset 6°	Offset Two Blades
No Fault	0.85	0.03	0.01	0.12
Offset 3°	0.22	0.77	0.01	0.00
Offset 6°	0.00	0.00	1.00	0.00
Offset Two Blades	0.35	0.00	0.01	0.64

Table A.29: Naïve Bayes classifier results for rotor fault detection for the HHT based C_l imbalance criteria.

Condition (Class) / Condition (Data)	No Fault	Fault
No Fault	0.12	0.88
Offset 3°	0.02	0.98
Offset 6°	0.00	1.00
Offset Two Blades	0.12	0.88

Table A.30: Naïve Bayes classifier results for rotor fault diagnosis for the HHT based C_l imbalance criteria.

Condition (Class) / Condition (Data)	No Fault	Offset 3°	Offset 6°	Offset Two Blades
No Fault	0.41	0.12	0.03	0.44
Offset 3°	0.77	0.11	0.02	0.10
Offset 6°	0.03	0.46	0.51	0.00
Offset Two Blades	0.39	0.05	0.00	0.56

Table A.31: Naïve Bayes classifier results for rotor fault detection for the HHT based C_l imbalance criteria after smoothing.

Condition (Class) / Condition (Data)	No Fault	Offset Two Blades
No Fault	0.38	0.62
Offset 3°	0.14	0.86
Offset 6°	0.00	1.00
Offset Two Blades	0.35	0.65

Table 10.32: Naïve Bayes classifier results for rotor fault diagnosis for the HHT based C_l imbalance criteria after Smoothing.

Condition (Class) / Condition (Data)	No Fault	Offset 3°	Offset 6°	Offset Two Blades
No Fault	0.70	0.18	0.00	0.12
Offset 3°	0.42	0.58	0.00	0.00
Offset 6°	0.00	0.24	0.76	0.00
Offset Two Blades	0.53	0.09	0.00	0.38

Table A.33: Naïve Bayes classifier results for rotor fault diagnosis using ensemble of STFT based Cl imbalance criteria and C_p error.

Condition (Class) / Condition (Data)	No Fault	Fault
No Fault	0.02	0.98
Offset 3°	0.00	1.00
Offset 6°	0.00	1.00
Offset Two Blades	0.00	1.00

Table A.34: Naïve Bayes classifier results for rotor fault diagnosis using ensemble of STFT based Cl imbalance criteria and Cp error.

Condition (Class) / Condition (Data)	No Fault	Offset 3°	Offset 6°	Offset Two Blades
No Fault	0.78	0.22	0.00	0.00
Offset 3°	0.01	0.99	0.00	0.00
Offset 6°	0.00	0.00	1.00	0.00
Offset Two Blades	0.00	0.00	0.00	1.00

Table A.35: Naïve Bayes classifier results for rotor fault detection using ensemble of STFT based C_l imbalance criteria after smoothing and Cp error.

Condition (Class) / Condition (Data)	No Fault	Fault
No Fault	0.05	0.95
Offset 3°	0.00	1.00
Offset 6°	0.00	1.00
Offset Two Blades	0.00	1.00

Table A.36: Naïve Bayes classifier results for rotor fault diagnosis using ensemble of STFT based C_l imbalance criteria after smooth and C_p error.

Condition (Class) / Condition (Data)	No Fault	Offset 3°	Offset 6°	Offset Two Blades
No Fault	0.96	0.04	0.00	0.00
Offset 3°	0.01	0.99	0.00	0.00
Offset 6°	0.00	0.00	1.00	0.00
Offset Two Blades	0.00	0.00	0.00	1.00

Table A.37: Naïve Bayes classifier results for rotor fault detection using ensemble of HHT based C_l imbalance criteria and Cp error.

Condition (Class) / Condition (Data)	No Fault	Fault
No Fault	0.82	0.18
Offset 3°	0.30	0.70
Offset 6°	0.00	1.00
Offset Two Blades	0.00	1.00

Table 10.38: Naïve Bayes classifier results for rotor fault diagnosis using ensemble of HHT based C_l imbalance criteria and C_p error.

Condition (Class) / Condition (Data)	No Fault	Offset 3°	Offset 6°	Offset Two Blades
No Fault	0.98	0.02	0.00	0.00
Offset 3°	0.10	0.90	0.00	0.00
Offset 6°	0.00	0.00	1.00	0.00
Offset Two Blades	0.00	0.00	0.00	1.00

Table A.39: Naïve Bayes classifier results for rotor fault detection using ensemble of HHT based C_l imbalance criteria after smoothing and Cp error.

Condition (Class) / Condition (Data)	No Fault	Fault
No Fault	0.86	0.14
Offset 3°	0.21	0.79
Offset 6°	0.00	1.00
Offset Two Blades	0.00	1.00

Table A.40: Naïve Bayes classifier results for rotor fault diagnosis using ensemble of HHT based Cl imbalance criteria after smoothing and Cp error.

Condition (Class) / Condition (Data)	No Fault	Offset 3°	Offset 6°	Offset Two Blades
No Fault	0.98	0.02	0.00	0.00
Offset 3°	0.02	0.98	0.00	0.00
Offset 6°	0.00	0.00	1.00	0.00
Offset Two Blades	0.00	0.00	0.00	1.00

A3. Drive Train Simulations.

Table A.41: Naïve Bayes classifier results for rotor fault detection for the STFT based C_l imbalance criteria for the optimal λ control.

Condition (Class) / Condition (Data)	No Fault	Fault
No Fault	0.45	0.55
Offset 3°	0.00	1.00
Offset 6°	0.00	1.00
Offset Two Blades	0.60	0.40

Table A.42: Naïve Bayes classifier results for rotor fault diagnosis for the STFT based C_l imbalance criteria for the optimal λ control.

Condition (Class) / Condition (Data)	No Fault	Offset 3°	Offset 6°	Offset Two Blades
No Fault	0.46	0.29	0.00	0.25
Offset 3°	0.00	0.87	0.03	0.11
Offset 6°	0.00	0.00	1.00	0.00
Offset Two Blades	0.67	0.02	0.00	0.31

Table A.43: Naïve Bayes classifier results for rotor fault detection for the STFT based C_l imbalance criteria for the fixed speed control.

Condition (Class) / Condition (Data)	No Fault	Fault
No Fault	0.13	0.88
Offset 3°	0.00	1.00
Offset 6°	0.00	1.00
Offset Two Blades	0.10	0.90

Table A.44: Naïve Bayes classifier results for rotor fault diagnosis for the STFT based C_l imbalance criteria for the fixed speed control.

Condition (Class) / Condition (Data)	No Fault	Offset 3°	Offset 6°	Offset Two Blades
No Fault	0.14	0.19	0.00	0.67
Offset 3°	0.00	0.63	0.00	0.37
Offset 6°	0.00	0.00	1.00	0.00
Offset Two Blades	0.10	0.25	0.00	0.65

Table 10.45: Naïve Bayes classifier results for rotor fault detection for the HHT based C_l imbalance criteria for the optimal λ control.

Condition (Class) / Condition (Data)	No Fault	Fault
No Fault	0.79	0.21
Offset 3°	0.15	0.85
Offset 6°	0.00	1.00
Offset Two Blades	0.01	0.99

Table A.46: Naïve Bayes classifier results for rotor fault diagnosis for the HHT based C_l imbalance criteria for the optimal λ control

Condition (Class) / Condition (Data)	No Fault	Offset 3°	Offset 6°	Offset Two Blades
No Fault	0.88	0.12	0.00	0.00
Offset 3°	0.23	0.29	0.00	0.48
Offset 6°	0.00	0.07	0.24	0.69
Offset Two Blades	0.02	0.17	0.10	0.71

Table A.47: Naïve Bayes classifier results for rotor fault detection for the HHT based C_l imbalance criteria for the fixed speed control

Condition (Class) / Condition (Data)	No Fault	Fault
No Fault	0.00	1.00
Offset 3°	0.00	1.00
Offset 6°	0.00	1.00
Offset Two Blades	0.00	1.00

Table 10.48: Naïve Bayes classifier results for rotor fault diagnosis for the HHT based C_l imbalance criteria for the fixed speed control.

Condition (Class) / Condition (Data)	No Fault	Offset 3°	Offset 6°	Offset Two Blades
No Fault	0.00	0.07	0.49	0.45
Offset 3°	0.00	0.23	0.10	0.67
Offset 6°	0.00	0.34	0.24	0.43
Offset Two Blades	0.01	0.52	0.10	0.36